Geofísica Internacional

Revista Trimestral Publicada por el Instituto de Geofísica de la
Universidad Nacional Autónoma de México

— Geofísica Internacional —

Contents

The 6 September 1997 (Mw4.5) Coatzacoalcos-Minatitlán, Veracruz, Mexico earthquake: implications for tectonics and seismic hazard of the region.

Shri Krishna Singh, Javier Francisco Pacheco, Xyoli Pérez-Campos, Mario Ordaz, Eduardo Reinoso

289

Assessment of groundwater flow in volcanic faulted areas. A study case in Queretaro, Mexico

Gil Humberto Ochoa-González, Dora Carreón-Freyre[*], Mariano Cerca and Margarita López-Martínez

Resumen

En este trabajo se integra la estratigrafía local y fallas como restricciones para un modelo numérico de flujo del agua subterránea en la parte norte del acuífero fallado del Valle de Querétaro. La información geológica de base fue establecida a partir de la reinterpretación de registros litológicos de pozos, fechamiento isotópico $^{40}Ar*/^{39}Ar$ de rocas y cartografía de campo. En particular, la datación isotópica permitió obtener el tiempo de emplazamiento de un dique magmático a lo largo de la falla de El Nabo. El aumento de la tasa de flujo y la temperatura en el pozo El Nabo sugieren que la falla y el dique transportan un flujo regional. Un modelo numérico fue implementado para evaluar las contribuciones de fallas y estructuras volcánicas en el flujo general de agua subterránea. El modelo realizado con el software *Visual-Modflow* y código *Modflow* 2000 fue parcialmente restringido por los resultados de una prueba de bombeo en pozo "El Nabo", el pozo más profundo (Lat. 20 ° 42 '14 "N, Long. 100 ° 28'45" O, aproximadamente de 1000 m de profundidad) ubicado en la zona de Querétaro. La interpretación de los resultados del modelo y las observaciones de campo sugieren que las fallas reciben un flujo regional, compartimentalizan el sistema, y son responsables de un importante aumento del gasto, de 6 a 47 l/s, cuando se la perforación del pozo El Nabo bajo de 850 m profundidad. El estudio que aquí se presenta permite la evaluación de fallas normales e intrusivos que determinan el flujo del agua subterránea y podría ser relevante para el conocimiento de la dinámica de flujo en valles volcánicos cercanos. El modelo numérico implementado basado en información geológica, permitió una mejor comprensión de los sistemas acuíferos complejos, lo que no se puede evaluar por métodos analíticos. Por otra parte puede ser una aplicación útil para una mejor interpretación de pruebas de bombeo y para añadir datos complementarios de otras pruebas y/o de análisis de hidrogeoquímica.

Palabras clave: Flujo de aguas subterráneas, sistema acuífero fallado, modelación numérica, estructuras volcánicas, diques, México.

G. H. Ochoa-González
Posgrado en Ciencias de la Tierra
Centro de Geociencias
Universidad Nacional Autónoma de México
Campus Juriquilla
Blvd. Juriquilla 3001
Col. Juriquilla, Querétaro, C.P. 76230
Querétaro, México

D. Carreón-Freyre[*]
Laboratorio de Mecánica de Geosistemas
Centro de Geociencias
Universidad Nacional Autónoma de México
Campus Juriquilla
Blvd. Juriquilla 3001
Col. Juriquilla, Querétaro, C.P. 76230
Querétaro, México
*Corresponding author: freyre@geociencias.unam.mx

M. Cerca
Laboratorio de Mecánica de Geosistemas
Centro de Geociencias
Universidad Nacional Autónoma de México
Campus Juriquilla
Campus Juriquilla
Blvd. Juriquilla 3001
Col. Juriquilla, Querétaro, C.P. 76230
Querétaro, México

M. López-Martínez
Departamento de Geología
Centro de Investigación Científica y Educación Superior de Ensenada
Carretera Ensenada-Tijuana No. 3918
Zona Playitas C.P. 22860
Ensenada, B.C., México

G. H. Ochoa-González, D. Carreón-Freyre, M. Cerca and M. López-Martínez

Abstract

This work integrates local stratigraphy and faults to constraint a numerical model of groundwater flow in the North area of the Valley of Queretaro aquifer. Basic geological information was established from the reinterpretation of well logs, $^{40}Ar^*/^{39}Ar$ dating of rocks, and field mapping. In particular, dating allowed to obtain the timing of emplacement of a magmatic dyke inferred to be emplaced along the El Nabo fault. The increase of flow rate and temperature in the El Nabo well suggest that the fault and dike transport a regional flow. A numerical model was implemented to evaluate the contributions of faulting and volcanic structures in the overall groundwater flow. The model, accomplished with the *Visual-Modflow* software and *Modflow* 2000 code, was partially constrained by the results of a pumping test in the El Nabo well, the deepest well (Lat. 20°42'14"N, Long. 100°28'45"W, ca. 1000 m depth) located in the Queretaro area. The interpretation of the model results and field observations suggest that faults collect the regional flow, compartmentalize the reservoir, and are responsible of the dramatic increase of flow rate from 6 to 47 l/s when drilling the El Nabo well below a depth of 850 m. The study presented here allowed the assessment of normal faults and intrusives determining groundwater flow and might be relevant to the knowledge of flow dynamics in nearby volcanic valleys. The analysis of the pumping test suggest the presence of two different groundwater flow systems: (1) a flow related with the limestone and shale unit and (2) a regional linear flow through faults. The implemented numerical model, based on geological information, allowed a better understanding of complex aquifer systems that cannot be evaluated by analytical methods. Moreover it can be a useful application for a better interpretation of pumping tests and to add complementary data of other pumping tests and/or hydrogeochemical analysis..

Key words: Groundwater flow, faulted aquifers, numerical modeling, volcanic structures, dykes, Mexicos.

Introduction

Understanding groundwater flow systems is crucial for the management of groundwater resources in Mexico because many areas in arid zones depend on groundwater as the main source for urban, agricultural, and industrial development. In the Valley of Queretaro Aquifer (VQA), many wells are drilled near or along major faults and the high variability of piezometric levels in relatively short distances evidence changes on hydraulic properties (Carreón-Freyre *et al*., 2005; Figure 1). Furthermore, the spatial distribution of extraction wells and drawdown zones in the VQA during the last 30 years suggests that faults compartmentalize the aquifer system (Carreón-Freyre *et al*., 2005). In the VQA, groundwater is extracted from depths greater than two hundred meters; at this depth, geological heterogeneity should be considered for evaluating groundwater flow patterns to allow an accurate estimation of groundwater resources. Thus, the VQA could be considered a faulted aquifer, where faults and fracture zones strongly influence the overall flow dynamics of the system (Caine *et al*., 1996; Allen and Michel, 1999) and the assessment of the hydrogeologic behavior of major structures can be as important as obtaining the hydraulic properties of the stratigraphic sequences. This work examines the role of major structures (e.g., faults and volcanic or plutonic bodies) as hydrogeological independent units, rather than only as hydraulic boundaries, and presents a numerical modeling of the groundwater flow conditions in the faulted VQA. Integration of representative geological data in the model included: (a) vertical variations by assigning a hydraulic conductivity (K) to each geological unit; (b) faults; (c) lateral truncation of the hydro-stratigraphic units and; (d) the presence of intrusive rocks (Walton, 1970; Ingebritsen *et al*., 2006; Zoback, 2007), in particular dikes (Kulkarni *et al*., 2000).

The study area is located in the northwestern part of the VQA system (Figure 1). The Valley of Queretaro is located in the central part of the Miocene to Recent Trans Mexican Volcanic Belt (TMVB; Ferrari, 2000; Alaniz-Alvarez *et al*., 2002) and is delimited by groups of N-S and NE-SW trending faults active at least since the Miocene (Alaniz-Alvarez *et al*., 2001). We aim at having a better understanding on the role of major structures in groundwater flow patterns in the VQA by integrating them in a numerical model.

Faulted aquifer systems

Previous works have documented the variations in hydraulics properties induced by the complex architecture of regional faults (MaClay and Small, 1983; López and Smith, 1995; López and Smith, 1996; Caine *et al*.,
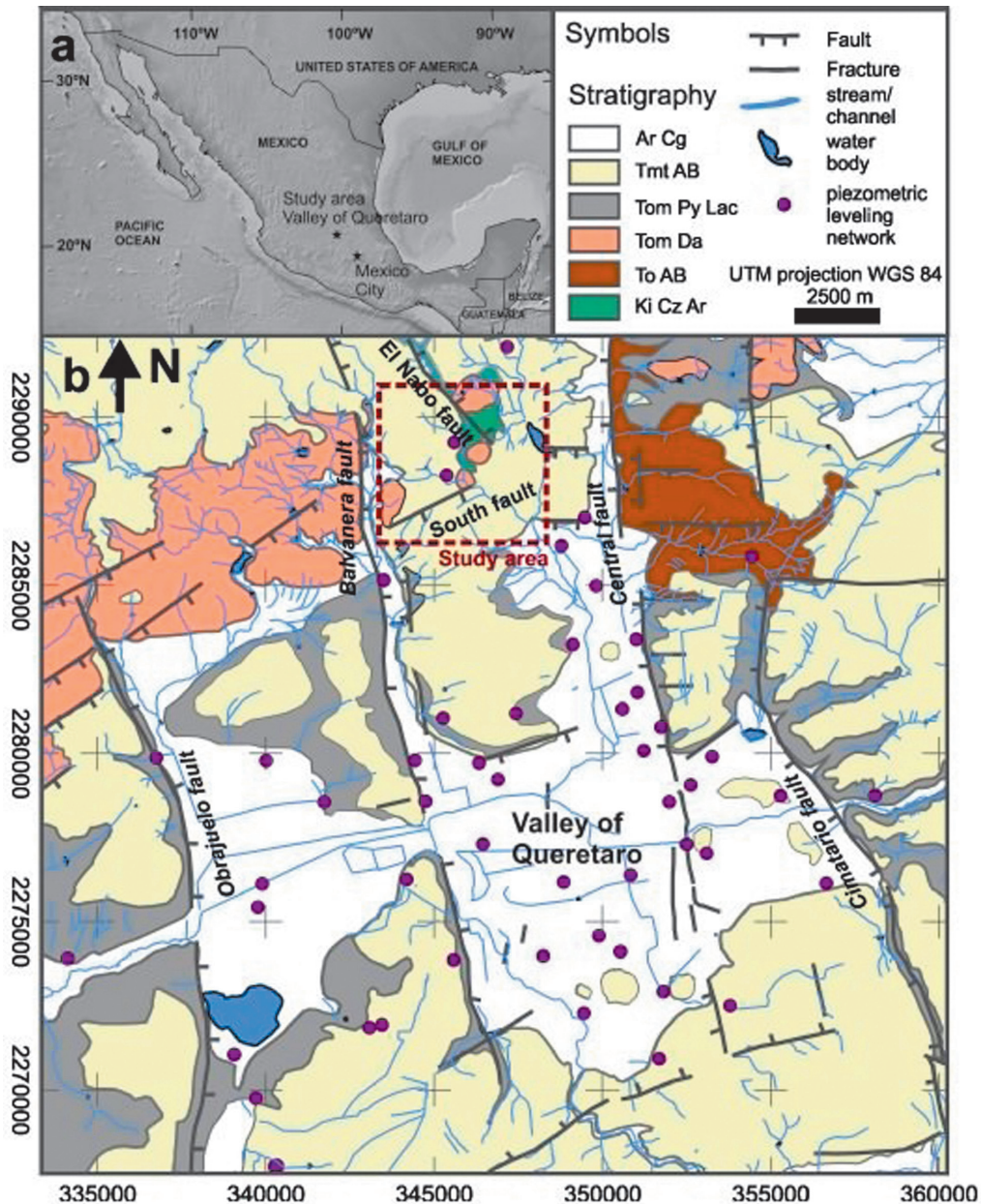
Figure 1. (a) The Valley of Queretaro is located in the central part of Mexico; (b) Geological map of the Valley of Queretaro. Dashed red square line on the geological map indicates the area considered in modeling, black lines are major faults. Green polygon represents the Cretaceous rocks exposed in the zone. Medium and light gray units represent Oligocene and Miocene volcanic rocks, respectively. (Modified form Carreon-Freyre *et al*., 2005).

1996; Allen and Michel, 1999; Carreón-Freyre *et al*., 2005; Anderson, 2006; Mayer *et al*., 2007; Delinom 2009; Rafini and Larocque, 2012). Anisotropy of hydraulic conductivity in faulted and stratified geological media determines groundwater flow patterns (Hsieh and Neuman, 1985). Regional faults represent an important heterogeneity influencing overall aquifer dynamics, not only determining preferential flow directions but also modifying their storage capacity (Pacheco, 2002; Burbey,

2008; Bense *et al*., 2013). Lithological changes and fractures in volcanic rocks, on the other hand, modify hydrogeological properties of geological units. A fault can be a preferential conduit for vertical flow, i.e., a "leaky fault", when the damaged zone is well developed and is laterally sealed (Zeidouni, 2012). Fault zones can also behave as leakage areas between aquifers by juxtaposing aquifers that would otherwise be separated by impermeable layers.

Major faults can behave as flow barriers or preferential channels depending on the hydraulic properties developed during deformation history (MaClay and Small, 1983; Caine *et al.*, 1996; Carreón-Freyre *et al.*, 2005; Mayer *et al.*, 2007; Delinom, 2009, Rafini and Larocque, 2012), or they can only separate units of different hydraulic conductivity (Allen and Michel, 1999; Mayer *et al.*, 2007); for instance, the vertical displacement of a fault can juxtapose permeable and impermeable layers in the direction perpendicular to the fault plane. In early models, faults were commonly considered as border conditions when assessing hydraulic parameters, even in stratified leaky systems (Rathod and Rushton, 1991).

The style of deformation and rupture of a fault zone strongly influences variations of its hydraulic properties. Caine *et al*. (1996) proposed four conceptual schemes for fault-related fluid-flow according to the distribution of conduits and barriers (localized and distributed) within fault plain. Anderson (2006) identified three essential hydraulic elements of a fault plane: (1) a low hydraulic conductivity core characterized by fault breccias, cataclastic rocks, and gouge; (2) an adjacent damaged zone characterized by an increase in the hydraulic conductivity caused by brecciation and fracturing and; (3) fresh unaltered rock with a characteristic hydraulic conductivity that can change in both sides of the fault because of the fault displacement.

A decrease in the hydraulic conductivity within a fault plane (flow barrier) can be associated with (Mayer *et al*., 2007; MaClay and Small, 1983): (1) cataclasis or grain size reduction; (2) juxtaposition of permeable and impermeable layers, displacements along the fault plane can decrease the possibility of flow through the fault and/or deviating flow along the fault; (3) rotation of plane and elongate detritus that became parallel to fault plane reducing the hydraulic conductivity in the orientation perpendicular to the plane; (4) presence of sedimentary materials with low hydraulic conductivity (e. g., clays) in the fault zone; and (5) chemical precipitation of mineral in the fault zone reducing permeability.

Furthermore, major faults often present associated or secondary planes and fractures that may cause contrasting hydraulic behaviors. In anisotropic media, each geological unit is represented by a hydraulic conductivity tensor considering three dimensional variations of hydraulic conductivity. In fractured rocks the tensor can align following the preferential orientation of fractures (Jourde *et al.*, 2007).

Geology of the Study Area (Northwest of the Valley of Queretaro Aquifer, VQA)

The regional geology of the VQA has been extensively studied in the last decades (Trejo-Moedano, 1989; Valdez-Moreno *et al.*, 1998; Aguirre-Díaz and Lopez-Martinez, 2001; Alaníz-Alvarez *et al.*, 2001, 2002; Carreón-Freyre *et al.*, 2005; Aguirre-Díaz *et al.*, 2005; Xu *et al.*, 2011). The Valley of Queretaro is a basin delimited by groups of N-S and NE-SW trending faults and volcanoes, located in the central part of the Trans Mexican Volcanic Belt (TMVB; Ferrari, 2000; Alaniz-Alvarez *et al.*, 2002; Figure 1). The N-S trending west-dipping Central fault is the eastern limit of the regional Queretaro graben (Figure 1). The other major faulting family (trending NE-SW) produced a nearly orthogonal pattern with the N-S system that has resulted in a mosaic formed by horsts, grabens, and half-grabens (Alaníz-Alvarez *et al.*, 2001, 2002; Carreón-Freyre *et al.*, 2005; Aguirre-Díaz *et al.*, 2005; Xu *et al.*, 2011) with varying vertical displacements, in some areas up to 400 m. Both fault systems have been active at least since the Miocene (e. g., Alaniz-Alvarez *et al.*, 2001; Zuñiga *et al.*, 2003; Aguirre-Díaz *et al.*, 2005) and both controlled the deposition of sediments and volcanic rocks in the VQA.

This study is focused on the northwestern part of the VQA (dashed square in Figures 1 and 2), a zone of groundwater recharge because of faulting (Conagua, 2003). The available information was compiled and integrated in a geological map with the hydrogeologic information of the VQA and surroundings. The local stratigraphy was established from the reinterpretation of well logs, ^{40}Ar*/^{39}Ar dating of magmatic rocks, and geologic mapping. The structural and stratigraphic setting of this part of the basin can be defined with sufficient detail and indicates that the geological evolution is more complex than hitherto recognized (Figure 2a). In this area, the Cenozoic volcanic and colluvial sequences cover partially the Cretaceous units that were uplifted by a shortening episode and thus are well exposed in the hanging wall. A schematic W-E geological cross section AA' was constructed using the lithological logs of water extraction wells available in the zone (Mompani II, El Nabo, UNAM, and El Salitre) (Figure 2).

The oldest sequence (Cretaceous) consists of volcano-sedimentary rocks, documented here for the first time in the Valley of Queretaro (Ki MsV, see below), a thick Albian limestone and shale sequence (Ki Cz, of 800 m thick), and a late Cretaceous shale and sandstone interbedded with argillaceous limestone (Ki Cz-Ar). The Cretaceous sequence is pervasively folded by shortening deformation.
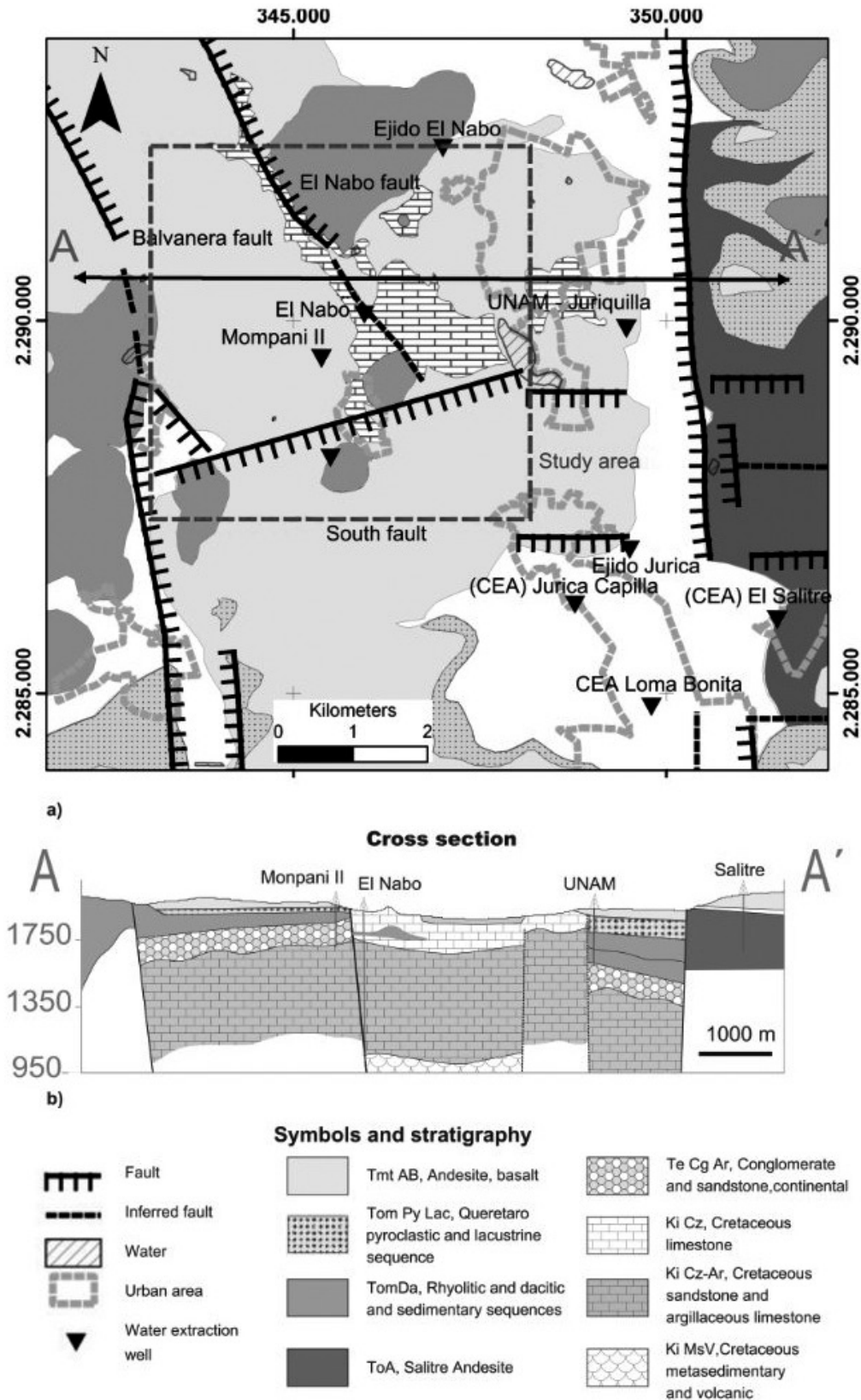
Figure 2. (a) Simplified geological map of the study area, the main structures considered in the model are the normal faults El Nabo, Balvanera and South. Logs of water extracting wells were projected to the A-A´ section shown in (b). The main stratigraphic units are presented in the cross section.

The Cenozoic sequence consists of a continental sedimentary unit with predominance of conglomerates and sandstone (Te Cg-Ar), overlain by a volcanic sequence with pyroclastic and sedimentary interbedded deposits. The Cenozoic sequence is fractured and affected by extensional faults. The Te Cg-Ar layer of probable Eocene age is present at the Mompani II well (at a depth of 200 m), and at the bottom of UNAM-Juriquilla and El Salitre

wells (Figure 3a). The volcanic rock sequence includes lavas such as the Salitre Andesite (ToA) and silicic domes (Tom Da; Juriquilla dacite; Alaniz-Alvarez *et al.*, 2002) of the Oligocene and early Miocene. An intrusive body of Oligocene age (ca. 30 Ma) is exposed in the zone of Juriquilla within the study area (Figure 2a). The pyroclastic and lacustrine sequences in the Queretaro area consist of tuffs and other pyroclastic deposits of 80 m in average of
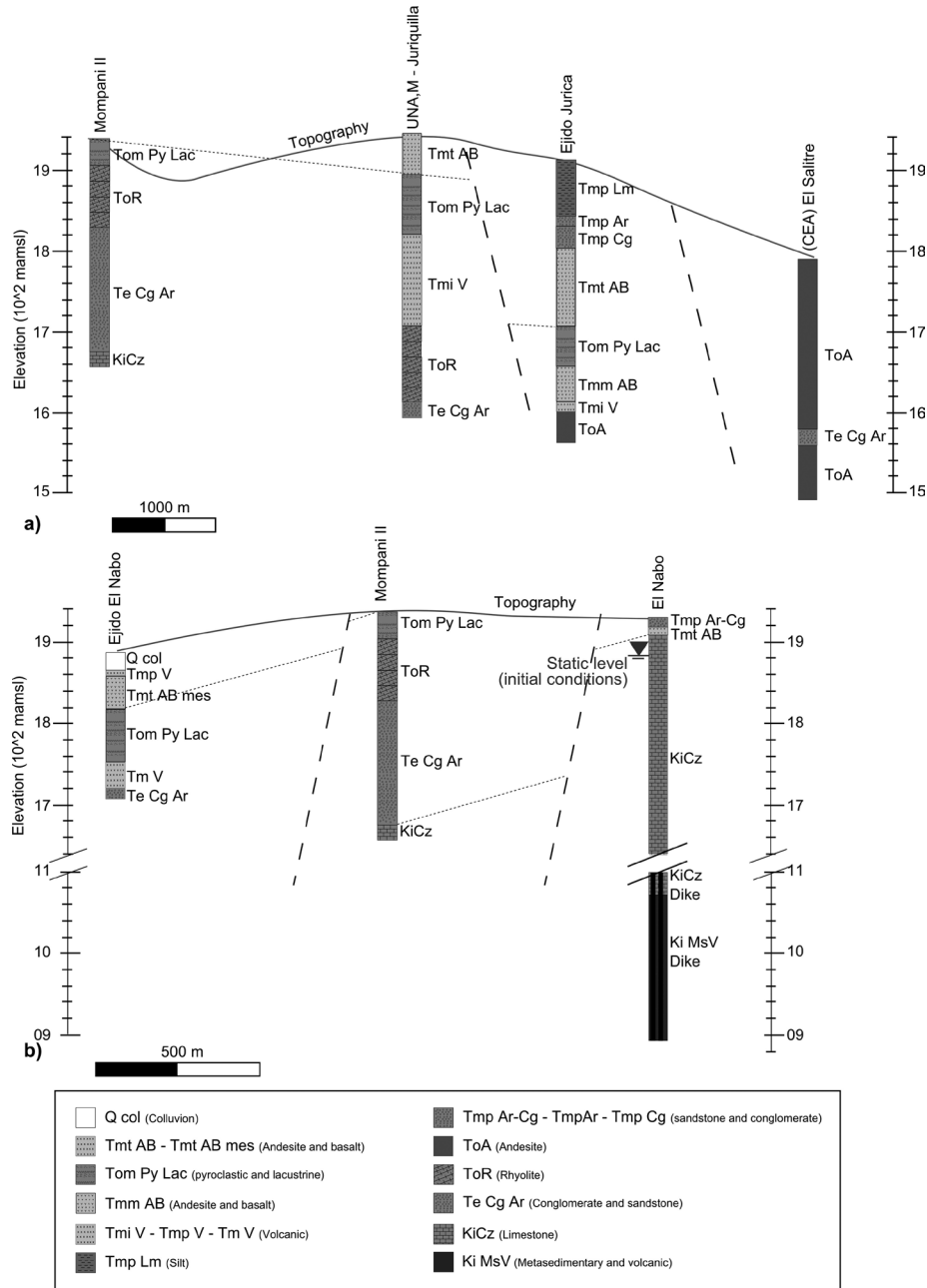
Figure 3. Stratigraphic correlation of the lithological logs of extraction wells used for the interpretation of the main structures and construction of the conceptual model. (a) Correlation of wells in the NW-SE direction including Mompani II, UNAM-Juriquilla, Ejido Jurica, and (CEA) El Salitre; (b) correlation in the N-S direction Ejido El Nabo, Mompani II, and El Nabo. The initial static water level in the El Nabo well is also shown.

thickness (Tom PyLac); and this unit includes the Ezequiel Montes Pumice, an important stratigraphic marker dated between 7.5 and 5.6 Ma (Aguirre-Díaz and López-Martínez, 2001). The coarse facies of this sequence (Tom PyLac) was the main hydrogeological unit exploited in the regional VQA, but is scarcely exposed in the study area, it is found in the upper part of the Mompani II log (Figure 3). Fissure basalts and lava flows (Tmt AB), ranging in age from 12 to 5 Ma (Aguirre-Díaz and López-Martínez, 2001) erupted from nearby volcanoes. The largest volcanic edifice, located 13 km to the NW from the studied area, is the La Joya Volcano ranging in age from 12 to 10 Ma (Valdez-Moreno *et al*., 1998).

The truncation and throw of the N-S trending extensional faults was inferred by the elevation differences among stratigraphic levels from the correlation of lithological logs presented in Figure 3. The vertical displacements are smaller than 200 m. From Figure 2b note that two additional buried faults nearby, and to west of UNAM well, were inferred in this work. Structurally, the study area is a block delimited by the major N-S trending *Balvanera* and *El Nabo* fault zones dipping to the northeast (Figure 4a). The South fault and other NE-SW trending fault segments delineate the limits of the block toward the south. Both faults systems have nearly vertical fault planes and their kinematics indicate dip-slip towards the center of the Queretaro Valley since Miocene time. These major faults include several parallel fault planes affecting areas with more than 50 m in width (Figure 4). Faults are partially exposed and their trace length was inferred by topography, field observations, and lithological correlations of well logs. The relative age of faulting in the region was analyzed in detail by Alaniz-Alvarez *et al* (2001); the older system corresponds to the South Fault that favors the emplacement of the Oligocene intrusive body. The Balvanera and El Nabo fault systems are younger and favor the Miocene volcanism through dykes emplaced along the faults planes (Figure 4). The *El Nabo Fault* is of particular relevance to this work, it is a nearly vertical fault partially exposed to the north of the study area where plateau lavas fill the hanging wall of the fault (solid line with thick marks in
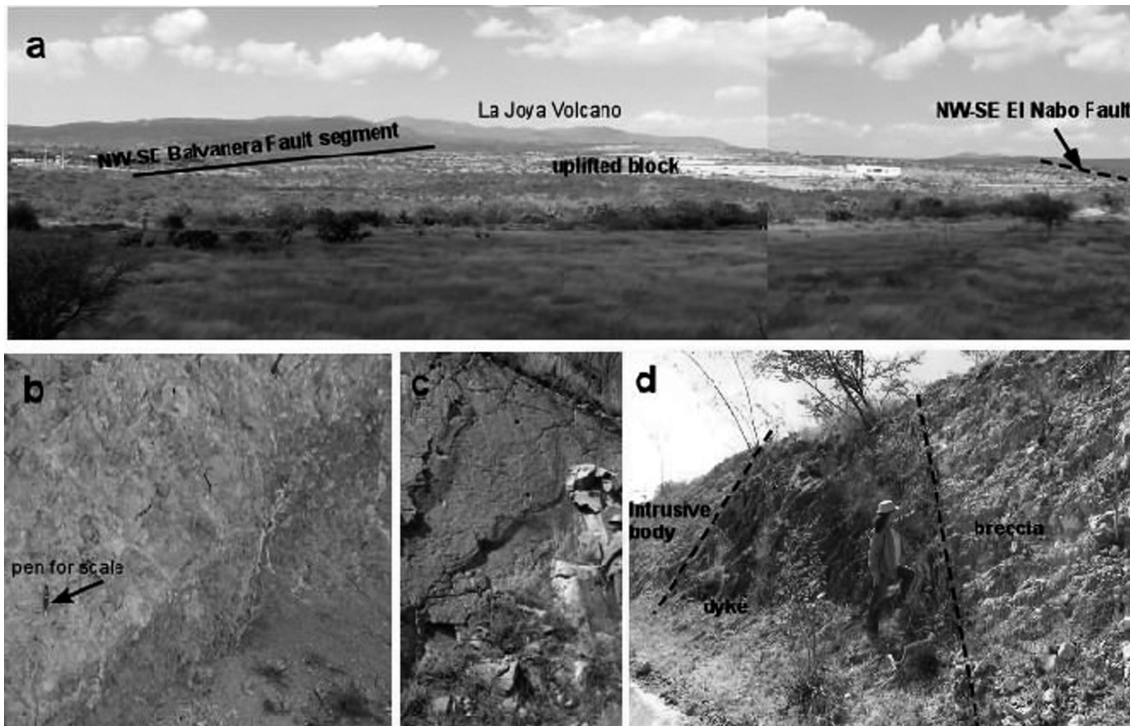
Figure 4. (a) General view to the NW of the study area, the escarp of the Balvanera fault can be observed, the trace of the El Nabo fault is inferred by a dotted line because it delimits NE side of the uplifted bock (horst). As reference the La Joya volcano is shown toward the NW of the study area; (b) close view in outcrop of the South Fault (pen for scale) showing the contact between the intrusive body at the left and evidence of hydrothermal activity; (c) outcrop of the intrusive body; (d) outcrop of a plane associated to the El Nabo fault zone, the contact with the intrusive body and the structure of a dyke with brecciated material are shown.

Figure 2a). Toward its southern part the fault is not clearly observed on surface but it can be inferred from the topographic relief and the interpretation of the stratigraphic records (dotted line in Figure 2a). A dyke emplaced along a fault plane parallel to El Nabo fault was observed at the surface northeastward of the El Nabo well (Figure 4b). All this information was integrated to constrain the numerical model.

Methodology

Stratigraphic correlation

The conceptual model of the study area is based on geological units with contrasting hydraulic properties, granular and fractured rock layers, truncated by major faults and volcanic edifices/bodies that may interrupt or favor lateral flows. Carreón-Freyre *et al*. (2005) correlated the hydrogeological units with lithostratigraphic units to describe the VQA and proposed a conceptual model of multilayer aquifer with groundwater flow varying from local to regional. The stratigraphic correlation of lithological logs for the Cenozoic was based on the reconnaissance of an andesitic-basaltic unit of late Miocene age, named Tmt AB, as an index layer. For instance, as shown in the record of the Ejido Jurica well (Figure 3a) the Tmt AB layer commonly is overlaid by a Miocene-Pliocene sedimentary unit, named Tmp Cg-Ar-Lm, and underlied by an Oligocene-Miocene pyroclastic and lacustrine unit, named Tom PyLac.

The Cretaceous units are more relevant to groundwater flow in this area and include sandstone and argillaceous sequences, limestone rocks, and a volcano-sedimentary sequence. These units were found during drilling of *El Nabo* well, which is the deepest in the study area and is located within a block where Tertiary sequences are partially eroded (Figure 3b). The contrasting stratigraphy and the vertical difference in elevation of the Ki Cz unit from 1680 to 1100 masl among the Mompani II and El Nabo records separated by approximately one kilometer suggested the presence of the El Nabo Fault at this location.

Drilling of the first 600 m depth of *El Nabo* well initiated in 2000 at this time the production of water was approximately 6 l/s. Extended drilling in *El Nabo* well from 600 to 1000 m depth was performed in 2007, the production of the well increased dramatically to 47 l/s after drilling at 850 m depth, that coincided with a lithological change from limestone to a volcano-sedimentary sequence (volcanic rocks and limestone) bearing biotite

minerals). Further evidence of the fault and its relevance to groundwater flow was obtained by the geochronological data of rock samples from the El Nabo well presented below.

Biotite age determination

In order to define the age of the basal volcanic unit, rock samples collected each 3 m during drilling from 800 to 1050 m depth were classified by the use of a 20x-40x stereoscopic magnifier, and some samples of interest were selected for thin section description. Biotite concentrates were selected for dating at depths between 850 and 950 m. These biotite concentrates were analyzed by the $^{40}Ar*/^{39}Ar$ technique at the Geochronology Lab in CICESE using a VG5400 mass spectrometer and a laser extraction system. The analytical details of the method can be consulted elsewhere (e.g., Cerca *et al*., 2007). Mineral concentrates were previously irradiated at the nuclear reactor of the University of McMaster in Hamilton, Ontario, Canada, using as monitor of irradiation two known-age samples of sanidine, FCT-2 of 27.84 ± 0.04 Ma and TCR-2 of 27.87 ± 0.04 Ma. All the experiments were made by step-heating by increasing the laser power from 0.2 to 8 watts and measuring the isotopic composition of argon released during each step. The reported age is calculated for each individual fraction and the integrated results adding individual steps in accordance to Hall (1981), and considering the corrections by discrimination, radioactive decay (Steiger & Jäger, 1977), the line background, and interference reactions from isotopes derived from Ca, Cl, and K. Results were grouped according to depth and size of the samples and are presented in a graph named age spectra. Correlation diagrams in which the relation $(^{40}Ar*/^{39}Ar_K)$ is given by the inverse of the intercept of the line defined by the data and is equivalent to the age in Ma are presented in a supplementary Figure (S1).

Integration of conceptual and numerical models

The conceptual model resulting from the interpretation of lithological logs, geological mapping, analysis of samples, and isotopic data is shown in Figure 5 (a, b). The wells integrated in the numerical model are El Nabo and Mompani II, 1100 and 250 m depth, respectively (Figure 5a). For the implementation of the numerical model, the volcanic sequences, sedimentary materials, and geological faults were considered as independent hydrogeological units; each one with a hydraulic conductivity tensor.

Groundwater simulation was accomplished with the *Visual-Modflow* software (Schlumberger Water Services, Inc) and the *Modflow* 2000 code (Harbaugh *et al*., 2000). In order to represent the hydraulic behavior of the mapped geological structures the numerical model was built with 100,000 cells, distributed in a horizontal grid of 100 x 100 cells in the N-S and E-W direction, each one represents a square of 2500 m². The model box is a square of 25 km² with a top surface with an average elevation of 1945 masl reproducing the actual topography and a flat surface at the bottom of the model (800 masl). The model box was divided in 10 horizontal layers of cells with variable thickness from the surface, according to the topography, to reach a bottom flat layer. Cells with similar hydraulic behavior were grouped to represent the geological units included in the model considering stratigraphic sequences and major structures. According to their physical characteristics, spatial distribution, and thickness, four geological units were defined in the conceptual model and represented in the numerical model shown in Figure 5a:

(1) *TomDa-Rhyolite*, this is the upper layer of the model, and groups the Cenozoic volcanic rocks including the volcanic and pyroclastic fractured sequences located above the piezometric level in the study area. These units, observed in the lithological records of the Ejido Jurica, UNAM-Juriquilla, and Ejido El Nabo wells, were not considered in the conceptual model because either they are located above the regional groundwater level (vadose zone) or are absent nearby the El Nabo well area (Figure 3). These units include: Late Miocene Andesites and Basalts (Tmt AB), Early Miocene Conglomerates and Sandstones Sandstones (Tmp Ar-Cg), and Quaternary Alluvium (Qal; Figure 2);
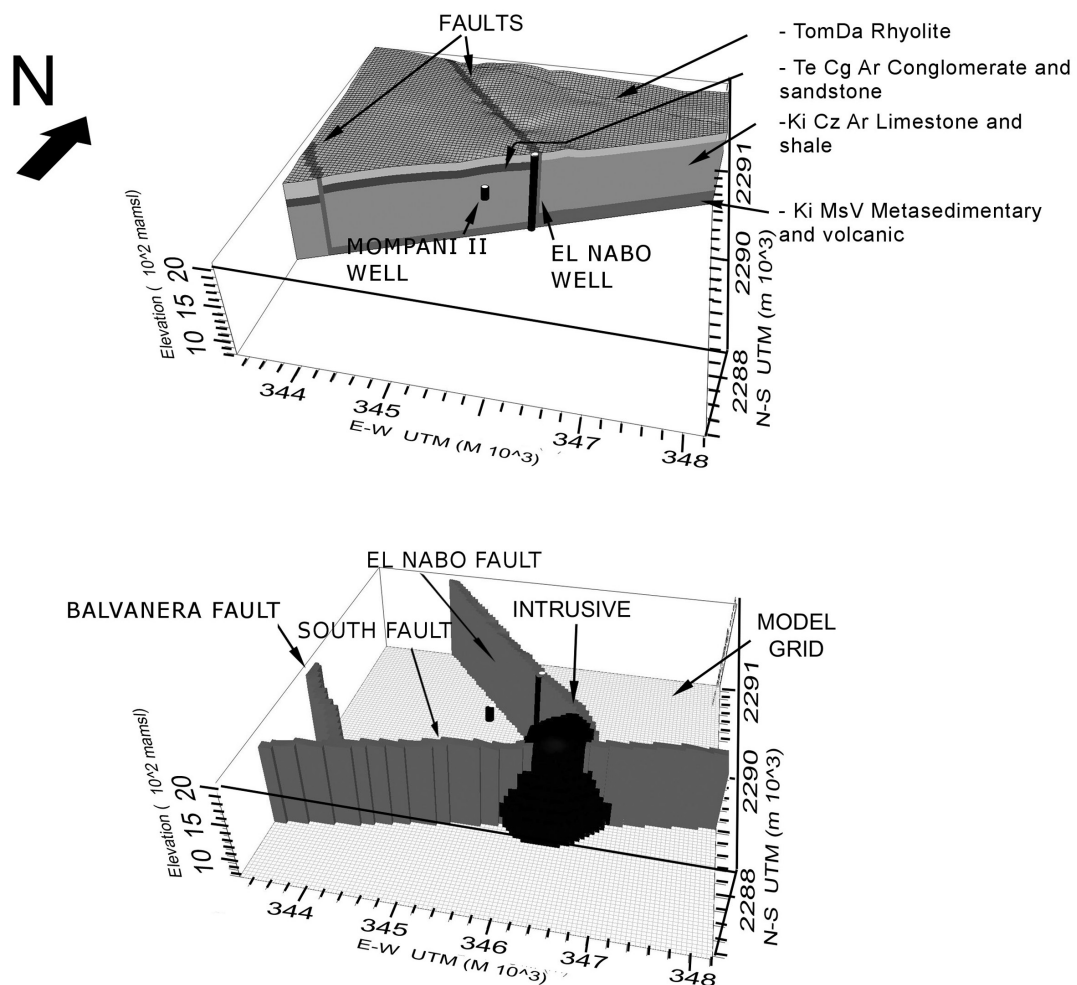
Figure 5. (a) Model box formed by an horizontal square grid of 25 km² and variable thickness layers. El Nabo and Mompani II wells were integrated in the model. Cells were grouped to represent hydro-stratigraphic layers with specific hydraulic properties. (b) Major geological structures in the model: (1) El Nabo fault-dyke, (2) Balvanera fault, (3) South fault and, (4) an intrusive body. The topographic surface is considered in the model.

(2) *Te Cg Ar Conglomerate and sandstone*, a sedimentary unit of conglomerate and sandstone found at the west of the El Nabo fault, was represented by a dark layer shown in the model of Figure 5a;

(3) *Ki Cz Ar Limestone and shale*, this unit includes Ki Cz and also the Ki Cz-Ar of sandstone and argillaceous limestone for modeling purposes, and;

(4) *Ki MsV Metasedimentary and volcanic* (Figure 5), located at the bottom of the model, corresponds in nature to the Cretaceous volcano-sedimentary unit (Ki MsV).

Faults are represented by groups of 50 m width vertically aligned cubic cells with specific hydraulic conductivity (gray cells in Figure 5b). The massive intrusive/subvolcanic body of 30 Ma is represented by a group of cells with a dome shape in the located central part of the model (black cells in Figure 5b). Major geological structures were considered as four individual units in the model: (5) the *El Nabo Fault*, (6) the *Balvanera Fault*, (7) the *South Fault* and, (8) the intrusive body placed in the lower part of the model (Figure 2 and Figure 5b).

Faulting and the intrusive body are thought to greatly influence groundwater by channelizing or arresting flow, or by interrupting the lateral continuity of the hydro stratigraphic units, such as the conglomerate and sandstone unit (*Te Cg-Ar)*. Truncation by faulting was suitable represented because each geological unit was composed by independent cells.

Once designed the geometry of the model, the initial and border conditions were established considering regional variations of the piezometric surface interpolated from 2004 and 2006 measurements (Figure 6). Previous work by Carreon-Freyre *et al*. (2005) indicated a regional gradient in the groundwater flow with a nearly north to south direction in the VQA. Regional piezometric were interpolated by krigging of the data from 40 water extraction wells located in the VQA, systematically monitored by the local agency of water (*Comisión Estatal de Aguas de Querétaro*, CEAQ) since 1996 (Carreón-Freyre *et al*., 2005). The interpolations show a persistent regional gradient with an approximate North-South trending. The wells located in the study area are El Nabo and Mompani II (Figure 1 and Figure 5a). A steady state numerical simulation was performed to establish the initial and boundary conditions (Figure 7b). Boundary effects were minimized by leaving a minimum radius of 2000 m from each well to the model borders.

Simulation of hydrodynamic conditions using the numerical model

A numerical simulation was performed to assess the hydrodynamic behavior of the system by the use of partial results of a pumping test. In the computational experiment the hydraulic properties were adjusted to correlate calculated and measured drawdown in the pumping and in one observation well.

A 260,000 s (72 hour) pumping test performed in the *El Nabo* well was simulated using the implemented numerical model. The location of the pumping test area is shown in Figure 2; the data record (water level and temperature) was made by a CTD Diver (*Schlumberger*) datalogger. This well is the single one in the region with about 1000 m in depth and therefore it was not possible to locate any observation well. The *Mompani II* well is located 1000 m to the SW, with a depth of 250 m. Because of the presence of the El Nabo Fault between the two wells no change in the hydraulic head during the pumping test was recorded at the Mompani II and thus, we assumed that groundwater flow in both wells were independent (possibly local and regional systems).

To accomplish the simulation, the hydraulic conductivities of the model and measured drawdown were closely fitted. We used a segment of the pumping test to simulate transient conditions generated by the pumping test. Continuous measurements of drawdown and temperature every 15 s are presented in Figure 8 (blue and green line respectively); blue squares indicate samples from the continuous measurements used for simulation. Because of the well depth only a part of the pumping test could be considered for adjustment. The first 10,800 s data (3 hours) were not considered because the pumping rate could not be maintained stable during this period and/ or a well storage effect should be considered (Allen and Michel, 1999), the same issues were considered for the interpretation of the recovery data.

Simulated and observed drawdown in the segment between 10,800 and 250,000 s (3 and 69 hours) of the El Nabo test were fitted by adjusting the hydrogeological properties of the main units (e.g., Allen and Michel, 1999). The estimation of these properties was achieved using the PEST (*Parameter Estimation Software*) algorithm (Harbaugh *et al*., 2000; Doherty, 2005) trough *Visual-Modflow*. The finite differences *Modflow* algorithm solved groundwater flow by adjusting hydraulic
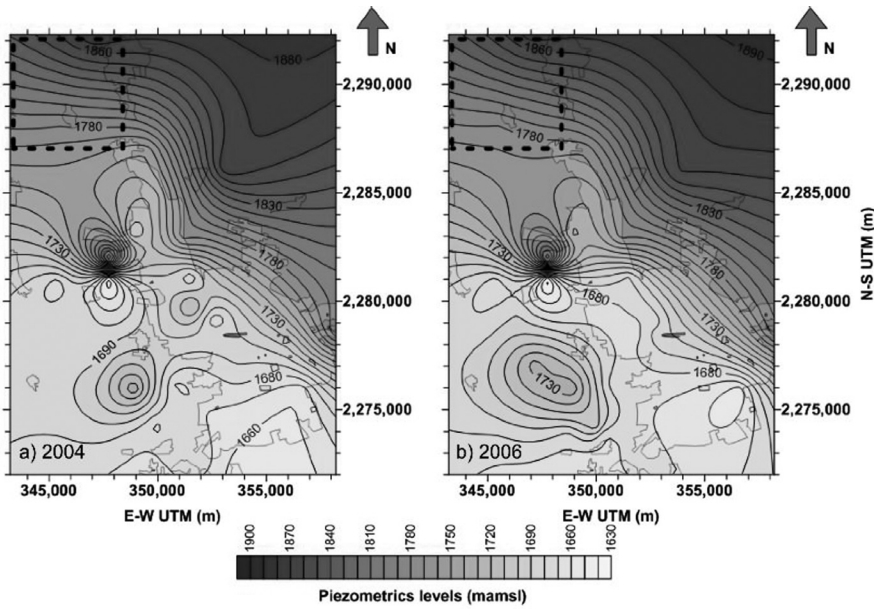
Figure 6. Piezometric levels measured in the Queretaro Valley for (a) 2004 and (b) 2006. The 2006 piezometric levels were used as initial condition for the model. Because the North-South hydraulic gradient, shown in the dashed square (modeled area), is persistent during 2004 and 2006 we considered steady state conditions.
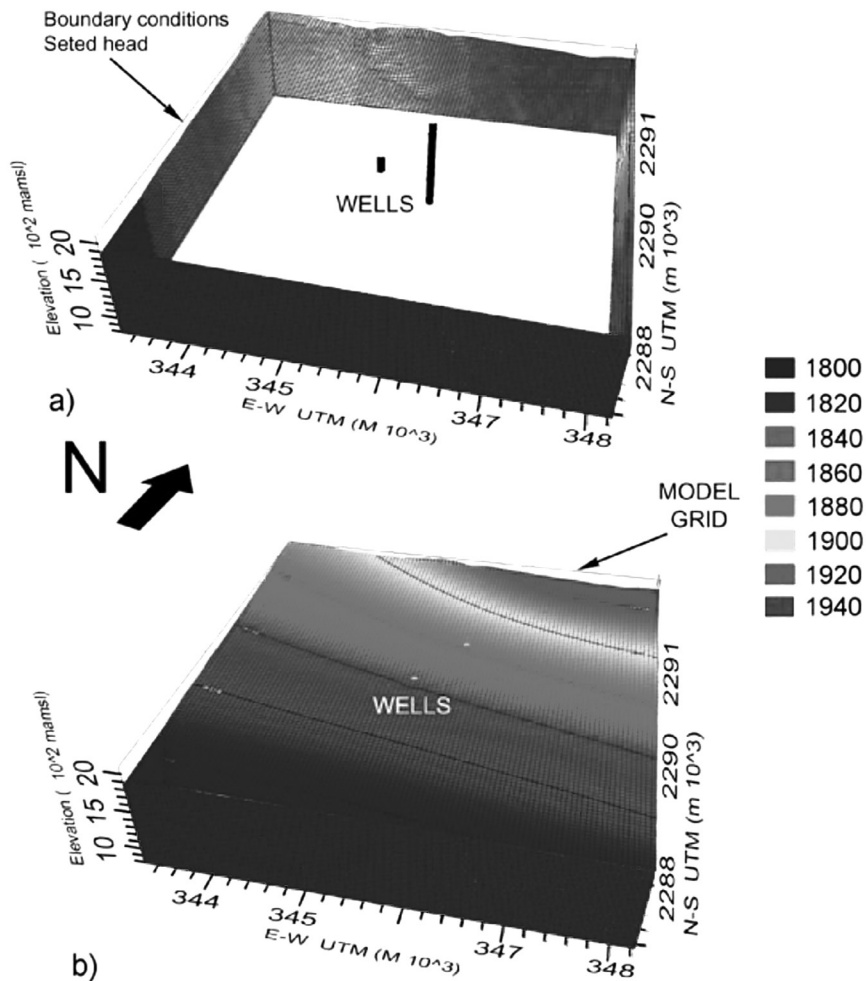
Figure 7. Piezometric conditions shown in the model box with (a) border and (b) initial conditions after the steady state measured in 2006 (see figure 6b).
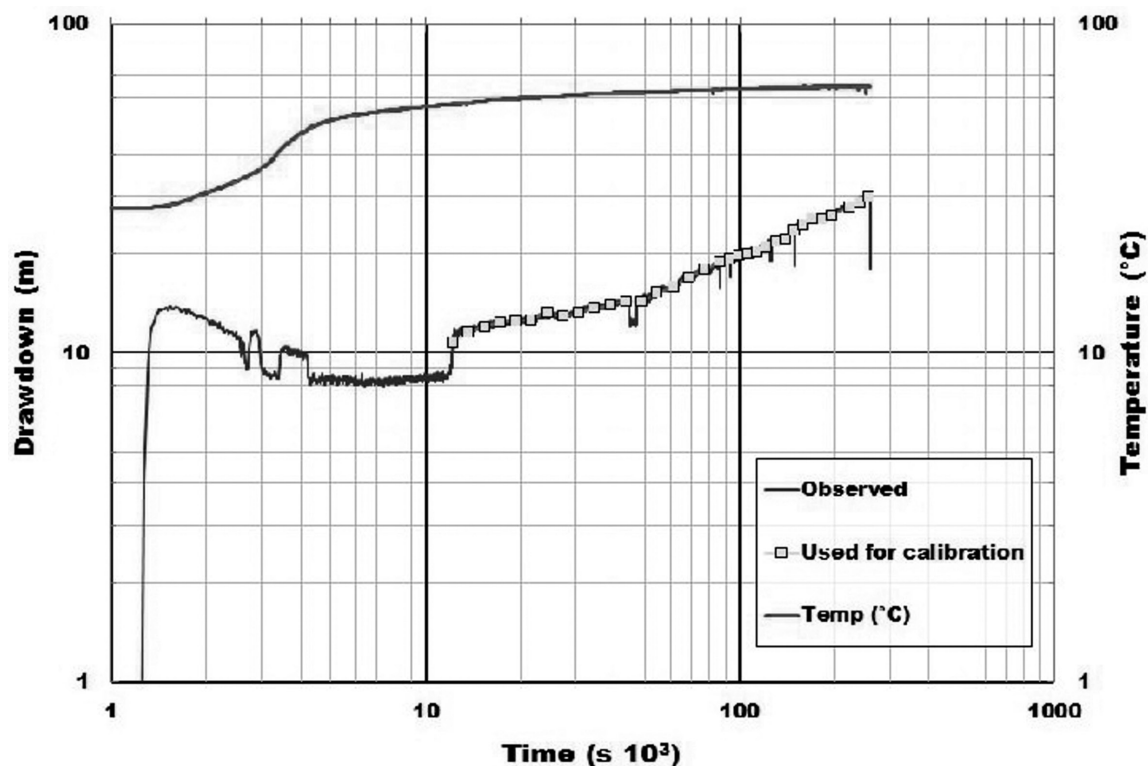
Figure 8. Drawdown measurements collected during the El Nabo pumping test. Blue line indicates continuous datalogger measurements, blue squares the sampled points for calibration. Green line indicates increasing temperature in the extracted water.

conductivities in three perpendicular directions, corresponding with the orientation of the grid to North-South, East-West, and vertically for this study case. The initial value of hydraulic conductivity (K) was established at 1e-04 m/s, corresponding to reported values for massive and fractured rocks (Walton 1970; Ingebritsen *et al*., 2006; Zoback, 2007).

The best fit of the observed and calculated drawdowns was achieved by using the hydraulic conductivities (K) values presented in Table 1, along two directions: horizontal E-W and vertically. The North-South values of K remained fixed at the initial value. The sensitivity values for the obtained hydraulic conductivities (Table 1) of the model vary with the distance between the geological units/faults and the pumping test zone. High sensitivity means a high influence of the geological unit in drawdown. The "limestone and shale" and "El Nabo fault" units show the highest sensitivity values (Table 1b). The high values in the El Nabo Fault are due to the fact that the pumping well is located along this fault. The lower obtained sensitivities correspond to the Balvanera and South faults, meaning that the

conductivity values of these units did not affect the calculated drawdown.

The results of the pumping test were analyzed by the derivative of the data obtained by applying the fixed-end-point method proposed by Bourdet *et al*. (1989) (orange line in Figure 9). The use of the derivative allows analyzing in detail pressure changes in drawdown plots (Bourdet *et al*., 1989; Spane and Wurstner, 1993; Tiab, 2005). The derivative was smoothed by the use of the third point before and after the point of interest to reduce the sample rate noise. The intersection between dyke/fault and the El Nabo well was analyzed by the semi-analytical solution of Butler and Liu (1991).

Discussion of results

The implemented model allowed representing the faulted system of the study area by the hydraulic conductivities assigned to specified geological units, including faults. In order to constrain the overall flow conditions regional measurements of hydraulic heads and geological observations were integrated.

Table 1. (a) East-West and vertical hydraulic conductivities obtained from simulation. (b) Table of sensitivity variability for PEST analysis, higher sensitivity values of the model are related to the El Nabo fault. See text for details

Hydraulic conductivity (m/s)	E-W	Vertical
Rhyolite	2.8E-05	6.1E-06
Conglomerate and sandstone	3.4E-05	4.0E-05
Limestone and shale	5.6E-02	1.3E-05
Basement Limestone	9.9E-05	8.8E-06
Nabo-Fault NW-SE	4.4E-07	4.9E-04
South fault NE-SW	1.2E+02	6.1E-06
Balvanera-fault NW-SE	5.1E-04	9.7E-06
Intrusive	6.15E-05	1.39E-05
a)		

Sensitivity	E-W	Vertical
Rhyolite	4.0E-03	0.0E+00
Conglomerate and sandstone	4.0E-03	4.0E-03
Limestone and shale	1.2E-01	1.6E-02
Basement Limestone	8.8E-03	1.3E-02
Nabo-Fault NW-SE	1.0E+00	2.9E-01
South fault E-W	1.2E-01	0.0E+00
Balvanera-fault NW-SE	4.0E-03	0.0E+00
Intrusive	0.0E+00	0.0E+00
b)		

Geological constraints for the implementation of the model

The Cretaceous sequence drilled in El Nabo well, composed by a limestone and shale unit (Ki Cz-Ar) that overlies a volcano-sedimentary sequence (Ki Mvs), was of the most importance to establish the geological constraints of the model. The volcanic character of the basal volcano-sedimentary sequence was interpreted from the drilling samples and was confirmed by the isotopic ages. The overlying limestone and shale unit is more than 800 m thick and is inter-bedded both with sandstone or clay. In nearby superficial outcrops this unit is deformed by folding and contains calcite veins and fractures. Rock samples obtained from depths below 850 m at the El Nabo well of the volcanic sequence contained a large quantity of biotite. Differences in the size and aspect of biotite defined two size populations: (1) between 425 and 710 μm and (2) between 250 and 425 μm. The age spectra obtained for both sizes confirms that they correspond also to two different age populations.

Figure 10a shows the age spectra for the biotite population 1 indicating a Miocene age. The weighted average for argon fractions was made by considering the consecutive fractions with greater radiogenic argon content and more than 10% of the total ^{39}Ar released. A representative age of t = 9.5 ± 0.1 Ma was selected from the weighted average of 13 fractions from different experiments in the age spectra diagram. This biotite population is characterized by a ratio ^{37}Ar$_{Ca}$/^{39}Ar$_K$ ≤ 0.5. The correlation diagrams obtained for these samples (Figure S1) show two isochron lines also converging at an age around 9.5 Ma. The Andesitic lava flows (Valdez-Moreno *et al*., 1998) cover most of the study area and have the same Miocene age obtained for biotite 1 population, the coincidence in age of the lavas and the biotite sampled at depth strongly support the interpretation that the lavas were feed by dikes emplaced along faults.

The biotite population 2 (Figure 10b) yielded older ages of ~100 Ma with age spectra diagram indicating a severe argon
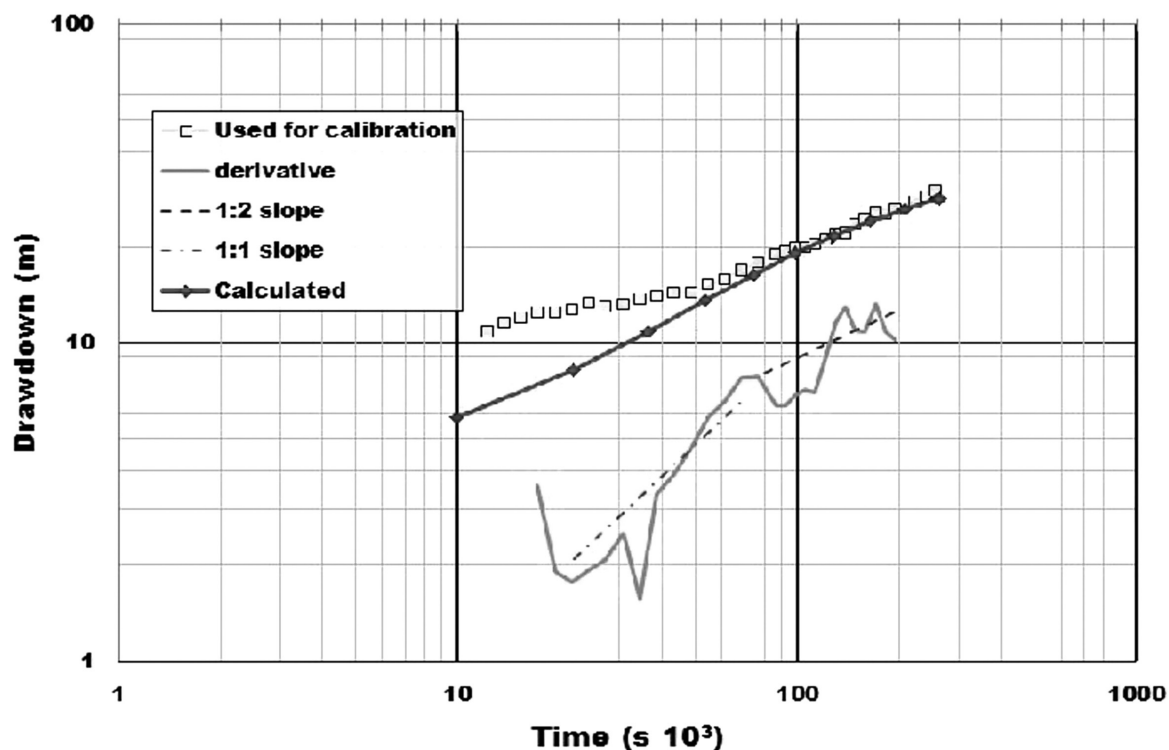
Figure 9. Measured drawdown during the pumping test at El Nabo (blue squares) and calculated curve using the implemented model. The derivative of the data obtained by applying the fixed-end-point method (Bourdet et al. 1989) is presented in a orange line. Derivative drawdown was analyzed by the semi-analytical solution of Butler and Liu (1991) obtaining 1:2 and 1:1 slopes.

loss. A reliable age cannot be obtained but the sequence is older than the minimum age obtained. This behavior was reproduced in the 855 m depth Biotite in duplicate experiments. A higher ratio of $^{37}Ar_{Ca}/^{39}Ar_K > 0.5$ compared with biotite population 1 clearly indicates a different composition. Because of the different isotopic behavior of these samples the biotite populations were plotted separately in the correlation diagram (Figure S1), in which the equivalent age is shown in the abscissa axis. The correlation using the fractions from 3 to 6 of the 1st experiment and the fractions 3 to 8 of the duplicate experiment in the biotite 2 population also indicates an age of ~100 Ma, for the *Ki Ms V* rock sequence.

The documented difference in age of the biotite populations strongly supports our interpretation of the presence of a Miocene magmatic dyke intruding the Cretaceous sequence as shown in the schema of Figure 10c. The presence of this fault has important implications in groundwater flow by the increasing of the hydraulic conductivity within the fault plane that was observed during drilling.

It has been documented that dikes open weakened fractures to conduct magma toward the surface and during their emplacement they can cause further brecciation of the fractured zone and the increase of hydraulic conductivity (Zoback, 2007; Anderson, 2006). Beside the presence of the dike, further evidences supporting the circulation of hydrothermal fluids along the fault include the presence of hydrothermally altered calcite veins in exposures and in drilling samples of the El Nabo well (Figure 4b). Present day hydrothermal activity along the fault was confirmed by the increase from 25 to 63°C in the temperature records during pumping test (green line, Figure 8).

In order to consider the role of major faults in groundwater flow we integrated the *El Nabo, Balvanera* and *South* faults in the model. *El Nabo* and *Balvanera* are sub-parallel normal faults with NW-SE orientation (panoramic view, Figure 4a). The *Balvanera Fault* has a throw of more than 200 m after the Miocene lavas emplacement. The *El Nabo Fault* is located in a block delimited by the regional graben faults as shown in the cross-section of Figure 2b. Several faults and fractures with similar

Figure 10. (a) $^{40}Ar/^{39}Ar*$ age spectra obtained for the biotite population 1 (small size) collected at different depths between 846 and 979 m in El Nabo well. The age obtained for this population is interpreted as evidence for a Miocene dyke intrusion. (b) $^{40}Ar/^{39}Ar*$ age spectra obtained for the biotite population 2 collected at the same depth interval of population 1. Although a reliable age cannot be assigned to the samples, a minimum age of 100 Ma is interpreted for the volcano-sedimentary sequence hosting the Miocene intrusion, (c) schematic section showing the intrusion of the volcanic dyke (Tmt AB, 10 Ma) within the Cretaceous sedimentary and volcanic units (host rocks: Ki Cz and Ki Ms V) that changes dramatically the hydraulic conductivity of the system by brecciation.
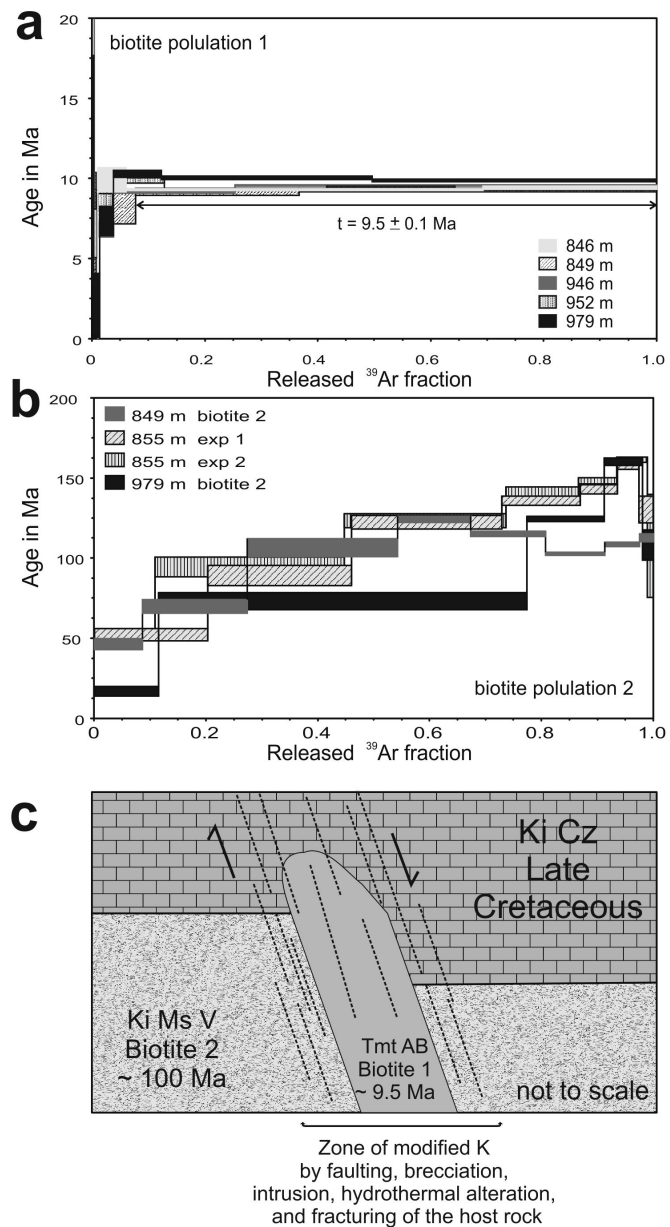
orientation were observed around the zone of the El Nabo well. The Cretaceous sedimentary sequences (Ki Cz-Ar) have a low hydraulic conductivity as shown by the low flow rate measured in the El Nabo well above 800 m depth (6 l/s). Nevertheless, flow rate increased to 47 l/s when drilling intersected the El Nabo Fault and dike at 850 m depth. We infer that the dike caused brecciation, fracturing, and hydrothermal alteration of the host rock and consequently an increase in the hydraulic conductivity. Evidence of other dikes emplaced on the *El Nabo Fault* area affecting other stratigraphic levels was observed in exposed parallel fault planes. For modeling purposes,

the *Balvanera Fault* features are assumed to be similar to the *El Nabo Fault* and was calibrated as an independent unit.

The exposed plane of the older age *South Fault* (Figure 4b) contains open fractures filled with sediments and calcite that precipitated by the circulation of hydrothermal fluids. The *South Fault* favored the location of the Oligocene sub-volcanic body (30 Ma, TomDa) of silicic composition (Alanis-Alvarez *et al*., 2002) observed as a dome structure at the surface (Figure 2). Given its large spatial dimensions this structure was considered as an individual unit in the numerical model (Figure 5b).

The geological evidences suggest that groundwater flow through faults is significant in the study area: thus, the model integrated an increase of conductivity along the El Nabo fault.

Assessment of groundwater flow in faulted and high heterogeneous areas

The numerical model was constrained by the results of the pumping test in El Nabo well. The record of the test was sub-sampled and the obtained drawdown plot is presented in Figure 9 (blue squares) along whit its derivative (Bourdet *et al*., 1989). Considering an infinite linear strip embedded in a host material (matrix) with differing hydraulic properties Butler and Liu (1991) presented derivative curves with slopes varying from 1:2 and 1:4 for a case in which hydraulic conductivity is much larger than the host material (matrix). In their analysis these slopes corresponded to an initial linear flow within the strip that changed to bilinear flow when the flow from host material contributes to discharge. The slopes obtained from the drawdown derivatives of the El Nabo well pumping test are shown in Figure 9; a slope 1:1 (green dashed line) for the 20,000-70,000 s (5-19 hour) interval and a slope 1:2 (black dashed line) for the last part of the data. The first slope (1:1) corresponds to the primary flow drawdown that may be explained by two conditions: (a) groundwater flow contributed by the limestone unit presenting high K values in the E-W direction and (b) is enclosed within the fault walls (Table 1) or, (2) non lineal flow inside the fault walls and constrained by the regional gradient, which magnitude is large enough to oppose flow toward the well.

The 1:2 slope may be related either to discharge of a lineal regional flow within the El Nabo Dyke/Fault (i.e. strip unit, Butler and Liu, 1991) or a new source of regional flow. Support evidence of the contribution of a hydrothermal deep groundwater flow system through the fault was provided by the increase in temperature while pumping (25 to 63°C, green line in Figure 8). The initial increase of temperature in a time interval of 83 minutes suggests mixing of local fresh groundwater and hydrothermal flow, with the presence of a preferential conduct through the magmatic dyke/fault.

The calibrated hydraulic conductivities (obtained using PEST software) were used to simulate the pumping test in the numerical model (red line; Figure 9). The wellbore storage may have caused the rapid initial drawdown of the El Nabo pumping test (the well is more than

1000 m depth and 6 inches in diameter). Time required for pumping stabilization (10,000 s, or approximate 3 hours, Figure 8) was not considered in the model, drawdown initiated from a relative zero value. A pseudo-steady flow regime observed in the 10,800-35,000 s (3-10 hour) intervals (Figures 8 and 9) was not completely adjusted by the calculated drawdown. From 20 hour (75,000 s) the numerical solution converges with the data and the model results are better fitted (Figure 9). In spite of the initial differences, we consider that model curve captures the overall behavior of the pumping test suggesting a similarity of hydraulic behavior between model and test.

The model allows discussing the contribution of each geological element in the overall hydraulic behavior of the system. Faults were considered as vertical planar structures with varying hydraulic conductivities according to the E-W or vertical groundwater flow direction. The block model of Figure 11 summarize the main groundwater flow results using the K values presented in Table 1, and shows the piezometric levels reached at the end of the pumping test simulation. Colors indicate piezometric levels, which range from 1925 in the north area to 1820 masl toward the south. The higher gradient is obtained toward the east of the *El Nabo Fault*. Arrows, indicating flow directions, show clearly that major structures (El Nabo and South faults) favor ground-water flow patterns along planes and also delimit compartments with differences in hydraulic behavior. Field observations show that the hydraulic interaction of the fault with the El Nabo well starts at 850 m of depth and the presence of hydrothermal groundwater can be interpreted in terms of ongoing deep lateral flow facilitated by the heterogeneous permeability within the fault-zone probably due to the dyke intrusion (López and Smith, 1995; Lopez and Smith, 1996). Horizontal flow predominates in the model while the flow patterns deviate along the geometric boundaries of the intrusive body, interrupting the connection between El Nabo and South faults, and following the regional N-S gradient.

Figure 12 shows one horizontal and two vertical cross sections (in the E-W and N-S directions) of the model (Figure 11) that allow to analyze the influence of major structures (El Nabo and South faults and the intrusive body) in groundwater flow patterns. In the horizontal cross section at 1400 masl of Figure 12a the northern segment of the *El Nabo Fault* act as a barrier by interrupting groundwater flow from north to south within the limestone and shale unit, also shown in the vertical BB' profile
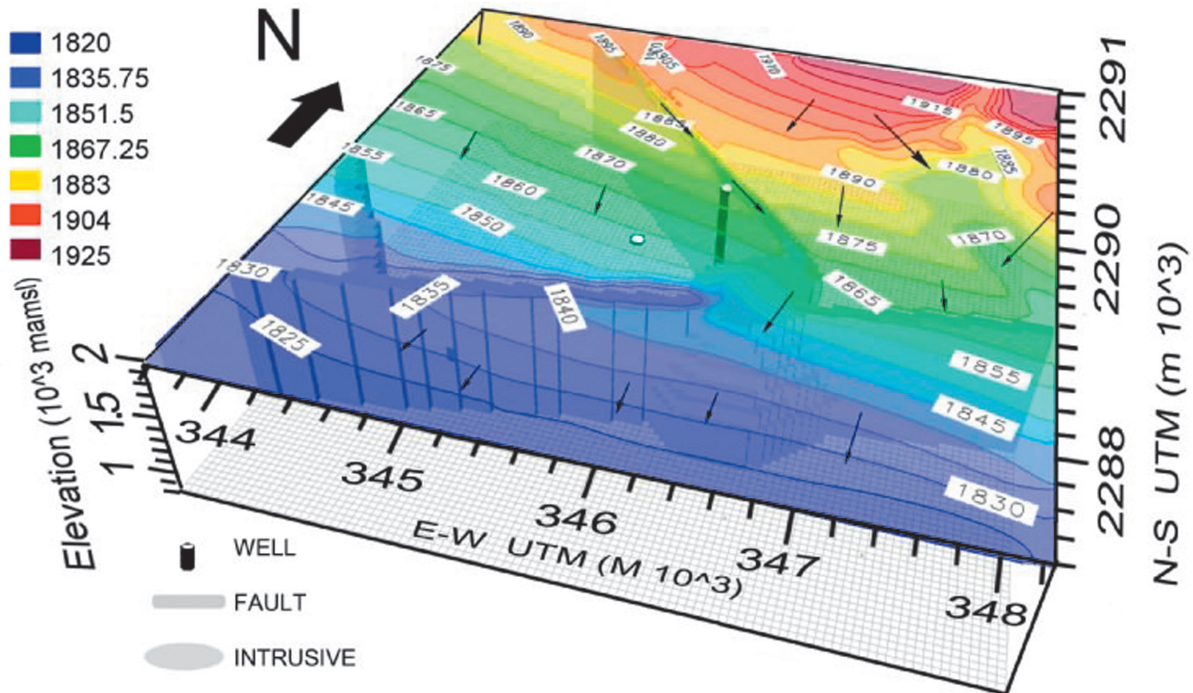
Figure 11. Model box of the study area presenting drawdown elevations and groundwater flow vectors after simulation of El Nabo pumping test using calibrated of hydraulic conductivity values shown in Table 1. Faults act as flow channel interfering with the regional flow gradient and compartmentalizing the aquifer system. Arrows show the direction and sense of flow. The large intrusive dome modifies flow in the fault. The El Nabo fault-dyke exerts a major influence in groundwater flow.

(Figure 12c). The hydraulic head observed at 1900 m north from the El Nabo fault decreases to 1840 m in the southern block. In the East-West cross section (AAʹ in Fig. 12b) the color scale indicates a difference in piezometric elevations of 40 m at both sides of the fault. In the model the regional gradient is interrupted by the *El Nabo Fault* that acts as a lateral flow barrier in the east-west direction, the vertical equipotential lines indicate vertical flow within the fault. The NE-SW orientation of the *South Fault* seems to favor channelized lateral flow towards the SW along the main fault plane. The *South Fault* yielded the highest K value in the horizontal E-W direction (Table 1). The model is not sensitive to this structure and this high value may be an artifact produced in the model by the equalization of drawdown and regional gradient. However, field data suggest also a higher K for the *South Fault* than for *El Nabo Fault*.

The 1:2 slope of the derivative curve (orange line, Figure 9) was interpreted as lineal flow within a high permeability channel with semi-permeable walls, interpretation consistent with the presence of *El Nabo Fault-Dyke* (Figure 12 b, c). The semi-permeable walls condition in

the model is represented by the equipotential lines at both sides of the faults. Smooth gradients within the stratigraphic units increase when crossing the fault indicating a high hydraulic gradient but with flow continuity. The limestone and shale unit also show hydraulic continuity with the fault to the west; whereas in the eastern part have a higher elevation suggesting a greater water contribution from the fault (Figure 12c).

Given that only one observation point could be considered, the El Nabo well is the deepest well drilled in the Queretaro area with most of the well depths about 300 m, analysis of representativeness of the obtained hydraulic conductivity was not possible to do. Nevertheless, the information yielded by the pumping test was useful for the calibration of the numerical model allowing simulating groundwater flow in the study area.

In summary, this work attempts to highlight the importance of integrating an accurate geological setting to understand groundwater flow dynamics in models of faulted aquifers in particular in cases were piezometric levels decrease constantly.
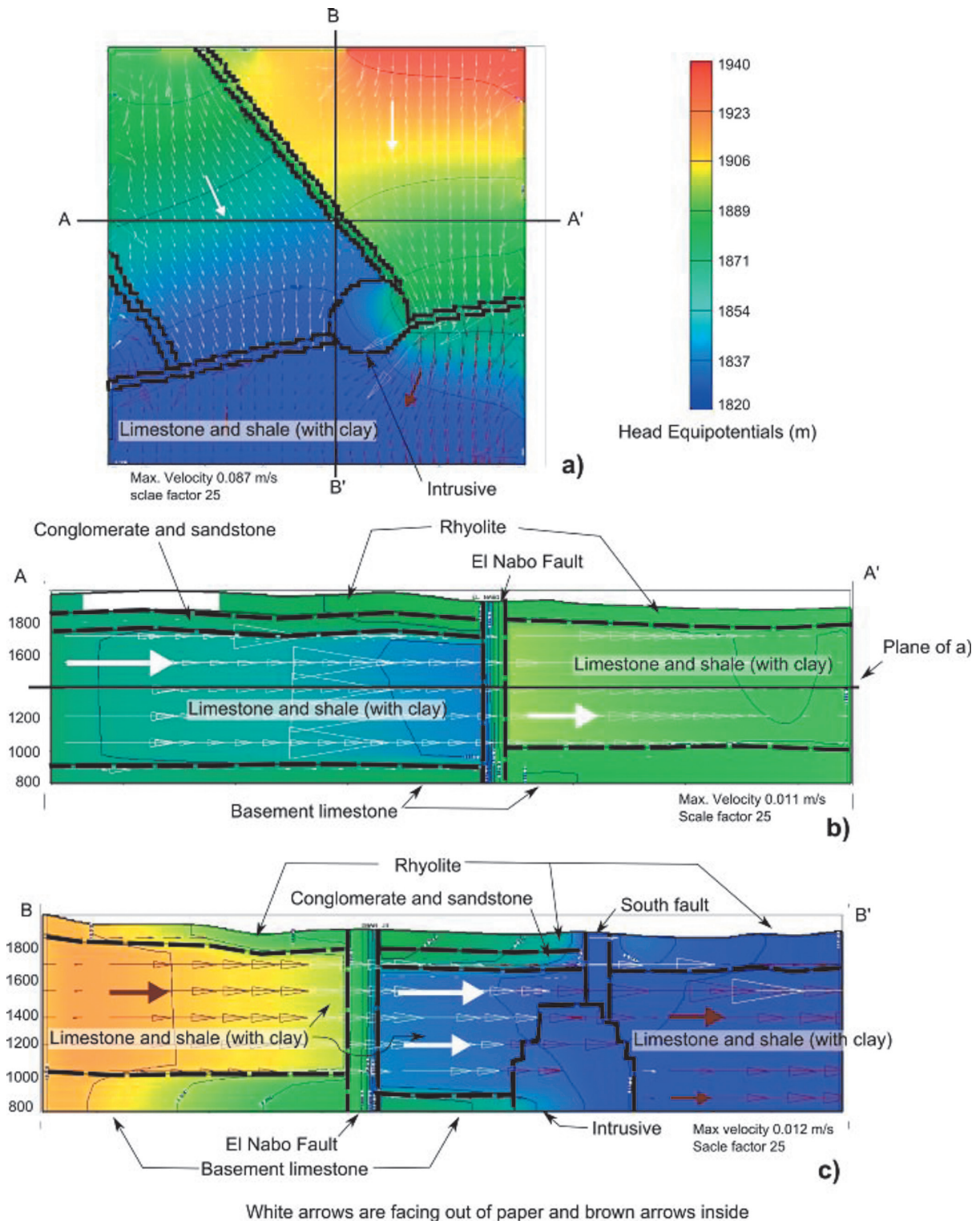
Figure 12. Horizontal and vertical sections of the model box are presented in Figure 11. Colors indicate variation of piezometric heads from 1940 to 1820 masl. (a) Horizontal cross section at 1400 masl (location shown in Figure 12b), the black lines represent the analyzed faults walls and intrusive body. (b) and (c) are two cross sections of the model box in the NS and EW directions respectively.

Fault zones in the study area have more than 50 m in thickness and several fault planes were observed where high and low K segments may coexist. Because the style and relative age of faulting determines variations in its hydraulic properties we consider that in faulted and deep aquifers (more than 200 m depth) the assessment of the overall flow dynamics is as, or more, important as obtaining specific hydraulic properties of the hydro-stratigraphic units.

Field evidences of present day hydrothermal water circulation within fault planes in the study area and the model results allow proposing that faults collect groundwater flow and explain the flow rate increase to 47 l/s at *El Nabo Fault*. Moreover, the Cretaceous sedimentary sequences show an overall low hydraulic conductivity. The magmatic dikes caused brecciation, open fractures, and hydrothermal alteration of the Cretaceous host rock and consequently enhancing its hydraulic conductivity (e.g., Zeidouni, 2012; Table 1). The South fault system favored the emplacement of the Oligocene intrusive body. Field observations suggest that this fault also favored fluid-flow

over time along open fractures partially filled with sediments and secondary fault planes in a zone more than 50 m in width. We have observed precipitation of calcite in fractures (Figure 4b), and probably infiltration of superficial water. Correspondingly, after the simulation the higher K values obtained in the East-West direction of the South Fault allowed the hydraulic continuity of the system, according with the regional gradient (Figure 11).

Conclusions

Implementation of the geological structure in a numerical groundwater flow model, along with the estimation of hydraulic conductivities by a pumping test, produced relevant information about flow dynamics in the faulted aquifer system at the north of the Valley of Queretaro. This methodology can be applied to study groundwater flow in other areas of the Queretaro Valley and elsewhere in central Mexico, where water is extracted from depths greater than 200 m and high uncertainty exist about the influence of major structures in groundwater flow conditions.
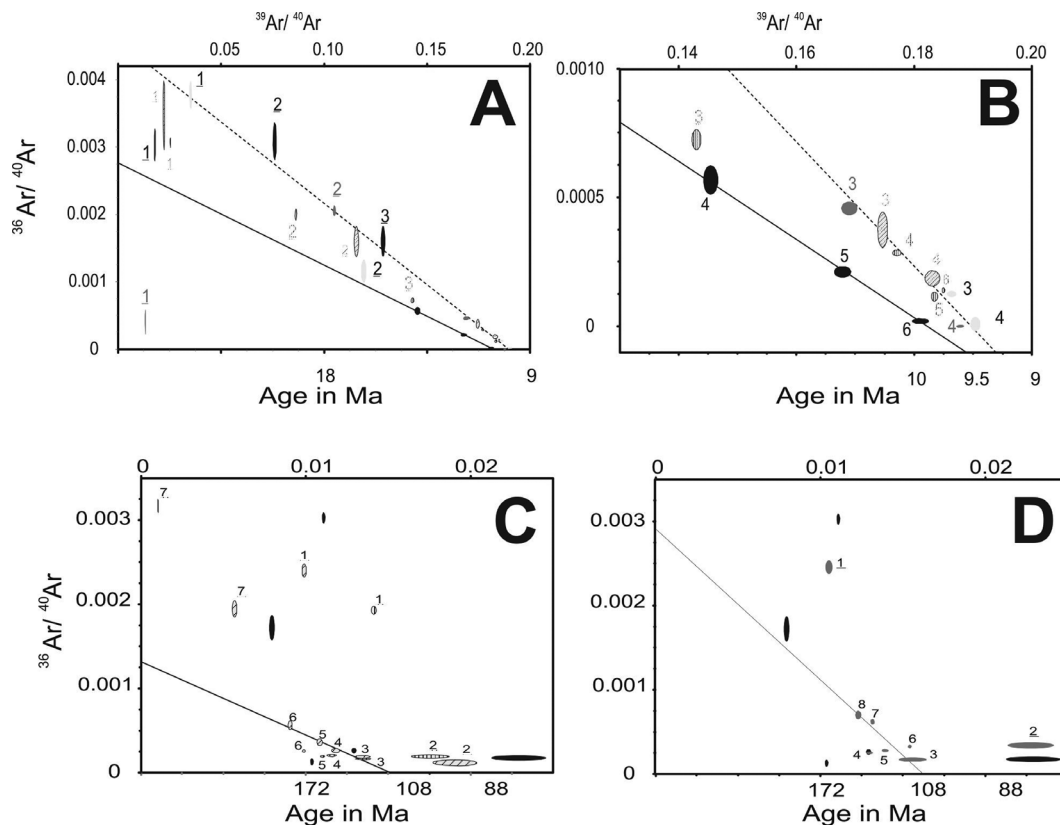
Figure S1. Correlation diagrams obtained for samples for Biotite Population 1 and 2. Isochron lines (A and B) yield an age around 9.5 Ma for samples of Biotite Population 1; whereas Biotite Population 2 (C and D) converge at an age around 100 Ma.

The study area is a block delimited by faults where the older geological units in the Queretaro Valley are exposed. Considering faults and truncation of hydrostratigraphic units in the sequence leaded to the reconnaissance of compartments in the aquifer system also reproduced in the model. The identification of groundwater flow patterns through the aquifer when modeling drawdown was consistent with measured piezometric levels. The derivative analysis of the pumping test suggests the presence of two different groundwater flow systems: (1) a flow, with slope 1:1, related to the limestone and shale sequence and, (2) a regional linear flow, with slope 1:2, transporting water through faults.

The numerical model along with the drawdown field observations allowed estimating relative values of hydraulic conductivity for eight geological units (Table 1). As expected, the model is sensitive to the fault located near the El Nabo well (Figure 1). Of importance to the study is the presence of volcano-sedimentary sequences below thick limestone units. Isotopic dating confirmed the presence of a Miocene magmatic dyke emplaced along the El Nabo Fault. Both the Balvanera and El Nabo fault systems favored the emplacement of Miocene volcanism through dykes along the faults planes (Figure 4). The presence of the fault-dyke was corroborated with stratigraphic correlation of a well log, and the results confirm its relevance to modify groundwater flow. The increased high flow rate in the El Nabo well pumping test (47 l/s) is an evidence of the high influence of the dike that allows groundwater to flow through the fault.

The obtained values agree with the conceptual model but connectivity between major faults cannot be evaluated only by the analysis of pumping tests. The numerical model allowed exploring the relevance of geological structures in the simulation of groundwater flow (Figures 11 and 12). In particular, the model results highlight how faults and intrusive bodies emplaced along faults modify groundwater flow by changing hydraulic properties and consequently flow direction. The model allowed improving the interpretation of the pumping tests. Numerical modeling is useful for a better understanding of complex aquifer systems that cannot be evaluated by analytical methods.

Acknowledgements

References

Aguirre-Díaz G.J., López-Martínez M., 2001, The Amazcala caldera, Querétaro, México. Geology and geochronology. *Journal of Volcanology and Geothermal Research,* 11, 203-218.

Aguirre-Díaz G.J., Nieto-Obregón J., Zúñiga R., 2005, Seismogenic Basin and Range and intra-arc normal faulting in the central Mexican Volcanic Belt, Querétaro, México. *Geological Journal,* 40, 215-243.

Alaniz-Álvarez S.A., Nieto-Samaniego A.F., Reyes-Zaragoza M.A., Orozco-Esquivel M.T., Ojeda-García A.C., Vassallo F.L., 2001, Estratigrafía y deformación extensional en la región San Miguel de Allende-Querétaro, México (Stratigraphy and extensional deformation in the San Miguel de Allende-Queretaro region, Mexico). *Revista Mexicana de Ciencias Geologicas,* 18, 129-148.

Alaniz-Álvarez S.A., Nieto-Samaniego A.F., Orozco-Esquivel M.T., Vassallo F.L., Xu S., 2002, El sistema de fallas Taxco-San Miguel de Allende: implicaciones en la deformación post-eocénica del centro de México (The fault system Taxco-San Miguel de Allende: implications for post-Eocene deformation of central Mexico) *Boletin de la Sociedad Geologica Mexicana,* 55, 12-29.

Allen D.M., Michel F.A., 1999, Characterizing a Faulted Aquifer by Field Testing and Numerical Simulation. *Ground Water,* 37, 718-728.

Anderson E.I., 2006, Analytical solutions for flow to a well through a fault. *Advances in Water Resources,* 29, 1790-1803.

Bense V.F., Gleeson T., Loveless S.E., Bour O., Scibek J., 2013, Fault zone hydrogeology. *Earth-Science Reviews*, 127, 171-192.

Bourdet D., Ayoub J.A., Pirard Y.M., 1989, Use of pressure derivative in well-test interpretation. *SPE Formation Evaluation* June, 293-302.

Burbey T.J., 2008, The Influence of Geologic Structures on Deformation due to Ground Water Withdrawal. *Ground Water,* 46, 202-211.

Butler J.J., Liu W.Z., 1991, Pumping test in non-uniform aquifers - the linear strip case. *Journal of Hydrology*, 128, 69-99.

Caine J.S., Evans J.P., Forster C.B., 1996, Fault zone architecture and permeability structure. *Geology*, 24, 1025-1028.

Carreón-Freyre D., Cerca M., Luna-González L., Gámez-González F.J., 2005, Influencia de la estratigrafía y estructura geológica en el flujo de agua subterránea del Valle de Querétaro (Influence of the stratigraphy and geologic structures on groundwater flow, Querétaro Valley). *Revista Mexicana de Ciencias Geologicas,* 22, 1-18.

Cerca M., Ferrari L., López-Martínez M., Martiny B., Iriondo A., 2007, Late Cretaceous shortening and early Tertiary shearing in the central Sierra Madre del Sur, southern Mexico: Insights into the evolution of the Caribbean–North American plate interaction: *Tectonics,* 26, TC3007, doi:10.1029/2006TC001981.

Conagua, 2003, Plan de manejo del Acuífero Valle de Querétaro. *Comisión Nacional del Agua*, México, 234 pp.

Delinom R.M., 2009, Structural geology controls on groundwater flow: Lembang Fault case study, West Java, Indonesia. *Hydrogeology Journal*, 17, 1011-1023.

Doherty J., 2005, PEST Model-Independent Parameter Estimation User Manual: 5th Edition Watermark Numerical Computing, 336 pp.

Ferrari L., 2000, Avances en el conocimiento de la Faja Volcánica Transmexicana durante la última década. *Boletin de la Sociedad Geologica Mexicana,* 53, 84-92.

Hall C.M., 1981, The application of K-Ar and 40Ar/39Ar methods to the dating of recent volcanics and the Laschamp event. PhD Thesis. University of Toronto. Canada.

Harbaugh A.W., Banta E.R., Hill M.C., Mcdonald M.G., 2000, MODFLOW-2000, the U.S. Geological Survey modular ground-water model - User guide to modularization concepts and the Ground-Water Flow Process. U.S. Geological Survey Open-File Report 00-92, 121 pp.

Hsieh P.A., Neuman S.P., 1985, Field determination of the three-dimensional hydraulic conductivity tensor of anisotropic media, 1. Theory. *Water Resources Research,* 21, 1655–1665.

Ingebritsen S.E., Sanford W.E., Neuzil C.E., 2006, Groundwater in Geologic Processes. 2nd Edition.: *Cambridge University Press*, 536 pp.

Jourde H., Fenart P., Vinches M., Pistre S., Vayssade B., 2007, Relationship between the geometrical and structural properties of layered fractured rocks and their effective permeability tensor. A simulation study. *Journal of Hydrology*, 337, 117-132

Kulkarni H., Deolankar S.B., Lalwani A., Joseph B., Pawar S., 2000, Hydrogeological framework for the Deccan basalt groundwater systems, west-central India, *Hydrogeology Journal*, 8, 368–378.

Lopez, D.A., Smith, L, 1995, Fluid flow in fault zones: analysis of theinterplay of convective circulation and topographically driven groundwater flow. *Water Resources Research,* 31, 1489-1503.

Lopez D.A., Smith L., 1996, Fluid flow in fault zones: influence of hydraulic anysotropy and heterogeneity on the fluid flow and heat transfer regime. *Water Resources Research,* 32, 3227-3235.

Maclay R.W., Small T.A., 1983, Hydrostratigraphic subdivisions and fault barriers of the Edwards Aquifer, south-central Texas, U.S.A. *Journal of Hydrology,* 61, 127-146.

Mayer A., May W., Lukkarila C., Diehl J., 2007, Estimation of fault-zone conductance by calibration of a regional groundwater flow model: Desert Hot Springs, California. *Hydrogeology Journal,* 15, 1093-1106.

Pacheco F.A.L., 2002, Response to pumping of wells in sloping fault zone aquifers. *Journal of Hydrology,* 259, 116-135.

Rafini S., Larocque M., 2012, Numerical modeling of the hydraulic signatures of horizontal and inclined faults. *Hydrogeology Journal*. doi: 10.1007/s10040-011-0812-4.

Rathod K.S., Rushton K.R. ,1991, Interpretation of Pumping from two-zone layered aquifers using a numerical model. *Ground Water,* 29, 499-509.

Spane F.A., Wurstner S.K., 1993, DERIV: A computer program for calculating pressure derivatives for use in hydraulic test analysis. *Ground Water,* 31, 814-822.

Steiger R., Jäger E., 1977, Sub commission on Geochronology: Convention on the use of decay constants in Geo and Cosmochronology. *Earth and Planetary Science Letters,* 36, 359-362.

Tiab D., 2005, Analysis of pressure derivative data of hydraulically fractured wells by the Tiab's Direct Synthesis technique. *Journal of Petroleum Science and Engineering,* 49, 1–21.

Trejo-Moedano A., 1989, Estratigrafía y propiedades mecánicas del subsuelo del valle de la zona urbana de Querétaro (Stratigraphy and mechanical properties of the subsoil in the urban zone of Queretaro). Universidad Autónoma de Querétaro, México, 115 pp.

Valdez-Moreno G., Aguirre-Díaz G.J., López-Martínez M., 1998, El volcán La Joya, estados de Querétaro y Guanajuato; un estratovolcán miocénico del Cinturón Volcánico Mexicano (The volcano La Joya, states of Queretaro and Guanajuato, a Miocene stratovolcano from Mexican Volcanic Belt). *Revista Mexicana de Ciencias Geologicas,* 15, 181-197.

Walton W.C., 1970, Groundwater Resources Evaluation. Mc. Graw-Hill, New York. 185 pp.

York D., Evensen N., Lopez-Martinez M., De Basabe D.J., 2004, Unified equations for the slope, intercept, and standard errors of the best straight line *American Journal of Physics,* 73, 367-375.

Xu S., Nieto-Samaniego A.F., Alaniz-Alvarez S.A., Cerca-Martinez L.M., 2011, Structural analysis of a relay ramp in the Queretaro Graben, central Mexico: Implications for relay ramp development. *Revista Mexicana de Ciencias Geologicas,.* 28, 275-289.

Zeidouni M., 2012, Analytical model of leakage through fault to overlying formations*. Water Resources Research* 48, W00N02, doi:10.1029/2012WR012582.

Zoback M.D., 2007, Reservoir Geomechanics. Cambridge Press, 449 p.

Zuñiga F.R, Pacheco J.F., Guzmán-Speziale M., Aguirre-Diaz G.J., Espindola V.H., Nava E., 2003, The Sanfandila earthquake sequence of 1998, Queretaro, México: activation of an undocumented fault in the northern edge of central Trans-Mexican Volcanic Belt. *Tectonophysics,* 361, 229-238. doi:10.1016/S0040-1951(02)00606-6.

Mesozoic gliding and Tertiary basin and range tectonics in eastern Sonora, Mexico

José Luis Rodríguez Castañeda*, Jaime Roldán Quintana and Amabel Ortega Rivera

Resumen

En el oriente de Sonora, México, se encuentran bien preservadas en rocas del Cretácico Superior de la región de Arivechi, estructuras de deformación compleja asociadas a movimientos verticales y actividad gravitacional como deslizamientos. Estas estructuras nos permitieron hacer la distinción entre estructuras de origen sin-sedimentario y de origen tectónico. Las rocas en Arivechi, de acuerdo con su litología y grado de deformación, se dividieron en dos unidades la Unidad Cañada de Tarachi (la más antigua) y la Unidad El Potrero Grande. La secuencia volcano-sedimentaria del Cretácico Superior tiene más de 6 km de espesor y consiste en una secuencia de toba riolítica, andesita, conglomerado, arenisca, limolita y lutita que fueron depositadas en la cuenca tras arco de Arivechi. Dentro de la Unidad Cañada de Tarachi se encontraron monolitos y bloques que son los que constituyen uno de los objetivos principales de esta investigación. La edad de los monolitos y bloques incluyen rocas del Proterozoico, Paleozoico y Mesozoico. Los monolitos del Proterozoico están dominados por arenisca de cuarzo y dolomía. Los monolitos del Paleozoico y Mesozoico consisten en caliza y lutita interestratificadas, conglomerado y roca ígnea. Dos de los bloques graníticos fueron fechados; uno de ellos en 76 Ma (edad U/Pb en zircón) y el segundo en 70 Ma (^{40}Ar/^{39}Ar roca total por calentamiento a pasos). Los monolitos sedimentarios muestran una transición gradacional desde capas coherentes en sus porciones superior y media, a una intensa deformación en sus bordes y bases. Las estructuras dentro de los megaclastos y bloques, así como las rocas que los rodean, se estudiaron a detalle, para reconstruir el origen y desarrollo estructural de los monolitos, bloques y rocas encajonantes. La nueva información estratigráfica y estructural nos permite inferir que la posible fuente de los monolitos y bloques fue una tierra positiva localizada hacia el oriente de Arivechi en el oeste de Chihuahua y oriente de Sonora, México, denominada la Plataforma de Aldama. Las estructuras identificadas consisten en pliegues y fallas normales. La vergencia de los pliegues sugiere que el depocentro estaba localizado hacia el oeste del área de estudio.

Se efectuó una reconstrucción de paleoesfuerzos con el fin de documentar la historia tectónica del margen oriental de la posible cuenca de tras-arco de Arivechi. Se utilizó el método de inversión de esfuerzos a partir de los datos de deslizamiento de las fallas aplicando el método *right-dihedra* mejorado, seguido por una optimización rotacional. El análisis estructural y la reconstrucción de esfuerzos muestran que la evolución cinemática Mesozoico-Cenozoico se caracterizó por extensión. Este régimen continuó después del Cretácico y ha sido identificado en el Mioceno. La secuencia de rocas fue modificada por una deformación Cenozoica tipo Cuencas y Sierras, caracterizada por fallamiento normal durante el Mioceno, como sugiere la reconstrucción de los paleoesfuerzos. Este último evento fue el resultado del cambio del régimen tectónico, de subducción de la placa Farallón al régimen de fallamiento transcurrente que da inicio al sistema de fallas San Andres-Golfo de California durante el Mioceno. La cronología de eventos identificados sugiere que la dirección de extensión NE-SW y ENE-WSW fueron seguidos por extensión E-W y WNW-ESE. Esto indicaría que la secuencia del fallamiento fue de NE-SW a ENE-WSW y, por último, a WNW-ESE.

Palabras clave: Tectónica por gravedad, Cretácico Superior, monolitos, bloques, deslizamiento por gravedad, paleo esfuerzos, Sonora.

J. L. Rodríguez Castañeda*
J. Roldán Quintana
A. Ortega Rivera
Estación Regional del Noroeste
Instituto de Geología
Universidad Nacional Autónoma de México

Blvd. Luis Donaldo Colosio y Madrid, CP 83000,
Hermosillo, Sonora
México
*Corresponding author: jlrod@unam.mx

J. L. Rodríguez Castañeda, J. Roldán Quintana and A. Ortega Rivera

Abstract

Complex deformational structures assigned to vertical movements, and gravitational activity, such as gliding, are well preserved in Upper Cretaceous rocks of the Arivechi region, Eastern Sonora, Mexico. These structures allow us to discriminate between synsedimentary and tectonic origins. The rocks at Arivechi have been divided into two units according to their lithology and degree of deformation, the Cañada de Tarachi (oldest) and El Potrero Grande units. The Upper Cretaceous volcano-sedimentary sequence is more than 6 km thick and consists mainly of andesite, rhyolithic tuff, conglomerate sandstone, siltstone, and shale-type rocks that were deposited in the Arivechi back-arc basin. Within the Cañada de Tarachi Unit, monoliths and blocks were found; these include rocks dating from Proterozoic, Paleozoic and Mesozoic times. The Proterozoic monoliths are dominated by quartz sandstone and dolomite and the Paleozoic and Mesozoic monoliths consist of limestone, shale, limestone-shale-sandstone, conglomerate and igneous rocks. Two granitic monoliths have been dated, one at 76 Ma (U/Pb zircon date) and the other at 70 Ma ($^{40}Ar/^{39}Ar$ whole rock step-heating). The sedimentary monoliths show gradational transitions from coherent beds to intense deformation along their edges and bases. The structure within the monoliths, blocks and surrounding host rocks was studied in detail. The new stratigraphic and structural data suggest that the monoliths and blocks may have originated at a positive land east of Arivechi, in western Chihuahua and eastern Sonora, Mexico, known as the Aldama Platform. The identified structures consist of folds and normal faults. Fold vergence suggests that the depocenter was located westward of the study area. A paleostress reconstruction documented the tectonic history of the eastern margin of the Arivechi back-arc basin. Stress inversion of fault slip data was achieved by an improved right-dihedra method followed by rotational optimization. The structural analysis and paleostress reconstructions showed that the Mesozoic-Cenozoic kinematic evolution was extensional and continued during Cretaceous times; it has also been identified in Miocene rocks. The rock sequence was modified by basin and range-type normal faulting, as suggested by our paleostress reconstruction. The last event is the result of the beginning of tectonic extension at the onset of the shift from a subduction regime toward a transform fault regime, i.e., from the subduction of the Fallaron plate to the San Andreas Gulf of California fault system during Miocene times. NE-SW and ENE-WSW extension was followed by E-W and WNW-ESE extension. The faulting sequence went from NE-SW to ENE-WSW and subsequently to WNW-ESE.

Key Words: Gravity tectonics, Upper Cretaceous monoliths, blocks, gravity gliding, paleostress, Sonora.

Introduction

The active margin of western North America, which encompasses eastern Sonora, is characterized by the development of extensive and thick Upper Cretaceous rocks units (Figure 1). It has been generally accepted that Upper Cretaceous deformation in eastern Sonora is associated with the compressional Laramide orogeny, characterized by the fold and thrust belt in the western United States. However, new studies in north-eastern Sonora suggest that compressional structures are related to gravitational gliding rather than thrusting and folding by tectonic compression. Gliding tectonics is a mechanism whereby large masses of rocks move down a slope under gravity, producing folding and faulting of varying extent and complexity (Allaby and Allaby, 1999).

The Arivechi region was selected for better understanding of the evolution of these structures in eastern Sonora. Previous studies have reported that Upper Cretaceous rocks exist and that deformation is related to tectonic compression (Fernández-Aguirre and Almazán-Vázquez, 1991; Fernández-Aguirre et al., 1995; Minjárez-Sosa et al., 1985; Palafox et al., 1984; Palafox and Martínez, 1985). A detailed stratigraphic, morphostructural integration with structural analysis of fragile and ductile mesostructures present in the Upper Cretaceous rocks, paleostress analysis, and geochronological studies were conducted in order to ascertain whether the structures were originated by extension or compression.

Geological framework

Our study area, located east of Arivechi, has been subjected to several studies of stratigraphy and paleontology and, to a lesser extent, structural geology. We defined two units of Mesozoic age: 1) Cañada de Tarachi Unit, and 2) El Potrero Grande Unit. A third unit is of Oligocene-Miocene age, the Sierra Madre Occidental volcanic sequence. The two Upper Cretaceous units constitute
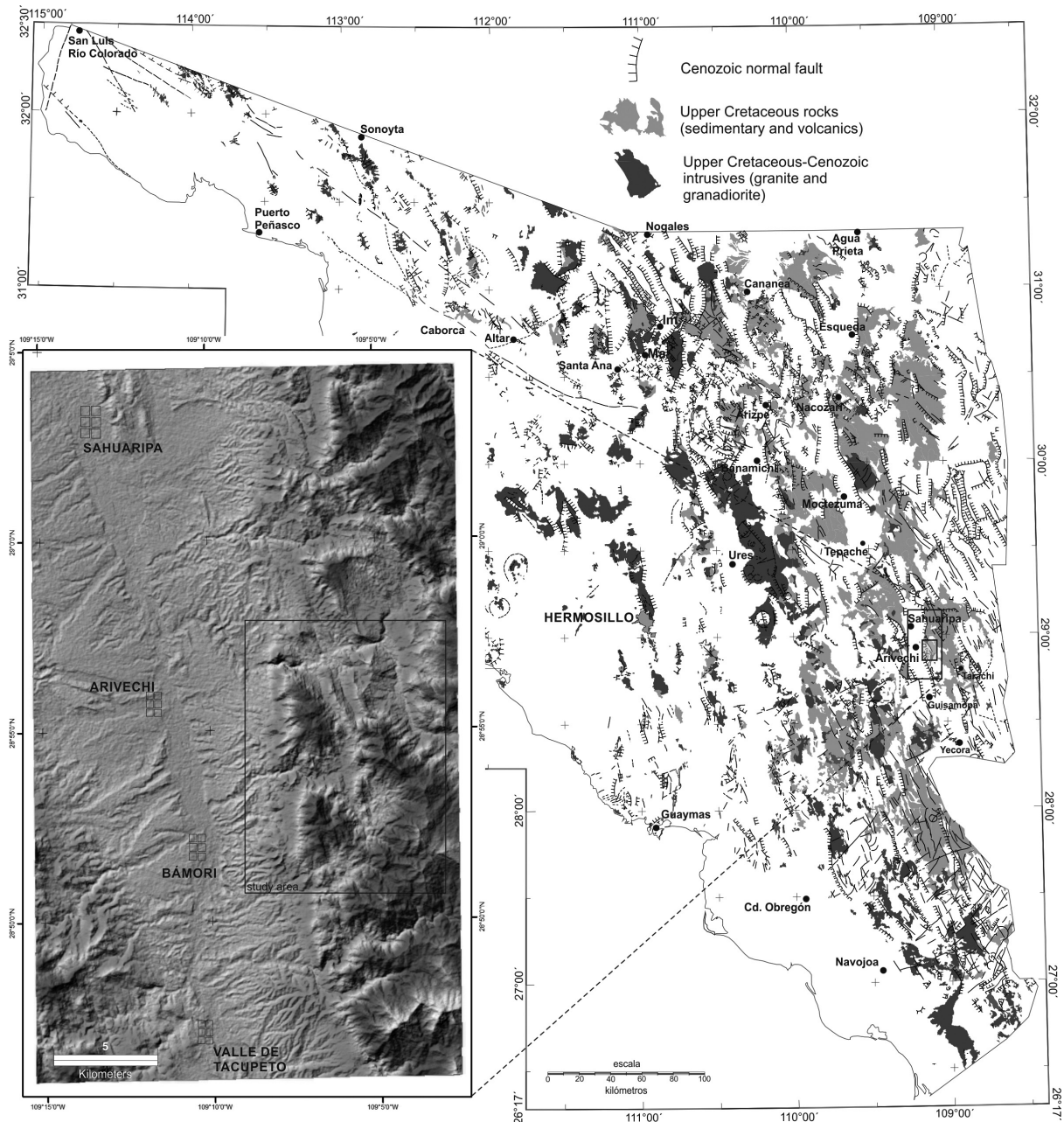
Figure 1. Location of the Arivechi region in eastern Sonora, Mexico and its relationship with the Upper Cretaceous rocks. Geologic information from the Servicio Geológico Mexicano (2008).

a volcano-sedimentary sequence of more than 6 km thickness. El Potrero Grande Unit (the youngest Cretaceous sequence) consists of conglomerate, sandstone, siltstone, and shale with interbedded andesite and diorite dikes and layers of rhyolitic tuffs. These rocks constitude a column more than 2,400 m thick, but this is merly part of a thicker sequence. The oldest unite include a large number of unusually well-exposed megaclasts of different lithogies and ages. A megaclast is a term used in grain-size schemes after modification of the Udden-Wentworth sedimentary grain-size scale devised by Blair and McPherson (1999), who proposed a new fraction in sediment size to account for clasts larger than 4.1m. They proposed four sizes for the megaclast fraction: *block* (4.1 to 65.5 m), *slab* (65.5 to 1049 m), *monolith* (1 to 33.6 km), and *megalith* (d_i from 33.6 to 1075 km). Megaclasts are associated to gravity sliding, or to vertical movements as described by various authors as olistoliths and olistostromes (Teale and Young, 1987; Heubeck, 1992).

Megaclasts have also been reported from numerous other tectonic environments; the Pyrenées (Johns *et al*., 1981), the Canadian Rockies (Cook *et al*., 1972), eastern Australia (Conaghan *et al*., 1976), the western US Cordillera (Heck and Speed 1987), the Apennines (Naylor, 1982; Teale and Young, 1987), the Avalonían Terrane of New England (Bailey *et al*., 1989), Hispaniola (Heubeck, 1992), global recent continental slopes (Prior *et al*., 1982), Alaska (Harp *et al*., 2003), the Valles-San Luis Potosi Platform (Carrasco-Velázquez., 1977), and north-eastern Sonora (McKee and Anderson, 1998; McKee *et al*., 2005).

Megaclasts (monoliths and blocks) as described by Blair and McPherson (1999), have been found and are common in eastern Sonora

Upper Cretaceous sequences (McKee and Anderson, 1998; Rodríguez-Castañeda, 2002; and McKee *et al*. 2005). These megaclasts have been linked to the emergence of a positive land, possibly related to the Late Jurassic Aldama Platform (Ramirez and Acevedo, 1957; Monreal, 1996; Haenggi, 2002; Anderson and Nourse, 2005) (Figure 2). The Aldama Platform is defined as an emerged land oriented NW-SE in north-west Chihuahua and eastern Sonora. Its extension toward north-eastern Sonora could be the Cananea High (McKee, 1991; Rodríguez-Castañeda, 2002). The Aldama Platform is bounded by faults related to the platform uplift. Uplift has been suggested as a mechanism of megaclast generation. It has been attributed to different causes but mainly to extension by reactivation of old faults and early Cenozoic pluton emplacement (Rodríguez-Castañeda,
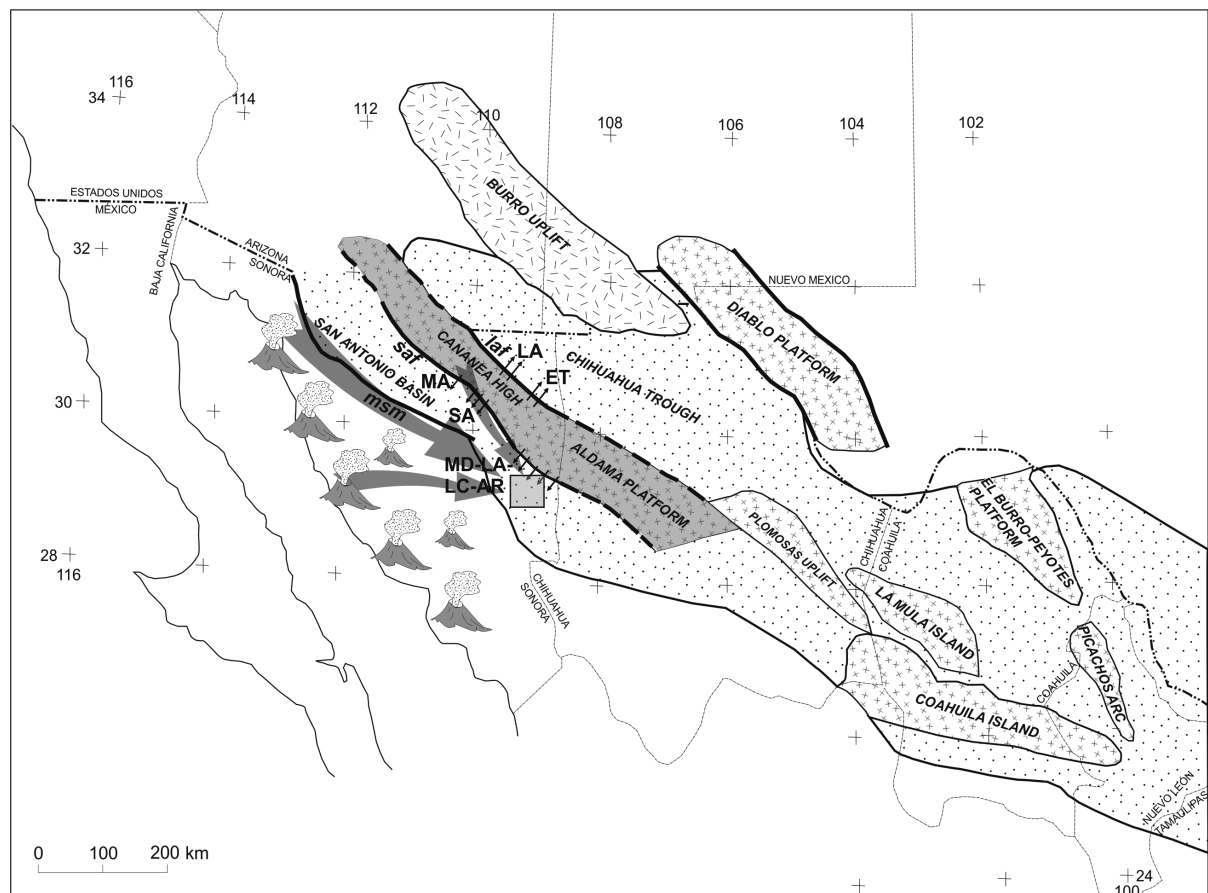
Figure 2. Map showing the paleogeography and structural elements that controlled the geologic evolution in the Upper Cretaceous. The Aldama Platform and its possible continuation towards the north-east of Sonora as the Cananea High were important elements in the evolution of the study area. The black arrows show the occurrence of slipped megaclasts and the gray arrows suggest the possible source of the sediments that constitute the rocky outcrops of the Upper Cretaceous in the study area (square). Megaclast localities: Los Ajos (LA), El Tigre (ET), Magdalena (MA), San Antonio (SA), La Madera (MD), Lampazos (LA), Los Chinos (LC) and Arivechi (AR), *msm* = Mojave-Sonora megashear, *saf* = San Antonio fault, *laf* = Los Ajos fault. Modified from Anderson and Nourse (2005) including Monreal (1996).

2002; Roldán-Quintana, 2002). Epiclastic, pyroclastic and reworked deposits have also been identified in the study area. Flows and pyroclastic rock falls, mass waste deposits and volcaniclastic turbidites are common in the sequence deposited in the Arivechi back-arc basin. Towards the top of the unit the finest sediments increase in proportion, marking the latest stage of the evolution of this type of basin (Spalletti, 2006).

Regional Geology

Although several studies have been carried out knowledge of Mesozoic geology in the Arivechi-Sahuaripa region is still sketchy. King (1939), Himanga (1977), Flinn (1977), Palafox and Martínez (1985), Minjarez *et al*. (1985), Pubellier (1987), and Fernández-Aguirre and Almazán-Vázquez (1991), among others, mainly focused on stratigraphic relationships; however, they also provide descriptions of structural.

Some of these descriptions are as follows: at Sierra El Chiltepín, 20 km north-west of Arivechi, Himanga (1977) described a fold and a thrust with a NW-SE orientation as a result of a NE-SW compression. In the Cerro Macho area, west of Arivechi, Flinn (1977) reported the existence of an exotic Lower Cretaceous thrusting over Upper Cretaceous-Paleogene rocks. Stewart *et al*. (2002) described Proterozoic (700 Ma) sedimentary rocks at Sierra El Chiltepín consisting of well-cemented quartz sandstone intercalated with limestone containing stromatolites, which thrust eastward over Lower Cretaceous rocks.

Also, south of Sierra Chiltepín, at Cerros La Sata and El Mogallón, located 9 km west of Arivechi, Almazán-Vázquez (1989) reported a package of Cambrian and Ordovician sedimentary rocks which are strongly dislocated by normal faults. He also reported outcrops of rocks of Jurassic and Cretaceous age similar to those exposed in the area of Arivechi.

On the other hand, in the Lampazos area, 40 km north-east of Arivechi, Herrera and Bartolini (1993) and González-León (1988) reported Laramidic structures in Lower Cretaceous rocks which consisted of parallel folds with north-east vergence, NW-SE reverse faults and overthrust faults. Bartolini (1993) suggested that the Cretaceous rocks of the Lampazos area correspond to isolated platform fragments with no genetic connection with the sequences exposed in central and northern Sonora. He suggested that in eastern Sonora Lower Cretaceous blocks relate to parts of the Aldama Platform in central Chihuahua and that they slide westward along a NW-facing slope.

East of Arivechi, at Cerros Las Conchas and El Palmar, King (1939) observed that Paleozoic rock slivers could be found on top of Cretaceous rocks, and Palafox and Martínez (1985) and Fernández-Aguirre and Almazán-Vázquez (1991) noted that the deformation of the Laramide Orogeny in the area of Arivechi is represented by tight folds, thrusts and small reverse faults. Minjarez-Sosa *et al*. (1985) believe the folds and reverse faults are the result of the Albian-Cenomanian deformation, as reported by Rangin (1977, 1982).

Likewise, Pubellier (1987) reported the presence of four deformational events in the Sahuaripa and Arivechi region: a Jurassic event responsible for the deposit of coarse clasts; a tectonic phase assigned to the Late Albian-Late Santonian that carried rock fragments of Proterozoic basement on top of Lower Cretaceous rocks with transport N-NE; the Laramide orogeny in the Paleocene, which folded the structures of the previous event with a south-westerly vergence trend which in turn were cut by intrusive rocks during the lower Eocene, and, finally, two extensional events expanding from the Miocene to the present, creating normal faulting.

In the Lampazos area, north of Sahuaripa, the Cretaceous sequence may be lithologically correlated with western Chihuahua Lower Cretaceous rocks (Monreal, 1995). The Cretaceous rocks exposed in Lampazos and Sierra Los Chinos represent basin facies, whereas Lower Cretaceous rock facies, in Sonora, are platform facies (Monreal and Longoria, 2000). According to González-León (1988), there are differences between the facies of these rocks and the Bisbee group; the rocks of Lampazos rather resemble rocks of the same age as those of Chihuahua.

Lastly, at Sierra Los Chinos, 30 km north of Sahuaripa, Monreal and Longoria (2000) and Díaz and Monreal (2008) concluded from the microfossil content that this area encompasses Lower Cretaceous rocks that correspond to the Chihuahua basin or to gradational facies between this basin and the Bisbee Basin.

Methodology

For better understanding and constraining of the sequence of geological events in the Arivechi region, geological mapping was conducted at a scale of 1:25,000. We also aimed to complete stratigraphic measurements and descriptions

of the lithology; measure and analyze the structural data obtained in the field; obtain paleostress tensors; construct the kinematics and paleostress evolution of the Arivechi area; determine the structural effects in the basin evolution; and discuss the implications of our results regarding the tectonic evolution of eastern Sonora. U/Pb zircon and ^{40}Ar/^{39}Ar geochronology was conducted for two selected rock samples.

U/Pb Method

The geochronology was carried out at the Centro de Geociencias Isotopic lab, UNAM. The method of dating is as follows. Laser ablation inductively-coupled plasma mass spectrometry (LA-ICPMS) U-Pb analyses were performed at the Laboratorio de Estudios Isotópicos (LEI), Centro de Geociencias, UNAM, employing a 193 nm excimer laser workstation (Resolution M-050) coupled with a Thermo X-ii quadrupole ICPMS. The protocol reported by Solari *et al*. (2010) was used, employing a 23 µm analytical spot and the Plešovice zircon (Slama *et al*., 2008) as bracketing standard. Time-resolved analyses were then reduced off-line with in-house developed software written in R (Solari and Tanner, 2011), and the output was then imported into Excel, where the concordia as well as age-error calculations were obtained with Isoplot v. 3.70 (Ludwig, 2008).

During the analytical sessions in which the data presented in this paper were measured, the observed uncertainties (1sigma relative standard deviation) on the ^{206}Pb/^{238}U, ^{207}Pb/^{206}Pb and ^{208}Pb/^{232}Th ratios measured on the Plešovice standard zircon were 0.75, 1.1 and 0.95 % respectively. These errors were quadratically added to the quoted uncertainties observed on the measured isotopic ratios of the unknown zircons. This last factor takes into account the heterogeneities of the natural standard zircons. Provided that the isotope ^{204}Pb, used to correct for initial common Pb, was not measured (because its tiny signal is swamped by the ^{204}Hg normally present in the He carrier gas), the common Pb was thus evaluated with the ^{207}Pb/^{206}Pb ratio, and all the analyses carefully graphed on Tera and Wasserburg (1972) diagrams. Correction, if needed, was then performed with the algebraic method of Andersen (2002). In figures, tables and results ^{206}Pb/^{238}U ages are used for zircons < 1.0 Ga, whereas ^{207}Pb/^{206}Pb ages are cited for older grains. The TuffZirc algorithm of Ludwig and Mundil (2002) was used to calculate the best mean of ^{206}Pb/^{238}U ages, which is preferred for estimating the apparent age of those young

zircons in which the ^{207}Pb signal is low and thus yields imprecise results. The ^{207}Pb/^{206}Pb ages were furthermore considered as minimum ages because of the effect of possible Pb loss. We sampled granitic megaclasts in the Cañada de Tarachi Unit.

^{40}Ar/^{39}Ar Method

A K-feldspar mineral separation from a selected rock sample was carried out by standard methods at the mineral separation laboratory at the Estación Regional del Noreste, Instituto de Geología, UNAM. Age analyses were carried out at Queen's University ^{40}Ar/^{39}Ar geochronology laboratory, Kingston, Canada. For each mineral separate, ~5–10 mg samples of material were wrapped in Al-foil and stacked vertically into Al canisters, which were then irradiated in the McMaster University Nuclear Reactor in Hamilton, Canada, with a ^{40}Ar/^{39}Ar flux monitor Hb3gr hornblende (1072 ± 11 Ma [2σ]; Roddick, 1983). Following irradiation, the samples and monitors were placed in small pits, ~2 mm in diameter, drilled in a Cu sample holder. The holders were placed inside a small, bakeable, stainless steel chamber with a Zn Se viewport connected to an ultra-high vacuum purification system. Monitors were fused in a single step; with a focused New Wave MIR-10 30 W CO_2 laser. For the step heating experiments, the laser beam was focused at different temperatures on mineral separates or whole rock samples in approximately 10 steps. The evolved gases were purified with an SAES C50 getter for ~5 min. Argon isotopes were measured with a MAP 216 mass spectrometer, with a Bäur Signer source and an electron multiplier. All data were corrected for blanks, atmospheric contamination, and neutron-induced interferences (Roddick, 1983; Onstott and Peacock, 1987). All errors are reported as ±2σ, unless otherwise noted, and dates were calculated using the decay constants recommended by Steiger and Jäger (1977).

Paleostress analysis

The stress inversion method was applied with Win_Tensor software (Delvaux, 1993). The inversion is based on the assumption that slip planes occur in the direction of the maximum resolved shear stress. The slip direction at a fault surface is inferred from the striations' slip-fiber lineations as a product of friction. Also, we determined the type of fault (normal or strike-slip) using drag folds that allowed us to discriminate faulting. Therefore, the strike and dip of the fault surfaces, the orientation of the lineation (pitch) and the sense of movement

identified at the fault surface were the data used for the inversion.

The obtained fault slip data were used to compute the four parameters of the reduced stress tensor according to Angelier (1994): the principal stress axes were S_1 (maximum compression), S_2 (intermediate compression) and S_3 (minimum compression), and the ratio of principal stress differences is $R = (S_2 – S_3) / (S_1 – S_3)$. The four parameters were determined by successive use of an improved version of the right dihedral method of Angelier and Mechler (1977) and a four-dimensional numeric rotational optimization using the Tensor computer program of Delvaux (1993).

Local Geology

In the study area two units of Upper Cretaceous age have been defined: 1) Cañada de Tarachi Unit, and 2) El Potrero Grande Unit and the Oligocene-Miocene Sierra Madre Occidental Cenozoic volcanic sequence (Figure 3).

Cañada de Tarachi Unit

The oldest unit, known as the Cañada de Tarachi, a name taken from the arroyo of the same name, is located south-east of Arivechi (Figure 3).The Cañada de Tarachi Unit consists of a sequence of conglomerate, sandstone, siltstone, shale, and interbedded
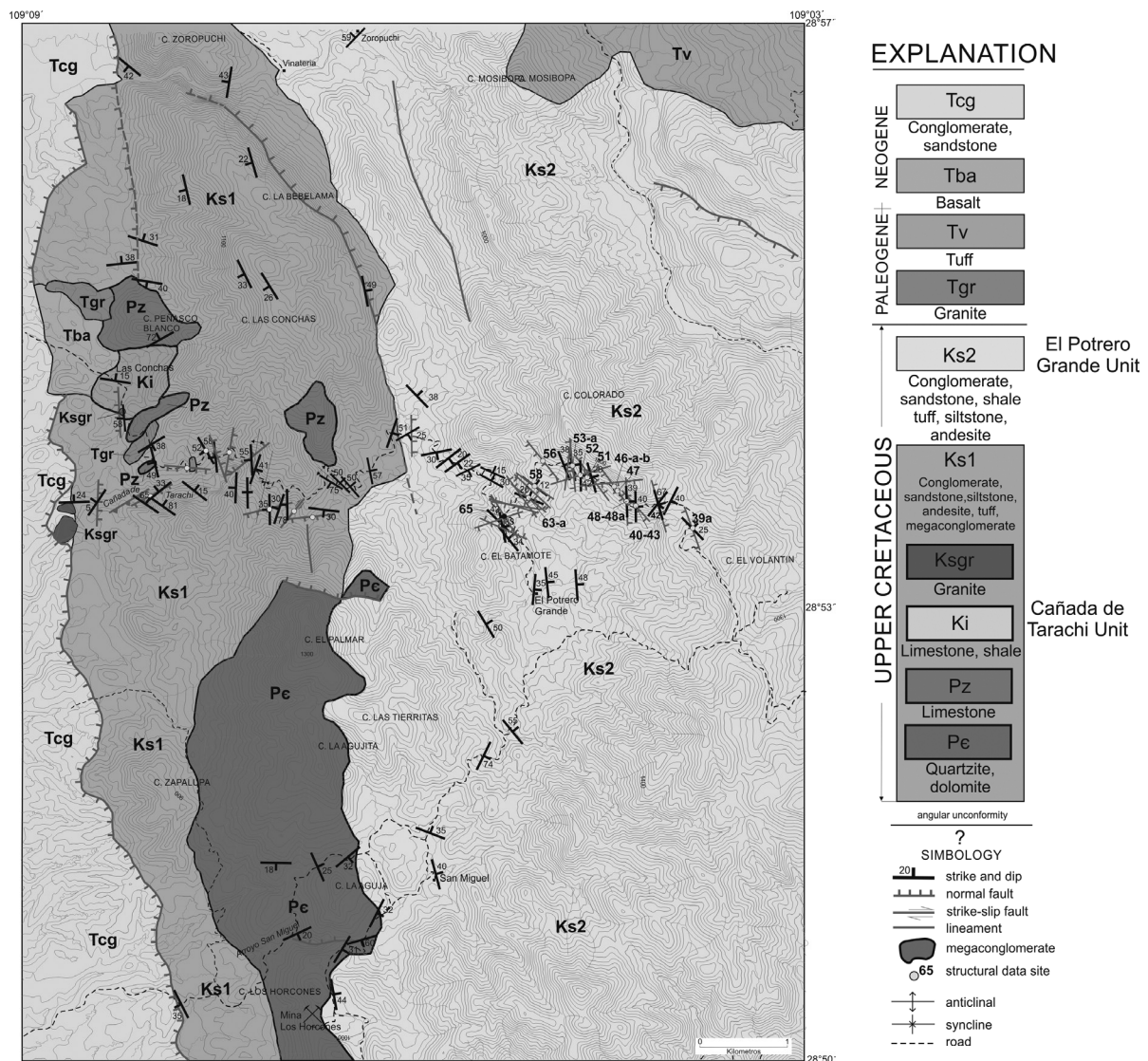
Figure 3. Geologic map of Cerro Las Conchas-Cerro El Volantín area, east of Arivechi, Sonora, Mexico.

andesitic tuffs, with a significant presence of monoliths (Blair and McPherson, 1999) comprised of Precambrian, Paleozoic and Mesozoic sedimentary and igneous rocks. The conglomerate beds in the sequence are composed of several lithologies located at different levels; some of them form a package over 100 m, but most are metric in thickness (Figure 4). The conglomerates originated as a debris flow. Some of the conglomerates in the lower level are of volcanic origin and rounded shape, well sorted, with clast size ranging between 2 and 10 cm, although a few of them measure 20 cm (Figure 4a and 4b); the conglomerates derived from sedimentary rocks are generally angular in shape and unsorted (Figure 4c and 4d).The whole Cañada de Tarachi Unit, on the other hand, records a strong deformation, which is believed to be synsedimentary and related to the gravitational movements of the megaclasts caused by vertical uplift and sliding, rather than the result of a compressive tectonic deformation.

The Precambrian monolith is exposed at Cerro El Palmar (Figure 5a), south of arroyo

Figure 4. Conglomerate in Cañada de Tarachi Unit showing variation in composition and poor sorting. Images a and b show a conglomerate consisting of rock clasts derived from volcanic rocks which are more or less spherical in shape. Images c and d show a conglomerate consisting mainly of angular-shaped sedimentary clast rocks in a quartz-rich matrix. Images e and f show a conglomerate exposed to the north of the area in Cerro Zoropuchi (f) and in the range to the right. Here, the conglomerate is entirely composed of both Paleozoic and Lower Cretaceous limestone rock rounded clasts.

Cañada de Tarachi. The monolith consists of layers of quartz sandstone and dolomite. It measures 7 km long and 2 km wide. The contact between rocks of the Neoproterozoic and the Cañada de Tarachi Unit are marked by a breccia over 10 m thick.

At the base of the monolith, near the contact with the Upper Cretaceous rocks, along the arroyo San Miguel an important finding was the presence of stromatolite fossils, possibly of the *Jacutophyton* genus, similar to those found in the Caborca region (Weber *et al.*, 1979) assigned to the Neoproterozoic. The monoliths of Paleozoic rocks (Figure 5b) are 2 km long, and consist of fossiliferous limestone and quartz sandstone which are assigned to the Mississippian by their fossil contents (Fernández-Aguirre and Almazán-Vazquez, 1991). These megablocks can be observed at Cerro Peñasco Blanco and Cerro Las Conchas.

At Cerro Las Conchas, another monolith composed of limestone, shale and sandstone and containing fossils from the Early Cretaceous (Fernández-Aguirre and Almazán-Vazquez, 1991) (Figure 3) is exposed. Bartolini (1993)

suggested that these megaclasts have better correlation with exposed units in western Chihuahua than with rocks of the same age cropping out in Sonora.

We found several megaclasts composed of granite, and from these we selected two for dating. One was collected in the arroyo Cañada de Tarachi and was dated by U/Pb zircon geochronology at 76.00 ± 2 Ma (Campanian, Late Cretaceous, Figure 6a and 6b, Table 1), and a second sample around 100 m distant was collected at the Arivechi-Tarachi road and dated by ^{40}Ar/^{39}Ar step-heating of a k-spar at 69.57 ± 0.48 Ma (Figure 6c, Table 2). It was noted that these megaclasts are not only found on top but also within the sequence, in smaller thicknesses of dozens of meters. The fact that these are glided fragments, and because of their size were not previously identified as megaclasts, was the main reason for assuming that the stratigraphy was complicated and incorrectly interpreted by previous authors. Hence, we consider that the exposures of Cerro Las Conchas and the Paleozoic limestones are actually gliding megaclasts that are not "in situ."
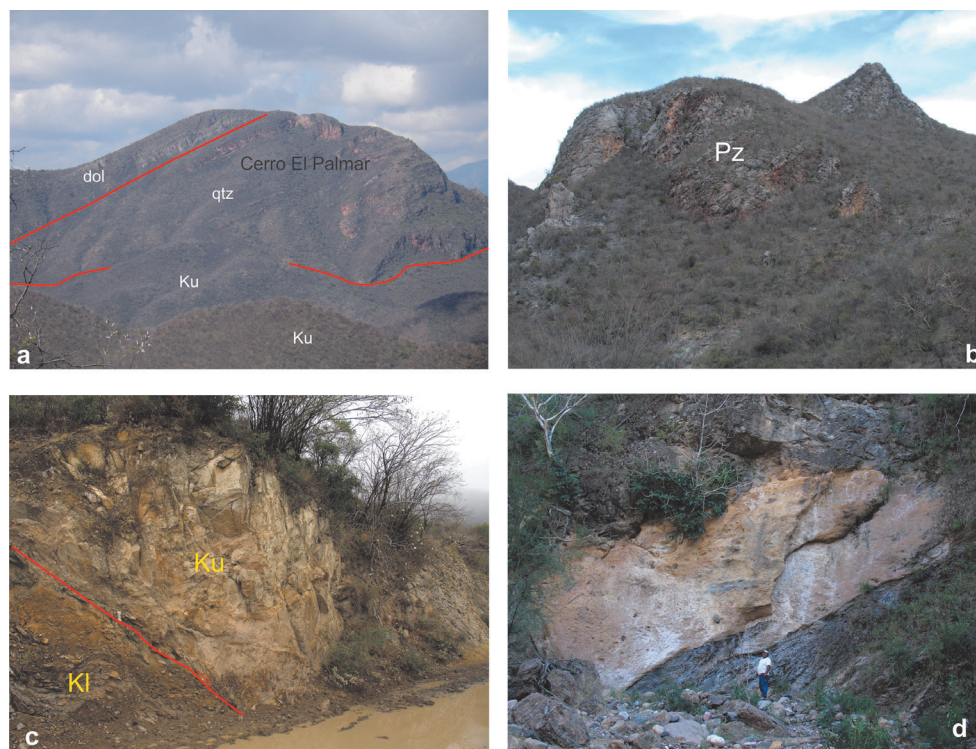
Figure 5. Megaclasts exposed in the Arivechi region. a) megaclast composed of quartzite and dolomite of Proterozoic age constituting Cerro El Palmar. In the forefront is the conglomerate that, together with the megablock, forms part of the Cañada de Tarachi Unit. dol = dolomite, qtz = quartzite, Ku = volcano-sedimentary rocks. b) Paleozoic limestone megaclast. North view. c) 76 Ma granite block (Ku) which is jammed in Lower Cretaceous rocks (Kl). Note the deformation in the rocks of the Lower Cretaceous (Ki). d) Megaclast of uncertain age embedded in the Cañada de Tarachi Unit. Outcrop along the arroyo Cañada de Tarachi.
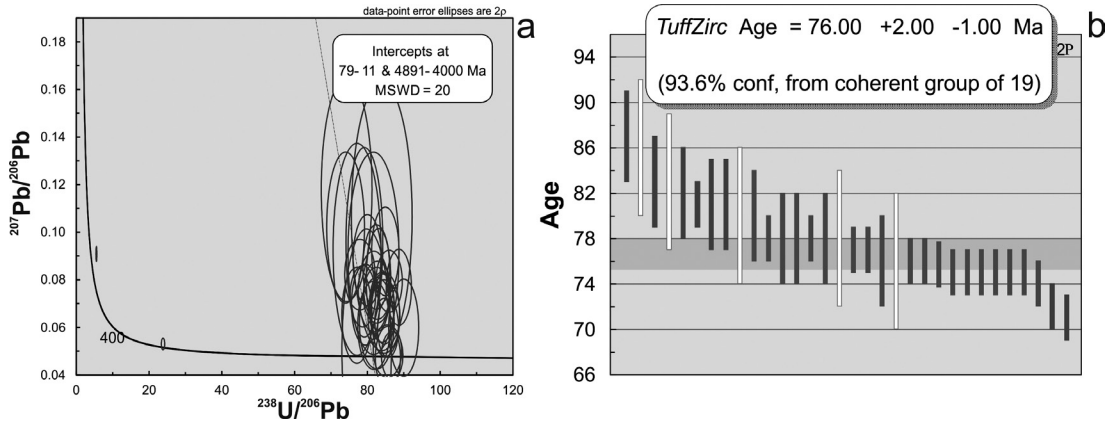
Figure 6. U/Pb zircon data from the granite megablock in the Cañada de Tarachi. a) Concordia curve for the A134-12 sample and b) Weighted mean age graph at 76 Ma.c) Ar/Ar data from the Arivechi-Tarachi road.

Table 1. U-Pb analytical data for zircons from sample in eastern Sonora, Arivechi region.

	U (ppm)	Th (ppm)	Th/U	207Pb/206P ±1s		207Pb/235l ±1s		206Pb/238l ±1s		208Pb/232T ±1s		Rho	206Pb/238 ±1s		207Pb/235 ±1s		207Pbl ±1s		Best age (Ma)±1s	
Zircon_01_A134_0	132	89	0.62	0.07556	0.00499	0.12377	0.0085	0.01209	0.00022	0.00398	0.0002	0.26	77	1	118	8	1083	120	77	1
Zircon_02_009	89	41	0.42	0.04985	0.02102	0.08613	0.0405	0.01253	0.00044	0.00396	0.0012	0.22	80	3	84	38	188	607	80	3
Zircon_04_011	169	164	0.89	0.06256	0.00394	0.1	0.0064	0.01181	0.00015	0.00388	0.00017	0.2	75.7	1	97	6	693	121	76	1
Zircon_05_012	77	54	0.65	0.10648	0.023	0.17487	0.0427	0.01191	0.00048	0.00346	0.00013	0.37	76	3	164	37	1740	375	76	3
Zircon_06_014	84	55	0.60	0.08532	0.00725	0.13924	0.0121	0.01213	0.00022	0.00387	0.0003	0.21	78	1	132	11	1323	149	78	1
Zircon_07_015	183	119	0.60	0.05961	0.00501	0.09596	0.0082	0.01167	0.00016	0.00381	0.00016	0.16	75	1	93	8	589	165	75	1
Zircon_08_016	88	46	0.48	0.06502	0.00823	0.11625	0.0156	0.01297	0.00028	0.00397	0.00009	0.19	83	2	112	14	775	243	83	2
Zircon_09_017	54	24	0.41	0.10192	0.01297	0.18986	0.0262	0.01351	0.00039	0.00394	0.00011	0.26	87	2	177	22	1659	216	87	2
Zircon_10_018	69	44	0.58	0.09574	0.01627	0.15783	0.0271	0.01263	0.00033	0.00391	0.00031	0.15	81	2	149	24	1543	300	81	2
Zircon_11_020	145	81	0.51	0.06455	0.00631	0.10525	0.0112	0.01182	0.00025	0.00362	0.00008	0.23	76	2	102	10	760	187	76	2
Zircon_12_021	115	74	0.59	0.06171	0.00784	0.10303	0.014	0.01211	0.00029	0.00373	0.00009	0.21	78	2	100	13	664	248	78	2
Zircon_13_022	170	105	0.57	0.04817	0.00409	0.07621	0.0066	0.01152	0.00016	0.00324	0.00017	0.17	74	1	75	6	108	164	74	1
Zircon_14_023	747	153	0.19	0.05302	0.00101	0.30621	0.0063	0.04194	0.00033	0.01285	0.00035	0.38	265	2	271	5	330	39	265	2
Zircon_15_024	162	101	0.57	0.05985	0.00834	0.0917	0.0136	0.01111	0.00021	0.00343	0.00009	0.22	71	1	89	13	598	270	71	1
Zircon_16_026	107	62	0.53	0.09189	0.00761	0.14917	0.0134	0.01177	0.00021	0.00347	0.00006	0.26	75	1	141	12	1465	142	75	1
Zircon_17_027	113	68	0.55	0.0681	0.00586	0.11014	0.0096	0.01189	0.00019	0.00345	0.00022	0.18	76	1	106	9	872	162	76	1
Zircon_18_028	291	305	0.96	0.06083	0.00759	0.10248	0.0142	0.01222	0.00027	0.00377	0.00007	0.32	78	2	99	13	633	245	78	2
Zircon_19_029	174	121	0.64	0.04999	0.00451	0.0806	0.008	0.01169	0.00022	0.00369	0.0001	0.23	75	1	79	8	195	177	75	1
Zircon_20_030	173	142	0.75	0.07936	0.00532	0.12459	0.0086	0.01163	0.0002	0.0034	0.00014	0.24	75	1	119	8	1181	120	75	1
Zircon_22_033	144	95	0.61	0.06527	0.00718	0.10488	0.0117	0.01177	0.00022	0.00376	0.00022	0.17	75	1	101	11	783	210	75	1
Zircon_23_034	122	98	0.74	0.08817	0.00785	0.15383	0.014	0.0125	0.00025	0.00409	0.00026	0.22	80	2	145	12	1386	155	80	2
Zircon_24_035	134	126	0.86	0.11804	0.01929	0.21902	0.0411	0.01346	0.00052	0.00386	0.00015	0.49	86	3	201	34	1927	273	86	3
Zircon_25_036	167	120	0.66	0.07309	0.00526	0.12506	0.0093	0.0127	0.00023	0.00384	0.00021	0.24	81	1	120	8	1016	132	81	1
Zircon_26_038	124	81	0.59	0.06843	0.00602	0.10815	0.0097	0.01191	0.0002	0.00366	0.00018	0.19	76	1	104	9	882	165	76	1
Zircon_27_039	150	119	0.73	0.04727	0.00538	0.0761	0.0092	0.01168	0.00019	0.00371	0.00021	0.23	75	1	74	9	63	242	75	1
Zircon_28_040	115	140	1.12	0.08211	0.00608	0.14711	0.0114	0.01283	0.00028	0.00426	0.00033	0.28	82	2	139	10	1248	149	82	2
Zircon_29_041	49	29	0.54	0.09109	0.01738	0.15376	0.0311	0.01224	0.00043	0.00361	0.00014	0.27	78	3	145	27	1448	399	78	3
Zircon_30_042	108	63	0.54	0.06953	0.00695	0.11963	0.0122	0.01258	0.00025	0.00338	0.00023	0.2	81	2	115	11	915	214	81	2
Zircon_31_044	114	71	0.57	0.07682	0.00653	0.11577	0.01	0.01128	0.00018	0.00302	0.00023	0.18	72	1	111	9	1117	175	72	1
Zircon_32_045	131	80	0.56	0.07508	0.00691	0.12143	0.0115	0.01223	0.00026	0.00405	0.00019	0.22	78	2	116	10	1071	191	78	2
Zircon_33_046	134	91	0.62	0.07349	0.00478	0.12048	0.0081	0.01211	0.00022	0.00386	0.00017	0.27	78	1	116	7	1027	135	78	1
Zircon_34_047	56	35	0.57	0.09276	0.0182	0.16579	0.0352	0.01296	0.00045	0.00382	0.00014	0.29	83	3	156	31	1483	410	83	3
Zircon_35_048	126	59	0.43	0.07996	0.0088	0.12791	0.0142	0.01204	0.0002	0.0042	0.00031	0.15	77	1	122	13	1196	227	77	1
Zircon_03_010	784	181	0.21	0.09084	0.00127	2.2649	0.0369	0.18068	0.0015	0.04054	0.00264	0.51	1071	8	1201	11	1443	27	1443	27

Table 2. $^{40}Ar/^{39}Ar$ analytical data from sample in eastern Sonora, Arivechi region.

Sample no	Mineral		J	± (1s)	% error		Int Age (Ma)	± (2 s)	with ± in J		Plateau Age ± (2s)	with ± in J	MSWD	% 39Ar			
JR13	KSP		0.003655	0.000006	0.16		68.84	0.52	0.57		69.51	0.49	0.54	1.20	87.76	Probability	Initial Ratio	Initial Ratio Error
Can/Pos	221/JR13	AOR13-13							IsoPlot PA-->		69.57	0.48	na	1.30	78.7	0.24	na	na
					Decay corrected true ratios				IsoPlot CA-->		70.07	0.65	na	1.70	100.00	0.06	284.30	6.60
Step no	Power	40Ar/39Ar	±	38Ar/39Ar	±	37Ar/39Ar	±	36Ar/39Ar	±	40Ar*/39Ar(K)	40Ar*	Cumulative	Age	±	Ca/K	±	Cl/K	±
	(%)		(1s)		(1s)		(1s)		(1s)		(%)	39Ar (%)	(Ma)	(1 s)		(1 s)		(1s)
1	2.5	67.695	0.577	0.221	0.006	0.133	0.211	0.203	0.004	7.803	1.137	11.5	1.23	50.73	7.29	0.24	0.39	0.0390	0.00
2	3.0	39.928	0.269	0.127	0.003	0.353	0.126	0.101	0.002	10.115	0.595	25.3	3.14	65.49	3.78	0.65	0.23	0.0217	0.00
3	3.5	24.151	0.150	0.068	0.002	0.482	0.097	0.049	0.001	9.801	0.359	40.6	6.24	63.50	2.28	0.88	0.18	0.0104	0.00
4	4.0	17.554	0.074	0.043	0.001	0.998	0.053	0.025	0.001	10.288	0.185	58.6	12.23	66.60	1.17	1.83	0.13	0.0056	0.00
5	4.5	15.658	0.065	0.032	0.001	1.302	0.060	0.017	0.001	10.685	0.179	68.2	18.19	69.11	1.13	2.39	0.16	0.0034	0.00
6	5.5	15.091	0.042	0.027	0.001	2.350	0.047	0.015	0.000	10.841	0.100	71.7	30.58	70.10	0.64	4.31	0.22	0.0023	0.00
7	6.5	13.992	0.042	0.023	0.001	2.189	0.044	0.011	0.000	10.860	0.098	77.5	41.85	70.22	0.62	4.01	0.20	0.0015	0.00
8	7.5	13.156	0.039	0.020	0.001	1.952	0.047	0.008	0.000	10.832	0.106	82.2	52.13	70.05	0.67	3.58	0.19	0.0011	0.00
9	8.5	12.381	0.044	0.018	0.001	1.581	0.049	0.006	0.000	10.859	0.097	87.6	61.81	70.22	0.62	2.90	0.16	0.0008	0.00
10	10.0	12.143	0.045	0.022	0.001	0.995	0.040	0.005	0.000	10.624	0.099	87.4	70.32	68.73	0.63	1.82	0.11	0.0016	0.00
11	12.0	12.122	0.054	0.033	0.001	0.690	0.042	0.005	0.000	10.669	0.115	88.0	77.72	69.01	0.73	1.26	0.10	0.0042	0.00
12	15.0	12.299	0.078	0.051	0.001	0.522	0.053	0.006	0.000	10.484	0.153	85.2	83.26	67.84	0.97	0.95	0.11	0.0083	0.00
13	18.0	12.902	0.079	0.066	0.001	0.513	0.095	0.008	0.001	10.548	0.185	81.7	87.88	68.25	1.17	0.94	0.18	0.0117	0.00
14	22.0	14.154	0.099	0.103	0.002	0.664	0.099	0.011	0.001	11.037	0.275	77.9	90.94	71.35	1.74	1.22	0.19	0.0200	0.00
15	30.0	15.351	0.093	0.145	0.002	0.733	0.038	0.016	0.000	10.645	0.149	69.3	100.00	68.86	0.95	1.34	0.09	0.0293	0.00

No fossils have been identified in the Cañada de Tarachi Unit, apart from those that are contained in the slipped blocks. This statement has genetic significance for the sedimentary environment. The absence of fossils could be interpreted as resulting from the development of these basins inland. In terms of the thickness of this unit, based on the conducted mapping and strike and slip directions, we estimated that it must have a minimum thickness of 2000 m.

Fossil studies carried out on the conglomerate clasts indicate Paleozoic and Early Cretaceous ages; therefore the Cañada de Tarachi Unit is situated in the Upper Cretaceous sequence. The 76 Ma U/Pb zircon date for the granite block at the Cañada de Tarachi Unit was interpreted as the crystallization date and the 70 Ma ^{40}Ar/^{39}Ar date was interpreted as the cooling age, i.e., postdating a Late Cretaceous age and suggesting that the onset of erosion was probably present by that time.

The base of the Cañada de Tarachi Unit is not exposed, but from correlation with other localities it has been interpreted as an angular unconformity unit over older rocks; in addition, the upper contact with the El Potrero Grande Unit is transitional to a younger volcaniclastic sequence.

El Potrero Grande Unit

This unit takes its name from the ranch located south-east of Cerro El Batamote (Figure 3). King (1939) defines this as the Potrero Formation, which seems to correspond to the same location, although he assigns it to the Albian. The El Potrero Grande Unit is much more of a volcano-sedimentary sequence than the Cañada de Tarachi Unit. The El Potrero Grande Unit consists of conglomerate, sandstone, siltstone, and shale with interbedded andesite, diorite strata dikes and layers of rhyolitic tuffs. These rocks together form a partial column more than 2,400 m thick (Figure 7). It must be said that we did not measure the entire El Potrero Grande Unit, because it is covered by Tertiary volcanic to the east.

The base of the unit consists of a section of conglomerates and volcanic rocks of andesitic composition that includes tuffs, continuing with shale, siltstone and sandstone that form a rhythmic sequence.

Isotopic K/Ar ages in biotite concentrates from volcanic rocks provided dates of 83.4 ± 4.17Ma (Pubellier, 1987), 84 and 86 Ma K-Ar, respectively, for two tuffs in the upper part of the sequence, indicating an Upper Cretaceous age for the sequence (Grajales-Nishimura *et al*., 1990). In the Sahuaripa-Natora road we dated a tuff in a similar section 20 km north of the area. The age sample was dated as 76.3 ± 1.98 Ma (U/Pb zircon at Geociencias isotopic Lab), placing it in the Campanian (Upper Cretaceous). We consider this tuff equivalent in age to tuffs in our study area.

The Upper Cretaceous in Arivechi, eastern Sonora was deposited in a deep sedimentary basin that received sediments from an existing volcanic arc and also accumulated sediments from both the exposed north-western and north-eastern basement.

Structural Geology

The structures found in the study area are normal and strike-slip faults, as well as mesoscopic folds. They are the result of two different processes recorded in the Upper Cretaceous units. The older mechanism is a Cretaceous gravitational gliding deformation, which affects only the Cañada de Tarachi Unit; the El Potrero Unit shows only extension and the associated structures.

Gliding tectonics is interpreted as a mechanism whereby large masses of rocks move down a slope under gravitational force, producing folding and faulting at different extents and complexity. The fine-grained rocks of the Cañada de Tarachi Unit are folded into smaller tight folds as seen along the arroyo Cañada de Tarachi. The structures are–considered synsedimentary in order to denote their inferred formational environment, and include extensional faulting and reverse faults and folds.

In northern Sonora, Rodriguez-Castañeda (2002) interpreted a similar sequence formed by gravitational re-sedimentation generated by tectonic activity along the south-west margin of the Cananea High, a positive land that could be the continuation of the Aldama Platform into Sonora.

The extensional faults are observed along the two units whereas contractional structures are restricted to the thin bedded sandstone and siltstone exposed in the front of the sliding mass observed in the Cañada de Tarachi Unit.

Fold data collected from the Cañada de Tarachi Unit indicate that folds are asymmetric and related to detachment surfaces. The fold vergence (Figure 8) suggests that the sequence was transported towards the south-west and to a lesser extent towards the north-east. Figure 9 corresponds to "Z" fold kinematic indicators, showing vergence towards the south-west. In Figure 9a the layer that serves as detachment
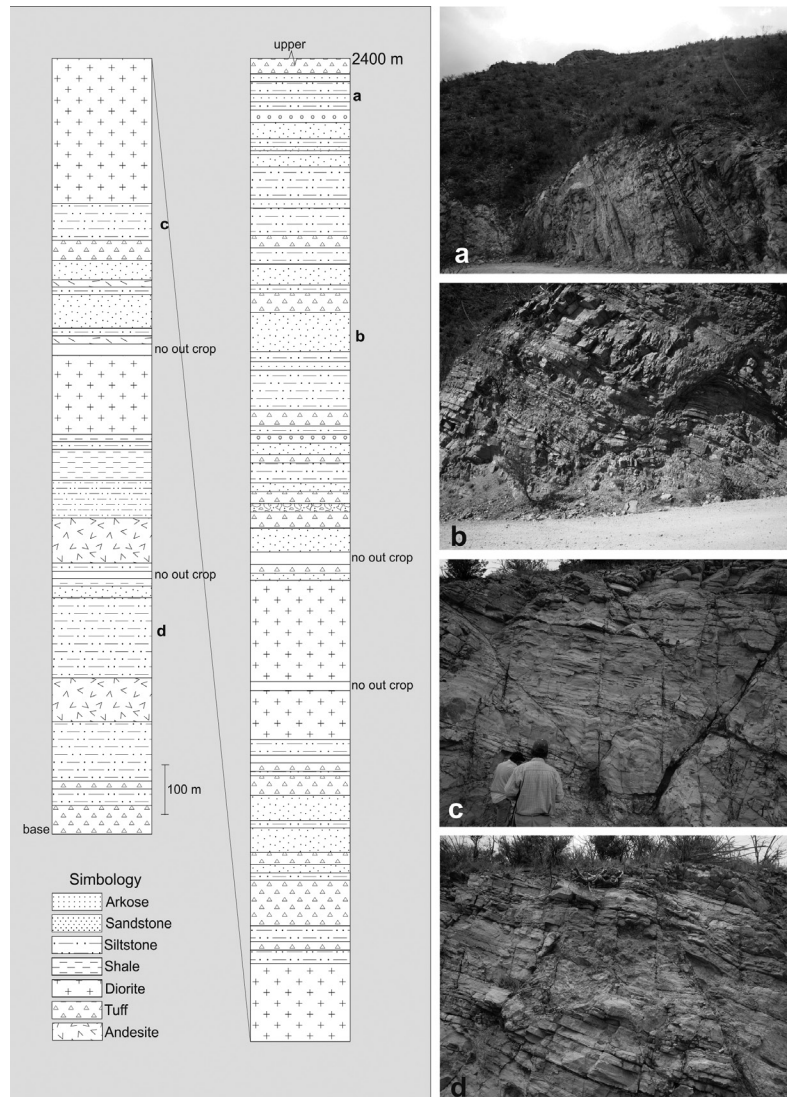
Figure 7. A 2,400 m measured column on a segment of the El Potrero Grande Unit, from the Cerro El Volantín to the Cerro El Batamote. Pictures go from top to bottom, i.e., from **a** to **d**. The **bold** letters in the lithologic column show the approximate location of the picture in the column. Compare the structures observed in the El Potrero Grande Unit with structures recorded in the Cañada de Tarachi Unit in Figure 9.

Simbology
- Arkose
- Sandstone
- Siltstone
- Shale
- Diorite
- Tuff
- Andesite

for the formation of folds has a 019 strike with a 30NW dip. Most of the folds display axial surfaces oriented NW-SE and plunging to the north-east with two *arrays*, one with an average of 83° and the second with an average of 34°.

The folds show no obvious genetic relationship to tectonic contraction within the megaclasts. It is clear that folds are related to a synsedimentary deformation corresponding to the emplacement of the megaclast as indicated by its geometry and location.

Normal faulting and paleostress reconstruction

To explain the tectonic processes from which the development of these structures originated, a paleostress field reconstruction is offered.

The paleostress analysis was performed with measured surface data collected over faults in the Upper Cretaceous rocks along the Arivechi-Tarachi road, in the section between Cerro Las Conchas and Cerro El Volantín and along the arroyo Cañada de Tarachi. The data sites are located in sedimentary rocks as much as in igneous rocks. The displacement over the measured faults is generally from centimeters up to meters, and the faults are normal, although some of them record a strike-slip component. In general, all the measured faults display good striations. The results obtained from the paleostress analysis are in shown in Table 3 and in Figures 10 and 11.

The evolution of the stress fields is shown in structural maps (Figures 12 and 13) with symbols indicating the two horizontal S_{Hmax} and
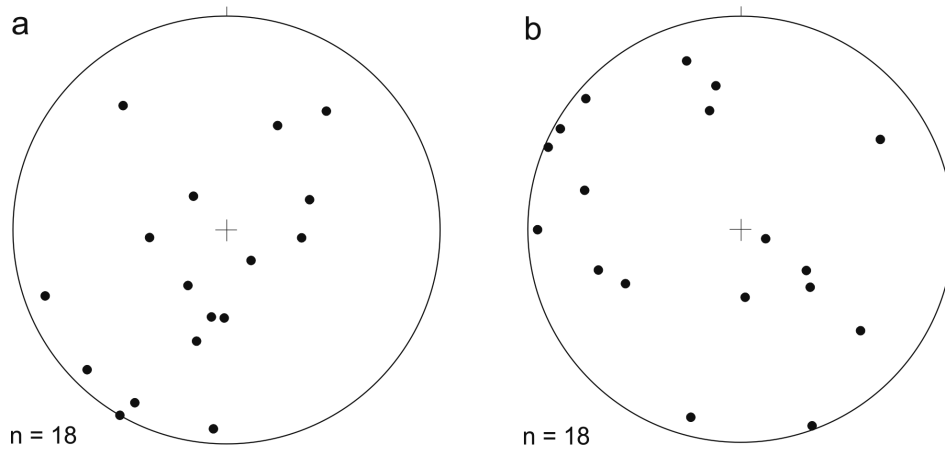
Figure 8. Folds in Cañada de Tarachi Unit. a) Poles of axial surfaces showing south-west vergence. b) Fold hinge lines showing a horizontal to sub-vertical plunge oriented NW-SE.
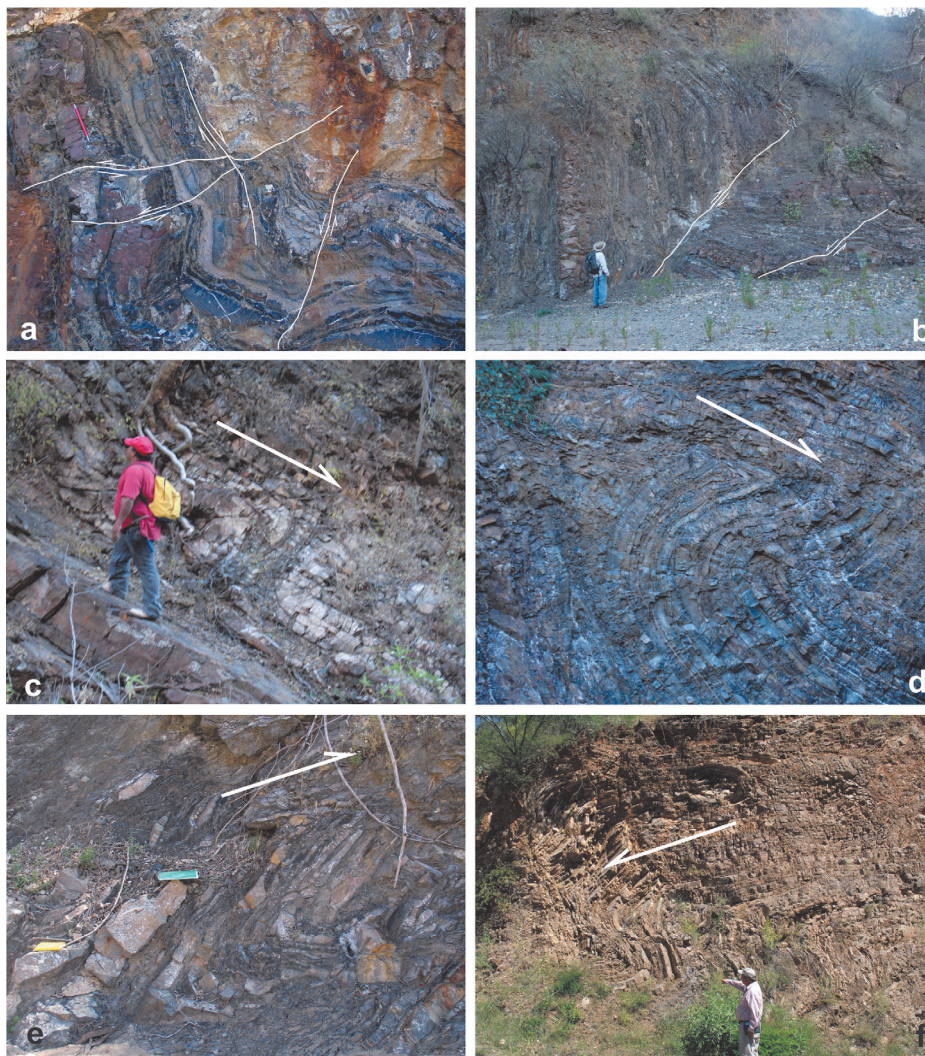
Figure 9. Intense deformation (a and b) recorded in the base of the Cañada de Tarachi Unit. Note the scale of deformation. Reverse and normal faults plus folds affect the sequence. Z folds recorded in the Cañada de Tarachi Unit (c, e, d) suggest transport to the south-west. In a, the bed where the man stand is the base of the detachment. The S fold on f crops out along the Arivechi-Tarachi road, also suggesting transport to the west.

S_{hmin}, with black inward arrows for compressive stress and white outward arrows for extensive stress. The length depends on the magnitude of the relative stress in function of the stress relation R and orientation of the principal stress directions. The vertical axis is indicated by an open circle for a compressive regime (vertical extension), by a dot for a strike-slip regime, and by a black circle for an extensive regime (vertical compression). The classifications proposed by Delvaux *et al*. (1995) for the stress tensors are: *radial / pure / strike-slip* extensive, *extensive / pure / compressive* strike-slip or *strike slip / pure / radial* compressive based on the relative magnitude of the intermediate axis and given by the stress relation R (Figure 14).

The orientation of the stress field was determined with the measured structures which show a clear sense of movement. Twenty-six sites were examined in the studied sector. The sites are located in outcrops of Upper Cretaceous rocks. The results of the inversion (Table 3) and their correlation allow the definition of several paleostress groups. The tensors are grouped according to their similarity, based on the direction of the main axes S_{Hmax}, S_{hmi}, the stress regime index and the stratigraphic relation.

The faulted sediments, which belong to the Cañada de Tarachi Unit, dip towards the north-east. Almost all the faults are normal

Table 3. Parameters of the paleostress tensors calculated for rocks of the Upper Cretaceous.

Data of Cañada de Tarachi Unit, ductile and fragile conditions

Site	Lithology	n	S1	S2	S3	R	R´	Type of tensor
A57-10	Conglomerate	8	109/45	317/42	214/14	0.44	0.44	Pure extensive
A57-10a	Conglomerate	8	019/24	184/65	288/06	0.44	1.56	Pure strike-slip
A71-10	Sandstone	7	260/58	099/31	004/08	0.42	0.42	Pure extensive
A72-10	Conglomerate	8	253/34	099/54	350/14	0.5	1.5	Pure strike-slip
A88-11	Sandstone	5	082/54	196/16	295/28	0.5	0.5	Pure extensive
A95-11	Sandstone	6	108/71	250/15	341/04	0.5	0.5	Pure extensive
A97-11	Sandstone	11	274/70	177/02	086/20	0.5	0.5	Pure extensive

Data El Potrero Grande Unit, fragile conditions

Site	Lithology	n	S1	S2	S3	R	R´	Type of tensor
A140-12	Sandstone	5	034/48	188/39	288/12	0.5	0.5	Pure extensive
A40-10	Tuff	6	098/39	257/00	360/11	0.5	1.5	Pure strike-slip
A41-10	Andesite	4	096/11	243/77	005/07	0.5	1.5	Pure strike-slip
A42-10	Andesite	8	325/38	107/46	220/20	0.5	0.5	Pure extensive
A43-10	Sandstone	7	333/42	111/39	221/22	0.5	0.5	Pure extensive
A46-10	Tuff	10	199/36	070/37	315/29	0.33	0.33	Pure extensive
A46-10a	Tuff	4	009/35	179/54	278/06	0.25	1.75	Compressive strike-slip
A46-10b	Tuff	8	067/68	329/03	238/23	0.38	0.38	Pure extensive
A47-10	Andesite	5	045/62	139/02	230/26	0.5	0.5	Pure extensive
A48-10	Andesite	14	100/44	256/43	359/14	0.5	0.5	Pure extensive
A48-10a	Andesite	4	097/35	248/51	356/14	0.5	1.5	Pure strike-slip
A51-10	Tuff	5	128/02	321/88	216/01	0.5	1.5	Pure strike-slip
A52-10	Tuff	6	161/77	069/00	339/08	0.88	1.12	Extensive strike-slip
A53-10	Sandstone	4	006/83	134/04	224/01	0.62	0.62	Pure extensive
A53-10a	Sandstone	5	090/64	347/07	253/28	0.5	0.5	Pure extensive
A56-10	Sandstone	5	113/35	274/53	016/09	0.7	1.3	Extensive strike-slip
A63-10	Tuff	5	174/80	306/07	036/06	0.4	0.4	Near pure extensive
A63-10a	Sandstone	5	051/66	163/09	256/14	0.5	0.5	Pure extensive
A65-10	Sandstone	4	324/29	147/61	054/01	0.5	1.5	Pure strike-slip

n= number of fault data used for stress tensor determination; s1, s2, s3 = plunge and azimuth of principal stress axes; R = stress ratio (s2 – s3)/(s1 – s3), R´ = tensor type index.

Figure 10. Paleostress reconstructions for the rocks of the Cañada de Tarachi Unit. Circle = S_1; Triangle = S_2; Square = S_3.
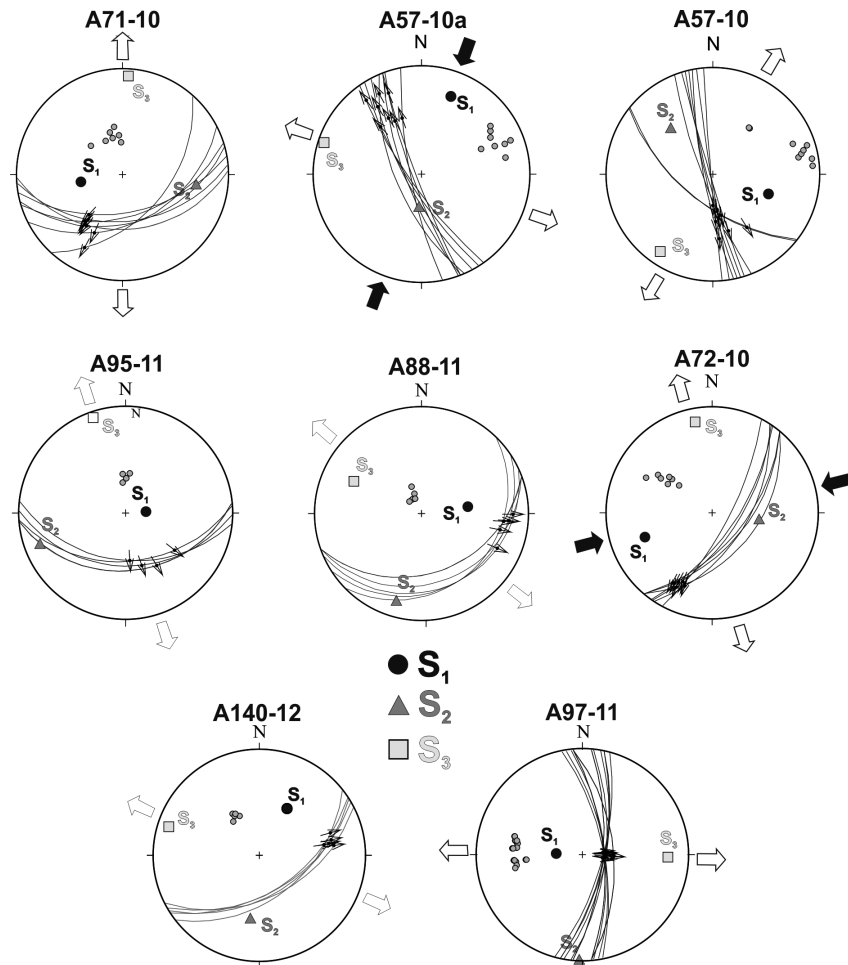
with oblique-slip motions predominating, but dip-slip and strike-slip are present and play an important role. Faults in Figure 13 show that the motion of these faults was induced by extension along a direction of S_3 NW-SE, NE-SW and E-W for dip-slip normal faults; whereas S_1 is in general NNE-WSW and ENE-WSW in relation to strike-slip faults (Figure 10).

On the other hand, at the El Potrero Grande Unit faults are dip-slip, oblique slip normal faults and strike-slip faults. The direction of S_3 is NE-SW for dip-slip normal faults; NE-SW, almost N-S, and NW-SE for the oblique normal faults, and the S_1 directions E-W, NW-SE, and WNW-ESW are related to strike-slip faults (Figure 11).

Evolution

The studies carried out in the area indicated the existence of two Cretaceous sequences differentiated by their composition and stratigraphic position. The observed structures are mesoscopic folds in the Cañada de Tarachi Unit and the development of normal faults and smaller proportion by strike-slip faults.

The Cañada de Tarachi Unit is characterized by intercalations of conglomerate, sandstone, siltstone, rhyolitic tuff and andesite, showing a strong deformation. The geographic extension of Precambrian, Paleozoic and Lower Cretaceous monoliths or remnant rocks suggests that they belong to a basement possibly located towards the east, in the State of Chihuahua. The fold vergence (Figure 8) indicates that the sequence was transported towards the south-west.

The directions of stress that we were able to determine from the Cañada de Tarachi Unit from normal oblique, normal dip-slip and strike-slip faulting are shown in Figures 10 and 12. Local results are given in Figure 12 for both minimum horizontal stress (S_3) and maximum stress (S_1). Extension stress (S_3) is more common than compression stress (S_1), because the normal faults (subverticalS_1) in the section are common whereas strike-slip faults moved when both compression and extension were horizontal (subverticalS_2). Normal faults with different orientations, such as NNW-SSE, NE-SW, E-W, and N-S, show high and medium dips (Figure 10). The
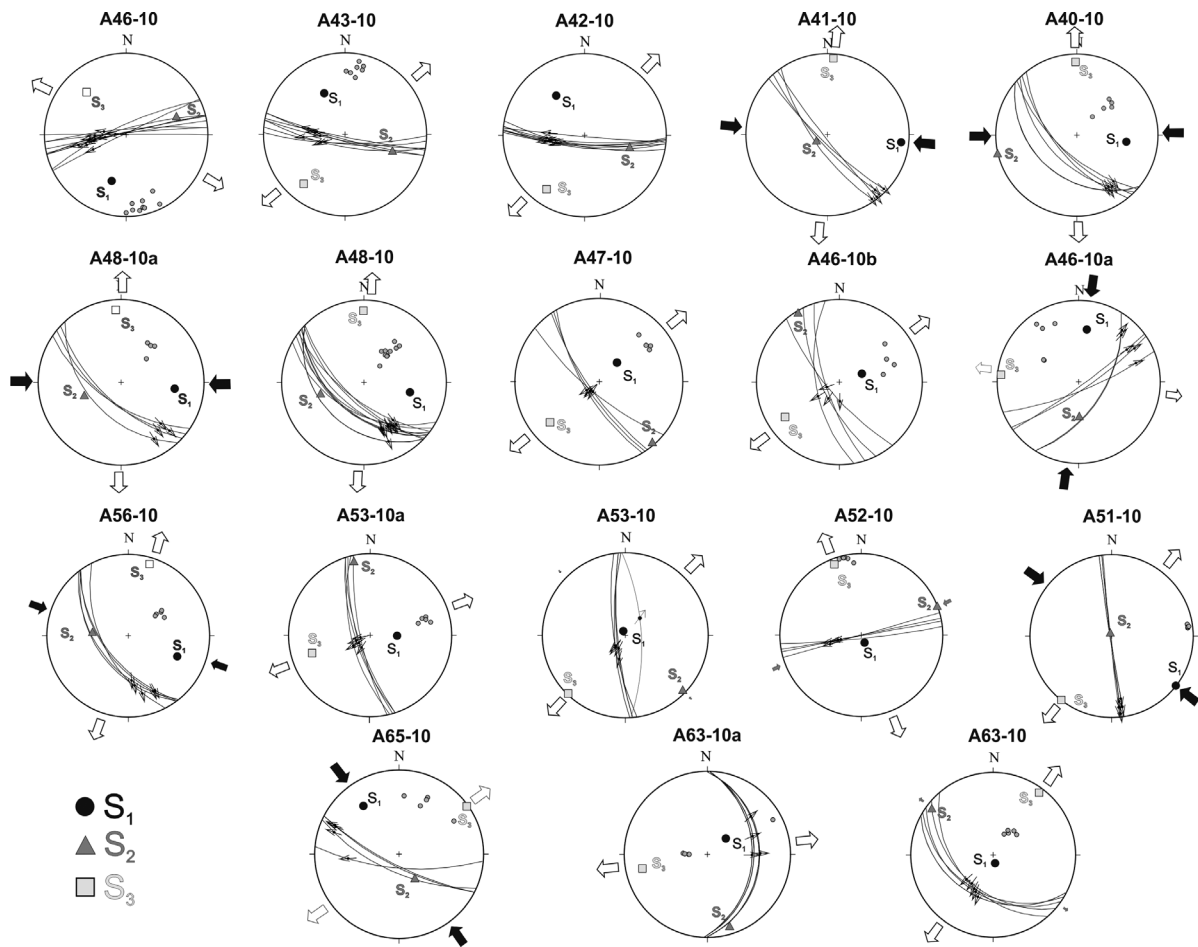
Figure 11. Paleostress reconstructions in the El Potrero Grande Unit. Circle = S_1, triangle = S_2, square = S_3.

faults with an oblique component in the NNW direction have high dips towards the west and were induced by the S_3 extension direction NE-SW; NE oblique faults have medium angle dips towards the south-east and are the result of a N-S and NW-SW S_3; E-W dip-normal faults dip towards the south with intermediate angles, whereas the N-S faults display high angle dips towards the east as a result of NNW S_3 and E-W S_3 directions, respectively (Figure 10). The strike-slip faults with NE-SW and NW-SE orientations characteristically have high angle dips associated with ENE-WSW and NNE-SSW compression (S_1), respectively (Figure 10).

The paleostress tensors are shown in Table 3 and in the structural planes of Figures 12 and 13. The tensors were grouped according to their similarities based on the stress regime and the direction of the stress axis. The paleostress is only recorded in Upper Cretaceous rocks, the reason why chronological ordering of paleostress data depends upon

rock comparison with other sites outside the study area.

The Cañada de Tarachi Unit is characterized by an extension regime and, to a lesser degree, by a pure strike-slip regime (Figure 13). The main axis of extension (S_3) is almost horizontal with a NW-SE main direction, and with a smaller proportion in a NE-SW direction. The main axis of compression, corresponding to the strike-slip movements,(S_1) is sub-vertical with a NE-SW direction. In conclusion, the previous analysis shows that at the time there was an extension regime with development of high angle normal faults.

Interpretation of the paleostress results in the El Potrero Grande Unit indicates a stress regime characterized by extension and strike-slip regimes, both well defined (Figure 13). The extension regime displays an S_3 closer to the horizontal in a NE-SW direction (Figure 13). The strike-slip regime is shown by a varying
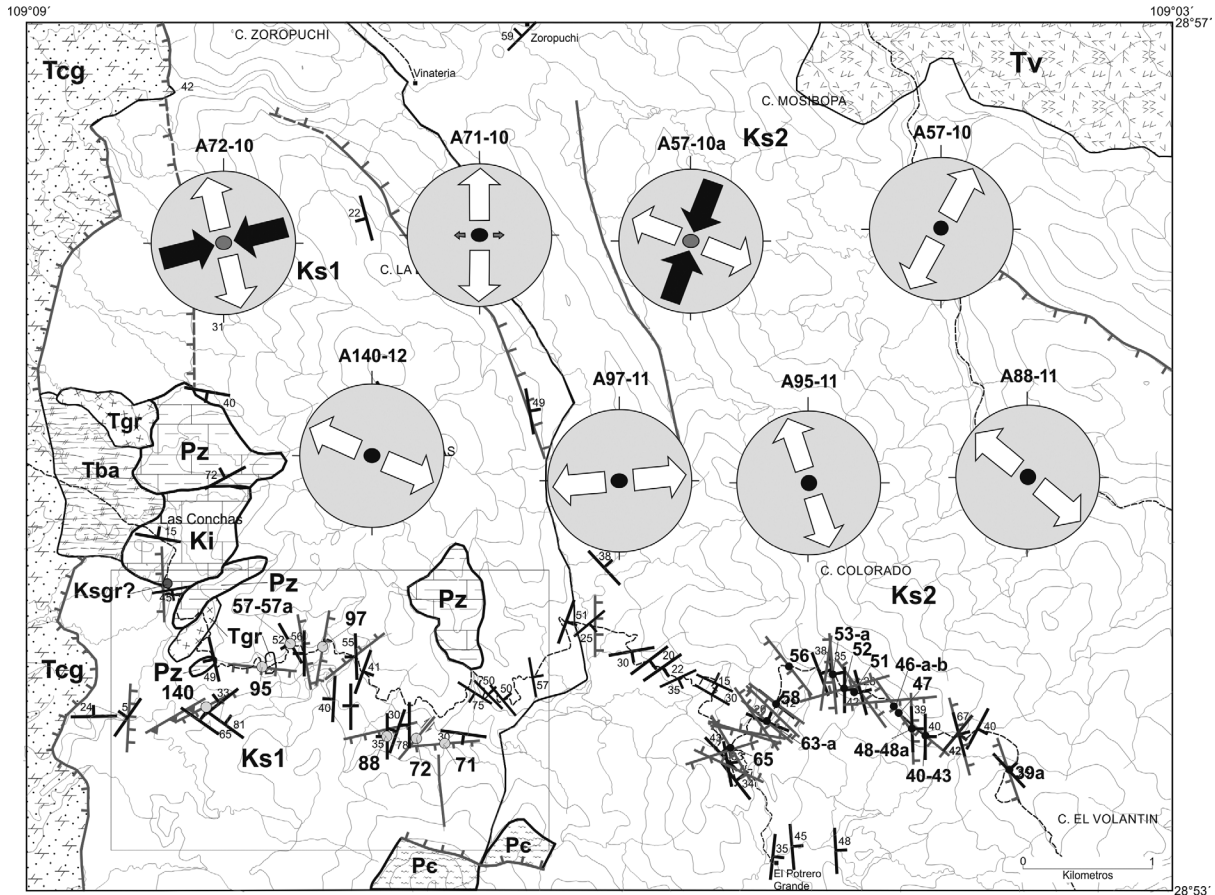
Figure 12. Orientation of the horizontal maximum and minimum stress in the Cañada de Tarachi Unit. The square shows the location of measured sites. Black arrow = S_1, white arrow = S_3. The central circle corresponds to S_1 when black and S_2 when gray.

main axis of compression S_1, almost horizontal in sites A41-10 and A51-10, sub-vertical in sites A40-10, A46-10a, A41-10, A48-10a, A56-10 and A65-10, and with almost E-W, NW-SE and N-S directions in site A46-10a. The stress of extension S_3 is horizontal to a N-S, NE-SW direction (Figure 13).

Discussions

The megaclasts identified in the study area range in age from the Proterozoic to the Mesozoic. Two megaclasts of granitic composition were dated, one by U/Pb date on zircon and one by $^{40}Ar/^{39}Ar$ step-heating date on K-spar, since they were less than 100 m apart, we assume that they were from the same pluton and therefore we can interpret the dates as concordant. One is an emplacement aged 76.0 ± 2.0 Ma by U/Pb zircon geochronology, and the second one gives a K-spar cooling age of 69.57 ± 0.48 Ma according to $^{40}Ar/^{39}Ar$ step-heating geochronology. It is assumed

that the megaclasts are part of the same pluton and were deposited at the same time as part of a debris flow in an alluvial slope. The ages of the granitic blocks suggest that the minimum age for the onset of the erosion is not earlier than 76 Ma according to the U/Pb date. The difference in zircon U/Pb and K-feldspars $^{40}Ar/^{39}Ar$ concordant dates (76 Ma and 70 Ma, respectively) suggest rapid uplift and erosion. As a consequence of these processes, rapid uplift and erosion, the column of Cretaceous sediments is more than 10 km thick. The absence of fossils and the rhytmitic sedimentation at the youngest unit suggests a neritic or a lacustrine continental environment.

From a tectonic perspective, it can be considered that the recognized megaclasts were formed in an extensional environment where topographic highs were formed, causing block gliding. Our hypothesis is that the Arivechi area was located near or at the edge of the Aldama Platform. It is probable that
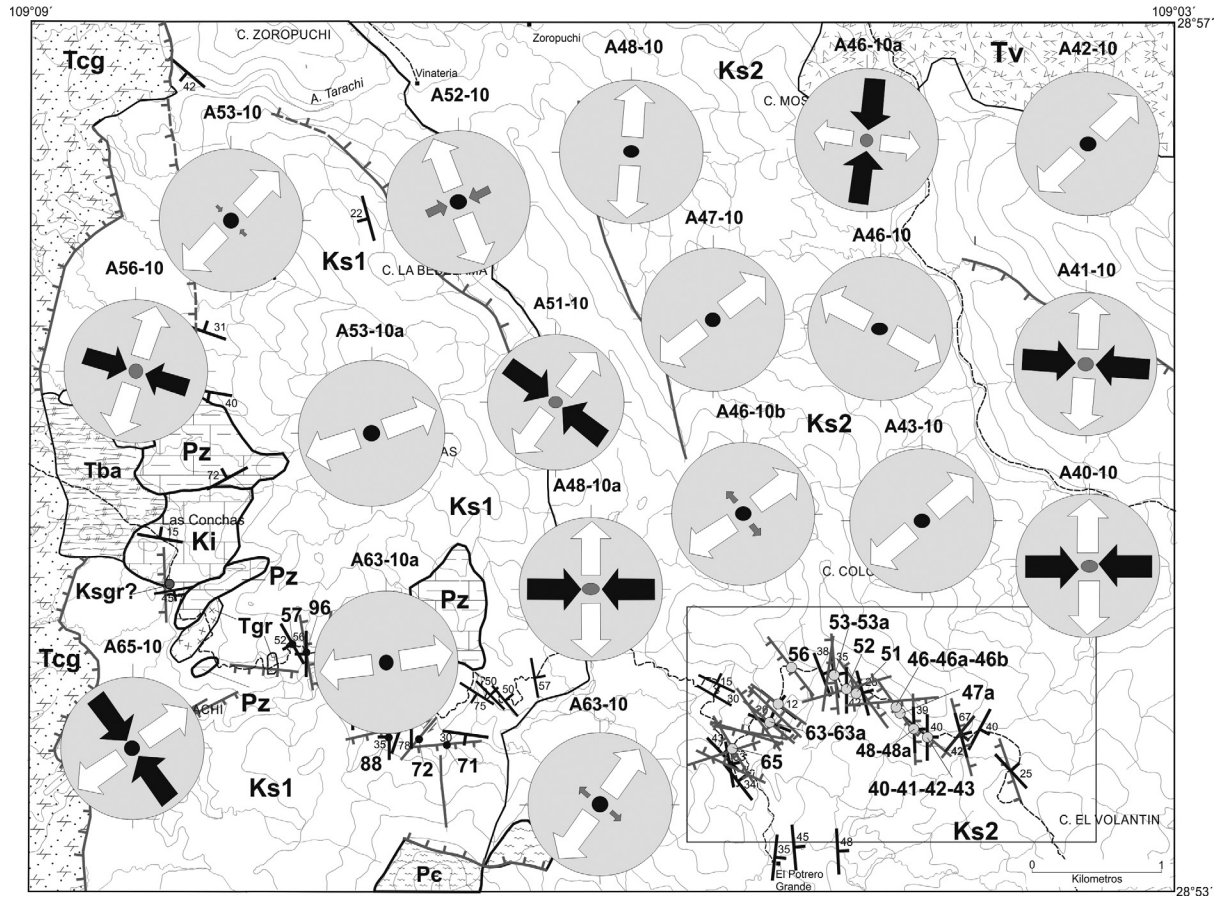
Figure 13. Orientation of the horizontal maximum and minimum stress in the El Potrero Grande Unit. The square shows the location of measured sites. Black arrow = S_1, white arrow = S_3. The central circle corresponds to S_1 when black and S_2 when gray.

the Aldama Platform continues to north-east Sonora as the Cananea High.

Other places with similar relationships in eastern Sonora near the study area are: Sierra La Madera, Lampazos and Sierra Los Chinos. In north-east Sonora along the margins of the Cananea High megaclasts were also identified at Sierra Los Ajos and Rancho San Antonio as well as in central Sonora in the Magdalena, Santa Ana and Tuape areas.

In the Arivechi-Tarachi area, east of Arivechi, two stress regimes have been recognized, one of pure extension and another with strike-slip displacement, affecting both Upper Cretaceous units exposed in the study area.

Prior to this study no paleostress data were reported for the area, but now we are able to compare the paleostress data with information reported by Rodríguez-Castañeda (2002) for the Rancho San Antonio area in north-eastern

Sonora, i.e., an andesitic dike that registered NE-SW (S_3 = N058) and WNW-ESE (S_3 = N283) extensions at the arroyo Las Minas. In another locality towards the south of the previous locality at Rancho El Babiso, on rocks of the Baucarit Formation, S_3 is oriented NE-SW (S_h= 073). Other studies that can help with the interpretation of the Arivechi data include the method used by Angelier *et al*. (1981) in Baja, California Sur (around Santa Rosalia) and Angelier *et al*. (1985) at the Hoover Dam, Nevada, United States; they identify a chronology of events where the directions of a NE-SW to ENE-WSW extension are followed by an E-W to WNW-ESE extension with clockwise rotation. These studies suggest that such directions of extension are a product of a Basin and Range type normal faulting regime; even though it is possible to consider that the faults affecting the two Late Cretaceous units of the study area are associated with the Basin and Range event.
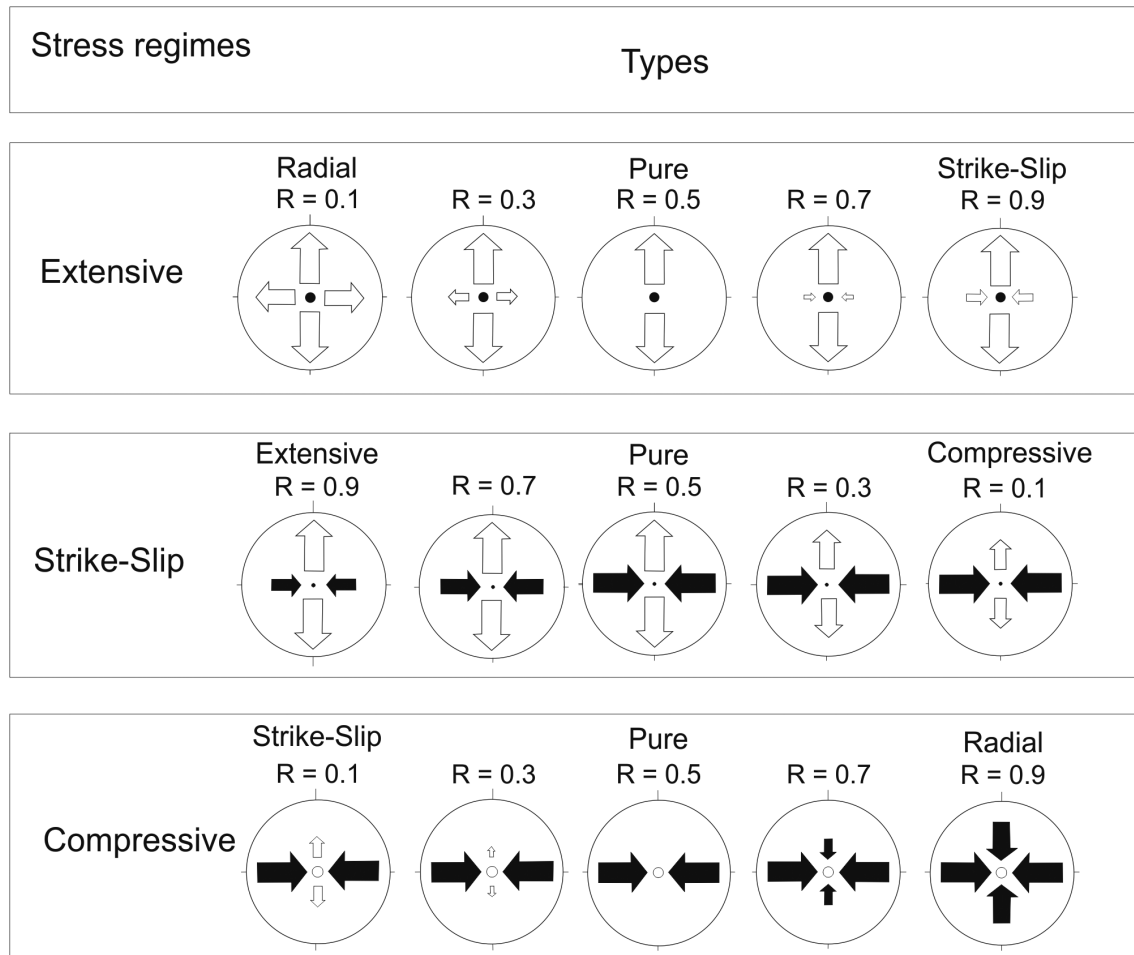
taken from Delvaux et al., 1995

Figure 14. Types of stress regimes and their representation on a map. Arrows indicate the azimuth of horizontal stress axes, with their length according to relative stress magnitude, in base of the stress ratio *R*. White outward arrows indicate extensive stress axes and black inward arrows compressive stress axes. Vertical stress axes are symbolized by a solid circle for extensive regimes (S_1 vertical), a dot for strike-slip regimes (S_2 vertical) or an empty circle for compressive regimes (S_3 vertical).

The faults with a strike slip to oblique component movement are associated with the extensional regime and not with a strike-slip phase of deformation. That means that the direction of extension was not always perpendicular to the strike of the faults. Alternatively, along either side of the mass there must be strike-slip accommodation of movement by faults, reflecting the surface outcrop of the detachment plane as a tear fault. Tectonic compression, sensu stricto, was not detected. The package that constitutes the Cañada de Tarachi Unit is molded by deformational gliding structures. The identified ductile structures are related to the gliding tectonics of the monoliths. Assuming that compression existed in the area as a result of the Laramide deformation, we should observe structures, such as folds, that indicate a

transport movement towards the north-east. Instead, the observed folding indicates a vergence towards the west and south-west. However, El Potrero Grande does not display these characteristics, indicating a different evolution of the tectonic environment.

Therefore, the development of basins and volcanism in central Sonora during the Triassic (Stewart and Roldán, 1991) and, later, the development of volcanism and the opening of basins during the Early and Middle Jurassic (Anderson and Nourse, 2005) mark an evolution associated with extension in a possibly thinned and warmed lithosphere. The sedimentation in the Upper Jurassic-Lower Cretaceous and Upper Cretaceous occurred under an extension environment, and indicates the completion of the evolution of the Mesozoic

basins that occurred before a period of stability and peneplanation in the Upper Cretaceous-Paleocene in north-west Sonora.

Conclusions

The volcano-sedimentary rocks of the Upper Cretaceous in the Arivechi comprise a sequence with sediment thickness of more than 6 km that was deposited in a back-arc basin. The stratigraphy of the Arivechi region consists of two Upper Cretaceous units: the Cañada de Tarachi Unit and the El Potrero Grande Unit. Both units show evidence of rapid denudation, magmatism and sedimentation developed in an extensional type regime environment.

An outstanding characteristic of the Cañada de Tarachi Unit is the presence of glided monoliths and blocks with tabular forms of diverse dimensions, from a few meters to several kilometers in length. Two of these megaclasts of granitic composition were dated: one at 76.0 ± 2.0 Ma by U/Pb zircon geochronology at the Cañada de Tarachi, and the second one at 69.57 ±0.48 Ma by $^{40}Ar/^{39}Ar$ step-heating of a K-spar along the Arivechi-Tarachi, road, interpreted as an emplacement and cooling age respectively, and a maximum age for the onset of erosion.

The recognized structures and the results of the paleostress study along with the stratigraphy demonstrate two periods of deformation. The first happened at the beginning of the Late Cretaceous, as shown by the presence of monoliths, blocks, and folds only in the Cañada de Tarachi Unit. The megaclasts were emplaced as slumps in soft sediments during successive mass movements derived from differential uplifts and associated gravitational gliding processes. Overall, the clasts deposited in the Arivechi basin are angular, unsorted monoliths, blocks and very coarse to fine slab. The back-arc Arivechi basin had to be a deep one, since a thick (6 km) detritus accumulation derived from a magmatic arc and basement source rocks can be observed. The origin of these uplifts was the result of several vertical regional movements of the Aldama Platform, as indicated by megaclasts interbedded in the sequence at different stratigraphic levels. The mechanism that originated uplifts suggests earthquakes, e.g., M 8, which occurred along the Denali fault in Alaska (Harp *et al.*, 2003), triggered the mass-sliding and generation of megaclasts.

The folds are associated with movements along a synthetic extensional detachment, linked to the evolution of the gliding masses.

The contact between megaclasts and the basal Cretaceous rocks are pervasively sheared because of the downslope transport. At the front and along the base of the megaclasts disintegration and a complex deformation associated with simple shear can be observed. The transport direction to W-SW is deduced from the kinematics of folds recorded in the Cretaceous Cañada de Tarachi Unit. Contractional structures are not observed in the El Potrero Grande Unit. Folds in the El Potrero Grande Unit are associated with the evolution of faults such as drag folds.

The second event was characterized by normal and strike-slip faults, which can be seen in both units. Paleostress analysis in the Arivechi region indicated that the area has undergone radial to NE-SW to NW-SE extension, and local compression in an E-W and NW-SE direction. The chronology of events identified suggests that the directions of extension NE-SW and ENE-WSW were followed by an E-W and WNW-ESE extension. This would indicate that the sequence of faulting went from NE-SW to ENE-WSW and later to WNW-ESE.

The presence of strike-slip faults is the result of a dominant extensional tectonic regime. It is thought that strike-slip faults were formed as a response to a main E-W and NW-SE compression stress, as a result of the reactivation of normal faults oriented NE-SW. Perhaps this reactivation occurred in faults during the sliding of masses and reactivated during the transformation of the tectonic regime during Miocene-Pliocene times. The NE-SW to WNW-ESE extension was in general the cause of the tilting towards the north-east of the Upper Cretaceous layers.

The structural analysis and paleostress reconstruction of the Arivechi area allow recognition of two major deformation events that can be related (1) to the Farallon oceanic lithosphere subduction under the North American plate and the opening of the back-arc basin and (2) a stress field characterized by extension related to the right lateral displacement between the Farallon and North American plates. In both Late Cretaceous units only extension is observed. This extension can be divided into two periods. The first one, during Lower Cretaceous times, is recorded in the structures and megaclasts observed at the Cañada de Tarachi Unit. These structures are the result of differential uplifts which caused the gravitational gliding masses and contractional structures. The second one is related to the basin and range Cenozoic normal faulting observed in both units. No evidence

of compressional tectonics is reported in this work.

The tectonic history of the Aldama Platform and the Cananea High is based upon their lithological constitution and structural heterogeneous basement, which are precursors of the faulting initiated at the end of the Early Cretaceous. Both structural elements were possibly active at least from the Jurassic (Aldama Platform) to the late Early Cretaceous in the light of the characteristics identified in the rocks involved in the sliding processes.

Acknowledgments

References

Allaby A., Allaby M., 1999, A Dictionary of Earth Sciences: Oxford University Press, 619 pp.

Almazán-Vázquez E., 1989, El Cámbrico-Ordovícico de Arivechi, en la región centro oriental del Estado de Sonora, *Revista Mexicana de Ciencias Geológicas,* 8, 1*, 58-66.*

Andersen T., 2002, Correction of common lead in U–Pb analyses that do not report 204Pb, *Chemical Geology,* 192, *59-79.*

Anderson T.H., Nourse J.A., 2005, Pull apart basins at releasing bends of the sinistral Late Jurassic Mojave-Sonora fault system, *in*: Anderson, T.H., Nourse, J.A., McKee, JW., Steiner, M.B. (eds.), The Mojave-Sonora megashear hypothesis: Development, assessment, and alternatives: *Geological Society of America, Special Paper,* 393, 97-122.

Angelier J., 1994, Fault slip analysis and paleostress reconstruction, in Hancock, P.L., (ed.), Continental Deformation. Pergamon, Oxford, 101-120 pp.

Angelier J., Colletta B., Anderson R.E., 1985, Neogene paleostress changes in the Basin and Range: A case study at Hoover Dam, Nevada-Arizona, *Geological Society of America Bulletin,* 96, 3*, 347-361*.

Angelier J., Colletta B., Chorowicz J., Ortlieb L., Rangin C., 1981, Fault tectonics of the Baja California Peninsula and the opening of the Sea of Cortez, Mexico, *Journal of Structural Geology,* 3, 4, 347-357.

Angelier J., Mechler P., 1977, Sur une méthod graphique de recherché des contraintes principal ségalement utilisable en tectonique et en seismologie: la méthode des diedresdroits. *Bulletin de la Société Geologique de France,* 7, 19, *1309-1318.*

Bailey R.H., Skehan J.W., Dreier R.B., Webster M., 1989, Olistostromes of the Avalonian terrane of southeastern New England, in Horton, J.W., Rast, N. eds. Mélanges and Olistostromes of the U.S. Appalachians: *Geological Society of America Special Paper* 228, p. 93-112.

Bartolini C., 1993, Fragments of the lower Cretaceous Chihuahua´s Aldama platform in eastern Sonora, Mexico: *Cordilleran Section, Abstracts with Programs, Geological Society of America,* 25, 5, 7.

Blair T.C., McPherson J.G., 1999, Grain-size and textural classification of coarse sedimentary particles. *Journal of Sedimentary Research,* 69, 1, 6-19.

Carrasco-Velázquez B., 1977, Albian sedimentation of submarine autochthonous and allochthonous carbonates, east edge of the Valle-San Luis Potosí platform, Mexico, in Cook, H.E., Enos, P., eds., Deep-Water Carbonate Environments, SEPM Special Publication 25, 263-272.

Conaghan P.J., Montjoy E.W., Edgecombe O.R., Talent J.A., Owen D.E., 1976, Nubrigyn Algal Reef (Devonian), eastern Australia: allochthonous blocks and megabreccias. *Geological Society of America Bulletin,* 87, 515-530.

Cook H.E., McDaniel P.N., Mountjoy E.W., Pray L.C., 1972, Allochthonous carbonate debris flows at Devonian bank ("reef") margins, Alberta, Canada. *Association of Canadian Petroleum Geologists Bulletin,* 20, 439-497.

Delvaux D., 1993, The TENSOR program for reconstruction examples from the East African and the Baikal rift zones: Terra Abstracts. *Abstract Supplement 1 to Terra Nova,* 5, 216.

Delvaux D., Moeys R., Stapel G., Melkinov A., Ermikov V., 1995, Paleostress reconstructions and geodynamics of the Baikal region, Central Asia, Part I. Palaeozoic and Mesozoic pre-rift evolution. *Tectonophysics,* 252, 61-101.

Díaz A., Monreal R., 2008, La Formación Los Picachos en la Sierra de Los Chinos, Sonora, México. *Boletín de la Sociedad Geológica Mexicana,* 60, 1, 111-120.

Fernández-Aguirre, M.A., Almazán-Velázquez E., 1991, Geología de la carta Arivechi (H12D56): Secretaría de Fomento Industrial y Comercio del Estado de Sonora, Dirección General de Fomento Minero, Mapa.

Fernández-Aguirre M.A., Grijalva-Haro A.S., Estrada-Cubillas R., 1995, Carta Geológica Sahuaripa, escala 1: 50,000: Secretaría de Desarrollo Económico y Productividad, Gobierno del Estado de Sonora. Mapa.

Flinn D.L., 1977, Geology of Cerro Macho area, Sonora, Mexico [Master thesis]. Flagstaff, Northern Arizona University, 73 pp.

García y Barragán J.C., Rodríguez-Castañeda J.L., 1996, Tectonic significance of Late Cretaceous conglomerates in north-central Sonora, México. *Geological Society of America, Abstracts with Programs,* 28, 7, 115.

González-León, 1988, Estratigrafía y geología estructural de las rocas sedimentarias Cretácicas del área de Lampazos, Sonora. *Universidad Nacional Autónoma de México, Instituto de Geología,* 7, 148-162.

Grajales-Nishimura J.M., Terrel D., Torres-Vargas R., Jacques-Ayala C., 1990, Late Cretaceous synorogenic volcanic/sedimentary sequences in eastern Sonora, Mexico. *Geological Society of America, Abstracts with Programs,* 22, 3, 26.

Haenggi W.T., 2002, Tectonic history of the Chihuahua Trough, Mexico and adjacent USA, Part II Mesozoic and Cenozoic. *Boletín Sociedad Geológica Mexicana, LV,* 1, 38-94.

Harp E.L., Jibson R.W., Kayen R.E., Keefer D.K., Sherrod B.L., Carver G.A., Collins B.D., Moss R.E.S., Sitar N., 2003, Landslides and liquefaction triggered by the M 7.9 Denali fault earthquake of 3 November 2003. *AUGUST GSA TODAY,* 4-10.

Heck F., Speed R., 1987, Triassic olistostrome and shelf-basin transition in the western Great Basin: paleogeographic implications. *Geologic Society of America Bulletin.* 99, 539-55l.

Herrera S., Bartolini C., 1983, Geología del área de Lampazos Sonora [Tesis Licenciatura]. Universidad de Sonora, Hermosillo, Sonora, México, p.120.

Heubeck C., 1992, Sedimentology of large olistoliths, southern Cordillera Central, Hispaniola. *Journal of Sedimentary Petrology,* 62, 3, 474-482.

Himanga J.C., 1977, Geology of Sierra Chiltepín, Sonora, México [Master thesis]. Flagstaff, Northern Arizona University, p.78.

Johns D.R., Mutil E., Rosell J., Séguret, M., 1981, Origin of a thick, redeposited carbonate bed in Eocene turbidites of the Hecho Group, south-central Pyrenees, Spain. *Geology,* 9, 161-164.

King R.E., 1939, Geological reconnaissance in the northern Sierra Madre Occidental of Mexico. *Geological Society of America, Bulletin,* 50, 1625-1722.

Ludwig K., 2008, Manual for Isoplot 3.7. Berkeley Geochronology Center Special Publication No. 4, rev. August 26, 77.

Ludwig K.R., Mundil R., 2002, Extracting reliable U–Pb ages and errors from complex populations of zircons from Phanerozoic tuffs. Goldchmidt Conference Abstracts 2002. *Geochim. Cosmochim. Acta,* 66, 15A, A463.

McKee M.B., 1991, Deformation and stratigraphy relationships of mid-Cretaceous mass gravity slides of a marine basin in Sonora, Mexico [PhD thesis]. Pittsburgh, PA, University of Pittsburgh, p. 286.

McKee M.B., Anderson T.H., 1998, Mass gravity deposits and structures in the Lower Cretaceous of Sonora, Mexico. *Geological Society of America Bulletin,* 110, 1516-1529.

McKee J.W., McKee M.B., Anderson T.H., 2005, Mesozoic formation, mass gravity sedimentation and inversion in northeastern Sonora and southeastern Arizona, in

Anderson, T.H., Nourse, J.A., McKee, J.W., Steiner, M.B., eds., The Mojave-Sonora Megashear Hypothesis: Development, Assessment, and Alternatives: Geological Society of America Special Paper 393, pp. 481-507.

Minjárez-Sosa I., Palafox J.J., Torres Y., Martínez J.A., Rodríguez B., 1985, Consideraciones respecto a la estratigrafía y estructura del área de Sahuaripa - Arivechi. *Universidad de Sonora, Boletín del Departamento de Geología*, 2, 1-2, 90-105.

Monreal R., 1995. Las facies marinas (Aptiano-Albiano) del Grupo Bisbee y cronocorrelativas en Sonora: México, Hermosillo, Son. *Universidad de Sonora, Boletín del Departamento de Geología,* 12, 1, 65-78.

Monreal R., 1996, Cretaceous stratigraphy and structure of the Sierra Grande, northeastern Chihuahua, in Jacques-Ayala, C., González-León, C.M., Roldán-Quintana, J., (eds.), Studies on the Mesozoic of Sonora and Adjacent areas: Boulder, Colorado. *Geological Society of America, Special Paper,* 301, 167-178.

Monreal R., Longoria J.F., 2000, Lower Cretaceous rocks of Sierra de Los Chinos, east-central, Sonora, Mexico. *Geofísica Internacional,* 39, 4, 309-322.

Naylor M.A., 1982, The Casanova Complex of the northern Apennines: a mélange formed on a distal passive continental margin. *Journal of Structural Geology,* 4, 1-18.

Onstott T., Peacock M., 1987, Argon retentivity of hornblendes: A field experiment in a slowly cooled metamorphic terrane. *Geochimica et Cosmochimica Acta,* 51, 2891-2903, doi:10.1016/0016-7037(87)90365-6.

Palafox J.J., Martínez J.A., 1985, Estratigrafía del área de Arivechi, Sonora. *Universidad de Sonora, Boletín del Departamento de Geología,* 2, 1-2, 30-56.

Palafox J.J., Minjárez J.L., Pubellier M., Rascón B., 1984, Sobre la presencia de rocas del Paleozoico Superior en el área de Arivechi, Sonora, México. *Universidad de Sonora, Boletín del Departamento de Geología,* 1, 1, 60-62.

Prior D.B., Bornhold D.B., Coleman J.M., Bryant W.R., 1982, Morphology of a submarine slide, Kitimat Arm, British Columbia. *Geology,* 10, 58S-592.

Pubellier M., 1987, Relations entre domaines cordillérain et mésogéen au nord du Mexique; étude géologique de la vallé de Sahuaripa, Sonora central [PhD thesis]. Paris, Université de Paris 6, 219 p.

Ramírez-M J.C., Acevedo-C. F., 1957, Notas sobre la geología de Chihuahua. *Boletín de la Asociación Mexicana de Geólogos Petroleros,* IX, 9-10, 583-770.

Rangin C., 1977, Tectónicas sobrepuestas en Sonora septentrional. *Universidad Nacional Autónoma de México, Boletín del Instituto de Geología,* 1, 44-77.

Rangin C., 1982, Contribution à l´étude géologique du Systeme Cordillérain du nord-ouest du Mexique [PhD thesis]. Paris, Université Pierre et Marie Curie, 588 p.

Roddick J., 1983, High precision intercalibration of 40Ar-39Ar standards. *Geochimica et Cosmochimica Acta,* 47, 887-898, doi:10.1016/0016-7037(83)90154-0.

Rodríguez-Castañeda J.L., 2002, Tectónica Cretácica y Terciaria en la margen suroeste del Alto de Cananea, Sonora, Norte Central [PhD Thesis]. México, D.F., Universidad Nacional Autónoma de México, 217 p.

Servicio Geológico Mexicano, 2008, Carta Geológica-Minera del Estado de Sonora, escala 1:500,000.

Slama J., Kosler J., Condon D., Crowley J., Gerdes A., Hanchar J., Horstwood M., Morris G., Nasdala L., Norberg N., Schaltegger U., Schoene B., Tubrett M., Whitehouse M.J., 2008, Plešovice zircon — A new natural reference material for U–Pb and Hf isotopic microanalysis. *Chemical Geology,* 249, 1-35, doi: 10.1016/j.chemgeo.2007.11.005.

Solari L., Gómez-Tuena A., Bernal J., Pérez-Arvizu O., Tanner M., 2010, U-Pb Zircon geochronology with an integrated LA-ICP-MS microanalytical workstation: Achievements in precision and accuracy. *Geostandards and Geoanalytical Research,* 34, 1, 5-18.

Solari L.A., Tanner M., 2011, UPb. age, a fast data reduction script for LA-ICP-MS U-Pb geochronology. *Revista Mexicana de Ciencias Geológicas,* 28, 1, 83-91.

Spalletti L.A., 2006, Curso Sedimentología. Facultad de Ciencias Naturales y Museo, UNLP.

Steiger R., Jäger E., 1977, Subcommission on geochronology. *Earth and Planetary Science Letters,* 36, 359-362, doi:10.1016/0012-821X(77)90060-7.

Stewart J.H., Amaya-Martínez R., Palmer A.R., 2002, Neoproterozoic and Cambrian strata of Sonora Mexico: Rodinian supercontinent to Laurentian Cordilleran margin, in Barth, A.P. (ed.), Contributions to crustal evolution of the southwestern United States: *Geological Society of America, Special Paper,* 365, 5-48.

Stewart J.H., Roldán-Quintana J., 1991, Upper Triassic Barranca Group, non-marine and shallow-marine rift-basin deposits of northwestern Mexico. *Geological Society of America, Special Paper,* 254, 19-36.

Teale T.C, Young J.R., 1987, Isolated olistoliths from the Longobucco Basin, Calabria. Southern Italy, in Leggett, J.K., Zuffa, G.G., eds., Marine Clastic Sedimentology. Graham and Trotman, London, pp. 15-88.

Tera F., Wasserburg G., 1972, U-Th-Pb systematics in three Apollo 14 basalts and the problem of initial Pb in lunar rocks. *Earth and Planetary Science Letters,* 14, 281-304.

Weber R., Ceballos-Ferriz S., López-Cortés A., Olea-Franco A., Singer-Sochet S., 1979, Los estromatolitos del Precambrico tardío de los alrededores de Caborca, Estado de Sonora, parte I; Reconstruccion de Jacutophyton Shapovalova e interpretación paleoecologica preliminar. *Universidad Nacional Autónoma de México, Instituto de Geología, Revista,* 3, 1, 9-23.

A parallel computing strategy for Monte Carlo simulation using groundwater models

Esther Leyva-Suárez, Graciela S. Herrera[*] and Luis M. de la Cruz

Resumen

En este artículo se presentan los resultados de una estrategia de paralelización para reducir el tiempo de ejecución al aplicar la simulación Monte Carlo con un gran número de realizaciones obtenidas utilizando un modelo de flujo y transporte de agua subterránea. Desarrollamos un script en Python usando mpi4py, a fin de ejecutar GWMC y programas relacionados en paralelo aplicando la biblioteca MPI. Nuestro enfoque consiste en calcular las entradas iniciales para cada realización y correr grupos de estas realizaciones en procesadores separados y después calcular el vector medio y la matriz de covarianza de las mismas. Esta estrategia se aplicó al estudio de un acuífero simplificado en un dominio rectangular de una sola capa. Presentamos los resultados de aceleración y eficiencia para 1000, 2000 y 4000 realizaciones para diferente número de procesadores. Eficiencias de 0,70, 0,76 y 0,75 se obtuvieron para 64, 64 y 96 procesadores, respectivamente. Observamos una mejora ligera del rendimiento a medida que aumenta el número de realizaciones.

Palabras clave: Agua subterránea, flujo y transporte, simulación Monte Carlo, cómputo paralelo distribuido, Python.

Abstract

In this paper we present the results of a parallelization strategy to reduce the execution time for applying Monte Carlo simulation with a large number of realizations obtained using a groundwater flow and transport model. We develop a script in Python using mpi4py, in order to execute GWMC and related programs in parallel, applying the MPI library. Our approach is to calculate the initial inputs for each realization, and run groups of these realizations in separate processors and afterwards to calculate the mean vector and the covariance matrix of them. This strategy was applied to the study of a simplified aquifer in a rectangular domain of a single layer. We report the results of speedup and efficiency for 1000, 2000 and 4000 realizations for different number of processors. Efficiencies of 0.70, 0.76 and 0.75 were obtained for 64, 64 and 96 processors, respectively. We observe a slightly improvement of the performance as the number of realizations is increased.

Key words: groundwater, flow and transport, Monte Carlo simulation, distributed parallel computing, Python.

E. Leyva-Suárez
Posgrado en Ciencias de la Tierra
Universidad Nacional Autónoma de México
Ciudad Universitaria
Delegación Coyoacán, 04510
México D.F., México

G. S. Herrera[*]
L. M. de la Cruz
Instituto de Geofísica
Universidad Nacional Autónoma de México
Ciudad Universitaria
Delegación Coyoacán, 04510
México D.F., México
[*]Corresponding author: ghz@geofisica.unam.mx

Introduction

Stochastic hydrogeology is a field that deals with stochastic methods to describe and analyze groundwater processes (Renard, 2007). An important part of it consists of solving stochastic models (stochastic partial differential equations) describing those processes in order to estimate the joint probability density function of the parameters (e.g., transmissivity, storativity) and/or state variables (e.g., groundwater levels, concentrations) of those equations or more commonly some of their moments. Monte Carlo simulation (MCS) is an alternative for solving these stochastic models, it is based on the idea of approximating the solution of stochastic processes using a large number of equally likely realizations. For example, the pioneering work on stochastic hydrogeology by Freeze (1975) applies this method.

The large number of realizations required by MCS can be very demanding in computing resources and the computational time can be excessive. Nowadays there exist many parallel computing platforms that can be used to alleviate this problem. Some previous works have focused in this direction, for example Dong *et al*. (2012) describe a parallelization strategy for stochastic modeling of groundwater systems using the Java Parallel Processing Framework (JPPF). This tool is very powerful and can be used as a GRID middle-ware (Foster *et al*., 2001) to distribute tasks across several computing systems. Dong *et al*. (2012) take advantage of this tool to avoid any modification of MODFLOW and related programs. However, when the JPPF is used in a cluster alone, a simply master-worker parallel model is obtained. They also report that the combination of two levels of parallelism, using a parallel solver to reduce the execution time by an order of two. However, this technique pays off only for very large grids, over 10^6 points. In our case, we do not require such massive grids.

In this paper, we propose a distributed parallel computing method for stochastic modeling with the software *Groundwater Monte Carlo* (GWMC), a component of the Groundwater Quality Monitoring (GWQMonitor) package (Herrera, 1998). GWMC is used together with an assimilation method called Ensemble Smoother of Herrera (ESH) in order to estimate groundwater contaminant concentration assimilating concentration data. The best known version of Ensemble Smoother was developed by van Leeuwen and Evensen (1996). Herrera de Olivares developed a version of the assimilation method independently,

and originally she called it static Kalman filter (Herrera, 1998).

Ground Water Monte Carlo (GWMC)

GWMC is a program written in FORTRAN by Herrera (1998), and subsequently modified by Olivares-Vázquez (2002).

It implements Monte Carlo simulation using a flow and transport simulator in which hydraulic conductivity is a random field and the contaminant concentration at the contaminant source is a time series at each node. Therefore, multiple realizations of those two parameters are obtained and for each realization the flow and transport equations are solved by the Princeton Transport Code (PTC), a finite element simulator (Babu *et al*., 1993). Finally, different averages of the concentration solutions are calculated to obtain their space-time mean vector and covariance matrix. In this paper, GWMC is parallelized in order to reduce the program execution time.

Methodology

The methodology implemented in this work is as follows:

Step 1. The input files for PTC are generated.

Step 2. The input files for GWMC are generated.

Step 3. A number of realizations of the natural logarithm of the hydraulic conductivity field are generated using the sequential Gaussian simulation (SGSIM) program (Deutsch and Journel 1997). This program generates standard normal simulated values with a given correlation spatial structure on a rectangular mesh.

Step 4. A transformation to get the hydraulic conductivity field (a lognormal field) is calculated for each realization using the Nrm2log program. This program transforms the standard normal values to a normal variable with a given mean and variance and then applies the exponential function to get the lognormal field.

Step 5. For each node at the source of contaminant concentration, the same number of realizations of time series is generated using the RandTS2 program.

Step 6. If the PTC finite element mesh is not equal to the SGSIM rectangular mesh, the SGSIM mesh is mapped into the nearest node of the PTC mesh.

Step 7. The generated hydraulic conductivity realization value is assigned to the corresponding node of the PTC mesh and the hydraulic conductivity PTC files are substituted with the new values.

Step 8. The contaminant concentrations at the source are substituted by the RandTS2 values in the PTC file for the transport boundary conditions.

Step 9. PTC is executed for each conductivity and source concentration realization (PTC solves numerically the flow and transport equation).

Step 10. Adding over the concentration solutions obtained in *step 8*, an auxiliary vector with the sum of concentrations for each node and time of interest is calculated and an auxiliary matrix with the sum of products of concentrations for each possible pair of space-time positions of interest is calculated.

Step 11. Combining the information contained in the auxiliary vector and the auxiliary matrix the spatiotemporal mean vector and covariance matrix of the contaminant concentration are calculated.

Step 12. The ESH is applied to estimate contaminant concentration.

Steps 6 to 10 are executed by GWMC and steps 3 to 11 are parallelized in this work.

Python - MPI

Python is an interpreter, interactive and extensible programming language used in a wide variety of applications. In particular, for scientific computing there exist many tools that ease the development of computational codes (Milman and Aivazis, 2011). Python can be combined easily with other programming languages, like C, C++ and Fortran, and also can be used to exploit high performance computing architectures by using MPI (Message Passing Interface) [Gropp *et al*., 1999] or CUDA (Compute Unified Device Architecture) [Kirk and Hwu, 2010]. Currently, almost any operating system supports Python in such a way that this programming language provides portability across many computing platforms.

In this work our main objective is to reduce the execution time of the complete process described in section 4. In order to avoid a complete re-design of our codes, written mainly in FORTRAN, we decided to use Python

and MPI for Python (MPI4PY) [Dalcin, 2012]. MPI4PY provides an object-oriented approach for MPI which allows us to distribute tasks using Python scripts. In the appendix we describe briefly the scripts developed in this work.

In figure 1 we sketch the parallelization process. The main idea is to re-use FORTRAN codes with minimal modifications inside a Python script. First, we initialize all the variables and determine the corresponding inputs for the different executable codes. Part of this process is done in a client machine, before the parallel execution. After that, the client submits a batch task to the cluster. Once the parallel execution starts, each processor generates its own input files labeled using the processor number. With the local inputs generated, we execute a group of realizations in each processor. The load balancing is done by the script, distributing the same number of tasks for each processor. Each realization solves the same problem but with different inputs, so the time required by each realization is almost the same. Since the number of realizations can be different for each processor, we need to use a barrier at the end of the parallel execution. However, the waiting time for the last processor is negligible. The calculation of the space-time mean and the covariance matrix is done in processor 1, which requires information from all the processors. Originally, this was done in GWMC. In our case, we removed the corresponding FORTRAN code from the program, and we put it in a separate subroutine that is called at the end of the script. However this change is very simple and straightforward. Finally, the last step (the ESH application) is done as a post processing step in the client machine.

Application problem

An aquifer of 804.7 by 804.7 m^2 is considered (figure 2a). A contaminant source is located on the left hand side border and the area is bounded by a river on the right hand side. This problem was slightly modified from the one presented by Herrera and Pinder (2005).

The objective is to estimate the contaminant concentrations of a moving plume during a 2-year period. The locations at which concentration estimates will be obtained are associated with the nodes of what we call the estimation mesh shown in Figure 2a. For each one of these locations, concentrations will be estimated every 121.7 days; this amounts to six times during the 2-year period.
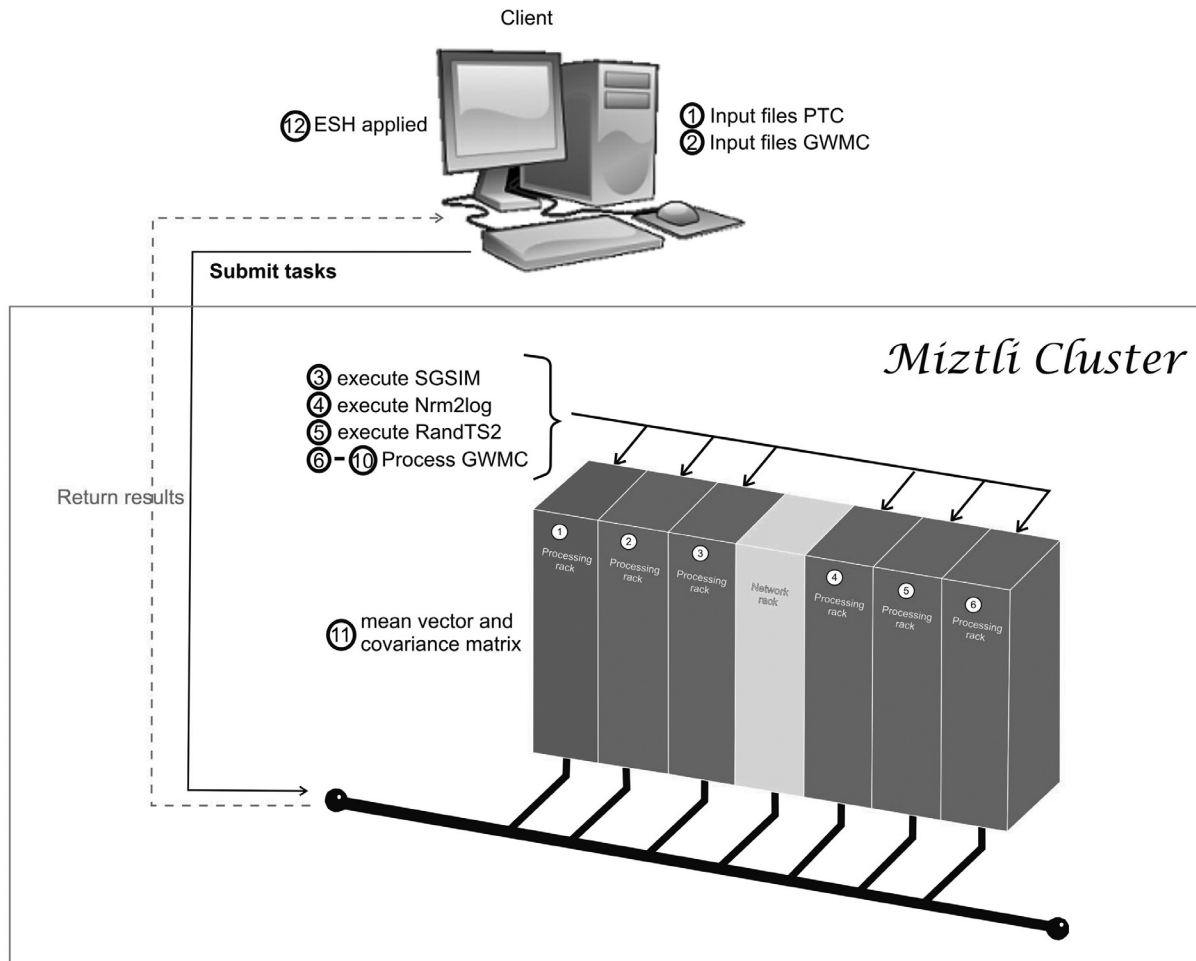
Figure 1. Parallelization process. Task 3 to 10 are done in parallel, while task 12 is calculated in processor 1.

(a)   (b)
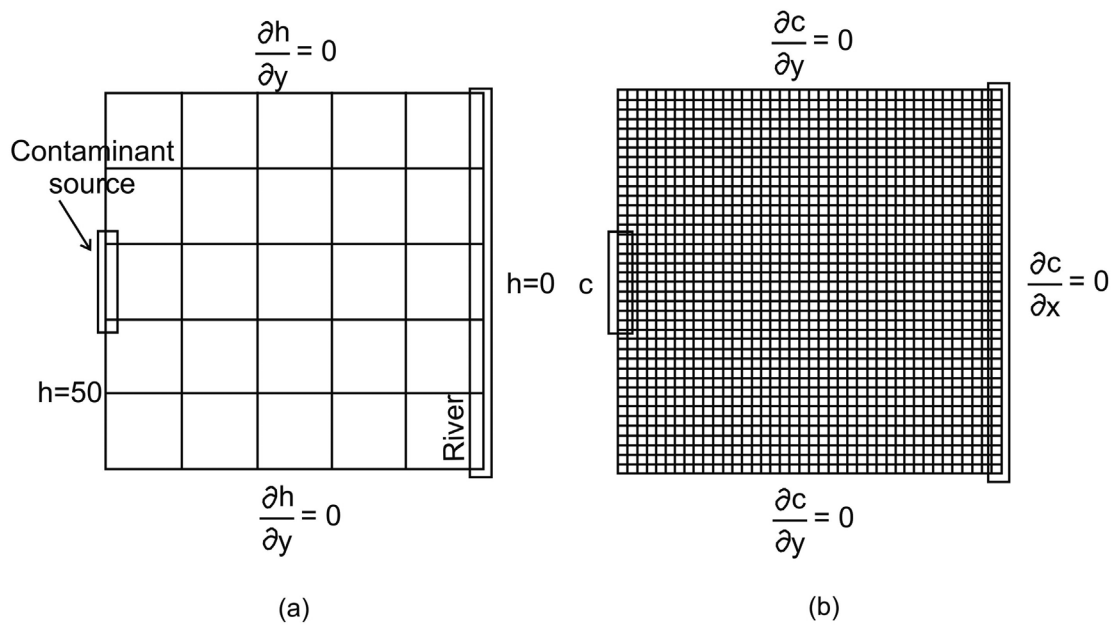
Figure 2. a) Problem set up with the estimation mesh and boundary conditions for the flow model (h is in meters), b) Stochastic simulation mesh and boundary conditions for the transport model (modified from Olivares-Vázquez, 2002).

Flow and transport model

The PTC is used in two-dimensional mode to solve the flow and transport model. The flow and transport equations coupled through Darcy's law, equations (1), (2) and (3) respectively, are used to describe the contaminant plume evolution:

$$\nabla \cdot (K \cdot \nabla h) - S_s \frac{\partial h}{\partial t} + Q = 0 \qquad (1)$$

$$\phi \frac{\partial c}{\partial t} + V \cdot \nabla c - \nabla \cdot (D\nabla c) - Q(c_0 - c) = 0 \qquad (2)$$

$$V = -K \nabla h \qquad (3)$$

where K is the hydraulic conductivity, h is the hydraulic head, S_s is the specific storage coefficient, Q is a source or sink term, c is the solute concentration, D is the hydrodynamic dispersion, c_0 is the concentration of the pumped fluid and ϕ is the effective porosity. The flow equation (1) describes the water flow through the aquifer; the transport equation (2) describes the changes in contaminant concentration through time for a conservative solute. Darcy's law (3) is used to calculate V, Darcy velocity. Boundary conditions for flow and transport are included in figures 2a and 2b, respectively. Concentration is given in parts per million (ppm) and hydraulic head in meters (m).

The numerical mesh used to solve the flow and transport equations is called the "stochastic simulation mesh"; it consists of 40x40 equally sized elements (figure 2b). For the transport model forty-eight time-steps are used to simulate a two-year period, 15.2 days each. For the flow model, all nodes of the left hand side boundary have a value of $h = 50\ m$, and all nodes of the right hand boundary have a value of $h = 0\ m$. The contaminant source is active during all of this period, with a constant concentration of $c = 50\ ppm$. Nodes that are not part of the contaminant source satisfy the condition $\frac{\partial c}{\partial x} = 0$. The aquifer is assigned a thickness of 55 m, a porosity of 0.25, a dispersivity of 33 m in the x direction and 3.3 m in the y direction.

Stochastic model

As was mentioned before, the hydraulic conductivity is represented as a spatially correlated random field; thus, the resulting velocity and dispersion fields, also become spatially correlated random fields.

For this example we will assume that the hydraulic conductivity field has a lognormal distribution, it is homogeneous, stationary and isotropic. The mean value of $F(x) = 1nK(x)$ is 3.055 and the semivariogram that represents its spatial correlation structure is an exponential model, i.e.:

$$\gamma_F(h) = \sigma_F^2 \left[1 - \exp\left(-\frac{h}{\lambda_F}\right)\right] \qquad (4)$$

where σ_F^2 is the variance of F with value 0.257813, and λ_F is its correlation scale equal to 80.467 m.

At each node the contaminant concentration is represented as a time series (Herrera and Pinder, 2005), through

$$c(t) = \exp(-14 + 3t + e(t)) \qquad (5)$$

where $e(t)$ is a zero-mean random perturbation, normally distributed and with a 0.1948 variance. For each source node, in every simulation time step, a different random perturbation is used. The time correlation of the random perturbations is modeled with the semivariogram

$$\gamma_e(t) = 0.1948 \left[1 - \exp\left(-\frac{t}{\lambda_e}\right)\right] \qquad (6)$$

with λ_e equal to 11 days.

For this example we used 1000, 2000 and 4000 realizations.

Estimation with the Ensemble Smother of Herrera (ESH)

As was mentioned before, Herrera (1998) developed the assimilation method independently of van Leeuwen and Evensen (1996), it was called static Kalman filter and later, static ensemble Kalman filter (EnKF) by Nowak *et al.* (2010).

Using the ESH we estimate the conservative contaminant concentration using existing data for a two-year period. The concentration estimates are obtained at the nodes of what we call the ESH-mesh, which is a submesh of the stochastic simulation mesh, which consists of 5x5 equally sized elements (this mesh is shown in figure 2a). For each of these positions, the concentrations are estimated six times over a period of two years, equivalent to 121.7 days. To apply the ESH it is necessary to calculate the space-time covariance matrix of the contaminant concentration.

Performance

We execute our codes on a HP Cluster Platform 3000SL "Miztli", consisting of 5,312 processing cores Intel E5-2670, 16 cards NVIDIA m2090, with 15,000 GB of RAM, and capable of processing up to 118 TFlop/s. The system has 750 TB of massive storage.

Parallel metrics

Some of the most commonly used metrics to determine the performance of a parallel algorithm are the speedup and efficiency.

The speedup (S_p) is defined as

$$S_p = \frac{T_1}{T_N} \qquad (7)$$

where T_1 is the running time of the algorithm on one processor and T_N is the running time of the algorithm on N processors.

The efficiency (E_p) is defined as

$$E_p = \frac{S_p}{N} \qquad (8)$$

where N is the number of processors in which the algorithm execution is carried out.

In this paper, these metrics are used to verify how efficient is the parallelization of GWMC.

The serial execution of GWMC for one thousand realizations took on average 24.5 minutes using PTC to solve the flow and transport equations.

Table 1. Speedup (S_p), efficiency (E_p) and Amdahl's law data with different number of processors for 1000, 2000 and 4000 realizations.

Realizations Processors	S_p 1000	2000	4000	E_p 1000	2000	4000	Amdahl's law 1000	2000	4000
1	1	1	1	1	1	1	1	1	1
2	1.96	1.88	1.90	0.98	0.94	0.95	1.99	1.99	1.99
4	3.96	3.47	3.75	0.99	0.87	0.94	3.99	3.99	3.97
8	6.22	7.25	7.12	0.78	0.91	0.89	7.97	7.98	7.88
12	11.36	9.89	10.30	0.95	0.82	0.86	11.94	11.96	11.73
16	14.33	13.50	12.49	0.90	0.84	0.78	15.90	15.93	15.52
24	21.38	17.29	19.34	0.89	0.72	0.81	23.77	23.85	22.92
32	26.75	26.80	25.04	0.84	0.84	0.78	31.60	31.74	30.09
48	40.47	39.50	37.62	0.84	0.82	0.78	47.10	47.42	43.79
64	45.06	48.64	49.07	0.70	0.76	0.77	62.41	62.96	56.70
80			59.85			0.75	77.52	78.39	68.88
96			72.18			0.75	92.45	93.68	80.40
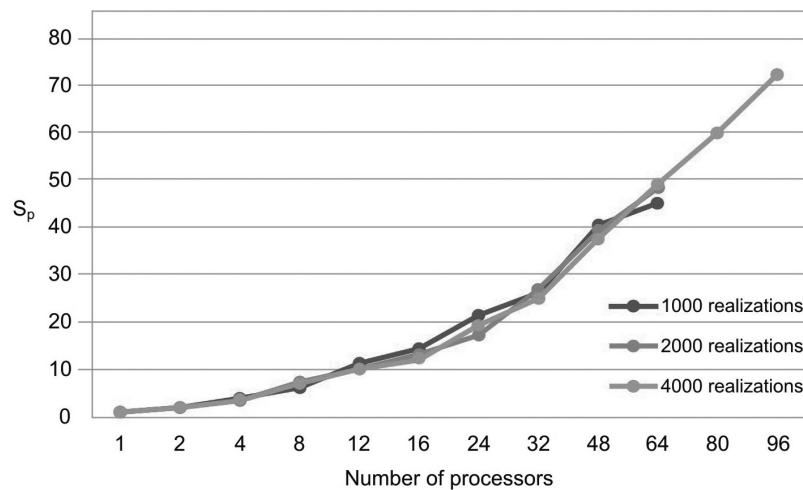
Figure 3. Speedup versus number of processors for 1000, 2000 and 4000 realizations.

The parallel Python script was executed for 1000, 2000 and 4000 realizations with different numbers of processors (see table 1). We observe that the speedup grows when the number of processors increases (figure 3). In figure 4 we see that the efficiency is more stable for the 4000 realizations case since it has fewer oscillations. For the 1000 realizations case, a speedup of 45.06 was obtained with 64 processors and a correspondingly efficiency of 0.70; for the 2000 realizations case, a speedup of 48.64 was obtained with 64 processors and a correspondingly efficiency of 0.76; for the 4000 realizations case, a speedup of 72.18 was obtained with 96 processors and a correspondingly efficiency of 0.75. The number of realizations has not much effect in the speedup and efficiency, since their values for the three cases for the same number of processors are similar.

Discussion

The elapsed time, the speedup and efficiency are limited by several factors: serial fraction of the code, load balancing, data dependencies and communications. In our case we have a minimal part of serial section: at the very beginning of the code, when the problem is set up in each processor; and at the end of the code when we join the results of all processors to calculate the mean vector and the covariance matrix. We have a very good load balancing due to the fact that each processor works on the same number of realizations. There are not data dependencies during calculations, except for the mean vector and covariance matrix calculations. Finally, the communications required to complete the calculations are also at the beginning and at the end of the code.

Almost all the factors that limit the efficiency of our code, can be taken in to account in the

serial fraction, because are present at the beginning and the end of the code, i.e. during the serial part of the execution. Therefore, using Amdahl's law (Ridgway *et al.*, 2005) we can predict the theoretical maximum speedup of the code beforehand. Amdahl's law formula is

$$Sp \le \frac{1}{f + (1-f)/p} \qquad (9)$$

where f represents the sequential fraction of the code and p is the number of processors.

The serial fraction is measured in time units, therefore, when we increase the number of realizations, the processors will have more work to do in parallel reducing the serial fraction as a consequence. This effect can be seen in the results presented in table 1 and in figures 3 and 4, where the speedup and the efficiency are more stable when the number of realizations is increased.

In figure 5, we compare our speedup results against Amdahl's law drawn for 4000 realizations. We observe that our results for the three cases are in very good agreement with the predictions of this law. The mean squared errors of our results, compared with the Amdahl's law, are 1.95, 1.86 and 1.43 for 1000, 2000 and 4000 realizations, respectively, which proofs also the effectiveness of our approach. Besides, the efficiencies obtained are also greater than 0.70, in such a way that our parallel codes are scalable (see Ridgway *et al.*, 2005).

Amdahl's law assumes a perfect load balancing. The definition of load balancing is in terms of the time t_i that each processor takes in its calculations during the parallel part. A good balancing is when all the t_i's have the same
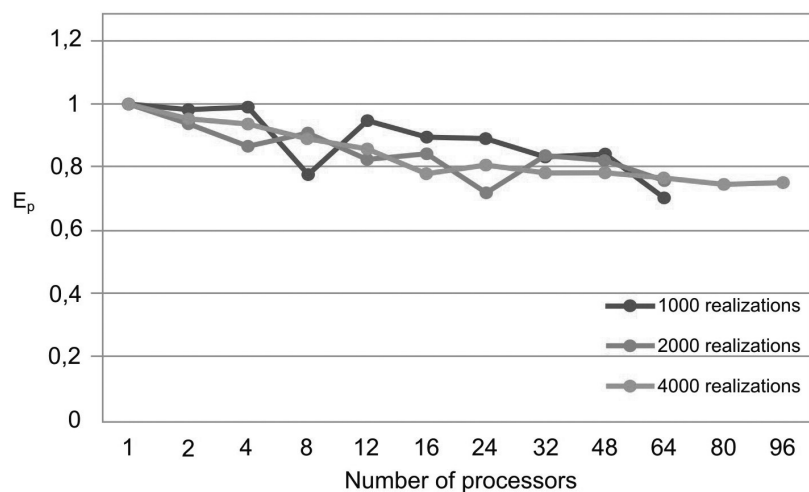
Figure 4. Efficiency versus number of processors for 1000, 2000 and 4000 realizations.
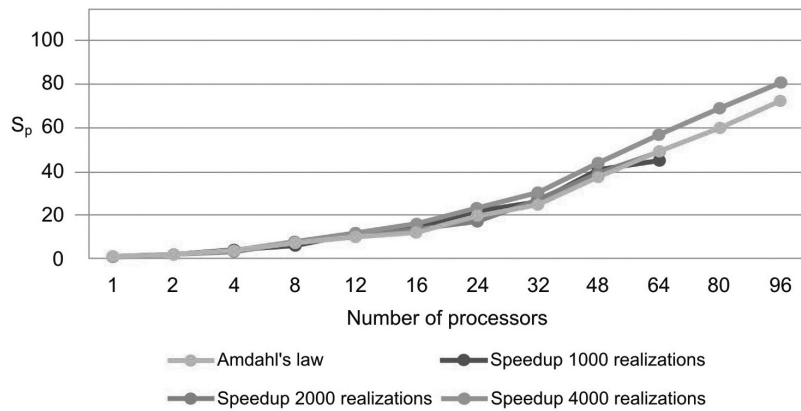
Figure 5. The comparative between the Amdahl's law and the speedup to 1000, 2000 and 4000 realizations.

value approximately. In terms of these t_i's the parallel time of the code will be $T_p = \max\{t_i : i = 1, ..., p\}$. It is reasonable to assume that the time of the whole process in one processor is $T_1 = \text{sum}\{t_i : i = 1, ..., p\}$. Then using the efficiency we have:

$$E_p = \frac{T_1}{pT_p} = \frac{sum\{t_i : i = 1,...,p\}}{p \max\{t_i : i = 1,...,p\}} \quad (10)$$

Therefore, we can write

$$E_p = \frac{average\{t_i : i = 1,...,p\}}{\max\{t_i : i = 1,...,p\}} \quad (11)$$

Hence, if the load balancing is bad, then the $\max\{t_i : i = 1, ..., p\}$ will be high, reducing the efficiency and speedup. In our case, we distribute the realizations on the processors evenly, producing averages and a maximum, of $t_i : i = 1, ..., p$, with very similar values.

Another important aspect in parallel applications is the communication between processors. In the cluster we used, the connections between processing nodes is based on Infiniband QDR 40 Gigabits per second technology. This network reduce drastically the communications time of our codes, besides we do not use exchange of information once the parallel process is initiated, only at the setup of the problem and at the end of the calculations. We also tested the same codes on a cluster with Ethernet interconnection but the results were not as good as with those obtained with the Infiniband technology.

Conclusions

In this paper, a parallelization strategy for Monte Carlo-type stochastic modeling, with PTC-related programs, has been described. The

software GWMC implements this process for one processor. Our strategy allows us to re-use all these codes, with minimal modifications.

The results obtained in parallel show that the performance is more stable as the workload for each processor is increased. In particular we obtained a very good efficiency for 4000 realizations and 96 processors. In this case we have an efficiency of 0.75 which makes our codes scalable and useful for large scale applications. During the development of this work, we have not installed any complicated software, we just use the common libraries installed in the Miztli cluster. In addition, we made a very simple modification of our original FORTRAN code to calculate the global covariance matrix.

We believe that our strategy is simple but effective for a large number of simulations and can be applied to study more complicated problems, where the execution times can be very large.

We show in figure 5 that the speedup of 1000, 2000 and 4000 realizations has a good load balancing, because the Amdahl's law assumes a perfect load balancing, and the speedup meets the conditions described in the discussion section, for this reason, we assume that our speedup had a good load balancing.

Appendix

In what follows we describe parts of the script written to parallelize the process described in section 4.

1) A first step is to create directories to facilitate the parallelization and storing of the information. We use the rank of the processor to define the name of each directory:

```
if os.path.isdir('%s' % t + '%d' % rank):
    shutil.rmtree('%s' % t + '%d' % rank)
os.mkdir('%s' % t + '%d' % rank)
os.chdir('%s' % t + '%d' % rank)
```

2) Four input files need to be modified, these are: gwqmonitor.par, sgsim.par, nrm2log.par and randTS2.par. Each file contains inputs for codes rndcsim, sgsim, nrlm2log and randTS2 respectively. Modification of file sgsim.par is shown below:

```
ofile = open("sgsim.par", 'w')
i=0
for line in lines:
    i+=1
    if i==21:
        ofile.write('%d \n' % local_
        realizaciones)
    elif i==25:
        j+=2
        ofile.write('%d \n' % j)
    else:
        ofile.write('%s' % line)

ofile.close()
```

3) All input files are copied in each cluster node in order to run the programs sgsim, nrm2log, randTS2 and GWQMonitor. Once the copy of the input files is done, we execute each one of these programs. Note that the FORTRAN executable codes are run using a system call from the python script:

```
os.system('./sgsim < sgsim.par > sgsim.
OUTPY')
os.system('./nrm2log > nrm2log.OUTPY')
os.system('./randts2 > randts2.OUTPY')

os.system('./gwqmonitor > gwqmonitor.
OUTPY')
```

4) For the calculation of the covariance matrix, we use a barrier to ensure that the information from the different processors has been arrived to the memory of processor that construct the covariance matrix. Calculation of the covariance matrix is carried out after this information is gathered.

```
MPI.COMM_WORLD.Barrier()
if (rank==0):
  def checkfile(archivo):
    import os.path
    if os.path.isfile(archivo):
     os.system('rm %s'%archivo)

  os.chdir('/home/estherl/NV3-MPI/')
  checkfile('covarianza.out')
  checkfile('media.out')
  print("tiempo sgsim = %e " % (t2-t1))
```

```
  print("tiempo nrmlog = %e " % (t3-t2))
  print("tiempo randts2 = %e " % (t4-t3))
  print("tiempo gwqmonitor = %e " % (t5-t4))
  os.system('./matriz %d' %size)
  os.system('mv meanvect*.out basura/')
  os.system('mv meanplume*.out basura/')
  os.system('mv covmatrx*.out basura/')
```

Observe that the steps 1) to 4) are all executed by all processors in parallel; it is only using the rank of each processor that is possible to assign different tasks to each processor. Actually, this latter is done in the step 4).

Acknowledgements

References

Babu D.K., Pinder G.F., Niemi A., Ahlfeld D.P., Stothoff S.A., 1993. Chemical transport by three-dimensional groundwater flows. Tech. Rep. 84-WR-3, Dep. of Civ. Eng., Princeton Univ., Princeton, N.J.

Dalcin L., 2012. MPI for Python, Release 1.3. URL: http://mpi4py.scipy.org/

Deutsch C.V., Journel A.G., 1997. GSLIB. Geostatistical Software Library and User's Guide. Ed. OXFORD UNIVERSITY PRESS, 2a. ed., New York, 1998, 369 p.

Dong Y., Li G., Xu H., 2012, Distributed Parallel Computing in Stochastic Modeling of Groundwater Systems. *Groundwater Journal*. 51, 2, 293–297 p.

Foster I., Kesselman C., Tuecke S., 2001, The Anatomy of the Grid: Enabling Scalable Virtual Organizations. *International Journal of High Performance Computing Fall*, 15, 200–222 p.

Freeze R.A., 1975, A stochastic-conceptual analysis of one dimensional groundwater flow in nonuniform homogeneous media. *Water Resources Research,* 11, 5, 725–741 p.

Gropp W., Lusk E., Skjellum A., 1999, Using MPI-2: Advanced Features of the Message-Passing Interface. MIT Press Cambridge, MA, USA. ISBN 0262571331.

Herrera de Olivares G.S., 1998, Cost Effective Groundwater Quality Sampling Network Design, Ph.D. Thesis, University of Vermont.

Herrera G.S., Pinder G.F., 2005, Space-time optimization of groundwater quality sampling networks. *Water Resources Research,* 41, 15 p.

Kirk D.B., Hwu W.-M.W., 2010, Programming Massively Parallel Processors: A Hands-on Approach. Ed. Morgan Kaufmann Publishers Inc., 1rs ed., San Francisco, CA, USA.

Milman K.J., Aivazis M., 2011, Python for Scientists and Engineers. *Computing in Science & Engineering,* 13, 9–12 p. URL: http://dx.doi.org/10.1109/MCSE.2011.36

Nowak W., De Barros F.P.J., Rubin Y., 2010, Bayesian geostatistical design: Task-driven optimal site investigation when the geostatistical model is uncertain. *Water Resources Research*, 46, W03535, doi:10.1029/2009WR008312.

Olivares-Vázquez J.L. Groundwater Quality Monitor GUI. User's Guide. 2002, 26 p.

Renard P., 2007, Stochastic Hydrogeology: What Professionals Really Need? *Groundwater,* 45, No. 5, 531–541 p.

Ridgway S.L., Terry C., Babak B., 2005, Scientific parallel computing. New Jersey, Princeton University Press, 372 p.

Van Leeuwen P.J., Evensen G., 1996, Data assimilation and inverse methods in terms of a probabilistic formulation. *Monthly Weather Review,* 124, 2898–2913 p.

Short Baseline Calibration using GPS and EDM Observations

Guadalupe Esteban Vazquez Becerra*, Rick A. Bennett, Mijaíl Cordero Chávez, Manuel E. Trejo Soto and José Ramón Gaxiola-Camacho

Resumen

Una investigación fue conducida para establecer y comparar una línea base de calibración a partir de mediciones realizadas a los GPS (Sistemas de Posicionamiento Global) y de taquímetro electrónico o EDM (Medición Electrónica de Distancia). El experimento se realizó en el campus de la Universidad Autónoma de Sinaloa (UAS) en Culiacán, México. El objetivo principal recae en la necesidad de establecer una línea base de calibración (~125 m), que permita la realización continua y permanente de mediciones con receptores geodésicos GPS y con EDM para garantizar y validar las precisiones especificadas por los fabricantes de tales instrumentos. Dentro de los instrumentos de medición de diferente tipo y marca comercial utilizados y comparados se encuentran tres tipos de receptores geodésicos GPS: Topcon Hiper Lite +, Ashtech Z-Xtreme y Leica SR500 y tres tipos de EDM: Topcon GTS-236W, Pentax R-326EX y Leica TC-407. Para el experimento, los componentes de la línea base de calibración fueron calculados usando las observaciones GPS de fase de diferencias dobles libres de ionosfera y procesadas utilizando el software científico PAGES (Program for the Adjustment of GPS EphemerideS). Las mediciones GPS fueron procesadas considerando intervalos de medición de 1 segundo, un ángulo de elevación de 10 grados, y órbitas precisas GPS diseminadas por el IGS (International GNSS Service). Por otra parte, la longitud de la línea base de calibración también fue directamente determinada con base en el promedio de 20 mediciones realizadas con cada EDM sobre los monumentos BASE1 y BASE2. Resultados obtenidos con GPS concuerdan entre las diferentes marcas de equipos con diferencias de ±2 mm, en contraste con los resultados obtenidos con EDM, los cuales difieren entre ±3 mm.

Palabras clave: Línea base, calibración, GPS, EDM.

Abstract

We conducted a baseline comparison for instrument calibration using GPS (Global Positioning System) and EDM (Electronic Distance Measurement) observations. The experiment was carried out at campus of the Autonomous University of Sinaloa (UAS) in Culiacan, Mexico. The main objective of this research was to establish a short (~125 m) baseline for calibration of geodetic-grade GPS and EDM instruments of different commercial brands to validate the precision specifications offered by the manufacturers of such instruments. We compared three types of geodetic-grade GPS receivers: Topcon Hiper Lite +, Ashtech Z-Xtreme and Leica SR500 and three types of EDM: Topcon GTS-236W, Pentax R-326EX and Leica TC-407. For the experiment, the baseline components were computed by using ionosphere-free double-difference (DD) GPS carrier phase observations processed using the PAGES software (Program for the Adjustment of GPS EphemerideS). The GPS data were processed with a 1-second sampling rate, 10-degree cutoff angle, and precise GPS orbits disseminated by IGS (International GNSS Service). The length of the calibration baseline was also obtained by averaging 20 measurements of line length directly recorded by the three different EDM instruments. GPS results agree among different brands with differences of ±2 mm in contrast with the resulting EDM values that differ within ±3 mm.

Key words: Calibration, baseline, GPS, EDM.

G. Esteban Vazquez B.
Mijaíl Cordero C.
Manuel E. Trejo
Faculty of the Earth and Space Sciences
Autonomous University of Sinaloa
Culiacan, Mexico.
*Corresponding author: gvazquez@uas.edu.mx

Rick A. Bennett
Department of Geosciences
University of Arizona
Tucson, AZ.

J. R. Gaxiola-Camacho
Department of Civil Engineering and Engineering Mechanics
University of Arizona, Tucson, AZ.

Introduction

The calibration of geodetic instruments such as geodetic-grade GPS receivers and EDM is of importance for applications requiring the highest precision. The accuracy specifications of the instruments provided by the manufacturers may be unachievable due to errors arising from environmental conditions (e.g., atmospheric water vapor and multipath characteristics) and experience of the instrument operator. Therefore, it is useful to understand the differences between the inherent instrument precision and the actual precision according to the type of instrument used in the presence of local environmental error sources. In order to quantify environmental error sources and verify manufacturer reported precision of such geodetic instruments, it is useful to cross validate measurements by means of a well-defined calibration baseline. A calibration-baseline is composed of two or more stable geodetic monuments at which measurements with multiple instruments of high precision are made in order to infer the absolute value of the resulting measurement. With a precisely calibrated baseline, the precisions performance of diverse types of geodetic instruments can be inter-compared. For the present study, we established a calibration-baseline at campus of the Autonomous University of Sinaloa (UAS); based on measurements with three different types of geodetic-grade GPS receivers, using a differential GPS technique, as well as series of EDM observations to cross validate the baseline length.

Previous investigators sought to validate calibration baselines using high-precision tape measuring techniques (Poling, 1965). When EDM became available in the United States of America in 1952, many errors with these geodetic electronic instruments were detected, because the technique is affected by variable atmospheric moisture and other uncertainties requiring detailed evaluation of baseline length repeatability. In 1963, the Coast and Geodetic Survey (C&GS) measured a linear array of monuments, which is registered as the first work of calibration to the EDM. This calibration baseline was originally available for use by federal agencies (Dracup *et al*., 1994). By the year of 1970, many calibration baselines became available for public use, because several of them satisfied the calibration standards of electronic instruments for short distances required for topographic and geodetic works (Dracup *et al*., 1994). Nowadays, the National Geodetic Survey (NGS) is responsible for the calibration of the electronic instruments of measurement for the public (Leick, 2004).

According to Fronczek (1977), the standard configuration of an NGS calibration baseline consists of one to four established monuments that form a total baseline length of 1,400 m, with intermediate distances of ~0 m, 150 m, and 430 m. Comparison analysis on short calibration baselines for less than 100 m and 200 m can be found at Psimoulis *et al*. (2004) and Grejner-Brzezisnka *et al*. (2006), respectively. Comparisons on longer baselines (10 to 50 km) or (26 to 300 km) are also discussed through Savage *et al*. (1996) and Eckl *et al*. (2001).

Calibration baseline experiment

The short calibration baseline presented in this study was conducted during three consecutive days: October 8, 9 and 10, 2010. Since the access to some of the equipment and components was limited, our baseline study focused on performing all test under similar atmospheric conditions; therefore, we tested GPS receivers and EDM at the same time periods over three consecutive days. The selected test area for the GPS and EDM measurements is located at UAS campus on top of the Faculty of Earth and Space Sciences (FACITE) and a facility building next to the Dentistry building (see Figure 1), where the surrounding environment represents rather optimal observability conditions with open sky and no obstructions. The monumentation for the short baseline experiment, located at UAS campus, consists of two concrete structural columns denoted as BASE1 and BASE2 (see Figures 2 and 3), that were designed to be part of the structural elements of the main frame of each building. BASE1 pillar is located on top of an educational building erected in a very rigid and reinforced foundation; as well as the BASE2 pillar, which is also part of a main educational facility building. In both cases, the main structure and the foundation of those buildings were designed and constructed following the current construction code in Mexico (RCDF-04, 2004); thus, such structural system provides the stability required to develop the analysis here described. In addition, each pillar also consist of very stable geodetic steel pins (stainless steel, 5/8-inch diameter) sunk directly into concrete pillars, with metal force-centered level mounts to guarantee accurate re-centering of the GPS antenna at each site each session (Zhang *et al*. 1997). The divot on top of the base pillar is then considered as the reference point for the measurement results, where a tribrach at each pillar was used to maintain the GPS antenna leveled and to keep the same antenna height (0.150 m) for
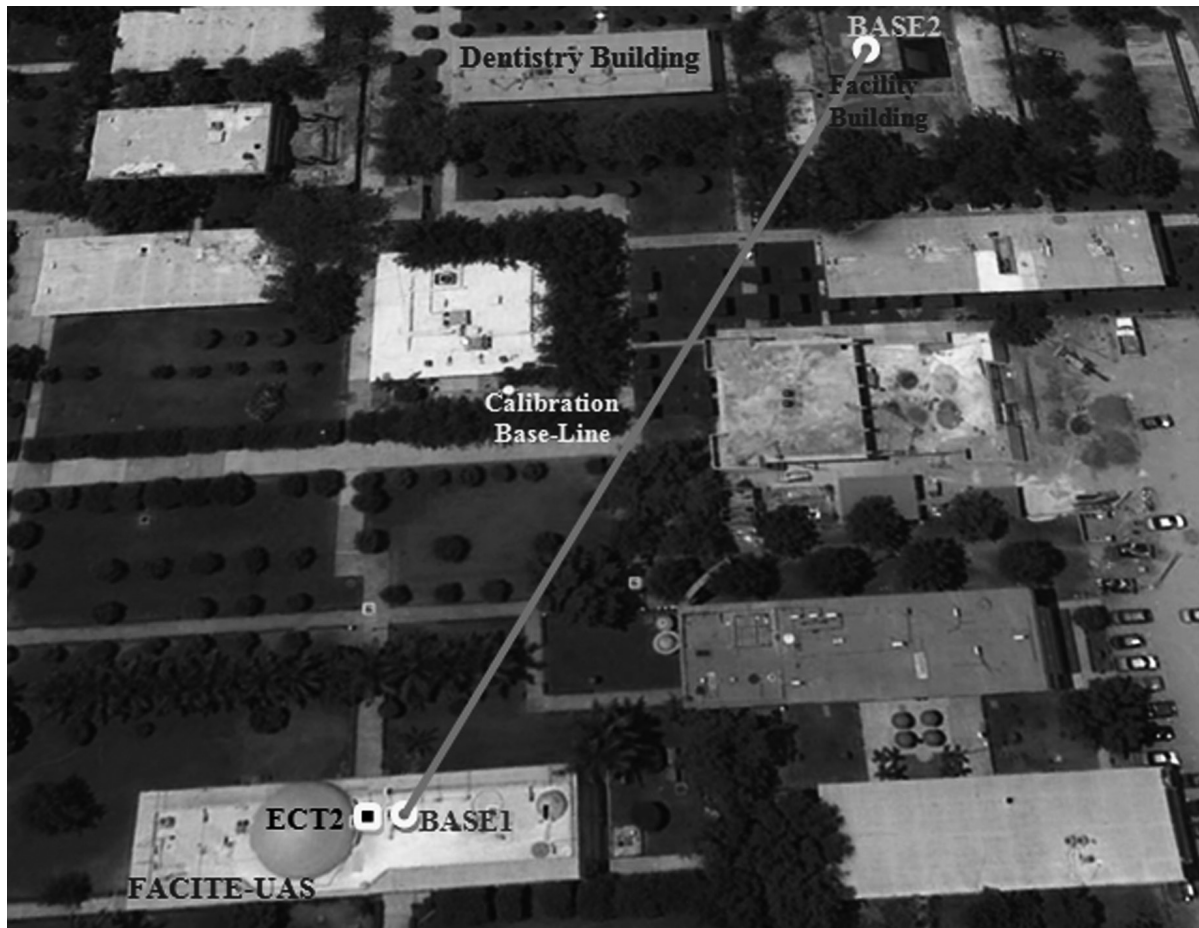
Figure 1.Calibration baseline experiment, image courtesy of Google Earth.

each survey session. First, the coordinates of BASE1 and BASE2 monuments were previously determined with a 2-hour GPS survey session with respect to the fixed base station (ECT2) and subsequently used as known and fixed for computing the calibration baseline length. In other words, we collected GPS data at 1-sec interval for 2-hours data span for 3-consecutive days, resulting in approximately 21,600 measurements for each GPS observable (e.g. L1, L2, C/A, P1 and P2) that were used to precisely define the coordinates of BASE1 and BASE2 pillars. The GPS survey tests performed to determine the coordinates of BASE1 and BASE2, which define the calibration baseline, are illustrated in Table 1. Here, the antenna type, NGS antenna designator and time duration (local time) of each measurement session are also presented including the percentage of GPS observables completed for the entire experiment. The last two columns of Table 1 show the values for the pseudorange multipath (MP1-RMS and MP2-RMS) that can be considered as a potential contributor that

might have an impact on GPS positioning results (Vazquez and Grejner-Brzezinska, 2012). The multipath effects presented in Table 1 at BASE1 and BASE2 range up to ~30 cm for the first day of the survey, when Hiper Lite antenna was used, compared to the second and third days that show roughly ~10 cm, when the Ashtech (ASH701975.01A) and Leica (LEIAT502) antennas were respectively used. In general, the experienced amount of pseudorange multipath seems to be reasonable and no reason to think in any negative influence in the positioning results.

GPS data processing technique

The GPS data were converted to the RINEX (Receiver INdependent EXchange) format (Gurtner 1994). The TEQC software (Test of Quality Check), provided by UNAVCO (University NAVstar Consortium), was used to verify the quality and integrity of the RINEX files (i.e., expected number of GPS observables and percentage completed, receiver multipath,

Table 1. GPS survey tests.

GPS Station	Antenna Type	NGS Antenna Designator	Start Local Time	End Local Time	Expected # of GPS Observables	Completed # of GPS Observables	%	MPI-RMS (cm)	MP-RMS (cm)
					October 8, 2010				
ECT2	Ashtech	ASH701975.01A	7:15:01	9:15:00	70,492	68,653	97	11.26	8.26
BASE1	Hiper Lite	TPSHIPER_LITE	7:15:01	9:15:00	70,293	70,281	100	29.56	26.60
BASE2	Hiper Lite	TPSHIPER_LITE	7:15:42	9:15:41	70,366	70,366	100	25.64	24.92
					October 9, 2010				
ECT2	Hiper Lite	TPSHIPER_LITE	7:15:01	9:15:00	70,350	70,348	100	30.20	27.66
BASE1	Ashtech	ASH701975.01A.	7:15:01	9:15:00	70,349	68,582	97	9.53	7.82
BASE2	Ashtech	ASH701975.01A	7:15:01	9:15:00	70,048	68,419	98	4.22	4.51
					October 10, 2010				
ECT2	Hiper Lite	TPSHIPER_LITE	7:15:47	9:15:46	70,062	70,042	100	31.54	29.67
BASE1	Leica	LEIAT502	7:15:24	9:15:23	70,597	69,593	98	2.95	4.98
BASE2	Leica	LEIAT502	7:30:01	9:30:00	70,107	70,101	100	1.01	1.40

Figure 2. Monumentation of BASE 1 site, located on top of the FACITE building; UAS campus. GPS Receiver Ashtech Z-Xtreme with Ashtech (ASH701975.01A) antenna, collecting data on October 9, 2010.

Figure 3. Monumentation of BASE 2 site, located on top of a facility building; UAS campus. GPS Receiver Leica SR500 with Leica (LEIAT502) antenna, collecting data on October 10, 2010.
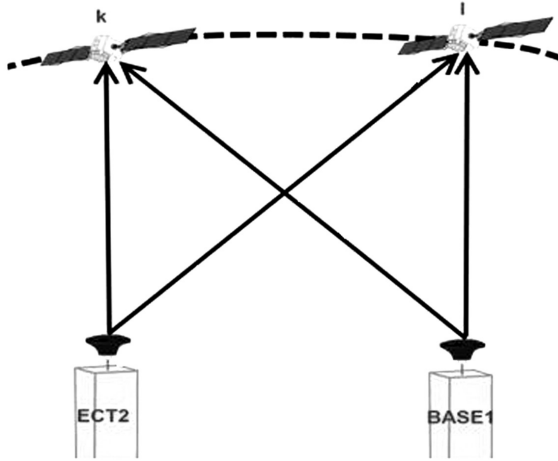
Figure 4. Double difference configuration between fixed (ECT2) station and unknown (BASE1) station.
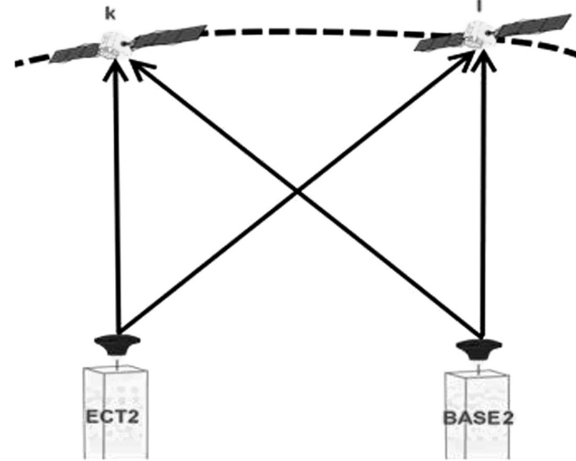
Figure 5. Double difference configuration between fixed (ECT2) station and unknown (BASE2) station.

and receiver clock drift). After the verification, the GPS data were processed with the PAGES software, (Mader *et al*. 1995; Eckl *et al*. 2001; Schenewerk *et al*. 2001). This GPS processing package was developed at the NGS and it has been shown by Grejner-Brzezisnka *et al*. (2006) to be suitable when comparing antenna calibration for baselines under 200 m. In order to provide an optimal solution, the PAGES software was configured to use the iono-free DD carrier phase combination given by Hofmann-Wellenhof *et al*. (2001):

$$\Phi_{ij,12}^{kl} = \rho_{ij}^{kl} + T_{ij}^{kl} + \alpha_1 \lambda_1 N_1 + \alpha_2 \lambda_2 N_2 + \alpha_1 \varepsilon_{ij,1}^{kl} + \alpha_2 \varepsilon_{ij,2}^{kl}$$

(1)

with

$$\alpha_1 = \frac{f_1^2}{f_1^2 - f_2^2} \quad \text{and} \quad \alpha_2 = -\frac{f_2^2}{f_1^2 - f_2^2}$$

where: i and j are subscripts that denote receivers, k and l are superscripts that denote satellites, ρ_{ij}^{kl} is the DD-geometric distance between the respective satellites and receivers, indicate that the carriers L_1 and L_2 are involved in the combination, T_{ij}^{kl} is the DD tropospheric refraction term, $\lambda_1 \approx 19$cm and $\lambda_2 \approx 24$cm are the wavelengths of the signals on the L_1 and L_2 carriers, respectively, N_1 and N_2 are the integer ambiguities associated with the phase measurements (in cycles) on L_1 and L_2, respectively, $\varepsilon_{ij,1}^{kl}$ and $\varepsilon_{ij,2}^{kl}$ are the random DD measurement noise terms (in meters) for the observed phases on L_1 and L_2, respectively. The main specifications for the GPS data processing included the use of a 1-sec sampling rate, 10° cut-off angle and use of precise final orbits

disseminated by IGS. Also, the carrier phase ambiguity parameters were fixed at the rate of 99-100% in the three consecutive day processing and antenna calibration parameters provided by NGS were used following Mader (1999).

In our case, the DD configuration can be established between the well-known base station (ECT2) with fixed coordinates and the unknown stations (BASE1 and BASE2) as shown in Figures 4 and 5.

Based on Equation (1), we can rewrite this equation according to the DD configurations (ECT2-BASE1) and (ECT2-BASE2) resulting:

$$\Phi_{(ECT2-BASE1)_{1,2}}^{kl} = \rho_{(ECT2-BASE1)}^{kl} + T_{ECT2-BASE1}^{kl}$$
$$+\alpha_1 \lambda_1 N_{(ECT2-BASE1)_1}^{kl} + \alpha_2 \lambda_2 N_{(ECT2-BASE1)_2}^{kl}$$
$$+\alpha_1 \varepsilon_{(ECT2-BASE1)_1}^{kl} + \alpha_2 \varepsilon_{(ECT2-BASE1)_2}^{kl}$$

(2)

and

$$\Phi_{(ECT2-BASE2)_{1,2}}^{kl} = \rho_{(ECT2-BASE2)}^{kl} + T_{ECT2-BASE2}^{kl}$$
$$+\alpha_1 \lambda_1 N_{(ECT2-BASE2)_1}^{kl} + \alpha_2 \lambda_2 N_{(ECT2-BASE2)_2}^{kl}$$
$$+\alpha_1 \varepsilon_{(ECT2-BASE2)_1}^{kl} + \alpha_2 \varepsilon_{(ECT2-BASE2)_2}^{kl}$$

(3)

with

$$\rho_{(ECT2-BASE1)}^{kl} = \rho_{ECT2}^k - \rho_{BASE1}^k - \rho_{ECT2}^l + \rho_{BASE1}^l$$

(4)

and

$$\rho_{(ECT2-BASE2)}^{kl} = \rho_{ECT2}^k - \rho_{BASE2}^k - \rho_{ECT2}^l + \rho_{BASE2}^l$$

(5)

From Equations (4) and (5) we have:

$$\rho^k_{ECT2} = \sqrt{\left(X_{ECT2} - X^k\right)^2 + \left(Y_{ECT2} - Y^k\right)^2 + \left(Z_{ECT2} - Z^k\right)^2} \tag{6}$$

$$\rho^l_{ECT2} = \sqrt{\left(X_{ECT2} - X^l\right)^2 + \left(Y_{ECT2} - Y^l\right)^2 + \left(Z_{ECT2} - Z^l\right)^2} \tag{7}$$

$$\rho^k_{BASE1} = \sqrt{\left(X_{BASE1} - X^k\right)^2 + \left(Y_{BASE1} - Y^k\right)^2 + \left(Z_{BASE1} - Z^k\right)^2} \tag{8}$$

$$\rho^l_{BASE1} = \sqrt{\left(X_{BASE1} - X^l\right)^2 + \left(Y_{BASE1} - Y^l\right)^2 + \left(Z_{BASE1} - Z^l\right)^2} \tag{9}$$

$$\rho^k_{BASE2} = \sqrt{\left(X_{BASE2} - X^k\right)^2 + \left(Y_{BASE2} - Y^k\right)^2 + \left(Z_{BASE2} - Z^k\right)^2} \tag{10}$$

$$\rho^l_{BASE2} = \sqrt{\left(X_{BASE2} - X^l\right)^2 + \left(Y_{BASE2} - Y^l\right)^2 + \left(Z_{BASE2} - Z^l\right)^2} \tag{11}$$

where X_{ETC2}, y_{ETC2}, Z_{ETC2} are the coordinates of the fixed base station (ECT2); X_{BASE1}, Y_{BASE1}, Z_{BASE1} are the coordinates for the first unknown station (BASE1); X_{BASE2}, Y_{BASE2}, Z_{BASE2} are the coordinates of the second unknown station (BASE2); X^K, Y^K, Z^K and X^l, Y^l, Z^l are the coordinates of satellites k and l, respectively.

Once we solved for the coordinates of the unknown stations (BASE1 and BASE2), the ellipsoidal distance for the calibration baseline was computed, using the following equation:

$$D_{Elip.} = \sqrt{\left(X_{BASE2} - X_{BASE1}\right)^2 + \left(Y_{BASE2} - Y_{BASE1}\right)^2 + \left(Z_{BASE2} - Z_{BASE1}\right)^2} \tag{12}$$

Then, we compute the distance in the Universal Transversal Mercator (UTM) projection given by:

$$D_{UTM} = D_{Elip.} * k_0, \tag{13}$$

where $D_{Elip.}$ is the ellipsoidal distance computed from GPS and k_0 is the deformation scale factor in the UTM projection.

Equation (13) represents the distance for the calibration baseline in the UTM projection; which is assumed to be represented in a plane to a local scale, because the EDM measurements were directly made on the ground. The deformation on D_{UTM} caused by the projection is taking into account by the scale factor k_0 that will correct for the GPS ellipsoidal distance when getting away from the central meridian (105° W) of the UTM projection. Once achieved this, a comparison between GPS and EDM was stated under such assumption.

Figure 6. EDM measurements with PENTAX R-326EX at BASE1 site (see BASE2 in the background), performed on October 8, 9 and 10, 2010.

Figure 7. Prism location at BASE2 site, Topcon prism as an example.

EDM measurements

The calibration-baseline derived from EDM was estimated from the average of the set of 20 length measurements performed with three different types of EDM (Topcon GTS-236W, Pentax R-326EX and Leica TC-407) between the BASE1 and BASE2 monuments. These measurements were conducted over the course of three consecutive days in order to help mitigating atmospheric errors. The PENTAX R-326EX is presented in Figure 6 as an example of how the EDM measurements were carried out with this instrument. Figure 7 illustrates the type of prism used; here a Topcon prism with 0/-30mm offset is presented as an example. In order to avoid errors from centering the instruments and prisms, we used force-centered level mounts to guarantee accurate re-centering. The prisms on the two pillars were mounted on tribrachs to guarantee the same line (horizontally). We also used prisms that are compatible with each type of EDM, because this allows for accurate determination of the constant error bias associated with each reflector, which represents a common error presented in this type of measurements. In addition, it is assumed in the present experiment that manufacturers were responsible and they properly applied the necessary corrections and reductions for atmospheric conditions (usually performed internally), as well as Earth's curvature and slope were taken into account.

Results and analysis

It is well-known that the accuracy of GPS positioning mostly relies on the geometric configuration of the observed satellites for a specific location where the GPS measurements are performed. DOP (dilution of precision) arises from this fact, since it is considered as geometric factor that amplifies the single range observation error that shows the positioning accuracy obtained from multiple GPS observations. DOP is very important for differential GPS, as both stations must use the same satellites. With the current full GPS constellation, the common observability should not be a problematic issue; due to the existing satellite availability. Based on these considerations, we decided to account for the DOP values: position (PDOP), horizontal (HDOP), vertical (VDOP), geometrical (GDOP) and time (TDOP), for the time-window of the three day GPS measurements of the experiment (October 8, 9 and 10, 2010). As a result of accounting for this accuracy factor, Figures 8, 9 and 10 show the computed DOP values, which were found to be less than 2 for the time when the GPS measurements were performed

(7:15 a.m. to 9:15 a.m.). However, it was found that the PDOP, which contributes more to determine the coordinates of BASE1 and BASE2, is less than 1.6, for the three days of the experiment. Therefore, with the obtained small PDOP values, it is feasible to expect millimeter accuracy on the positioning results, as it was obtained in all presented solutions.

For comparison, the performance or accuracy specifications of the different type and commercial brand of geodetic-grade GPS receivers and EDM provided by the manufacturer are shown in Table 2, given in units of millimeters plus parts per million (mm + ppm). These specifications for GPS receivers show that based on the obtained coordinates from two GPS stations (i.e. BASE and BASE2), one can compute the length of the calibration baseline; while specifications for EDM refer to the direct measurement of the baseline between the two stations. The last column of Table 2 shows what we called the permissible accuracy (σ) for a ~125 m calibration baseline. In other words, σ represents the reference value in terms of accuracy that can be permitted when using a GPS receiver or EDM to determine the magnitude of such calibration baseline. The resulting calibration baseline values from GPS were computed by means of Equation (12), whereas the length of the calibration baseline derived from EDM was directly obtained based on the average of a set of 20 measurements with each type of EDM, between BASE1 and BASE2. Making the corresponding assumptions regarding that the EDM worked properly and it was correctly centered and leveled as well as the prisms located at the two monuments; then the error propagation is presented in Table 3.

In Table 3, σ_N and σ_E represent the standard deviations values obtained when computing the coordinates of BASE1 and BAS2 stations, by using different types of GPS receivers. In contrast, σ_{EDM} corresponds to the standard deviation value computed from the set of 20 measurements with each brand of EDM considered in the experiment. Also, it can clearly be observed in Table 3 that all standard deviation values, for both GPS and EDM, are within the computed permissible accuracy (σ) presented in Table 2. Once we obtained the calibration baseline results from both GPS receivers and EDM, we made a comparison between them. In this assessment, the resulting baseline values from GPS are assumed to be the "true or reference" for the comparison. The reported weighted mean value from GPS is 124.2497 m., whereas the mean from EDM is 124.2472 m, which shows a 2.5 mm difference (Figure 11). It should be point it out
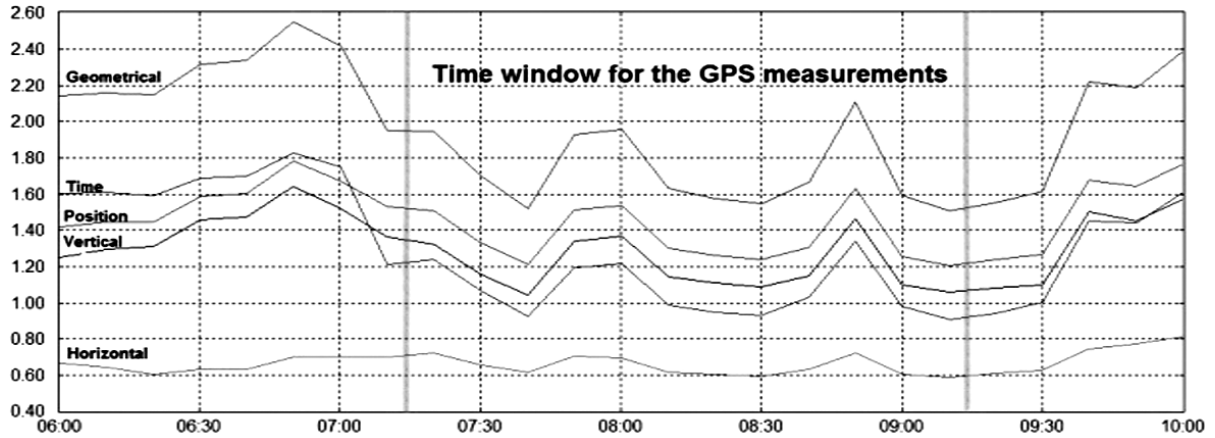
Figure 8. Dilution of precision (DOP): geometrical (GDOP), Position (PDOP), Vertical (VDOP), Horizontal (HDOP) and Time (TDOP) for GPS measurements; October 8, 2010.
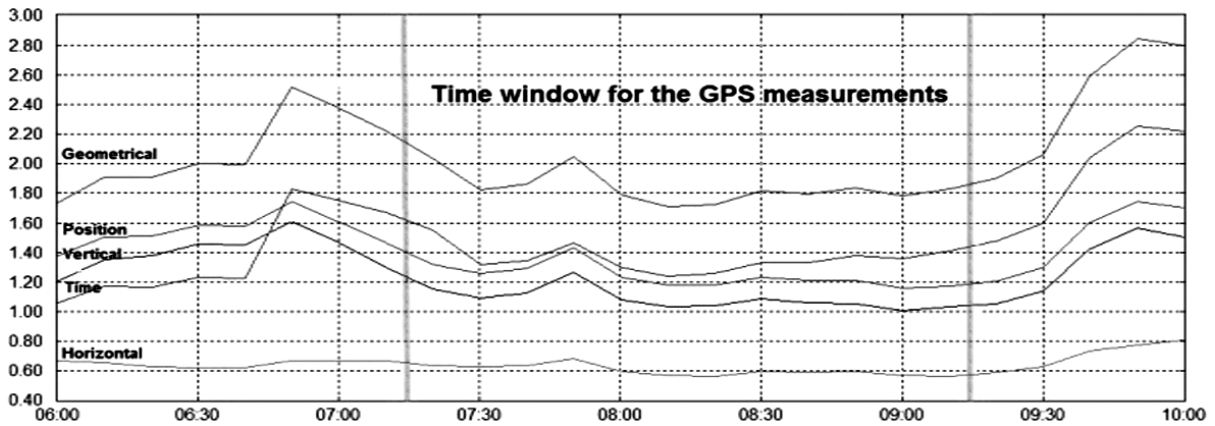

Figure 9. Dilution of precision (DOP): geometrical (GDOP), Position (PDOP), Vertical (VDOP), Horizontal (HDOP) and Time (TDOP) for GPS measurements; October 9, 2010.
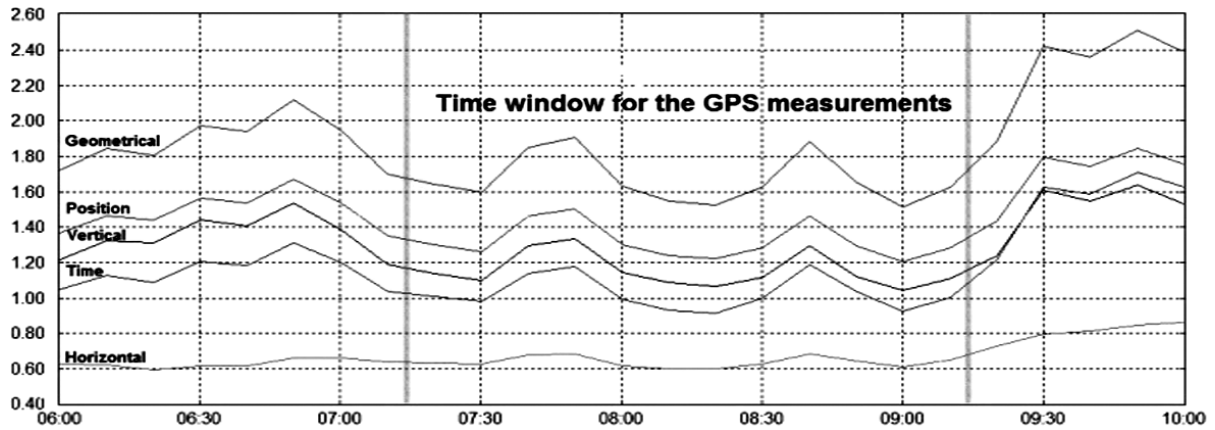

Figure 10. Dilution of precision (DOP): geometrical (GDOP), Position (PDOP), Vertical (VDOP), Horizontal (HDOP) and Time (TDOP) for GPS measurements; October 10, 2010.

Table 2. GPS and EDM accuracy specifications provided by the manufacturer and computed permissible accuracy (σ) for the ~125 m calibration baseline.

GPS Receiver with (Antenna Type)	Accuracy Specifications (static)	Computed Permissible Accuracy (σ)
Topcon Hiper Lite + (Hiper Lite)	3mm +0.5ppm -	3.06 mm
Ashtech Z-Xtreme (Ashtech)	5mm + 1.0ppm	5.12 mm
Leica SR530 (Leica)	3mm + 0.5ppm	3.06 mm
EDM Type		
Topcon GTS-236W	±2mm + 2ppm	±2.25 mm
Pentax R-326EX	±3mm + 2ppm	±3.25 mm
Leica TC-407	±5mm + 2ppm	±5.25 mm

Table 3. Resulting calibration baseline values from GPS and EDM.

GPS Receiver with (Antenna Type)	Resulting Baseline (m)	σ_{EDM} (mm)	σ_E (mm)
Topcon Hiper Lite + (Hiper Lite)	124.249	1.04	1.13
Ashtech Z-Xtreme (Ashtech)	124.251	1.72	1.85
Leica SR530 (Leica)	124.250	1.27	1.39
Weighted Mean:	**124.2497**		

EDM Type	Resulting Baseline (m)	σ_{EDM} (mm)
Topcon GTS-236W	124.248	±2.01
Pentax R-326EX	124.247	±3.09
Leica TC-407	124.245	±5.05
Weighted Mean:	**124.2472**	

that the weighted mean values were computed assigning more weight to the GPS receivers and EDM's that reported more stable results according to the obtained standard deviations values.

In addition, the standard deviation values from both GPS and EDM results lie within the computed permissible accuracy. When comparing GPS receivers vs. EDM of the same commercial brand, it was found that Topcon Hiper Lite + and the Topcon GTS-236W experienced a 1 mm difference for the resulting baseline. If we consider that the computed permissible accuracy when performing measurements with the Topcon GTS-236W is ±2.25 mm, then 1 mm difference can be interpreted as 44% of such permissible accuracy. Next, a 4 mm difference was obtained when comparing the Ashtech Z-Xtreme and the Pentax R-326EX. This 4 mm difference represents a little bit more than the defined "tolerable accuracy of 1 σ.", which is the assumed expected precision value when performing a measurement with the proposed EDM. It should be point out that both instruments are not exactly of the same commercial kind; however, an assumption of treating them as the same brand was made here in the comparison, since the Pentax R-326EX EDM could properly be used to compare to the Ashtech Z-Xtreme receiver. Leica SR530 and Leica TC-407 comparison shows the largest difference (5 mm). Even thought, this 5 mm difference is slightly large with respect to the 4 mm from the previous comparison, it represents less than (1 σ) because Leica TC-407 has larger range in the permissible accuracy than the Pentax R-326EX.
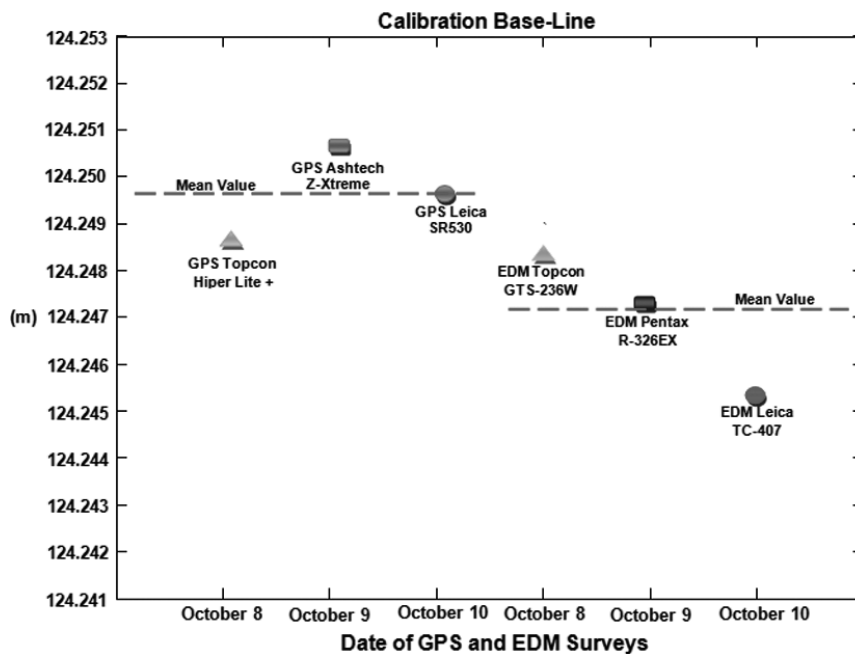
Figure 11. Calibration base-line results from GPS and EDM.

Finally, when comparing GPS receivers vs. EDM of different commercial brand, Topcon Hiper Lite + vs. Pentax R-326EX gives a 2 mm difference, which represents 0.62 σ. On the other hand, there is a difference of 4 mm on the comparison between Topcon Hiper Lite + and Leica TC-407. In this case the 4 mm difference can be translated to 0.76 σ. The Ashtech Z-Xtreme and Topcon GTS-236W comparison reveals just a 3 mm difference. Larger differences (6 mm) occurred when comparing Ashtech Z-Xtreme and Leica TC-

407. However, this 6 mm value is just 14% above the 1 σ; given the permissible accuracy for the Leica TC-407 is ±5.25 mm. When comparing Leica SR500 and Topcon GTS-236W, differences of 2 mm can be found (or 0.89 σ) and the comparison between Leica SR500 and Pentax R-326EX gives a difference of 3 mm, which represents 0.92 σ. Table 4 shows the summary of the resulting calibration baseline values obtained from GPS vs. EDM, and their comparison, including the permissible accuracy (σ) and the accuracy factor (τ). The accuracy

Table 4. Summary of the resulting calibration baseline values obtained from GPS vs. EDM.

GPS Receiver with (Antenna Type)	Resulting Baseline From GPS (m)	EDM Type	Resulting Baseline From EDM (m)	Deviation w.r.t. true value (mm)	Permissible Accuracy (σ) (mm)	Accuracy Factor (τ)
Topcon Hiper Lite + (Hiper Lite)	124.249	Topcon GTS-236W	124.248	1	±2.25	0.44
		Pentax R-326EX	124.247	2	±3.25	0.62
		Leica TC-407	124.245	4	±5.25	0.76
Ashtech Z-Xtreme (Ashtech)	124.251	Topcon GTS-236W	124.248	3	±2.25	1.33
		Pentax R-326EX	124.247	4	±3.25	1.23
		Leica TC-407	124.245	6	±5.25	1.14
Leica SR350 (Leica)	124.250	Topcon GTS-236W	124.248	2	±2.25	0.89
		Pentax R-326EX	124.247	3	±3.25	0.92
		Leica TC-407	124.245	5	±5.25	0.95

factor (τ) means "times the tolerable accuracy of 1 σ.", which is the assumed expected deviation value when performing a measurement with EDM. According to the comparison presented in Table 4, there is not a logical correspondence between permissible accuracy (σ) and accuracy factor (τ), based on the deviation with respect to the true value. This issue can be directly attributed to the fact that permissible accuracy (provided by the manufacturer) is not consistently based on the brand of EDM considered in the experiment. A clear example can be observed when comparing deviations with respect to true value for Pentax R-326EX and Leica TC-407. That is, an increment on the deviation values is reflected in a decrement in the accuracy factor (τ), which is the opposite than one may expect.

Based on the above analysis where proper measurements and computational procedures were followed, we now performed a hypothesis testing by using a two-tailed test in order to address the concern about if the three types of EDM are working within their accuracy specifications. In other words, we need to determine more rigorously if EDM are providing correct results when comparing to the GPS mean value, which is assumed as the true value for the calibration baseline. It is expected that the EDM observed distances will be rejected if they are statistically either to short or too long as compared to the mean of the resulting calibration baseline from GPS. From the proposed test we need to verify that: H_0: $\mu=\tilde{y}$ vs. H_a: $\mu\neq\tilde{y}$, where H_0 is the null hypothesis, H_a is the alternative hypothesis, μ is mean value from GPS and $\tilde{y}$ is the mean value from EDM. After applying the well-known t distribution in the computations and taking into account different levels of significances (5%, 2% and 0.2%), the final decisions for accepting are presenting in Table 5.

Table 5. Hypothesis testing for the calibration baseline from GPS and EDM.

EDM Type	Level of Significance ($\alpha/2$)		
	5%	2%	0.2%
	(0.025)	(0.010)	(0.001)
Topcon GTS-236W	Fail	Fail	Pass
Pentax R-326EX	Fail	Fail	Fail
Leica TC-407	Fail	Fail	Fail

According to the results presented in Table 5, only Topcon GTS-236W at 99.8% lies within the indicated confidence interval and it passed the test. Pentax R-326EX was too closed to fulfill the condition of passing the test at 0.2% significance level, but it fail for the three levels of significance (5%, 2% and 0.2%). Additionally, with Leica TC-407 was rejected; thus, it also fails the test. This issue can be attributed to the fact that this EDM was the least accurate when performing the baseline measurements and also provides larger range of computed permissible accuracy derived from accuracy specifications of the manufacturer. However, for those EDM that fails to contain the calibration baseline value (at any specific significance level), there is no a strong reason to be concerned about the calibration status of these instruments, since they diverge within 1 to 5 mm with respect to the true value from GPS.

Conclusions

The establishment of calibration-baseline (BASE1-BASE2) by means of GPS measurements was performed very precisely, and fulfilled the accuracy standards according its dimensions (~125 m) for the proposed experiment. Resulting calibration baseline values from GPS compared very-well among different brands with differences of ±2 mm in contrast with the resulting EDM values that differ within ±3 mm. EDM measurements also show a slightly greater discrepancy in comparison with the permissible accuracy. It was also found a difference of 2.5 mm in the mean values from GPS vs. EDM. Of the EDM brands tested, the Topcon GTS-236W preformed the best (±1mm up to ±3mm), followed by the Pentax R-326EX (±2mm up to ±4mm) and finally the Leica TC-407 (±4mm up to ±6mm). In the case of the established tolerable accuracy of 1σ, all EDM fulfill this condition when comparing results with true values from Topcon Hiper Lite + and Leica SR350 GPS receivers. The 1σ condition fails for the three EDM when comparing results with respect to mean value from Ashtech Z-Xtreme GPS receiver. From the hypothesis testing, only two EDM: Topcon GTS-236W and Pentax R-326EX contain the calibration baseline value at 2% and 0.2% level of significance, respectively; however, this is not a powerful reason to be concerned about the calibration status of the EDM Leica TC-407 which entirely failed the tests, because of its large accuracy specifications provided by its manufacturer. The methodology, measurements and computations used in this research for the baseline calibration (BASE1 and BASE2) followed the strict requirements according

G. Esteban Vazquez B., Rick Bennett, Mijaíl Cordero C., Manuel E. Trejo and J. Ramon Gaxiola-Camacho

to the accuracies of the employed geodetic-grade GPS receivers and EDM. Therefore, it is recommended that this calibration baseline serves as reference for further calibration of geodetic equipment at the FACITE-UAS.

Acknowledgments

Refferences

Dracup Joseph F., Fronczek Charles J., Tomlinson Raymond W., 1994, Establishment of calibration base lines. NOAA technical memorandum NOS NGS 8. February, 1-18.

Eckl M.C., Snay R.A., Soler T.A., Cline M.W., Mader G.L., 2001, Accuracy of GPS-derived relative positions as a function of interstation distance and observation-session duration. *Journal of Geodesy*, 75, 633-640.

Fronczek C.J., 1977, Use of calibration baselines. NOAA Technical Memorandum NOS NGS-10, 38 pp. National Geodetic Information Center, Rockville, MD 20852.

Grejner-Brzezinska D.A., Vázquez G.E., Hothem L., 2006, Geodetic Antenna Calibration Test in the Antarctic Environment. ION GNSS 19th International Technical Meeting of the Satellite Division, 26–29 September 2006, Fort Worth, TX, pp. 2798–2806.

Gurtner W., 1994, *RINEX: The Receiver Independent Exchange Format. GPS World* 5, 7, 48-52.

Hofmann-Wellenhof B., Lichtengegger H., Collins J., 2001, GPS Theory and Practice. (5th edition) Springer-Verlag Wien New York.

Leick A., 2004, GPS Satellite Surveying, 3rd Edition, Wiley, New Jersey, 435 pages.

Mader G., 1999, GPS antenna calibration at the National Geodetic Survey, *GPS Solutions*, 3, 1, pp. 50-58.

Mader G.L., Schenewerk M.S., Ray J.R., Kass W.G., Spofford P.R., Dulaney R.L., Pursell D.G., 1995, GPS orbit and earth orientation parameter production at NOAA for the International GPS Service for Geodynamics for 1994 in Zumberge, J.F. *et al*., (eds) International GPS Service for Geodynamics, 1994 Annual Report, 197-

212, Jet Propulsion Lab., California Institute of Technology, Pasadena, CA.

Poling A.C., 1965, A taped base line and automatic meteorological recording instruments for the calibration of electronic distance measuring instruments. *International Hydrographic Review,* XLII, 2, 173-184.

Psimoulis P.A., Kontogianni V.A., Nickitopoulou A., Pytharouli S.I., Triantafyllidis P., Stiros S.C., 2004, Estimating the Optimum Duration of GPS Static Observations for Short Baseline Length Determination in Greece. Proceedings of the FIG Working Week, Athens, Greece, 22–27 May.

RCDF-04, 2004, "Reglamento de Construcciones para el Distrito Federal (RCDF)", Gaceta Oficial del Distrito Federal, décima cuarta época, Enero, 2004.

Savage J.C., Lisowski M., Prescott H., 1996, Observed discrepancy between Geodolite and GPS distance measurements, *J. Geophys. Res*., 101, 25,547-25,552.

Schenewerk M.S., Marshall J., Dillinger W., 2001, Vertical Ocean Loading Deformations Derived from a Global GPS Network. *Journal of the Geodetic Society of Japan.* 47, 1, 237-242.

Vazquez G.E., Grejner-Brzeziska D.A., 2012, A Case Study for Pseudorange Multipath Estimation and Analysis: TAMDEF GPS Network, *Geofísica Internacional*, 51, 1, 2012, pp. 63-72.

Zhang J., Bock Y., Johnson H., Fang P., Williams S., Genrich J., Wdowinski S., Behr J., 1997, Southern California Permanent GPS Geodetic Array: Error analysis on daily position estimates and site velocities. *Journal of Geophysical Research,* 102, B8. l8, 035-055.

Meteoric isotopic gradient on the windward side of theSierra Madre Oriental area, Veracruz – Mexico

Juan Pérez Quezadas[*], Alejandra Cortés Silva, Salvatore Inguaggiato, María del Rocío Salas Ortega, Juan Cervantes Pérez and Victor Michael Heilweil

Resumen

Se caracterizó la composición isotópica $\delta^{18}O$ ‰ y δD‰, del agua meteórica en el flanco oriental de la Faja Volcánica Transmexicana, sobre un transecto de 90 km que parte de nivel de mar hasta 4220 msnm. Las muestras de lluvia fueron colectadas, durante los años 2007 a 2012, en temporada de lluvia (mayo a Octubre). Se obtuvo una Línea Meteórica Local (LML) bajo una regresión lineal la cual queda descrita por $\delta D = 7.4\ \delta^{18}O + 7.3$, $R^2 = 0.99$. Esta línea tiende a separarse de la Línea Meteórica Mundial (LMM) donde la precipitación ocurre a altitudes mayores a 3000 msnm, debido a un enriquecimiento en Deuterio. El resultado obtenido en esta investigación fue comparado con los datos isotópicos, colectados en el Puerto de Veracruz, extraídos de la base de datos de la Red Mundial de Isótopos en Precipitación. El gradiente altitudinal de $\delta^{18}O$, es descrito por una regresión lineal $\delta^{18}O = -2.1\ (Z\ km) - 5.56$, $R^2 = 0.86$, la cual implica un gradiente vertical de -0.21 ‰/ 100m. Finalmente, el registro isotópico en agua meteórica durante los años de observación en esta investigación muestra un enriquecimiento en $\delta^{18}O$ y δD a una altitud aproximada de 1400 msnm, probablemente influenciado por la topografía y/o relacionado por efectos isotópicos de tormentas tropicales, típicas de estas latitudes. Esta caracterización aumentará la comprensión de importantes procesos hidrológicos y proporcionará la base para futuras investigaciones hidrológicas.

Palabras clave: Isótopos estables, gradiente isotópico, Veracruz México, composición isotópica, precipitación.

Abstract

The isotopic composition ($\delta^{18}O$, δD‰) of precipitation in the windward side of the Sierra Madre Oriental on the eastern flank of the Mexican Volcanic Belt was characterized along a 90 km transect from sea level up to an altitude of 4220 meters. Rain samples were collected during the rainy season (May through October) from 2007 through 2012. The Local Meteoric Water Line (LMWL), determined with linear regression of isotope results, is $\delta D = 7.44\ \delta^{18}O + 7.3$, $R^2 = 0.99$. This line departs from the Global Meteoric Water Line (GMWL) for precipitation at altitudes greater than 3000 masl due to deuterium enrichment processes. The results obtained in this research were compared with isotopic data of the Global Network of Isotopes Precipitation (GNIP) data base from the port of Veracruz. The altitude (Z) gradient of $\delta^{18}O$ was also determined by the linear regression of precipitation data, resulting in the relation $\delta^{18}O = -2.1Z - 5.56$, $R^2 = 0.86$, where Z is altitude in kilometers. This implies a $\delta^{18}O$ vertical gradient of -0.21 ‰/ 100 m, which falls within the normal range described in the literature for tropical areas. Finally, the isotopic record of meteoric waters during the years of observation shows anomalous enrichment in $\delta^{18}O$ and δD at an altitude of about 1400 m, probably influenced by the local topography and/or an isotope effect related to tropical storms typical of this latitude. This characterization will increase the understanding of important hydrological processes and will provide a foundation for future hydrological research.

Key words: Stable isotopes, isotopic gradient, Veracruz, México, isotopic composition, precipitation.

J. Pérez[*]
Centro de Geociencias
Universidad Nacional Autónoma de México
Campus Juriquilla
Querétaro, Qro., México
*Corresponding autor: pquezadas_1@hotmail.com

A. Cortés
Instituto de Geofísica,
Universidad Nacional Autónoma de México
Ciudad Universitaria
Delegación Coyoacán, 04510
México, D.F., México

S. Inguaggiato
National Institute of Geophysics and Volcanology
Palermo, Italy

M. R. Salas
J. Cervantes
Centro de Ciencias de la Tierra
Universidad Veracruzana
Xalapa, Veracruz, México

V. Heilweil
U.S. Geological Survey-
Utah Water Science Center
Salt Lake City, U.S.A.

Introduction

The isotopic characterization of local rainfall in water-resource studies is very important, considering that such precipitation typically represents the primary source of recharge to groundwater systems. This isotopic signature can subsequently be used to trace groundwater flow within the aquifer. On the basis of 400 stable isotopic (δ^2H and $\delta^{18}O$) samples of water (rivers, rain and snow) at different geographical locations, the linear relationship δ^2H (δD) = $8\delta^{18}O$ + 10 was defined by Craig (1961) as the Global Meteoric Water Line (GMWL). Dansgaard (1964), using data from GNIP (Global Network of Isotopes in Precipitation, 2012), found that isotopic ratios of monthly precipitation recorded at stations located in the northern continental hemisphere complied with the GMWL. Significant deviations from the GMWL line, however, were observed relative to other continents and islands. These deviations were attributed to differences in the local weather conditions and in the processes controlling precipitation. The analysis of the GNIP data for the periods 1960-1978 and 1960-1987 were reported by Yurtsever and Gat (1981) and Rozanski et al. (1993), respectively. Using the same methodology described by previous authors, the IAEA (International Atomic Energy Agency, 2005) processed data from 1961 to 2000 and found that the arithmetic mean of the isotopic ratios in precipitation recorded from 410 stations distributed globally are well-described by the equation: δD = 8.07 (± 0.02) $\delta^{18}O$ + 9.9(± 0.1), R^2 = 0.98. The deuterium excess can be described globally as d_{ex} δ^2H - $8\delta^{18}O$.The weighted averages of long-term precipitation for the same period (1961-2000) were calculated by GNIP from a subset of measurements during years for which more than 70% of precipitation during that year was analyzed for a given isotope (with a minimum requirement of at least one full year of data). The weighted average correlation is δD= 8.14 (± 0.02) $\delta^{18}O$ +10.9 (± 0.2), R^2 = 0.98.

There are several widely documented effects that control the spatial variation of the isotopic composition in the meteoric waters including altitude, latitude, continental, amount and season (Clark and Fritz, 1997). Of these, altitude (topography) is considered the most important factor. It has been shown that on the windward side of the mountains, the $\delta^{18}O$ and δD ratios of rain decrease (become isotopically depleted) with increasing altitude. This is mainly due to the combination of two factors: (1) rainfall becomes progressively depleted by the loss of isotopically heavy isotopes as rain events progress in a topographically up gradient direction and, (2) the temperature is lower and thus the condensate becomes isotopically enriched because of fractionation (Clark and Fritz, 1997). Other hydrologic factors may affect the stable isotopic signature of precipitation at windward tropical forests. Vogelmann (1973) showed that evapotranspiration in a cloud forest of eastern Mexico was subsequently recycled as fog precipitation, which could affect its isotopic content. This process of fog interception was quantified in a cloud forest of Puerto Rico (Holwerda et al., 2010), accounting for about 10% of the total precipitation.

The objective of this study is the isotopic characterization of precipitation on the windward (Atlantic) side of the Sierra Madre Oriental in the State of Veracruz, the most populated part of the State of Veracruz. The main scope of this work is the spatial and temporal isotopic characterization of meteoric waters and their possible relationship with dominant isotopic effects in our study area. Because the isotopic meteoric line varies with region, it was important to determine a local meteoric water line. Local conditions can also be described by the vertical isotopic gradient and the deuterium excess (d_{ex}), which can be used assess the difference between local conditions in Veracruz compared with to the global meteoric water line δD = 8 $\delta^{18}O$ + 10 (Craig, 1961). In this research, we show the isotopic relationship between $\delta^{18}O$‰ and δD‰ measured in the cumulative rainfall as a time series based on samples was collected during six rainy seasons (2007-2012). Importantly we evaluate the isotopic gradient along a topographic transect from sea level to an altitude of over 4000 m. This characterization will increase the understanding of important hydrological processes and will provide a foundation for future hydrological research.
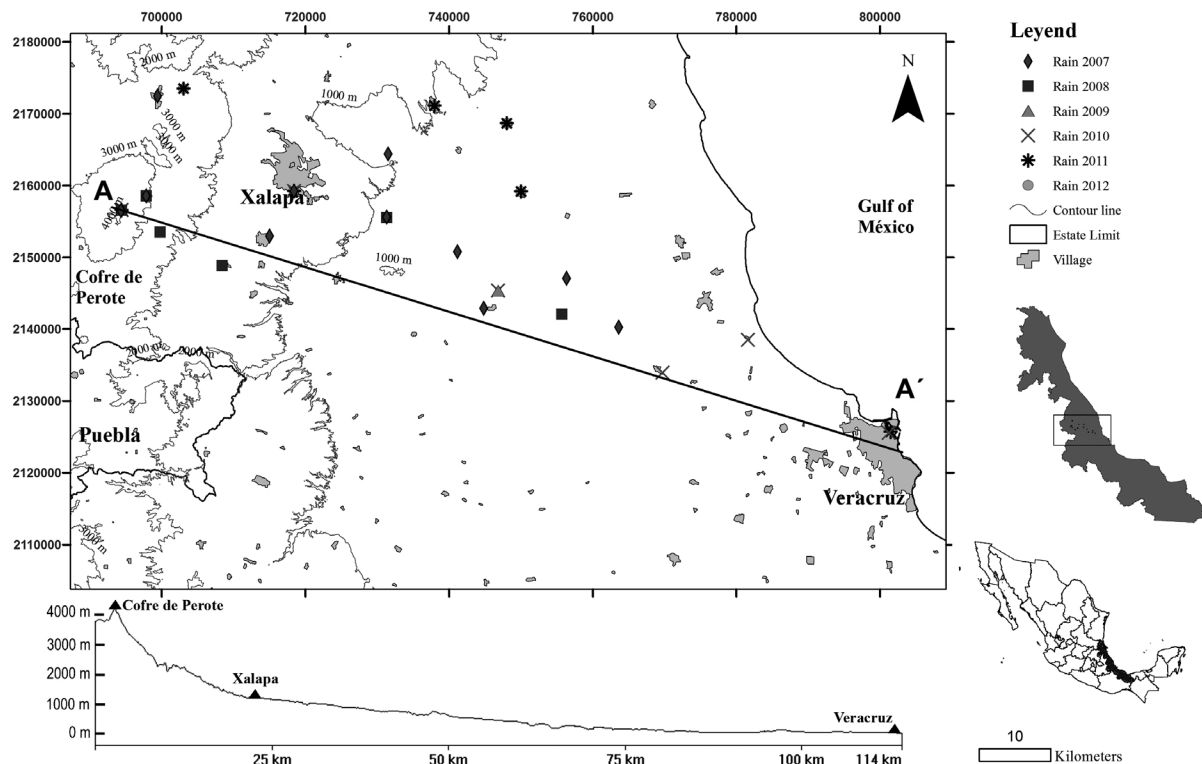
Study area

The 2000 km^2 study area is located in the central part of the state of Veracruz, Mexico, between 2110000 and 2180000 UTM coordinates north latitude (Figure 1). Its shape is elongated in an orientation northwest to south east (approximately 90 km long) and narrower from northeast to southwest (approximately 20 km wide). It is bounded on the east by the Gulf of Mexico and to the west by the Sierra Madre Oriental. The topographic relief is variable and characterized by two main areas: a lower and flatter area located along the coast, and a higher and steeper area located along the Sierra Madre Oriental (Tejeda et al., 1989; Barradas et al., 2004).The altitudinal gradient is extremely large rising from sea level at the

Port of Veracruz to 4220 masl at the peak of the extinct Cofre de Perote volcano (cross-section A-A' of Figure 1).The isotopic gradient and precipitation patterns in the study area are greatly influenced by this topography.

The climate within the study area varies from "tropical wet-and-dry" (average annual temperature > 18°C and more than 150 mm precipitation during the summer months) at the Port of Veracruz to "humid subtropical" (average temperature > 10°C during the warmest months and more than 1200 mm precipitation during the rainy season) in the Sierra Madre Oriental (http://geo-mexico.com/?p=9512). The maximum monthly air temperature ranges from 12°C at Tembladeras to 23°C at the Port of Veracruz (Figure 2). The seasonal variation of temperature at each of the three weather stations oscillates 4, 8 and 6 °C at 3000 masl, 1400 masl, and at sea level, respectively. The primary controls on the climate within the study area are the topography and the atmospheric circulation systems prevailing during the different seasons (Mosiño and Garcia 1973). These result in the occurrence of the rainy season during

the summer and autumn. Although the study area is located in the tropics, precipitation is also affected by extra-tropical (mid-latitude) phenomena. Precipitation data during 1981-2010 from three precipitation stations located along the A-A' transect (Figure 1) at Tembladeras, Xalapa, and the Port of Veracruz (3000 m a.s.l.,1400m a.s.l, andat sea level, respectively) illustrate the strength of rainy season during the months of May through October. More than 80% of total annual rainfall occurs during these months, (Figure 2). It is also interesting that the monthly amount during the rainy season is similar for both the high-altitude station (Tembladeras) and the low-altitude station (Port of Veracruz). In contrast, precipitation at Xalapa is much less. While rainfall during the months of July and August exceeds 300 mm at both Tembladeras and the Port of Veracruz, precipitation during the same months at Xalapa is less than 200 mm. It is theorized that a local vertical circulation pattern caused by a barometric pressure anomaly causes a microclimate that brings drier air to the Xalapa area during the summer months.

Figure 1. Geographyc map and topographic section of the up wind Sierra Madre Oriental study area from Cofre de Perote (A) to Veracruz (A'); location of precipitation stations shown by black triangles.

There is also a large variability in total annual rainfall within the study area. Total annual rainfall varied from 2076 to 1206 mm at the Veracruz GNIP Station during 1962-1988. It is known that the effects of global phenomena such as El Niño - Southern Oscillation (ENSO; Rasmusson and Wallace, 1983), or La Niña (the negative phase), can result in excess rain in some parts of the state of Veracruz during the summer (Magaña *et al*., 2003). The Pacific Decadal Oscillation (PDO; Mantua *et al*., 1997), in its negative phase, can also induce excessive rain in southern portion of the state of Veracruz (Mendez *et al*., 2010). Lastly, the Atlantic Multidecadal Oscillation (AMO; Sutton and Hodson 2005) can increase the frequency of hurricanes, causing excessive rainfall in the State of Veracruz, (Vazquez, 2007).

The amount and relative $\delta^{18}O$‰ isotopic composition of monthly precipitation measured by the IAEA during 1962-1988 at the Port of Veracruz (Global Network Isotopic Precipitation, 2012) is shown in figure 3. The annual weighted isotopic composition for rainfall calculated by GNIP for the period 1962-1988 (Long Term Mean) is: $\delta^{18}O = -4.09 \pm 1.31$ ‰, n = 110, and $\delta D = -26.8 \pm 9.7$ ‰, n = 78. Separately, we calculated the weighted isotopic composition of rainfall for just the rainy season (May through October) with $\delta^{18}O$‰ and δD‰ of - 4.2 ‰ and - 24.2 ‰, respectively. Because these are not significant differences, it is assumed that the weighted isotopic composition precipitation during the rainy season is representative of the annual rainfall in the study area. Figure 3 shows an inverse relationship between cumulative precipitation and $\delta^{18}O$ values. Yet during the "canicular days" (July and August), $\delta^{18}O$‰ values increased by more than 1‰.
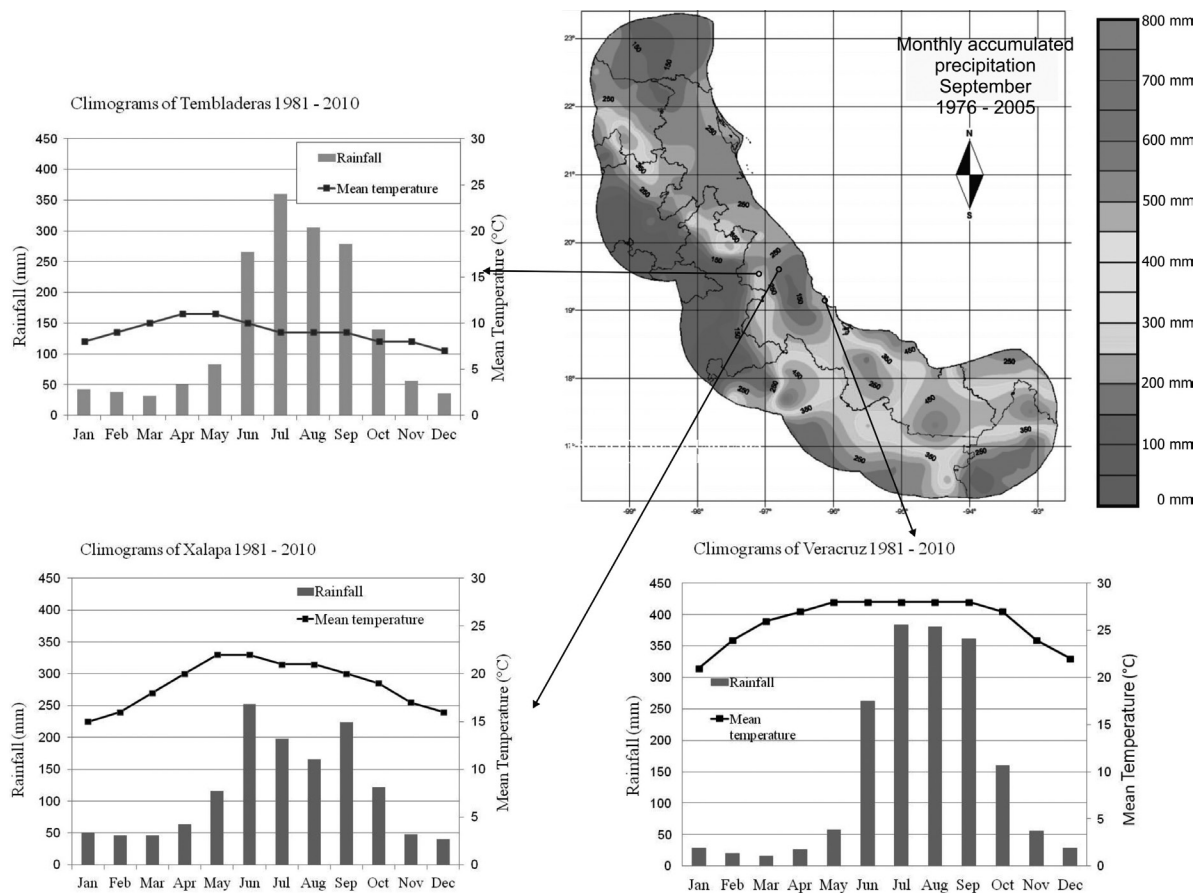
Figure 2. Displays climograms located in the town of Tembladeras, Xalapa and Veracruz, located at 3000 masl., 1400 masl, and sea level, respectively (modified from Tejeda *et al*., 1989). Precipitation at the Port of Veracruz and at Tembladeras is concentrated in the months of June to September, with magnitudes as large as 350 mm. In contrast, the majority of rainfall in Xalapa is distributed over the months of May to October, with monthly averages less than 250 mm.

Figure 3. Monthly arithmetic average of $\delta^{18}O$‰ and monthly precipitation average (mm) accumulated from 1962 to 1988. Source: GNIP, IAEA, http://www-naweb. iaea.org/napc/ih/IHS_ resources_gnip. html.
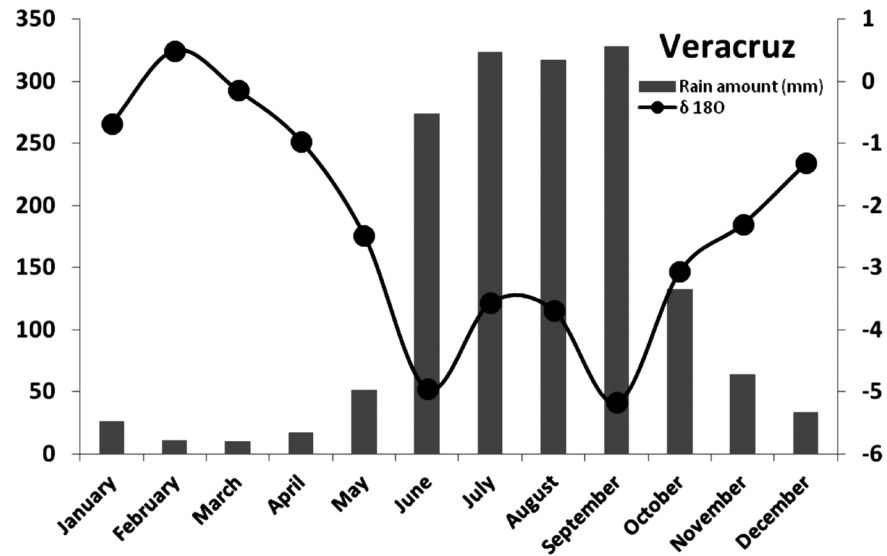
Methodology

To achieve the objectives of this study, a network of temporary rain collectors were deployed along a transect from the Port of Veracuz at sea level to Cofre de Perote at 4220 mamsl. Rainfall was collected during the rainy season for a period of 6 years (2007 through 2012). Composite samples were collected at each site that included all precipitation during each rainy season (May through October). These were collected with a standard rain gauge by taking a composite sample of meteoric water over the entire rainy season. The rain gauge consists of a plastic funnel with a diameter of 40 cm connected to a storage container with sufficient capacity to store up to 5000 mm of precipitation. The container is covered by three heat insulating materials: Poly foam, Mylar, and aluminum foil. 250 ml of inert Nujol mineral oil was added to minimize evaporation (Cortés *et al*., 2001). At the end of each rainy season, an aliquot of 60 ml of water was collected from each sample container and transferred to high density polyethylene bottles (Nalgen brand).

The sites for the composite rainfall collectors were selected based on proximity to meteorological stations of the National Weather Service of Mexico that record the amount of precipitation. Before the rainy season of 2007, 11 rain gauges were installed at altitudes ranging from 8 masl at Veracruz and Antigua to 4220 masl at Cofre de Perote. These gauges were spatially distributed, as shown in figure 1. Because of logistical problems, the network was modified every year by changing the number and location of the collectors. Seven rain

gauges we installed during the rainy season of 2008, three of which were at the same sites as the previous year. Four gauges were installed during 2009, with three re-occupying previous sites. Eight gauges were installed during 2010, with four re-occupying previous sites. During both 2011 and 2012, gauges were installed at the seven sites (the same locations for both years), with three re-occupying previous sites. Over the 6-year collection period, therefore, a total of 44 collectors were utilized. The estimation of the elevation of the installed rain gauges was recorded with GPS integrated barometric altimeter (Garmin Etrex Summit brand, accuracy of ± 3 m), calibrated at sea level and compared with the topographic maps (1:50,000) published by INEGI (National Institute of Statistics, Geography and Informatics).

The collected rain samples were analyzed for $\delta^{18}O$‰ and δD‰ at the Mass Spectrometry Laboratory (MSL) of the Institute of Geology at the National Autonomous University of Mexico (UNAM). The analytical uncertainties (1σ standard deviation) reported by the MSL-UNAM are $\delta^{18}O$ ~± 0.1 ‰ and δD ~± 1 ‰. Based on these, the estimated 1σ standard deviation for d_{ex} is $\pm\sqrt{[\sigma(\delta D)^2 + 64\ \sigma(\delta^{18}O)^2]}$, or ± 1.3 ‰. Replicate isotopic analyses were run for ten percent of samples to verify these analytical uncertainties. The reported values of $\delta^{18}O$‰ and δD‰ are normalized to the international standards V-SMOW and SLAP, according to the recommendations of the IAEA, (Gonfiantini, 1978). Composite rainy season stable isotope values of samples collected at the 44 sites during this study were compared

with data from the Port of Veracruz station, which was operated from 1962-1988 jointly by the Global Precipitation Isotopic Network (GPIN) and the International Atomic Energy Agency. The station has a record of 139 isotopic couples (δ^{18}O‰ and δD‰), 189 Tritium values, monthly precipitation, mean ambient temperature and vapor pressure (www.iaea. org / water, GNIP).

Results and discussion

Table 1 shows the isotopic results of the meteoric water samples collected during 2007-2012. δ^{18}O ranges from - 3.3 ‰ to −15.3 ‰ and δD from −17.2 ‰ to −106.3‰.

Both isotopic ranges are large compared to the respective analytical uncertainties, ± 0.1 ‰ for δ^{18}O and ± 1.3 ‰ for δD. The isotopic pairs of δ^{18}O‰ and δ^2H‰ ranged from -3.3‰ and -17.2‰ at the Port of Veracruz (8 masl) in the rainy season of 2009 to -15.3‰ and -106.3‰ at Cofre de Perote (4200 masl) in the rainy season of 2007. These values are consistent with 2008-2010 precipitation data for Veracruz reported by Goldsmith *et al*. (2011). The deuterium excess values ranges between 7.0‰ and 17.4‰; the highest d$_{ex}$ value was recorded at Cofre de Perote, indicating the largest separation from the LMWL.

Figure 4 shows the isotopic results for the study area, compared with the Global Meteoric Water Line, GMWL (Craig, 1961). Applying a linear regression on these results, the Local Meteoric Water Line (LMWL) for the upwind Sierra Madre Oriental study area is described by the equation δD= 7.44 δ^{18}O + 7.3. The deuterium excess for the more isotopically depleted samples can be seen by their slight divergence from the GMWL. This LMWL is similar to δD = 7.42 δ^{18}O + 7.9 for the Port of Veracruz (GNIP, 2014) but differs from another reported for the Coatepec area, also in the State of Veracruz, of δD = 8.21 δ^{18}O + 18.5 (Goldsmith; 2011). Our LMWL for the upwind Sierra Madre Oriental study area also differs from those reported for other parts of Mexico: δD = 7.46 δ^{18}O + 8.9 for the Colima Volcano area in the Mexican Pacific (Hartsough *et al*., 2008); δD = 8 δ^{18}O + 11 for the central highlands of Mexico (based on data collected during the same years as for the Port of Veracruz; Cortes *et al*., 1997); and δD = 7.7 δ^{18}O + 10.8 for the Transmexican Volcanic Belt (which is almost identical to theGMWL). These different LMLs show how the stable isotopic composition of precipitation is strongly influenced by local climatic conditions.
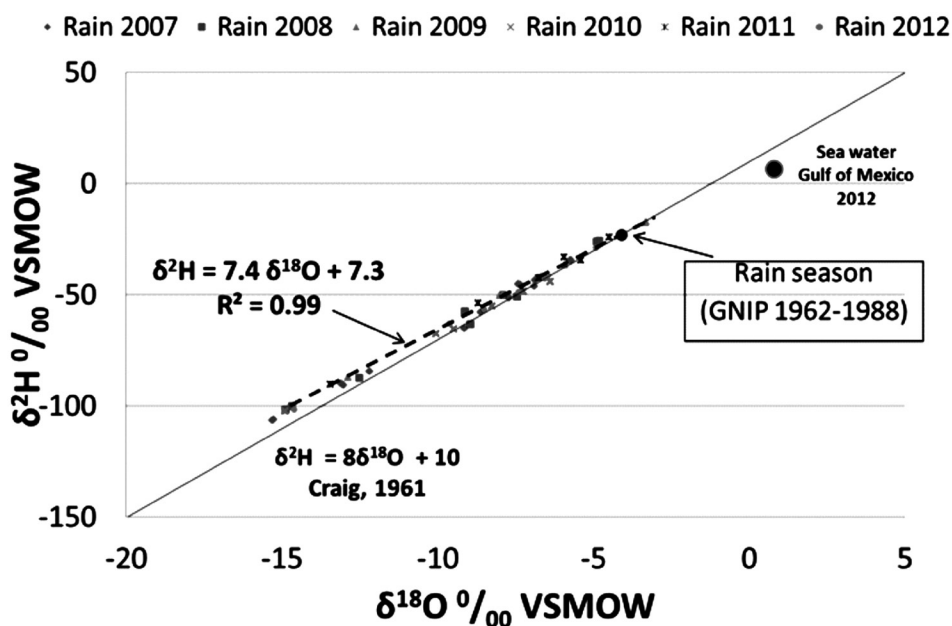
Figure 4. δ^{18}O‰ and δ^2H‰ of precipitation samples collected 2007 through 2012 and the resulting linear regression (Local Meteoric Water Line, LML) for the upwind Sierra Madre Oriental study area, compared with the Global Meteoric Line (GML).

Table 1. Stable isotope ratios δ¹⁸O‰ and δD‰ vs V-SMOW of accumulated rainfall in the upwind Sierra Madre Oriental study area, during the rainy seasons from 2007 through 2012.

Name	Altitude (m a.s.l.)	2007 δ¹⁸O‰	δ²H‰	d-excess [‰]	2008 δ¹⁸O‰	δ²H‰	d-excess [‰]	2009 δ¹⁸O‰	δ²H‰	d-excess [‰]	2010 δ¹⁸O‰	δ²H‰	d-excess [‰]	2011 δ¹⁸O‰	δ²H‰	d-excess [‰]	2012 δ¹⁸O‰	δ²H‰	d-excess [‰]
Cofre de Perote	4220	-15.3	-106.3	15.9	-14.9	-101.5	17.4	-12.9	-87.2	15.7	-14.9	-102.3	16.8	-13.4	-90.2	17.4	-14.6	-101.8	15.2
Tembladeras	3081	-13	-90.8	13.3	-12.5	-87.5	12.5												
Pocitos	2464				-9.1	-57.7	15.2												
Las Vigas	2442	-12.2	-84.6	13.0															
Loma de Tablas	2275													-8.7	-53.7	15.7	-9.6	-63.2	13.8
Ixhuacán	1690										-6.4	-44.0	7.0						
Xalapa	1448	-7.3	-45.4	13.4				-8.0	-50.4	13.7	-9.5	-65.4	10.5	-5.9	-33.1	14.4	-7.9	-50.3	13.3
Totutla	1374										-10.1	-67.4	13.0						
Xico	1354				-7.9	-50.4	13.0												
Coatepec	1189	-6.9	-43.5	11.5															
Alto Lucero	1078																		
Dos Ríos	950	-8.6	-57.9	11.0	-9	-63.5	8.1												
Loma de Rogel	710	-9.2	-65	8.2															
La Reforma	691													-6.7	-42.2	11.7	-7.3	-48.9	9.8
Cerro Gordo	601	-7.7	-51.3	10.4															
Carrizal	441	-6.9	-46.3	8.8															
La Cumbre	375							-5.9	-36.5	10.9	-8.2	-55.1	10.9						
Actopan	268													-5.4	-34.3	8.9	-7.4	-48.9	10.1
Rinconada	263				-7.5	-51.1	8.5												
Buena Vista	199	-6.8	-42.5	11.6							-6.6	-42.1	10.7						
Tamarindo	140	-5.7	-34.3	11.6															
Paso de Ovejas	30										-6.5	-42.5	9.4						
Veracruz	8				-4.8	-25.7	12.9	-3.3	-17.2	9.3				-4.5	-24.0	12.0	-4.9	-28.9	10.1
La Antigua	8										-7.3	-48.6	9.5						

The vertical isotopic gradient of precipitation along transect A-A' (figure 1) of the study area was determined least squares linear regression of $\delta^{18}O$ versus altitude for meteoric water samples collected during 2007-2012, yielding the relation $\delta^{18}O = -2.1*Z$ (km) $- 5.56‰$; $r^2 = 0.87$ (Figure 5a). The same vertical gradient was also found for precipitation in the Central Mexican Plateau (Durazo, 2008; Cortés and Durazo, 2001), but with a smaller y intercept value $-3.26‰$. A similar vertical isotopic gradient was calculated for deuterium: $\delta D = -15.3*Z$ (km) $- 34.5$; $r^2 = 0.83$. In addition, an abrupt enrichment in $\delta^{18}O$ and δD occurs at altitudes between 1,000 to 1,400 meters in the study area.This is may becaused by local topographic condition and/or an isotopic shift caused by tropical storms. But because this anomaly is located in an area with frequent fog, it may instead be caused by condensation processes under equilibrium isotope exchange (Gonfiantini *et al.*, 2001). A third possible cause is plant evapotranspiration which, in tropical areas, may form mists and clouds that are isotopically depleted.

The temporal isotopic variation at 3 sites located at different altitudes (Veracruz, Xalapa and Cofre de Perote) shows that during years characterized by heavy rainfall, the isotope composition is lighter (figure 6). This is particularly evident during 2010, the wettest year of the 6 year study due to a large number of storms in the Atlantic Ocean (five hurricanes, 13 tropical storms and one tropical depression; CONAGUA, 2012). This correlation between precipitation and isotopic depletion may be caused by cloud formation higher in the atmosphere during larger storms (Dansgaard, 1964).
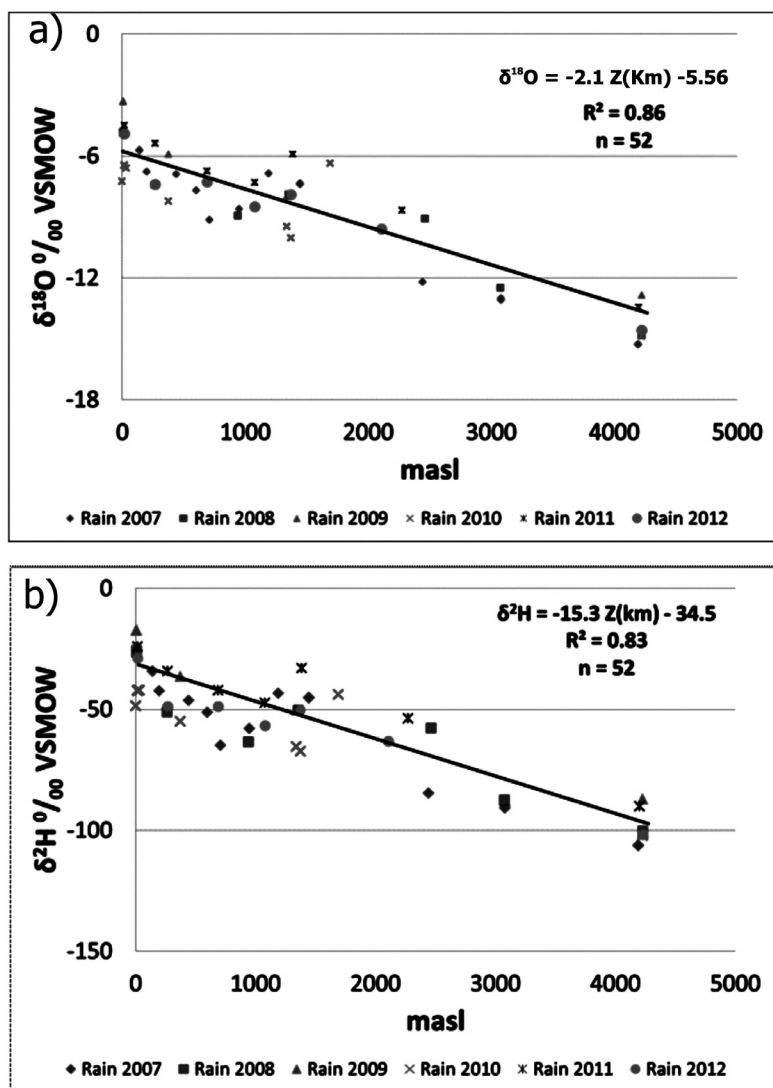
Figure 5. Vertical isotopic gradient of (a) $\delta^{18}O‰$ and (b) δD during the rainy season.

Figure 6. Temporal behavior of $\delta^{18}O$‰, for meteoric water samples from 2007 to 2012, at three different altitudes: Veracruz, Xalapa, and Cofre de Perote at 8, 1448 and 4220 masl, respectively.
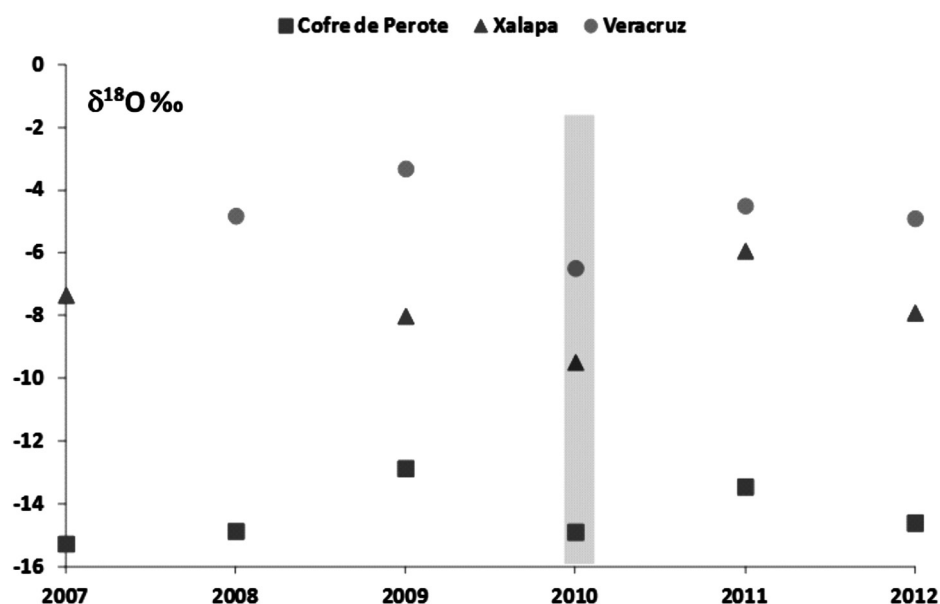
Concluding Remarks

The stable isotope composition of rainy season precipitation has been characterized for the windward (Atlantic) side of the Sierra Madre Oriental, located on eastern flank of the Mexican Volcanic Belt in the State of Veracruz. The cumulative rainfall during the rainy season from May to October accounts for over the 80% of the total annual rainfall in the study area. Average isotopic values were measured in 44 cumulative precipitation samples collected during the rainy seasons of 2007 through 2012 collected at altitudes ranging from 8 to 4220 masl. The results are comparable with previously reported annual weighted averages for the Port of Veracruz (GNIP, 2012), supporting the methodology of focusing only on sample collection during the rainy season. A local meteoric water line of $\delta D = 7.44\ \delta^{18}O + 7.3$ was determined from these isotopic results. In addition, calculated vertical isotopic gradients for $\delta^{18}O$ and δD are - 2.1 ‰ km^{-1} and - 15.3 ‰ km^{-1} respectively. These gradients are consistent with previously reported gradients in Veracruz and at similar latitudes elsewhere in central Mexico. A mid-altitude isotopic anomaly near Xalapa, however, indicates that this isotopic gradient may cause an under estimation or over estimation of the calculated altitude of precipitation in particular cases, depending on local orographic precipitation and/or extreme weather conditions. The results of this study can be utilized to improve the understanding of groundwater recharge processes. In particular, this information can be used to evaluate the source altitude of precipitation recharging aquifers in this part of eastern Mexico.

Acknowledgment

References

Barradas V.L., Cervantes J., Puchet C., 2004, Evidencia de un cambio climático en la región de las grandes montañas del Estado de Veracruz, México. En García Codrón, J. C., C. Diego Liaño, P. Fernández de Arróyabe, C. Garmendia y D. Rasilla (editores). El Clima entre el Mar y la Montaña. Pp. 213-219. Publicaciones de la Asociación Española de Climatología (AEC) Serie A, No. 4. Universidad de Cantabria, Santander, España. ISBN:84-8102-384-1.; D.L.:SA-1453-2004

Clark I., Fritz P., 1997, Isotopes in hydrogeology. Lewis. Boca Raton.

CONAGUA. 2012. Análisis de las temporadas de huracanes de los años 2009, 2010 y 2011 en México. ISBN: 978-607-8246-30-4.

Cortés A., Durazo J., Farvolden R.N., 1997, Studies of isotopic hydrology of the basin of Mexico and vicinity: annotated bibliography and interpretation. J*ournal of Hydrology* 198, 1-4, 346-376.

Cortés A., Durazo J., 2001, Tendencia del Oxígeno-18 en la precipitación del centro de México. *Ingeniería Hidráulica en México*. XIV, 2 pp. 93-102.

Craig H., 1961, Isotopic variations in meteoric waters. *Science*, 133: 1702-1703.

Dansgaard W., 1964, Stable isotopes in precipitation. *Tellus,* 16, 438-468.

Durazo J., 2008, Modern precipitation in central Mexico and its hydrological manifestations in the valley of Toluca. Reportes Internos 2008-5 del Instituto de Geofísica. Universidad Nacional Autónoma de México. México, D. F.

Goldsmith G., 2011, Stable isotopes reveal linkages among ecohydrological processes in a seasonally dry tropical montane cloud forest. *Ecohydrology*. DOI:10.1002/eco.268.

Gonfiantini R., 1978, Standards for Stable Isotope Measurements in Natural Compounds. *Nature,* 271. 5645.

Gonfiantini R., Roche M.A., Olivry J.C., Fontes J.C., Zuppi G.M., 2001, The altitude effect on the isotopic composition of tropical rains. *Chemical Geology,* 181, 147-167.

Hartsough P., Poulson S.R., Bondi F., Galindo-Estrada I., 2008, Stable isotope characterization of the ecohydrological cycle at a tropical treeline site. *Artic, Antartic. and Alpine Research,* 40, 2, 343-354.

Holwerda F., Bruijnzeel L.A., Oord A.L., Scatena F.N., 2010, Fog interception in a Puerto Rican elfin cloud forest: a wet-canopy water budget approach. In Tropical Montane Cloud Forests, Science for Conservation and Management, Chapter 29 in Bruijnzeel L.A.,pp. 282-292.

International Atomic Energy Agency, 2005. Isotopes in the water cycle. Past, present and future of a developing science.*Springer*, 381 p.

Magaña V., Vazquez J.L., Pérez J.L., Pérez J.V., 2003, Impact of El Niño onprecipitation in Mexico, *Geofísica Internacional,* 42, 313-330.

Mantua N.J., Hare S.R., Zhang Y., Wallace J.M., Francis R.C., 1997, A Pacific decadal climate oscillation with impacts on salmon. *Bulletin of the American Meteorological Society*, 78, 1069-1079.

Méndez González J., Ramírez Leyva A., Cornejo Oviedo A., Zárate Lupercio A., Cabazos Pérez T., 2010, Teleconexiones de la Oscilación Decadal del Pacífico (PDO) a la precipitación y temperatura en México, en Investigaciones Geográficas, 73, pp. 28 – 79.

Mosiño P., García E., 1973, The climate of Mexico, in*Climates of North America.* R.A. Bryson and F.K. Hare (editores), Elsevier. Países Bajos.

Rasmusson E., Wallace M., 1983, Meteorological Aspects of the El Niño/Southern Oscillation, *Science*, 16, pp. 1195 -1202.

Rosanski K., Araguás-Araguás L., Gonfiantini R., 1993, Isotopic patterns in modern global precipitation. In: Continental Isotope Indicators of Climate, American Geophysical Union Monograph.

Sutton R., Hodson D., 2005, Atlantic Ocean Forcing of North American and European Summer Climate", *Science*, 1, pp. 115 – 117.

Tejeda A., Acevedo F., Jáuregui E., 1989, *Atlas Climático del Estado de Veracruz.* Colección Textos Universitarios. Universidad Veracruzana. 150 pp.

Vázquez Aguirre J.L., 2007, *Variabilidad de la precipitación en la República Mexicana,* Tesis de Maestría en Física de la Atmósfera, UNAM, 110 pp.

Vogelmann H.W., 1973, Fog precipitation in the cloud forest of eastern Mexico. *BioScience* 23, 2, 96-100.

Yurtsever Y., Gat J., 1981, Atmospheric waters. Stable Isotope Hydrology: Deuterium and Oxygen-18 in the Water Cycle. (J.R. Gat, R. Gonfiantini, Eds) Technical Reports Series 210, IAEA, Vienna, 103-142

Evidence of pre-Columbian settlements in the forest of the Tuxtla Volcanic Field, Veracruz, Mexico

Araceli Zamora-Camacho, Juan Manuel Espíndola[*], Peter Schaaf, Angel Ramírez, María de Lourdes Godínez Calderón

Resumen

El campo volcánico de los Tuxtlas se localiza en el margen occidental del Golfo de México, en el estado de Veracruz, México. El campo está compuesto por cuatro grandes estructuras volcánicas y cientos de conos volcánicos, domos de lava y maares. En el pasado, el área estuvo cubierta por una densa selva en cuyos márgenes florecieron varias de las antiguas ciudades del Veracruz central y meridional. En el interior del bosque no se han encontrado ruinas arqueológicas, aunque los actuales habitantes del área encuentran frecuentemente fragmentos de cerámica que atestiguan la presencia de lo que pudieron ser pequeños asentamientos con un régimen seminómada. Desafortunadamente los objetos hallados son removidos de su sitio y son difíciles de fechar. Sin embargo, en el curso del estudio de los depósitos volcánicos del área se reconocieron cuatro unidades litoestratigráficas distintas relacionadas con eventos de flujos de lodo en cuyo interior se encontraron objetos y fragmentos de cerámica y en algunos de ellos carbón. Secciones de los depósitos fueron observados en detalle y muestreados para su análisis granulométrico y datación. Las muestras de carbón fueron datadas por medio de métodos estándar de radiocarbono (C-14) y las muestras de cerámica por la técnica de termoluminiscencia (TL). Las muestras arrojaron edades de 1176±100 (TL) años antes de ahora (BP, por sus siglas en inglés), 1385±70 años BP, 1157±105 (TL) años BP, y 2050+245-235 (C-14) años BP. Dado que dentro de la selva no existen materiales adecuados para la producción de cerámica, su procedencia es incierta; las ciudades prehispánicas mas grandes y cercanas se localizan hacia el occidente del campo volcánico (Tres Zapotes y Matacapan).

Palabras clave: Campo volcánico de los Tuxtlas, fechamiento de cerámica por Termoluminiscencia, Mesoamérica Precolombina.

J. M. Espíndola[*]
P. Schaaf
A. Ramírez
Instituto de Geofísica
Universidad Nacional Autónoma de México
Ciudad Universitaria,
Delegación Coyoacán, 04510
México D.F., México
[*]Corresponding autor: jmec@unam.mx

M. L. Godinez[3]
Universidad Nacional Autónoma de México
Instituto de Geografía
Universidad Nacional Autónoma de México
Ciudad Universitaria,
Delegación Coyoacán, 04510
México D.F., México

A. Zamora-Camacho
Centro de Sismología y Volcanología de Occidente
Centro Universitario de la Costa
Universidad de Guadalajara
Av. Universidad 203
Delegación Ixtapa, 48280
Puerto Vallarta
Jalisco, México

A. Zamora-Camacho, J. M. Espíndola, P. Schaaf, A. Ramírez, M. L. Godínez

Abstract

The basaltic Los Tuxtlas Volcanic Field (LTVF) is located at the western margin of the Gulf of Mexico in the State of Veracruz, Mexico. The field is a massif composed of four large volcanic structures and hundreds of scoria cones, lava domes and maars. This area was in the past covered by a dense forest in whose margins flourished several of the ancient cities of importance in central and southern Veracruz. Within the forest no enduring archeological ruins have been found; but the present inhabitants of the area frequently find fragments of ceramics and stone that attest to the presence of what could have been small settlements with a seminomadic regime. Unfortunately the objects found have been removed from their emplacement and are difficult to date. However in the course of our study of the volcanic deposits in the area we found four mudflow deposits containing pre- Columbian pottery objects and shards, as well as charcoal in some of them. Sections of the deposits were observed in detail and sampled for granulometric analysis. The charcoal samples were dated using standard radiocarbon methods (C-14); where charcoal was absent the pottery shards were dated with thermoluminescence (TL) techniques. The samples from these sites yielded ages of 1176±100 years BP (TL), 1385±70 BP years (C-14), 1157±105 years BP (TL), and 2050+245-235 years BP (C-14). Since in the area there is no clayey and silty material suitable for production of pottery; the closest and largest prehispanic cities, *Tres Zapotes* or *Matacapa*, are located to the west of the LTVF..

Key words: Tuxtla volcanic field, Thermoluminescence dating in ancient ceramics, Precolumbian mesoamerica.

Introduction

The basaltic Los Tuxtlas Volcanic Field (LTVF) also known as Tuxtla Volcanic Field, and Los Tuxtlas Massif, is located in the Mexican State of Veracruz (Figure 1), where it emerges from the lowlands of the western margin of the Gulf of Mexico. Composed of four large volcanoes and more than 250 cones and maars, it spans approximately 200,000 km2 an area known as *La region de los Tuxtlas* (Los Tuxtlas Region). Nelson and Gonzalez-Caver (1992) dated the rocks of the LTVF, and found that they can be grouped in two age groups separated by a hiatus of about 1.8 Ma, they dubbed these groups as the 'Older Volcanic Series' (OVS; 7 to 2.6 Ma BP) and the 'Younger Volcanic Series' (YVS; 8Ka BP–Present). Nelson *et al*. (1995) found that in the LTVF alkaline rocks are prevalent, although not unique, and considered that some rocks of the LTVF had signatures of subduction related to the Cocos plate. Nevertheless researchers such as Verma (2006) consider that the origin of the LTVF is not related to the subduction of the Cocos plate thereby the problem of its origin is still unsolved. In this paper we will focus in an area surrounding San Martin Tuxtla volcano, which constitutes most of the YVS (Figure 1). Due to the fertility of the soils formed from the basaltic rocks and heavy rainfalls, the area covered by rocks of the younger series, is nowadays the center of a 1551.2 km^2 forest reserve (Figure 1). In the past, however, the rainforest covered the entire volcanic field and beyond. At the margins of the LTVF important pre-Columbian settlements of different cultures flourished. To the west, the city of *Tres Zapotes* was occupied by the Olmec and later cultures for almost two millennia (900 BC to 900 AD). Some 30 km to the east, the city of *Matacapan* had also a long occupational history. Apparently, the site was first occupied during the Pre-classic period but it thrived in the classic and late classic periods (~100 AD -900AD), when it had a "key role in the trading network dominated by Teotihuacan", the dominant culture in central Mexico in those times (Santley *et al.*, 1984; Diehl, 2000). Smaller archeological constructions have been found to the southeast of the volcanic field and on the western side of Catemaco lake, but none in the area surrounding San Martin Tuxtla (Figure 2). However, in that area the villagers have found numerous artifacts in stone and ceramics, which being removed from its original place are difficult to date or conjecture about their emplacement. Looking for evidence about possible pre-Columbian settlements in those areas we were able to find pottery shards and charcoal fragments in four mudflow deposits. The pottery fragments correspond to the domestic type of pottery, which does not allow its cultural identification, but their age can be determined through thermo-luminescence methods. In this paper we present the general characteristics of the deposits were the objects were found, of the fragments and their ages whenever possible. We believe this findings are relevant to the historical and environmental studies on the area.
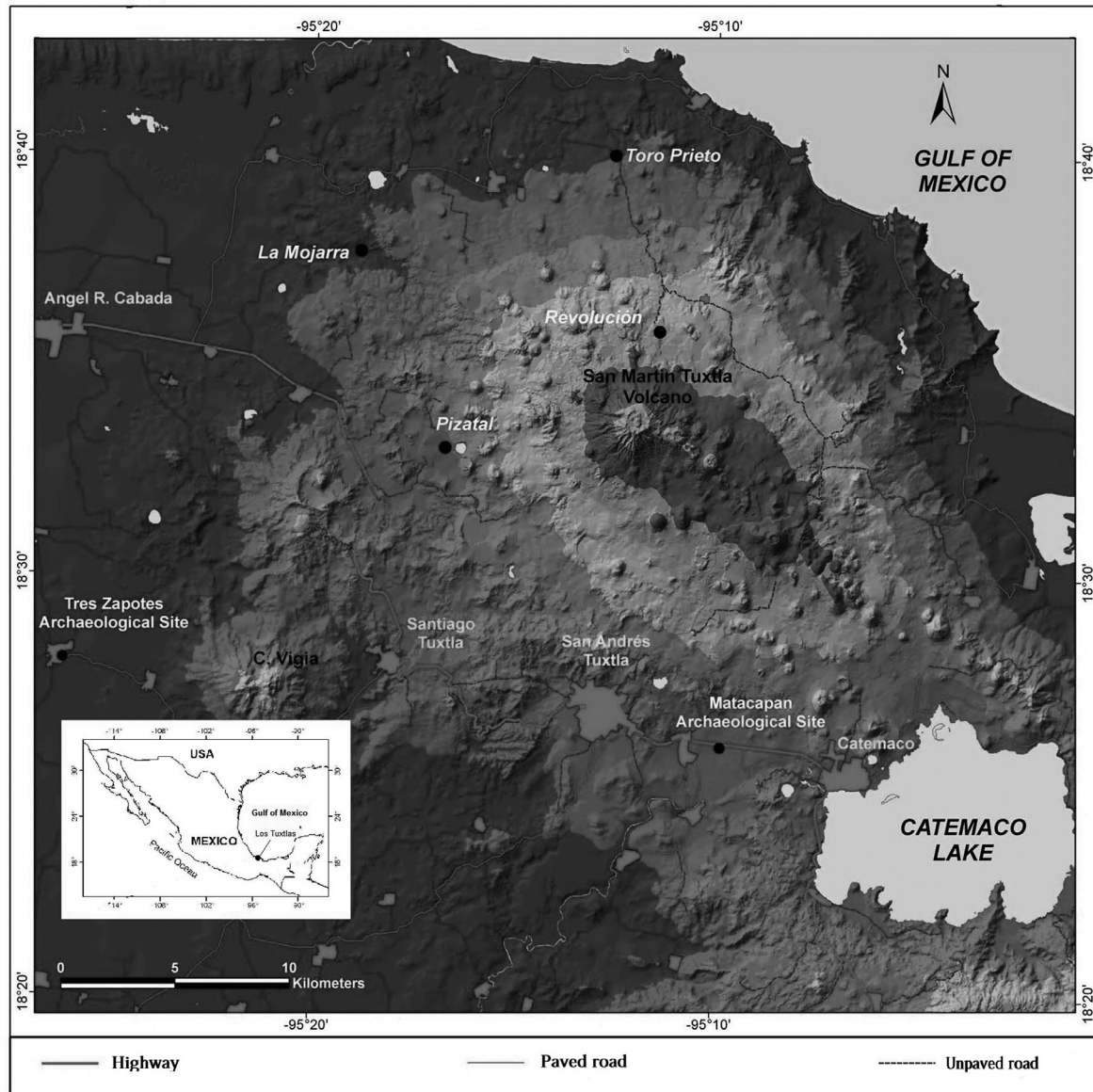
Figure 1. Location of Los Tuxtlas Volcanic Field and study sites: Revolución de Arriba, Pizatal, La Mojarra and Arroyo Toro Prieto.

Geographical characteristics of the LTVF

The LTVF has a tropical climate influenced by the trade winds of the northern hemisphere, which bring a significant precipitation during the summer season. In addition, rainfalls occur also at other times firstly because tropical storms and hurricanes extend the rainy season into the fall, and secondly because during the winter season the displacement of cold air masses from the north also cause precipitations (Gutiérrez García and Ricker, 2001). The average mean temperature is 25° and the average annual precipitation goes from 805 mm at the town of R. Cabadas to 1962 mm at Catemaco, with peak intensities greater than 400 mm (Gutiérrez García and Ricker, 2011). Most of the original forest was converted into farmland either to grow sugar cane or pasture for livestock. In fact, the first sugar cane plantation in Mexico was established in the nearby lowlands to the west by Don Hernán Cortés, the Spanish conqueror. As mentioned before nowadays an area of 15.1 km2 centered at San Martin Tuxtla Volcano has been declared Biosphere Reserve under UNESCO's Man and Biosphere Program (SEMARNAP, 1998). The area constitutes a
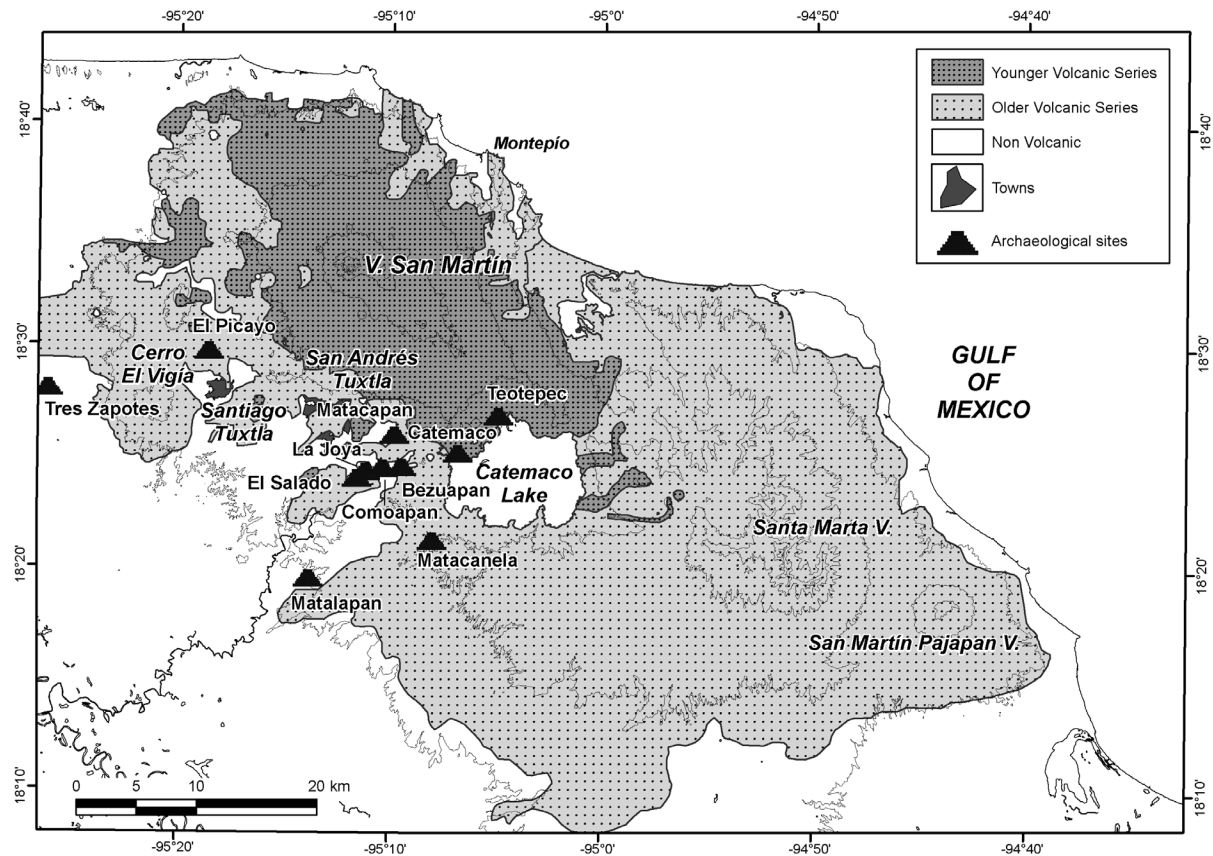
Figure 2. Generalized geology and archaeological sites at Tuxtla Volcanic Field (Geology modified after Nelson and González-Caver, 1992; Archaeological sites after Santley *et al.*, 1984).

conjunction of the northernmost tropical forest, the temperate forest of central Mexico and the endemic environment. Therefore, it became the habitat of a large diversity of species both animal and vegetal, which unfortunately have diminished with time (González-Soriano *et al.*, 1997). The drainage for the area is provided by numerous streams in a radial pattern with center in San Martin Tuxtla volcano most of them intermittent but also a few perennials fed by the numerous springs in the area. The soils of the Region, mostly andisols and alfisols, were derived from the basaltic products of the many eruptions in the Field; its formation is very rapid due to the large precipitations and tropical climate (Flores-Delgadillo, 1999). The landforms of the Region are predominantly lava and scoria domes and cones, maars and four large composite volcanoes. The slopes of Volcanoes San Martin Tuxtla, Cerro el Vigia, The Santa Marta complex, and San Martin Pajapan are slanted at different angles acquired during their formation and subsequent erosion. In the region of study, San Martin Volcano, the tallest

of all, has been classified as shield volcano (Simkin and Siebert, 1994) and is composed of lava flows, and ash and lahar deposits. This volcano presented the latest stage of volcanism with an eruptive event in 1793, which lasted more than 6 months in its explosive stage and about 2 years in an effusive phase (Espindola *et al.*, 2009). The cones of the study area (YVS) show height to base diameter ratios between 0.125 and 0.18. These values correspond to heights between 20 and 240 m with an average value of 80 m. These data suggests that the cones of this area are less than 50,000 years old (Reinhardt, 1991).

Characteristics of the Mudflow deposits and objects collected

Figure 1 shows the locations were mudflows with pottery shards were found, these were named: "Revolución de Arriba", "La Mojarra", "Pizatal", and "Arroyo Toro Prieto". Deposits at those locations exhibit the following characteristics:

Revolución de Arriba Mudflow Deposit (Site 1: 18° 35.871', 95° 11.401)

It is located some 300 m to the SE of the village of *Revolución de Arriba* it is a brown, whitish brown when dry, massive deposit with dispersed centimeter sized fragments of dark red scoria, small pieces of charcoal and pottery shards (Figures 3a, b). A few hundred meters to the east of this site (Site 2: 18° 35.825', 95°11.356') another similar outcrop is found under a layer of reworked gray ash. This deposit contains more abundant potshards and charcoal (Figure 3c). The pottery shards are centimeter-sized fragments of very coarse pottery. The proximity to the previous site and the similarity in age suggests that both sites belonged to the same settlement. Both sites are located close to the margin of an intermittent stream. The grain size distribution of this deposit is shown in (Figure 3d). The amount of clay size particles varies between 6% and 12% of the total and we therefore the deposit can be considered as non-cohesive (Scott, 1988).

La Mojarra Mudflow Deposit (Site 2: 18° 37.711'; 95° 18.860')

It is located in the outskirts of the village of La Mojarra (note that this is not the same town where the famous Stella 1 of early

Mesoamerican origin was found, which in Figure 1 appears farther west). The deposit covers the margins of a perennial stream crossed by a road in whose lateral cuts it is exposed (Figures 4a, b). It is reddish brown, massive with dispersed fragments of whitish, angular cobbles, and abundant pottery shards, some of which could be reassembled into a complete bowl-like piece of pottery (Figure 4c). A few obsidian blades were also present. The deposit is also non-cohesive since its grain size distribution, shown in Figure 4d; presents only a 3% amount of fines. However the presence of a horizon of several tens of centimeter blocks gives the impression in some parts of being a debris flow.

Pizatal Mudflow Deposit.(Site 3: 18°37.711', 95° 18.860')

This deposit is located near Pizatal (also spelled Pisatal) crater lake, a maar of about 500 m in diameter, and covers an extension on which sugar cane is nowadays planted (Figures 5a, b). The deposit is exposed on the sides of the road, which is leveled every year to facilitate the transportation of the sugar cane by trucks; it is brown, light brown when dry, massive, with some rounded pebbles. The deposit contains many pottery shards, some of them from more elaborate artifacts than in the above deposits,

a)

b)

c)

d)
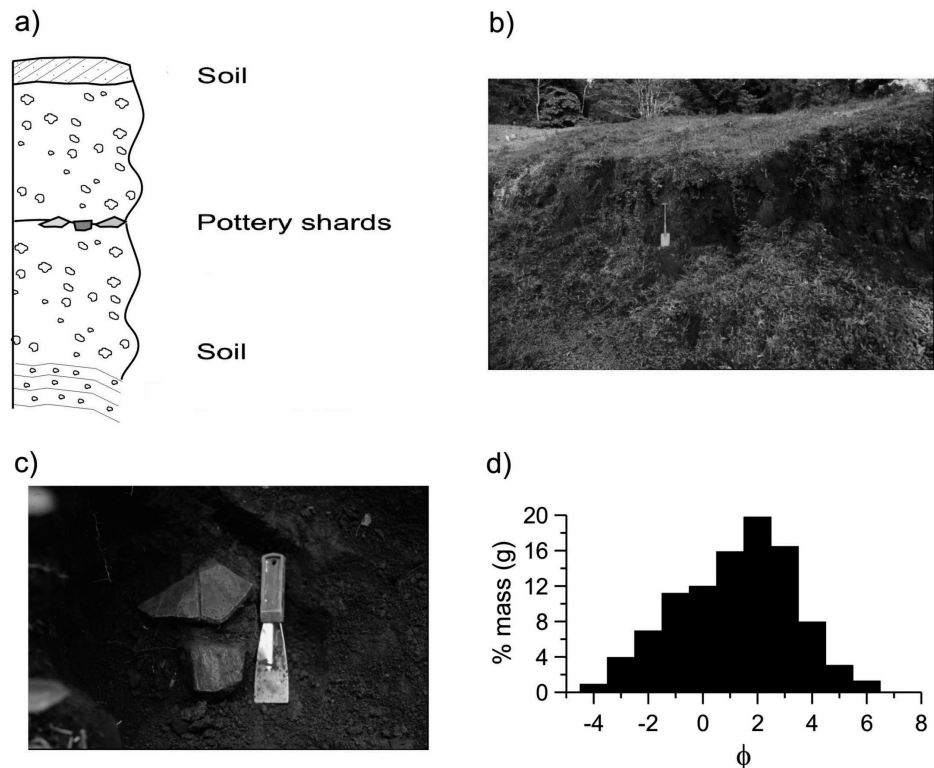
Figure 3. Revolución de Arriba. (a) Schematic section of the deposit. b) Aspect of the deposit. The insert shows some of the fragments collected at this site. (c) Granulometry of the deposit
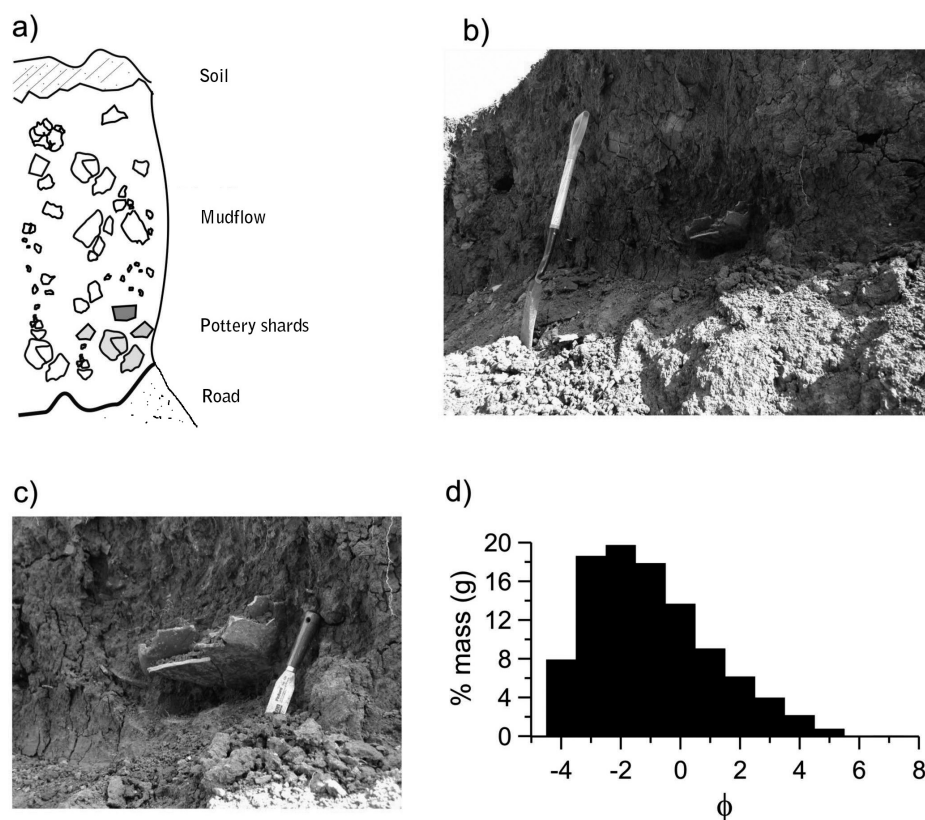
Figure 4. La Mojarra. (a) Schematic section of the deposit. (b) Aspect of the deposit. The insert shows some of the fragments collected at this site. (c) Granulometry of the matrix of the deposit at La Mojarra.

for instance Figure 6c shows what seems to be a bottle stopper in the shape of an animal's head. Findings like this are frequent, mostly after heavy rains, according to villagers of the nearby towns. This deposit might originate from overspills from the Pizatal crater lake, an event that occurred even in recent times. The grain size distribution of the deposits appears in Figure 5d, and the amount of fines is 19%. Unfortunately this deposit could not be dated by radiocarbon, since we could not find any charcoal sample, and the thermoluminescence results did not provide a reliable age due to the failure of the additive dose procedure, probably as a result of a non-favorable composition of the ceramic.

Arroyo Toro Prieto Mudflow Deposit (Site 4: 18° 38.229', 95° 12.037')

This deposit forms the banks of the intermittent *Arroyo Toro Prieto* stream, and is exposed by a deep trail cutting across the banks and riverbed. The deposit is brown and massive (Figures 6a, b). It contains small fragments of charcoal and some brittle, centimeter-sized, scattered pottery fragments with very rounded edges (Figure 6c). Even from its appearance this deposit seems to be older than the other deposits. Its grain size distribution is shown in Figure 6d, with an amount of fines of 13%.

Dating methods

The charcoal samples were collected in aluminum sheets and sent for dating to the Laboratory of Isotope Geochemistry of the University of Arizona, Tucson, Arizona, USA where they were dated using beta counting techniques (Table 1). The thermoluminescence analyses on pottery shards were carried out by the authors at the Laboratory of Thermoluminescence of the Instituto de Geofísica at UNAM (Spanish acronym for the National Autonomous University of México). The samples were collected from the inside the deposits at about 30 cm from the surface exposed to the light and deposited immediately in thick black plastic bags. The U, Th and K concentrations in the matrix surrounding the samples were measured *in-situ* for annual dose rate determinations in with a portable gamma ray spectrometer. The laboratory treatment of the samples is explained in Ramirez *et al*. (2010). In our particular case the correction for water content was made considering water saturation in the samples because of the high rainfall rates at the TVF region. The amount of water in the samples was determined from the difference in weight between dried and water saturated samples. As an example of the TL analyses leading age calculation Figure 7 shows the natural TL curve of sample SM03-8.

The plateau test for verification of the stability region of the spectrum is displayed in Figure 8, which in this case is between 275°C and 425°C. Figure 9 shows the results of the additive dose method for calculation of the equivalent dose (Q). The results for the supralinearity correction are shown in Figure 10.

Results

The results of the C-14 and thermoluminescence analyses are shown in Tables 1 and 2. The pottery shards from Arroyo Toro Prieto and Pizatal did not yield results amenable to sound estimates of the age, except to rule them out as modern. The ages provided by the samples show that the deposits are as old as 1000 years and 2050 (+245 -235) BP. The last age corresponds to the arroyo Toro Prieto deposit and agrees very well with its characteristics, with less, small, rounded and very soft shards suggesting an older age than the age of the other ceramics. At the two close sites of *Revolución de Arriba* we obtained TL ages 1157±105, 1156±80 and 843±50 BP and C-14 ages 1385±70, 1555±70. The differences in age are significant but can be attributed to several causes, the C-14 ages were taken from samples of charcoal of unknown origin, probably from logs of aged trees. The sample with the younger TL age (843±50 BP), having

been collected from the upper part of the deposit could have been deposited and closed to light at a much later date. The same can be said of the samples from la Mojarra, which yielded ages of 1 697±65 the sample collected from the lower part of the deposit and 1 176±100 the sample from the upper part.

Discussion and conclusions

The presence of the objects described attest to the presence of human activity in the forest. Since the objects are varied, have remained to this day and were located close to riverbeds it is reasonable to assume that the human presence occurred in small settlements in the forest, and that they carried out a seminomadic regime or else more enduring constructions could be found. The objects themselves indicate that: (a) these people traded goods with places where ceramics and obsidian could be obtained, (b) seems reasonable to think that other settlements were present at those times but due to their regime of life no material remaining of their presence has been preserved The ages obtained belong roughly to two periods in the historian's scheme of Mesoamerica. The age of the deposit Arroyo Toro Prieto falls at the beginning of the classical or late pre-classic period, when the Olmec culture had been reduced to Tres Zapotes
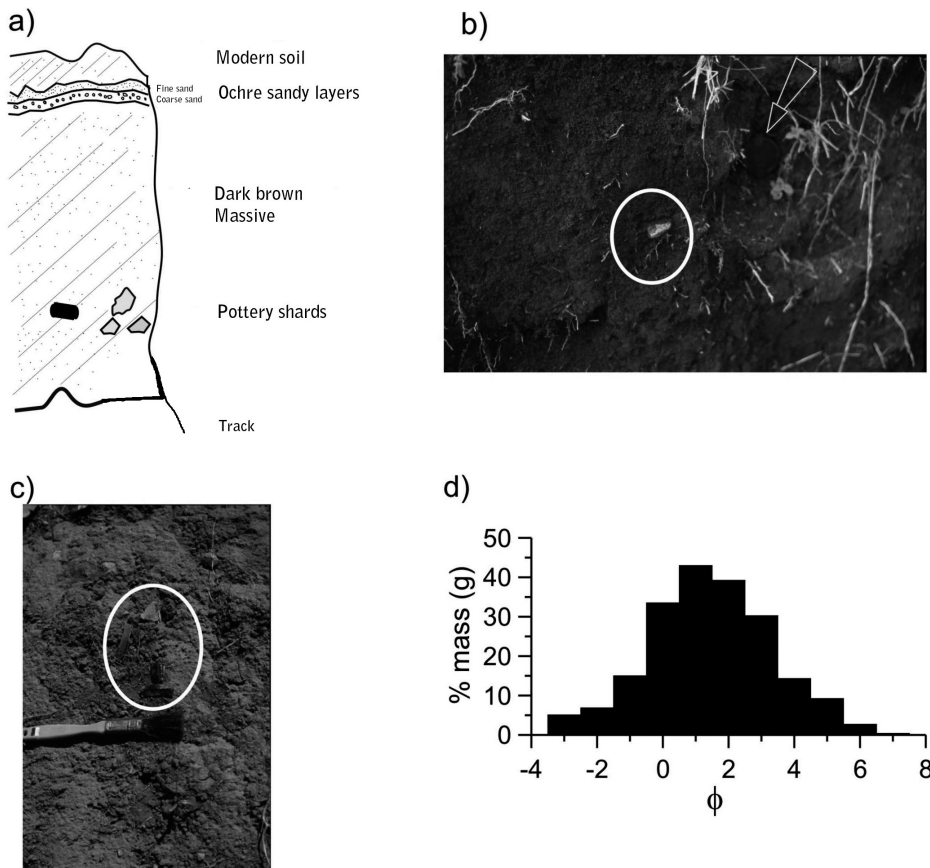
a)

b)

c)

d)
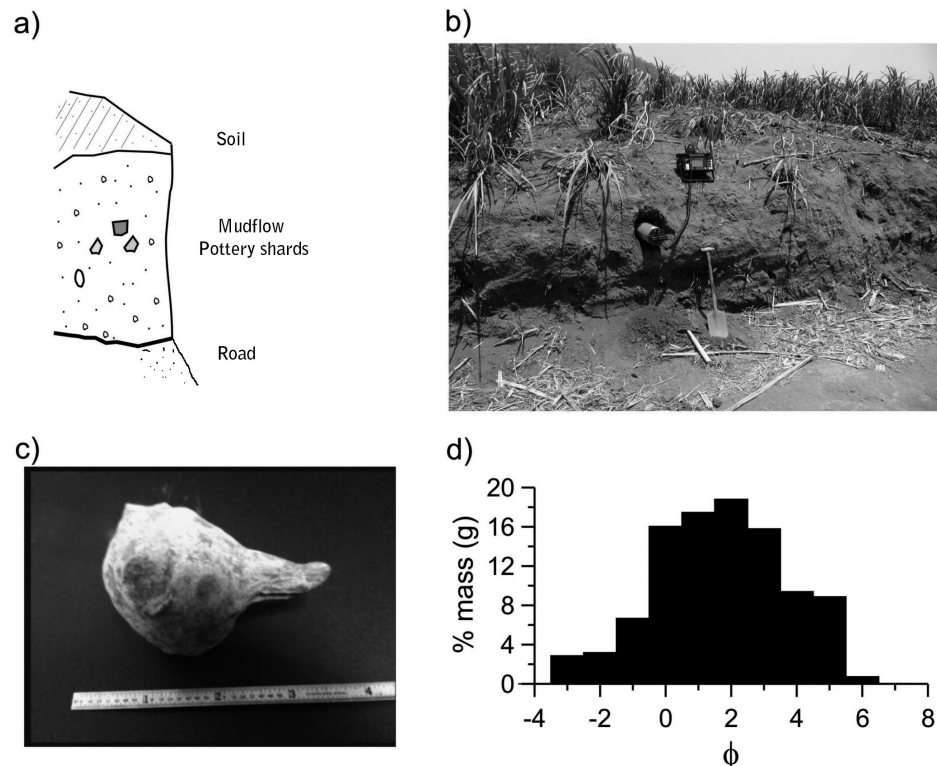
Figure 5. Lago Pizatal. (a) Schematic section of the deposit. (b) Aspect of the deposit. The insert shows some of the fragments collected at this site.(c) Granulometry of the matrix of the deposit.

Tabla 1. Radioisotope concentrations in soil and samples.

|	Ceramic			Soil		
	[238]Uranium [ppm]	[232]Thorium [ppm]	[40]Potassium [%]	[238]Uranium [ppm]	[232]Thorium [ppm]	[40]Potassium [%]
SM03-6 INF	5.120	5.780	0.987	0.530	6.430	0.250
SM03-6 SUP	5.150	5.420	0.690	0.530	6.430	0.250
SM03-8	5.840	9.600	1.441	0.370	4.000	0.150
SM03-9-INF	6.060	8.950	1.590	0.390	4.330	0.160
SM03-9-SUP	6.200	6.370	0.950	0.390	4.330	0.160

(Pool, 2007). The samples from the other three sites belong to the post classic period well within the era of increasing ruralization of the population in the Matacapan area (Santley *et al.*, 1984). These data suggest that the occupation of the forest surrounding the San Andres Tuxtla volcano area by small human settlements occurred some 2000 years BP and roughly 1000 years BP as well. Some of these settlers were probably driven out of the forest by the volcanic activity of San Martin volcano or any of the hundreds of monogenetic vents

in the field. According to the chronicler of San Andrés Tuxtla, Medel y Alvarado (1963), an eruption from San Martin Tuxtla in 1530 led to the foundation of today's Santiago Tuxtla. Although there is no evidence to this claim, but old narratives picked up by this author, it would not be an uncommon episode: However, there is proof that in the last 2000 years at least 3 cone and maar forming eruptions occurred near Matacapan, leaving deposits in the site and its surroundings (Reinhardt, 1991). Due to the heavy precipitation in the

Figure 6. Arroyo Toro Prieto (a) Schematic section of the deposit. (b) Aspect of the deposit. The insert shows some of the fragments collected at this site.(c) Granulometry of the matrix of the deposit.

Figure 7. Natural thermoluminescence of sample SM03-8.
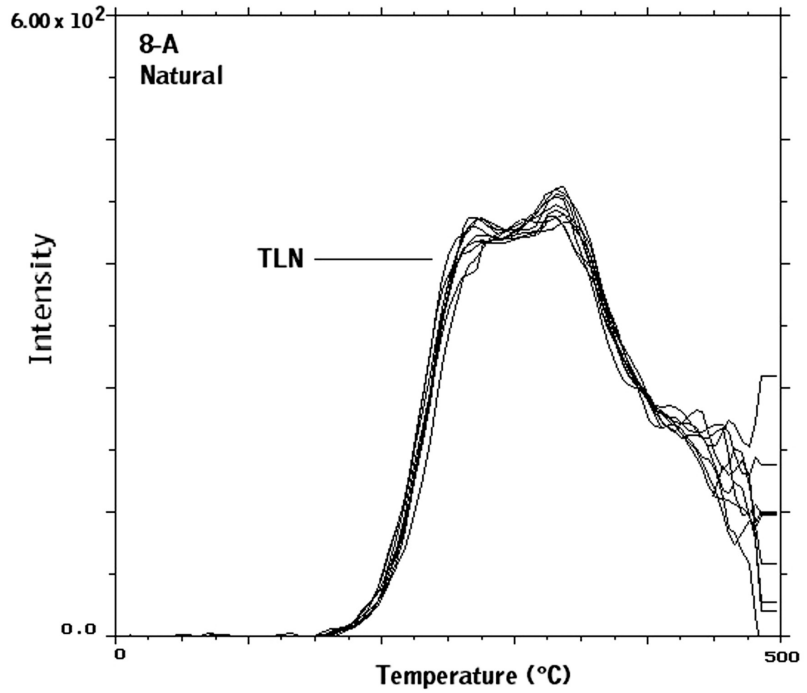
Figure 8. Plateau test for verification of the stability region of the spectrum, which for sample SM03-8 is between 275°C and 425°C.
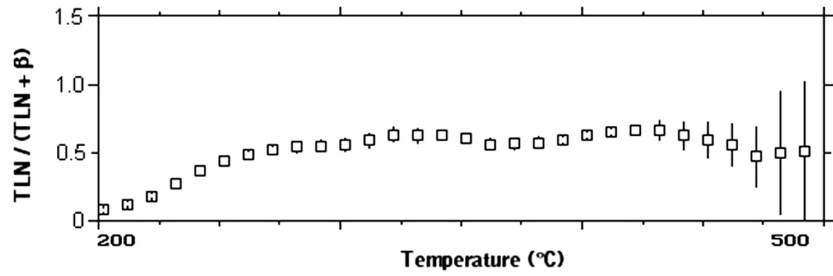
Figure 9. Results of the additive method for calculation of the equivalent dose (Q).

Figure 10. The results for the supralinearity correction.

Table 2. Radiocarbon and Thermoluminescence ages and other relevant data.

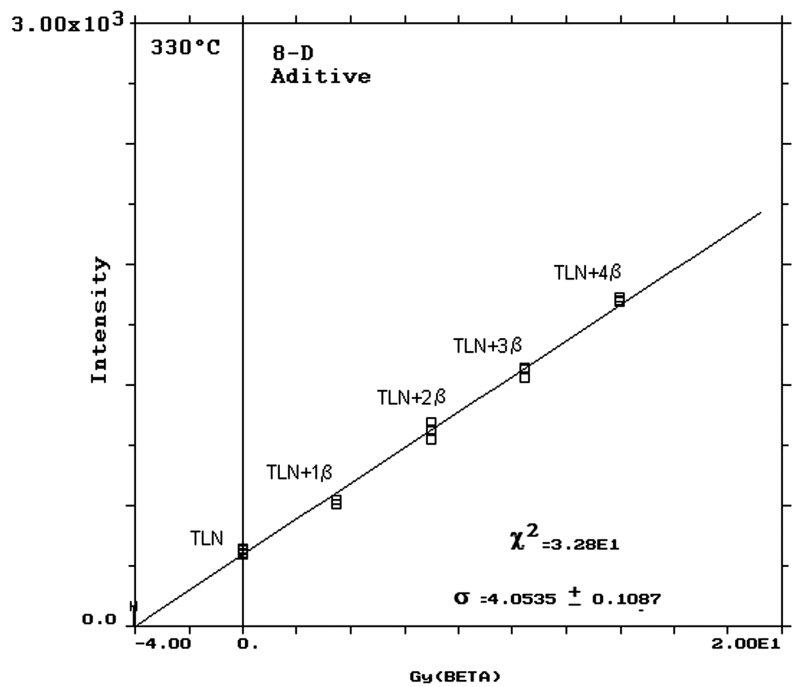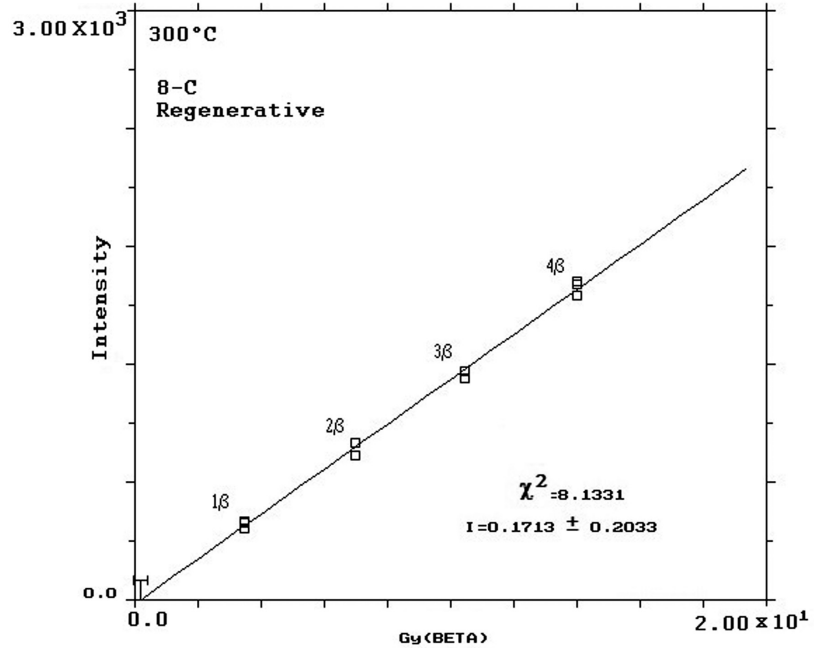| Sample	Paleodoses (Gy)	Anual Dose Rate (Gy/año) (1x10^{-3})	Age (years)	Site	Radiocarbon*	UA Sample Number*
SM03-5SUP	X	X	Not modern	Pizatal	X	
SM03-6INF	5.53±21	3.257±.09	1 697±65	La Mojarra	X	
SM03-6SUP	3.64±.31	3.094±.06	1 176±100	La Mojarra	X	
SM99-5INF			X	Revolución de Arriba site 1	1385±70	A-11104
SM03-8	4.16±.38	3.595±.08	1 157±105	Revolución de Arriba site 1	1555±70	A-11105
SM03-9INF	4.40±.30	3.806±.09	1 156±80	Revolución de Arriba site 2	X	
SM03-9SUP	3.92±.24	4.650±.09	843±50	Revolución de Arriba site 2	X	
SNM02-20	X	X	Not modern	Toro Prieto	2050+245-235	A-12647**

*Dating was carried out at the Laboratory of Isotope Geochemistry, Department of Geosciences, The University of Arizona, Tucson, Arizona
** counted 4000 minutes

area those communities were also subjected to flooding and mudflow hazards. The presence of numerous mudflow deposits in the edifice of San Martin Volcano indicate that this phenomenon is recurrent and continues into our days. The non-cohesive nature of the deposits indicates that the mass movements are due to unstable non consolidated materials.

Acknowledgments

References

Diehl R.A., 2000, Pre Columbian Cultures of the Gulf Coast. In: Adams, R.E.W., MacLeod, M. J. History of the Native Peoples of the Americas. V. 2, Mesoamerica, Cambridge University Press. Cambridge, ISBN: 9780521351652.

Espíndola J.M., Zamora-Camacho A., Godínez M.L., Schaaf P., Rodríguez-Elizarraras S., 2009, The 1793 eruption of San Martin Tuxtla volcano, Veracruz, México. *Journal of Volcanology and Geothermal Research*, 1, 1, 1-21.

Flores-Delgadillo L., Sommer-Cervantes I., Alcalá-Martínez J.R., Álvarez-Sánchez J., 1999, Estudio morfogenético de algunos suelos de la región de Los Tuxtlas, Veracruz, México. *Revista Mexicana de Ciencias Geológicas*, 16, 1, 81-88.

Gutiérrez García G., Ricker M., 2001, Climate and climate change in the region of Los Tuxtlas (Veracruz, Mexico): A statistical analysis, *Atmósfera,* 24, 4, 347-373.

González Soriano E., Dirzo R., Vogt R.C., 1997, Introducción General. in Gonzalez Soriano E., Dirzo R., Vogt R. C. (eds) Historia Natural de los Tuxtla, .Universidad Nacional Autónoma de México, México.

Medel y Alvarado L., 1963, Historia de San Andrés Tuxtla, Veracruz, 1532–1950, Primera edición facsimilar, 1993. Gobierno del Estado de Veracruz, México. 1, 13–132.

Nelson S.A., González-Caver E., 1992, Geology and K-Ar dating of the Tuxtla Volcanic Field, Veracruz, Mexico. *Bulletin of Volcanology* 55, 85-96.

Nelson S.A., González Caver E., Kyser T.K., 1995, Constraints on the origin of alkaline and calc-alkaline magmas from the Tuxtla Volcanic Field, Veracruz, Mexico. *Contrib. Mineral. Petrol*., 122, 191–211.

Pool C.A., 2007, Olmec Archaeology and Early Mesoamerica. Cambridge University Press, Cambridge, U.K., ISBN 978-0-521-78882-3.

Ramírez A., Schaaf P., Ortiz E., 2010, Analysis of Zapotec ceramics of the Caxonos River Basin, Oaxaca, Mexico, by Thermoluminescence (Tl). *Mediterranean Archaeology and Archaeometry*, 10, 121-127.

Reinhardt B.K., 1991, Volcanology of the younger volcanic sequence and volcanic hazards study of the Tuxtla volcanic field, Veracruz, Mexico, M.Sc. Thesis, Tulane University, 147 pp.

Santley R.S., Nelson S.A., Reinhardt B.K., Pool C.A., Arnold III P.J., 2000, When day turned to night. Volcanism and the Archeological Record from the Tuxtla Mountains, Southern Veracruz, Mexico. In: Bowden G, Reycraft RM (eds) Environmental disaster and the archaeology of human response. Albuquerque, Maxwell Museum of Anthropology, Anthropology Papers 7, pp 143–162.

Santley R.S., Ortiz Ceballos P., Killion T., Arnold P., and Kerley, J., 1984, Final Field Report of the Matacapan Archaeological Project: the 1982Season. Research Paper Series, No. 15, Latin American Institute, University of New Mexico, Albuquerque.

Scott K.M., 1988. Origins, behavior, and sedimentology of lahars and lahar-runout flows in the Toutle–Cowlitz river system. United States Geological Survey. Professional. Paper 1447-A, 74 pp.

SEMARNAP, 1998. Decreto de Reserva de la Biosfera, la región de Los Tuxtlas. Secretaría del Medio Ambiente, Recursos Naturales y Pesca, 23 de noviembre. Diario Oficial de la Federación DXLII (16), 6-21, Mexico.

Simkin T., Siebert L., 1994, Volcanoes of the World. Smithsonian Institution, *Geoscience Press Inc.*, Tucson, Arizona. 349 pp.

Verma S.P., 2006, Extension related origin of magmas from a garnet-bearing source in Los Tuxtlas volcanic field, Mexico. *Int. J. Earth Sci.,* 95, 871–901.

The 6 September 1997 (M_w4.5) Coatzacoalcos-Minatitlán, Veracruz, Mexico earthquake: implications for tectonics and seismic hazard of the region

Shri Krishna Singh*, Javier Francisco Pacheco, Xyoli Pérez-Campos, Mario Ordaz and Eduardo Reinoso

Resumen

Analizamos el sismo del 6 de septiembre de 1997 (M_w4.5), que se produjo a unos 25 km al SE de Coatzacoalcos, Veracruz. El sismo fue registrado por la estación local TUIG de banda ancha de (tiempo S-P = 5 s). Las polaridades de la onda P a distancias regionales y telesísmicas, y el modelado de las formas de onda de desplazamiento en TUIG sugieren un mecanismo focal inverso ($\phi = 150°$; $\delta = 70°$; $\lambda = 90°$). En la misma región ocurrió un sismo destructivo el 26 de agosto de 1959 (M_w6.4), a una profundidad similar y con un mecanismo similar. El análisis del sismo de 1997 refuerza la conclusión anterior de que la corteza inferior bajo la cuenca del Coatzacoalcos-Minatitlán, está en un régimen de esfuerzos de fallamiento inverso, en contraste con la parte superficial de la corteza que se caracteriza por un fallamiento normal; esto implica una permutación con la profundidad de los esfuerzos principales máximo y mínimo. Esto está de acuerdo con las observaciones, en otros sitios, que el estado de esfuerzos en las cuencas sedimentarias pueden ser diferentes del que se tiene a mayor profundidad.
Mecanismos focales están disponibles para siete sismos en y cerca del Golfo de México. Todos estos eventos muestran en la región una corteza media y baja en un régimen de fallamiento inverso. La tendencia observada de los ejes P de estos sismos se puede explicar por una o más de las siguientes causas: acoplamiento fuerte a lo largo de la interfase de la placa en subducción fuera de la costa en Tehuantepec; el movimiento absoluto de la placa de América del Norte; y el hundimiento de la litosfera debido a la acumulación de la carga de los sedimentos.
Usamos los registros del sismo de 1997 como función de Green empírica para simular los movimientos de tierra en la región epicentral de un sismo de M_w6.4 postulado en la cuenca Comalcalco. Bajo supuestos razonables, los valores esperados de aceleración, velocidad y desplazamiento picos son 120-260 gales, 12 a 28 cm/s, y 6 a 11 cm, respectivamente. La extensa licuefacción reportada en Coatzacoalcos durante el sismo de 1959, M_w6.4, sugiere que los sedimentos de la cuenca se comportan de manera no lineal bajo tal excitación.

Palabras clave: Sismo de Jáltipan, movimientos fuertes, tectónica del Golfo de México, peligro sísmico del Golfo de México.

S.K. Singh*
X. Pérez-Campos
Instituto de Geofísica
Universidad Nacional Autónoma de México
Ciudad Universitaria
Delegación Coyoacán, 04510
México D.F., México
*Corresponding author: krishnamex@yahoo.com

J.F. Pacheco
Observatorio Vulcanológico y Sismológico
de Costa Rica
Universidad Nacional

M. Ordaz
E. Reinoso
Instituto de Ingeniería
Universidad Nacional Autónoma de México
Ciudad Universitaria
Delegación Coyoacán, 04510
México D.F., México

Abstract

We analyze the 6 September 1997 M_w4.5 earthquake, which occurred about 25 km SE of Coatzacoalcos, Veracruz. The earthquake was recorded by the local broadband station TUIG (S-P time = 5 s). P-wave polarities at regional and teleseismic distances and modeling of the displacement waveforms at TUIG yields a thrust-faulting focal mechanism ($\phi = 150º$; $\delta = 70º$; $\lambda = 90º$). In the same region a destructive M_w6.4 earthquake occurred on 26 August 1959 at a similar depth and with a similar mechanism. The analysis of the 1997 event reinforces a previous conclusion that the lower crust beneath the Comalcalco basin is in a thrust-faulting stress regime, in contrast to the shallow part of the crust, which is characterized by normal-faulting; this implies a permutation with depth of the maximum and minimum principal stresses. It agrees with observations elsewhere that the state of stress in sedimentary basins can be different from the one at greater depth.

Focal mechanisms are available for seven earthquakes in and near the Gulf of Mexico. All of these events indicate a thrust-faulting type stress regime at mid- and lower-crustal levels. The observed trend of the P axes of these earthquakes can be explained by one or more of the following causes: strong coupling along the subduction plate interface offshore Tehuantepec; absolute motion of the North American plate; and downwarping of the lithosphere due to sediment loading.

By using the recordings of the 1997 event as empirical Green's function, we simulate the ground motions in the epicentral region of a postulated M_w6.4 earthquake in the Comalcalco basin. Under reasonable assumptions, the expected peak acceletion, velocity and displacement are 120-260 gal, 12-28 cm/s, and 6-11 cm, respectively. The extensive soil liquefaction in Coatzacoalcos during the 1959, M_w6.4, earthquake suggests that the sediments of the basin behave nonlinearly under such excitation.

Key words: Jáltipan earthquake, strong motion, tectonic of the Gulf of México, seismic hazards of the Gulf of México

Introduction

A detailed analysis of the M_w4.5 earthquake of 6 September 1997, which occurred near Coatzacoalcos-Minatitlán, Veracruz, is of interest for three reasons. First, the surface and the near-surface information from volcanic alignments, borehole elongations, and unpublished PEMEX seismic sections points to active normal-faulting in the region (Suter, 1991). The focal mechanism of an earthquake which occurred nearby on 26 August 1959 (M_w6.4), however, shows thrust faulting at a depth of about 26 km (Wickens and Hodgson, 1967; Suárez, 2000; see Figure 1). It is, therefore, of interest to know whether the 1997 earthquake confirms such a change in the stress regime (permutation of the least and maximum principal stresses) with depth in the region. In most regions, the stress regime at relatively shallow depth agrees with that at mid-crustal depth. There are some exceptions (see, e.g., Zoback and Zoback, 1991) and one such exception appears to be the coastal plain of the Gulf of Mexico (Frohlich, 1982; Zoback and Zoback, 1991; Suter, 1991). Another classical example is the decoupling of the stress field across the basal detachment of the Jura fold-thrust belt; the near-surface stress field is different from that in the basement (Becker *et al.*, 1987).

Second, the earthquake of 26 August 1959 caused serious damage to the towns of Jáltipan, Coatzacoalcos, and Minatitlán (Figueroa, 1964; Rosenblueth, 1964; Reséndiz, 1964). The latter two towns have become important industrial centers related to the intense activity of PEMEX, the national petroleum company, and population has grown by 22% in the last 10 years to reach more than half million people (INEGI, 2010). For this reason, it is important to estimate ground motions that may be expected in these towns if an earthquake, such as that of 1959, were to recur in the region. We may use the records of the 1997 earthquakes obtained at the near-source broadband station of TUIG as empirical Green's function to simulate the corresponding motions from an M_w6.4 event. Although the station is about 25 km SE of Coatzacoalcos-Minatitlán, the geology of these sites is roughly similar; to a first approximation, the results for the TUIG site may be valid for the entire region in case of an earthquake at about the same focal distance from TUIG as the event of 1997.

Finally, a study of the 1997 earthquake (and other events in and along the Gulf of Mexico) has an important bearing on the seismic safety of the Laguna Verde nuclear power plant (Figure 1) as well as the hydrocarbon exploration and production facilities in this region.

Figure 1. Earthquakes in and near Gulf of Mexico with known focal mechanism. Source parameters of the events are listed in Table 2. Focal mechanisms show that the mid- and lower crust of the Gulf is under compressive stress regime. Dotted lines indicate the bathymetry of the Gulf and gray dashed lines denote the limits of the buried salt deposits. LVPP = Laguna Verde Power Plant. Triangle shows location of station TUIG.
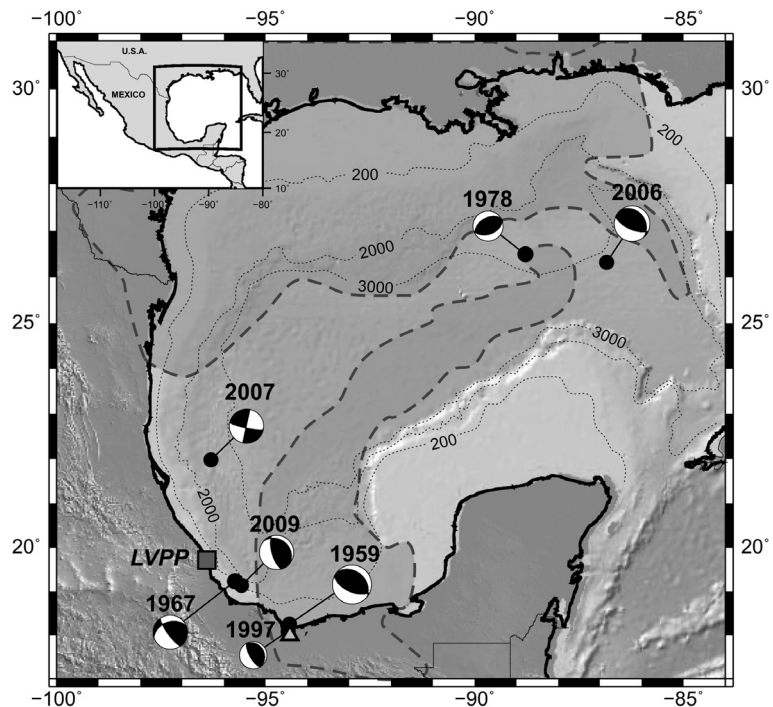

Data and analysis

The 1997 earthquake was recorded by the local broadband station TUIG (S-P time = 5 s) and by seven other broadband stations of the National Seismological Service (SSN), which were located at epicentral distances greater than 260 km. The reported coda-wave magnitude, M_c, is 4.3. The epicenter of the event, given by the SSN, is 18.146 ºN and 94.499 ºW. However, its focal depth could not be constrained. The epicenter and focal depth reported by the National Earthquake Information Center (NEIC), U.S. Geological Survey, are 18.017 ºN and 94.396 ºW and 33 km, respectively. This depth was fixed by NEIC in the location of the earthquake.

For moderate Mexican earthquakes it is now possible to obtain a regional centroid moment tensor (CMT) solution using relatively long-period regional waveforms (see, e.g., Pacheco and Singh, 1998). Unfortunately, the seismograms of the 1997 earthquake show little energy at periods greater than 10 s because of its relatively small magnitude. At shorter periods, a detailed three-dimensional crustal structure is needed to model the observed seismograms but is currently lacking for the region. For these reasons it was not possible to obtain a CMT solution by inverting the regional waveforms.

A single, near-source, three-component broadband recording can be used to find a reliable location, origin time, and focal mechanism of an earthquake, provided that a rough initial guess of the mechanism is available from other data (see, e.g., Kanamori *et al*., 1990; Singh *et al*., 1997, 2000a). The calculation of the location and origin time requires clear first arrivals on each of the three components of the ground motion as well as the knowledge of the local crustal structure. Figure 2 shows acceleration, velocity and displacement traces at TUIG during the 6 September 1997 earthquake. Figure 3 illustrates the initial part of the three components of displacement at TUIG. Note that the horizontal components have been amplified by a factor of 20. The incidence of initial P-wave at the station is nearly vertical. Nevertheless, it can be seen that the station is located in the NW quadrant with respect to the source. The amplitude towards west at time 0.172 s is 3.5 times that towards north. It follows that the station azimuth, ϕ_s, is 286º. Before proceeding further with the analysis of the source parameters of this earthquake, we summarize our knowledge of the local crustal structure.

Crustal structure of the region

The P-wave speed, α, in the shallow crust south and near Coatzacoalcos is available from
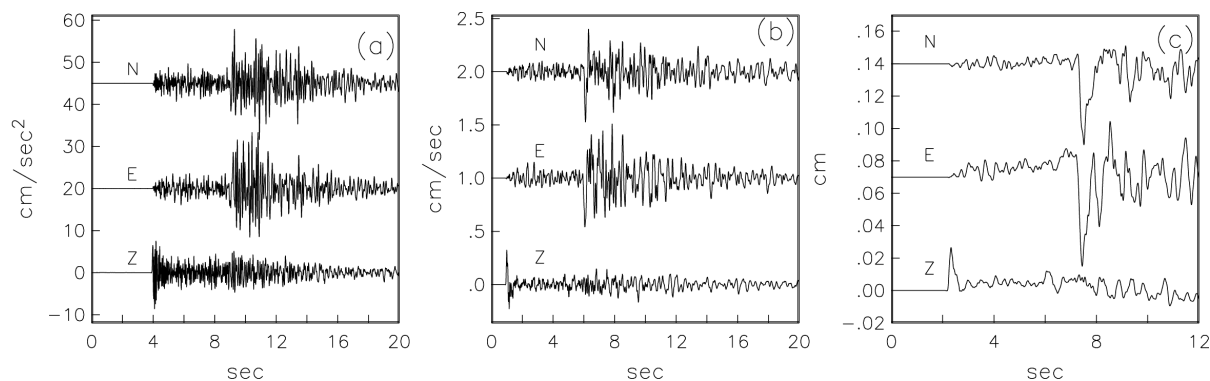
Figure 2. Seismograms at station TUIG during the 6 September 1997 earthquake. (a) Acceleration, (b) velocity, and (c) displacement. The traces in (b) and (c) have been obtained by integration of the accelerograms shown in (a).
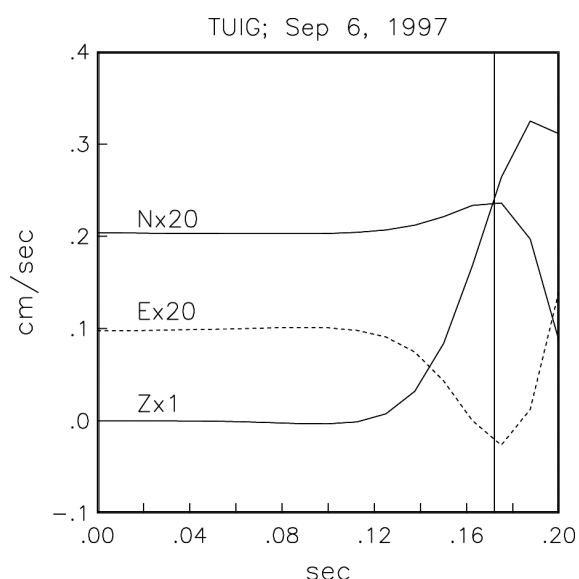
Figure 3. Initial part of the three components of displacement at TUIG. The horizontal components have been multiplied by 20.

exploration seismology carried out by PEMEX (A. Camargo, personal communication, 1997). The crust consists of a 1.8 km thick layer with α = 2.5 km/s, overlying a layer of α = 4.25 km/s. The thickness of the second layer exceeds 3.4 km, the maximum depth reached by boreholes.

Based on receiver function analysis, Cruz-Atienza (2000) reports sediment thickness of 16 km below TUIG. N. Shapiro (unpublished report) inverted group velocity dispersion curve corresponding to the region between the City of Oaxaca and TUIG. In the inversion, Shapiro fixed the thickness of the first layer and α values of the first and the second layers to the values given by PEMEX. The shear-wave speeds, β, of the first and second layers were taken as 1.4 km/s and 2.4 km/s, respectively. The crustal model adopted from the results of Cruz-Atienza (2000) and N. Shapiro, and used by us in generating synthetic seismograms, is given in Table 1. In this table, the densities and the quality factors, Q, of the layers have been taken arbitrarily; the results are not very sensitive to their choices.

Source parameters of the earthquake

Based on the crustal model in Table 1 and the (S-P) time of 5 s at station TUIG, the maximum depth of the earthquake, Hmax, assuming the station to be located directly above the focus, is 30.9 km. If the thickness of the second layer in Table 1 is taken as 10 km, then Hmax becomes 34.8 km. Near-vertical incidence at TUIG may be a consequence of both small epicentral distance as compared to the source depth, and refraction of waves caused by progressively lower seismic speeds near the surface.

Table 1. Crustal model near Coatzacoalcos used in the synthesis of ground motion.

Layer	Thickness km	P-wave speed α, km/s	S-wave speed β, km/s	Density gm/cm³	Quality Factor Q_α	Q_β
1	1.8	2.80	1.40	2.70	80	40
2	15.6	4.25	2.40	2.80	300	200
3	∞	6.50	3.75	2.85	400	300

Figure 4, top, shows P-wave first-motion polarities at those Mexican and teleseismic stations where they could be read unequivocally. These data suggest a thrust-faulting earthquake with possible strike-slip component. The first motion polarities provide some constrains on the azimuth ($140º ≤ \phi ≤ 190º$) and the dip ($45º ≤ \delta ≤ 85º$) of one of the nodal planes but the rake, λ, of this plane can vary between 35º and 120º. To determine the focal mechanism, we performed a waveform inversion of the displacement traces recorded at TUIG. For the inversion the event was approximated by a point-source shear dislocation. Synthetic seismograms include near- and intermediate-field contributions (Singh *et al*., 2000a). The effect of the free surface is approximately taken into account by multiplying the infinite-space synthetics by two. This approximation is acceptable if the epicentral distance, Δ, is smaller than the depth, H. We took the station azimuth, ϕ_s, as 286º, the take-off angle from the source, i_h, as 170º, and the angle of incidence at the surface, i_o, as 5º from

the vertical. Based on the observed P-pulse on the Z-component (Figure 2c), we chose a triangular source with duration, τ, of 0.38 s. We varied the azimuth, dip, and rake within the ranges mentioned above. No contradiction of the first motion polarities was allowed. The two nodal planes obtained from the inversion are: $\phi = 150º$; $\delta = 70º$; $\lambda = 90º$ and $\phi = 330º$; $\delta = 20º$; $\lambda = 90º$. The observed and synthetic seismograms are shown in the bottom left of Figure 4.

We generated synthetic seismograms corresponding to this focal mechanism and the crustal model given in Table 1. Bouchon's (1982) discrete wave number algorithm was used in the computation. We again took $\phi_s = 286º$ and $\tau = 0.38$ s. A good fit between observed and synthetic seismograms at TUIG was found for an epicentral distance of 7 km, a depth of 30 km, and $M_0 = 6.0\times10^{15}$ N-m ($M_w4.5$) (Figure 4, bottom right). Table 2 summarizes the relevant source parameters of this earthquake.
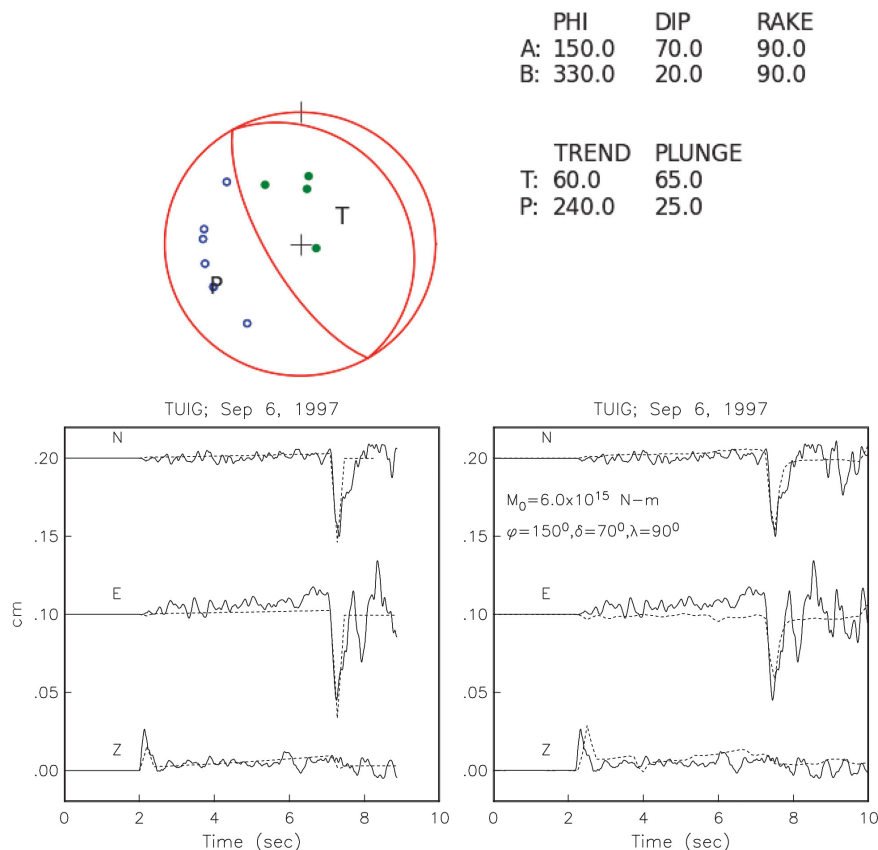
Figure 4. (Top) *P*-wave first motions of the 1997 earthquake plotted on lower-hemisphere, equal-area projection. With the exception of TUIG, all Mexican broadband stations recorded dilatation (open circles). Three teleseismic stations and TUIG show compression (solid circles). Focal mechanism, $\phi = 150º$; $\delta = 70º$; $\lambda = 90º$, which satisfies first-motion data, and the waveform at TUIG is shown. (Bottom, left) Comparison of observed and infinite-space synthetic seismograms at station TUIG. (Bottom, right) Comparison of observed and synthetic seismograms at station TUIG. Synthetics were computed using crustal model and focal parameters given in Tables 1 and 2, respectively.

Stress regime of the Gulf coast region of Coatzacoalcos-Minatitlán

In spite of some uncertainty in its focal mechanism, there is no doubt that the 1997 earthquake was a thrust event with, probably, some strike-slip component. Its source was below the Comalcalco basin at a depth of about 30 km. As mentioned earlier, the surface and the near-surface information from volcanic alignments, borehole elongations, and unpublished PEMEX seismic sections in the Gulf coast basin region of Coatzacoalcos-Minatitlán suggest active normal-faulting in the upper few kilometers (Suter, 1991). Thus, there is a change of stress regime from extension in the sediments of the upper crust to shortening in the mid- and lower crust indicated by focal mechanisms (Figure 1). A similar change of stress regime with depth is reported in the central Gulf of Mexico by Frohlich (1982) from an analysis of an earthquake in 1978 at the edge of the Mississippi Fan at a depth of 15 km (Figure 1). Other cases of stress change below sedimentary basins are discussed in Zoback and Zoback (1991). Extension in upper part of crust is probably controlled by gravitational load and major topographic gradient, at least in the adjacent Veracruz basin.

Table 2 lists seven intraplate earthquakes located in and near the Gulf of Mexico with known focal mechanisms. It includes the earthquakes of 1978 and 1997. The locations of these events and their focal mechanisms are illustrated in Figure 1. For the earthquakes of 2007 and 2009, more than one solution is available (Table 2). For these two earthquakes, the Global CMT location and focal mechanism is shown. As most intraplate regions, the Gulf is characterized by thrust-type stress regime (Zoback et al., 1989). The orientations of the P-axes of the 1959, 1967, 2006, 2007 and 2009 earthquakes range between N30ºE and N65ºE. These are consistent with reported offshore stress orientations near the same region, inferred from breakouts (Zoback et al., 1990; Suter, 1991; World Stress Map, http://dc-app3-14.gfz-potsdam.de/, 12 May 2015). These orientations fall between the directions of: (1) the relative convergence of the Cocos and North American plates and (2) the absolute motion of the North American plate. Perhaps both the relative convergence and the absolute motion are responsible for the observed P-axis, with the former playing a more dominant role for events in and near the SSW Gulf due to their relative proximity to the middle America subduction zone (earthquakes of 1959, 1967, 1997, and 2009) and the latter being dominant for the events of 2006 and 2007 which are relatively far from the plate boundary. For the 2006 earthquake, sliding of Sigsbee salt and landslide have also been suggested as possible causes (Nettles, 2007; Franco et al., 2013).

Table 2. Source parameters of earthquakes in and near Gulf of Mexico.

No.	Date	Latitude ºN	Longitude ºW	Depth km	M_w	Focal Mechanism ϕ'º	δ'º	λ'º
1[a]	26 Aug 1959	18.26	94.43	21	6.4	309	32	102
2[b]	11 Mar 1967	19.23	95.74	26	5.7	250	39	20
3[c]	24 Jul 1978	26.49	88.79	15	5.0	225	49	111
						240	63	52
4[d]	06 Sep 1997	18.08	94.47	30	4.5	330	20	90
5[e]	10 Sep 2006	26.32	86.84	30	5.9	324	28	117
6[e]	23 May 2007	21.98	96.31	24	5.6	102	80	-1
		(22.02	96.27	11	5.6	95	71	-16)[f]
		(21.98	96.14	44	5.5	106	83	8)[g]
7[e]	29 Oct 2009	19.14	95.58	17	5.7	310	25	59
		(18.95	95.69	16	5.4	288	26	4)[g]

[a] Location from International Seismological Summary, ISS; depth, focal mechanism, and M_w from Suárez (2000).

[b] Location from International Seismological Centre, ISC; depth, focal mechanism, and M_w from Suárez (2000).

[c] Location, depth, and focal mechanism from Frohlich (1982). The two mechanisms are extreme types consistent with first-motion data.

[d] This study.

[e] Global Centroid Moment Tensor (CMT) catalog.

[f] Source parameters listed in http://www.eas.slu.edu/eqc/eqc_mt/MECH.NA/20070523190916/index.html

[g] Franco et al. (2013)

Dewey and Suárez (1991) and Suárez (2000) suggest that the intraplate, mid- and lower-crust compression below the Comalcalco basin, as revealed by the 1959 and 1967 earthquakes, may be a consequence of strong coupling along the plate interface where the Tehuantepec ridge subducts below Mexico. This may also be true for the 1997 and 2009 earthquakes. If so, then, unlike subduction of many other ridges (Kelleher and McCann, 1976), the Tehuantepec ridge does not subduct aseismically. Since there is no clear evidence for major/great earthquakes in the Tehuantepec region during the last two centuries (see, e.g., Singh *et al*., 1981), it could mean that the recurrence period of such events in this segment is much greater than in other segments along the Mexican subduction zones where it is ~ 30 to 75 years (Singh *et al*., 1981; Astiz and Kanamori, 1984).

As for the 1978 Mississippi Fan earthquake (Figure 1), the P-axis does not follow the trend of the other events. The compressional nature of this earthquake was interpreted by Frohlich (1982) as a consequence of downwarping of the lithosphere due to sediment accumulation.

Expected ground motions in the Coatzacoalcos-Minatitlán region from a postulated M_w6.4 earthquake

The earthquake of 1959 destroyed a majority of the dwellings in the town of Jáltipan (Rosenblueth, 1964). Many buildings suffered structural or foundation failures in Coatzacoalcos and Minatitlán (Marsal, 1961; Reséndiz, 1964). The land near the port of Coatzacoalcos subsided. Some of the effects of the earthquake were attributed to partial liquefaction of sand and silt (Marsal, 1961). Modified Mercalli (MM) intensities in these towns during this earthquake were VIII (Figueroa, 1964). The 1959 earthquake was not an isolated event. The epicenter of the earthquake of 11 January, 1946 was apparently close to that of 1959 (Figueroa, 1964). The earthquake of 1946 was assigned a magnitude of 6.0 (Figueroa, 1970) and a MM intensity of VII in Coatzacoalcos (Figueroa, 1964). The towns of Coatzacoalcos and Minatitlán are now important centers of national petroleum activity. Thus, it is of significant earthquake engineering interest to estimate the ground motions in these towns during a future local M_w6.4 earthquake.

To estimate the ground motions from an M_w6.4 earthquake, we used the recording of 1997 earthquake as an empirical Green's function (EGF) and a method proposed by Ordaz *et al*. (1995) which is based on adding N scaled EGF records, each differed in time by a random delay. The probability distribution of the delays is such that, on average, the simulations follow an ω^2-spectral scaling at all frequencies. The method requires specification of the seismic moment, M_0, and the stress drop, $\Delta\sigma$, of both the EGF and the target earthquake. In our case, M_0 of the EGF is 6×10^{15} N-m and that of the target event is 5×10^{18} N-m (M_w6.4). A rough estimate of the static stress drop of the EGF can be obtained from the following considerations. For a circular rupture, the radius, a, of the fault can be estimated by (Boatwright, 1980):

$$a = (v\,\tau_{1/2})/(1 - v\sin\theta/c), \qquad (1)$$

where $\tau_{1/2}$ is the rise time of the far-field pulse, v is the rupture speed, c is the wave speed, and θ is the take-off angle measured from fault normal. For this event, $\tau_{1/2}$ is about 0.19 s (Table 2, Figure 2c). For S wave, $c = \beta$, which we take as 3.75 km/s (Table 1). Assuming $\phi = 330°$; $\delta = 20°$; $\lambda = 90°$ as the fault plane and $i_h = 170°$, θ is ~10°. For $v = 0.9\beta$, we obtain a fault radius $a = 0.76$ km (equation 1). For a circular fault, $\Delta\sigma$ is related to M_0 and a by (Keilis-Borok, 1959):

$$\Delta\sigma = (7/16)(M_0)/a^3, \qquad (2)$$

which gives $\Delta\sigma$ of ~ 6 MPa for the EGF. In the simulations, we take $\Delta\sigma$ of the EGF and the target event to be either 6 MPa or 12 MPa. Typical simulated acceleration, velocity, and displacement traces, corresponding to $\Delta\sigma = 6$ MPa for both events, are illustrated in Figure 5. In the figure, we compare deterministic, synthetic displacement seismograms with ones obtained by random summation of EGF. The synthetics were generated at TUIG for an event with $M_0 = 5\times10^{18}$ N-m (M_w6.4), located at the same focus as the 1997 earthquake, and having the same focal mechanism. The duration of the source time function, τ, of Mexican earthquakes is related to their seismic moment by

$$M_0 = (6.7\times10^{16})\tau^s \qquad (3)$$

(Singh *et al*., 2000b). Thus, the estimated τ for the target event is 4.2 s. A point source with a triangular source-time function of 4.2 s duration and the crustal structure given in Table 1 were taken for the computation. The *PGD* values are within a factor of two of each other. Both calculations show important near-field contribution (the ramp-like wave between P and S wave).
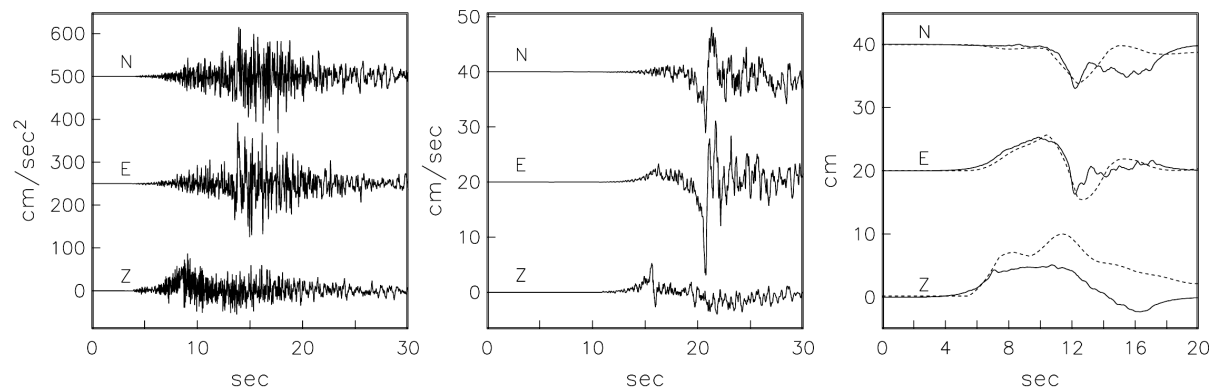
Figure 5. An example of simulated acceleration, velocity, and displacement traces in the epicentral region from a postulated M_w6.5 earthquake, using recording of the 1997 earthquake as empirical Green's function (stress drop of EGF = stress drop of target earthquake = 6 MPa). The right frame also shows, by dashed lines, the deterministic, synthetic displacement seismograms at TUIG for an M_w6.5 earthquake located at the focus of the 1997 event.

Results of simulation for various combinations of $\Delta\sigma$ are summarized in Table 3. The expected horizontal *PGA*, *PGV*, and *PGD* range between 120 and 260 gal, 12 and 28 cm/s, and 6 and 11 cm, respectively.

Although the ground motions estimated by random summation of the EGF are reasonable, there are several factors which introduce uncertainties in these results. The stress drop of the EGF event is uncertain and that of the target earthquake is assumed. The directivity of the source may give rise to greater or smaller ground motions than those computed by our method. Finally, a single EGF may not be adequate to sample the entire fault plane of an M_w6.4.

We emphasize that this synthesis of the ground motion is based on the assumption of linear elastic response of the sediments. Almost certainly the shallow sediments of the Gulf basin will behave nonlinearly under such excitation, as was the case during the 1959 earthquake. In view of the uncertainties, the observed ground motions may easily differ by a factor of 2 or 3 from the expected ones. This however is usually the case in ground motion predictions.

Conclusions

Our analysis shows that the 6 September 1997 earthquake (H = 30 km; M_w4.5), like the nearby earthquake of 26 August 1957 (H = 21 km; M_w6.4), was a thrust event. The event confirms a previous conclusion that while the upper sediments of the Gulf coast basins are in an extensional (normal fault-type) stress regime, the mid- and lower crust is in a shortening (thrust fault-type) stress regime (Dewey and Suárez, 1991; Suter, 1991), which implies a permutation between the vertical and maximum horizontal principal stresses. Upper crust is under extension probably because of gravitational loads and high topographic gradient; the stress field of middle to lower crust may be controlled by far-field loads at convergent plate margin and/or absolute plate motion.

Our estimation of ground motion in the epicentral region of Comalcalco basin due to a postulated M_w6.4 earthquake indicates that peak acceleration, velocity, and displacement (assuming linear behavior of the sediments) may be in the range of 120-260 gal, 12-28 cm/s, and 6-11 cm, respectively. These, then, are also

Table 3. Simulated peak ground motions for a postulated M_w6.4 earthquake using recordings of the 1997 earthquake as EGF.

Stres Drop, MPa EFG/Target	PGA, cm/s^2			PGV, cm/s			PGD, cm		
	N	E	Z	N	E	Z	N	E	Z
6/6	146	173	103	13.2	18.7	6.8	8.8	6.5	6.1
6/12	213	262	161	20.0	27.6	9.2	10.7	7.2	6.4
12/12	171	198	124	17.9	25.8	8.7	10.6	7.1	6.3
12/6	121	127	88	11.8	17.5	6.0	8.5	6.4	6.0

our estimations of the ground motions during the 1959, M_w6.4, earthquake. These estimations were obtained using 6 September 1997 event as an empirical Green's function under various simplifying, though reasonable, assumptions. They are valid for sites with local geology similar to that of station TUIG. The estimation of ground motions at other nearby sites, such as Minatitlán, may be calculated if their site responses are known. Subjected to such ground motions the sediments of the Gulf Coast are likely to behave nonlinearly and may liquefy, as was the case during the 1959 earthquake.

Acknowledgments

References

Astiz L., Kanamori H., 1984, An earthquake doublet in Ometepec, Guerrero, Mexico. *Phys. Earth Planet. Interiors*, 34, 24-45.

Becker A., Blümling P., Müller W.H., 1987, Recent stress field and neotectonics in the Eastern Jura Mountains, Switzerland. *Tectonophysics*, 135, 277-288, doi: 10.1016/0040-1951(87)90112-0.

Boatwright J., 1980, A spectral theory for circular seismic sources: simple estimates of source dimension, dynamic stress drops, and radiated energy. *Bull. Seism. Soc. Am.*, 70, 1-28.

Bouchon M., 1982, The complete synthetics of crustal seismic phases at regional distances. *J. Geophys. Res.*, 87, 1735-1741.

Cruz-Atienza V.M., 2000, Inversión global con algoritmos genéticos y cristalización simulada aplicada a funciones de receptor: modelos estructurales de velocidades para la corteza en la República Mexicana. Tesis, p. 215, Facultad de Ingeniería, Universidad Nacional Autónoma de México.

Dewey J.W., Suárez G., 1991, Seismotectonics of middle America, *in* Slemmons, D.B., Engdahl, E.R., Zoback, M.D., and Blackwell, D.D., eds., Neotectonicas of North America, Boulder, Colorado, *Geol. Soc. Am.*, Decade Map, V. 1, 309-321.

Figueroa J., 1964, El macrosismo de Jáltipan. 1. Sismologia. *Ingeniería*, July, 357-362.

Figueroa J., 1970, Catálogo de sismos ocurridos en la República Mexicana. Report 272, Instituto de Ingeniería, Universidad Nacional Autónoma de México, 88 p.

Franco S.I., Canet C., Iglesias A., Valdés-González C., 2013, Seismic activity in the Gulf of Mexico. A preliminary analysis. *Boletín de la Sociedad Geologíca Mexicana*, 65, 447-455.

Frohlich C., 1982, Seismicity of the central Gulf of Mexico. *Geology,* 10, 103-106.

INEGI, 2010, Censo de Población y Vivienda, Instituto Nacional de Estadística y Geografía.

Kanamori H., Mori J., Heaton T.H., 1990, The 3 December 1988, Pasadena earthquake (M_L = 4.9) recorded with the very broadband system in Pasadena. *Bull. Seism. Soc. Am.*, 80, 483-487.

Keilis-Borok V., 1959, On estimation of displacement in an earthquake source and of source dimension. *Ann. Geofis.(Rome)*, 12, 205-214.

Kelleher J., McCann W., 1976, Buoyant zones, great earthquakes, and unstable boundaries of subduction. *J. Geophys. Res.*, 81, 4885-4908.

Marsal R., 1961, Behavior of a sandy uniform soil during the Jaltipan earthquake, Mexico. *Proc. V Intern. Conf. Soil Mech. and Foundation Eng.*, V. 1, 229-233.

Molnar P., Sykes L.R., 1969, Tectonics of the Caribbean and middle America regions from focal mechanisms and seismicity. *Geolog. Soc. Am. Bull.*, 93, 514-523.

Nettles M., 2007, Analysis of the 10 February 2006 Gulf of Mexico earthquake from global and regional seismic data, *in* Proceedings of Annual Conference, Offshore Technology, Houston, Texas.

Ordaz M., Arboleda J., Singh S.K., 1995, A scheme of random summation of an empirical Green´s function to estimate ground motions from future large earthquakes. *Bull. Seism. Soc. Am.*, 85, 1635-1647.

Pacheco J., Singh S.K., 1998, Source parameters of two moderate Mexican earthquakes

estimated from a single-station, near-source recording, and from MT inversion of regional data: a comparison of the results. *Geofísica Internacional*, 37, 95-102.

Reséndiz D., 1964, El macrosismo de Jáltipan. 2. Suelos. *Ingeniería*, July, 362-379.

Rosenblueth E., 1964, El macrosismo de Jáltipan. Introducción. *Ingeniería*, July, 357.

Singh S.K., Astiz L., Havskov J., 1981, The seismic gaps and recurrence periods of large earthquakes along the Mexican subduction zone: a reexamination. *Bull. Seism. Soc. Am.*, 71, 827-843.

Singh S.K., Pacheco J., Courboulex F., Novelo D., 1997, Source parameters of the Pinotepa Nacional, Mexico, earthquake of 27 March, 1996 (M_w=5.4) estimated from near-field recordings of a single station. *J. Seism.*, 1, 39-45.

Singh S.K., Ordaz M., Pacheco J.F., Courboulex F., 2000a, A simple source inversion scheme for displacement seismograms recorded at short distances. *J. Sesism.*, 4, 267-284.

Singh S.K., Pacheco J.F., Ordaz M., Kostoglodov V., 2000b, Source time function and duration of Mexican earthquakes. *Bull. Seism. Soc. Am.,* 90, 468-482.

Suárez G., 2000, Reverse faulting in the Isthmus of Tehuantepec: Backarc deformation induced by the subduction of the Tehuanlepec ridge, *in* Delgado-Granados, H., Aguirre-Diaz. G., and Stock, J. M., eds., Cenozoic Tectonics and Volcanism of Mexico, Boulder, Colorado, *Geol. Soc. Am*., Special Paper 334, 263-268.

Suter M., 1991, State of stress and active deformation in Mexico and western Central America, *in* Slemmons, D.B., Engdahl, E.R., Zoback, M.D., and Blackwell, D.D., eds., Neotectonics of North America, Boulder, Colorado, *Geol. Soc. Am*., Decade Map, V. 1, 401-421.

Wickens A.J., Hodgson J.H., 1967, Computer reevaluation of focal mechanism solutions, 1922-1962, Dominion Observatory, Ottawa, Publications 33, 233 p.

Zoback M.L., *et al.*, 1989, Global pattern of tectonic stress, *Nature*, 343, 291-298.

Zoback M.L., *et al*., 1990, Stress map of North America, Geological Society of America, The Decade of North American Geology, Continent-scale map- 005, 1:5,000,000.

Zoback M.D., Zoback M.L., 1991, Tectonic stress field in North America and relative plate motion, *in* Slemmons, D.B., Engdahl, E.R., Zoback, M.D., and Blackwell, D.D., eds., Neotectonics of North America, Boulder, Colorado, *Geol. Soc. Am*., Decade Map, 1, 339-366.